Control of Crystallization by Polymer Additives

Von der Naturwissenschaftlichen Fakultät der

Gottfried Wilhelm Leibniz Universität Hannover

zur Erlangung des Grades

Doktor der Naturwissenschaften (Dr. rer. nat.)

genehmigte Dissertation

von

Maxim Benjamin Gindele, *M.Sc.*

2023

Difficulties strengthen the mind, as labor does the body.

\- *Lucius Annaeus Seneca*

Abstract

Understanding how crystallization processes are controlled by polymer additives is relevant for a vastly diverse number of fields, for example in biomineralization, where the morphology of minerals is controlled by proteins or in scale inhibition strategies in industrial plants, in which macromolecules are added to prevent the precipitation of minerals. While numerous investigations have focused on elucidating additive-controlled crystallization, a detailed understanding of the underlying mechanisms is still desired. Herein, based on calcium carbonate as a mineral system, a comprehensive study on the manifold effects of selected polycarboxylate additives on the distinct species along the crystallization pathway is presented. Poly(glutamic acid) and poly(aspartic acid) are chosen as additives, as these polyaminoacids resemble biomineralization-associated peptides, as well as poly(acrylic acid), a commercially used scale inhibitor. Using potentiometric titrations, it is shown that even the basic interaction of polycarboxylates with calcium ions is more complex than commonly assumed. Quantitative determination of the Langmuir parameters of the binding process reveals that higher order effects and contributions arising from the whole polymer chain play a significant role, while the chemistry of the monomer unit constituting the polymer plays a subordinate role. The results put a question mark on whether the binding processes can be accurately described using solely the Langmuir binding model that assumes non-interacting binding sites. The investigation of the following stages of the crystallization pathway reveals that the polymer additives show the largest effect in the stabilization of liquid-like mineral precursors. A key step of this inhibition is the additive-driven binding of bicarbonates. Quantitative evaluation of ion association in the prenucleation regime reveals that more than 20% of bicarbonate species are bound in mineral precursors at pH 9.8, which can also be detected in isolated solid amorphous intermediates. Surprisingly, the protons introduced by bicarbonates are highly mobile, causing the formation of amorphous mineral ion conductors, which opens up possibilities for novel applications of mineral materials. The importance of liquid-like precursors for the mineral formation pathway is still highly debated in the community, and they are often ignored in the explanation of crystal formation. Using a refined gas diffusion method, it is demonstrated that liquid-like precursors show sufficient kinetic stability to be detected, both in presence of polymers and in additive-free systems. Observing the time dependent formation and transformation of the precursors shows that they play an important role in the early stages of crystallization and must be generally considered for the interpretation of gas diffusion experiments. Regarding the technological application of liquid-like minerals, a new and easily scalable synthesis method is presented, which solves existing limitations of the available synthesis methods. The "scalable controlled synthesis and utilization of liquid-like precursors for technological applications" (SCULPT) method effectively allows the isolation of the precursor on a gram scale and to access to the full potential of these mineral precursors for material synthesis. Implementing the gained insights into the current picture of nonclassical mineral formation, which was subject of many advancements in recent years, an updated view on additive-controlled mineralization is presented. The discoveries presented in this work are beneficial for the scientific and industrially-related communities far beyond the field of nucleation and crystallization mechanisms, such as materials chemistry, and improve the understanding of the mechanisms underlying biomineralization and mineral formation in general.

Keywords: calcium carbonate • polycarboxylates • liquid-like minerals • nonclassical nucleation • amorphous materials

Acknowledgements

This doctoral thesis is based on experimental work that was carried out between June 2018 and November 2022 at the Leibniz University Hannover and the University of Konstanz. Without the help and support of numerous people this work would not have been possible, therefore I would like to express my gratitude to those who have helped and supported me along the way.

My biggest thanks go to Prof. Dr. Denis Gebauer for providing me the opportunity to work in his research group and for his invaluable guidance and helpful discussions during performance of this work.

I am also thankful for Prof. Dr. Marie Weinhart and Dr. Encarnación Ruiz-Agudo for being referees for this work and Prof. Dr. Armin Feldhoff for being chair of the examination board.

I am grateful for Dr. Guinevere Mathies and Prof. Dr. Christine Peter and the respective research groups for the helpful discussions and collaborations during this doctoral thesis. In addition, acknowledgement is addressed to Katharina Nolte, Dr. Fritz Schulze-Wischeler, Stephan Siroky, Michael Voggel, Lars Bolk, Cristina Ruiz-Agudo and Yu-Chieh Huang for their help and assistance. Special thanks go to Stella Kittel for her support in all questions ranging from performance of analytical experiments, organizational issues or any topic related beyond science.

Furthermore, I like to thank all bachelor and master students that have contributed to this work: Eduard Groß, Luisa Steingrube, Sina Nolte, Daniel Boemke, Katharina Stock, Johannes Rochau, Krzysztof Malaszuk, Kristina Kebel and Teodora Ilić.

I also like to thank all members of the research group of Prof. Dr. Denis Gebauer for the many discussions throughout the years and the very nice time shared together. It was always an excellent atmosphere in the group. This is also regarding all members of the groups of Prof. Dr. Denis Gebauer and Prof. Dr. Helmut Cölfen in Konstanz, where I started the work on this thesis.

I am very grateful towards Dr. Miodrag Lukić and David McDonogh for proofreading this work.

In addition, I thank all members of the GDCh young chemists' society (JCF) for the nice time spent together in Hannover and Konstanz. I like to express special thanks to the FJS 2022 organization team around Janina Carolin Höner and Karen Hindricks. Organizing this conference together was certainly one of the highlights in the last years.

I thank all my friends for their company and the encouragements throughout the last years and during my studies.

Finally, I thank my family for their unconditional support. Without them, this would not have been possible.

Table of Contents

Chapter 1   **Introduction**

1.1   Calcium Carbonate Crystallization and Nucleation Theories

Crystallization, the formation of crystals, is one of the most studied processes in chemistry. Already at the end of the 18th century, scientists were interested in crystallization processes, as they are key in understanding the structure of formed crystals and therefore the properties of the resulting materials.[1] Besides the relevance in material science, crystallization plays also a big role as a separation method, especially in technological applications.[2] In living systems numerous inorganic and organic crystals are formed that are essential for life, ranging from the formation of teeth and bones to biomineralization processes, through which whole exoskeletons are formed.[3]

Especially calcium carbonate ($CaCO_3$) biominerals, present for example in sea urchin spines and mollusk shells, are well studied, as these minerals are easily accessible, show a rich polymorphism, and a high crystallization control is achieved during their formation.[4] The crystallization control is usually associated with organic macromolecules that modulate the nucleation and growth of the biominerals. Until this day, living systems show an unparalleled degree of crystallization control compared to *in vitro* experiments.[5] Achieving a similar degree of crystallographic control in artificial environments has high potential for the synthesis of advanced and biomimetic materials.[6] Studying crystallization processes in $CaCO_3$ systems, especially regarding additive-controlled scenarios, therefore is of high interest toward synthesis of new $CaCO_3$ materials. In addition, the knowledge gained from these investigations can be transferred to other systems, such as calcium phosphates, which have huge relevance in biomedical applications.[4]

One of the main reasons why biomineralization processes are still unparalleled in terms of crystallization control is the lack of understanding the crystallization process itself. Several theories have been developed to describe the nucleation and mineral formation process,[7-8] however, a comprehensive and universally accepted theory is still missing, especially when considering more complex additive-controlled systems. In the last decades, existing theories for nucleation and growth have therefore been questioned, refined, and substituted with new views to better describe the structures visible in nature and laboratory experiments.[9]

1.1.1   Classical nucleation theory and prenucleation cluster pathway

Already more than 100 years ago Gibbs developed the basis of the classical nucleation theory (CNT), which received several refinements in the 20th century.[10] In brief, CNT describes nucleation through addition of individual ions (or other monomeric constituents) to a growing crystal nucleus. The initial nucleus is thereby formed due to microscopic structural fluctuations of the solution.[7] Due to the surface tension of the growing particle, the formation of a surface is accompanied by an energy cost, while the bulk free energy upon incorporation of monomeric

units from the solution into the particle decreases, as long as the solution is supersaturated. This interplay of free energy cost proportional to the surface of the particle and free energy gain proportional to the volume of the particles results in an energy barrier, whose maximum defines the critical radius. Upon exceeding the critical nucleus size, the particle can grow to a macroscopic size by attachment of monomers, i.e., ions in case of $CaCO_3$ (Figure 1.1, top).[7]
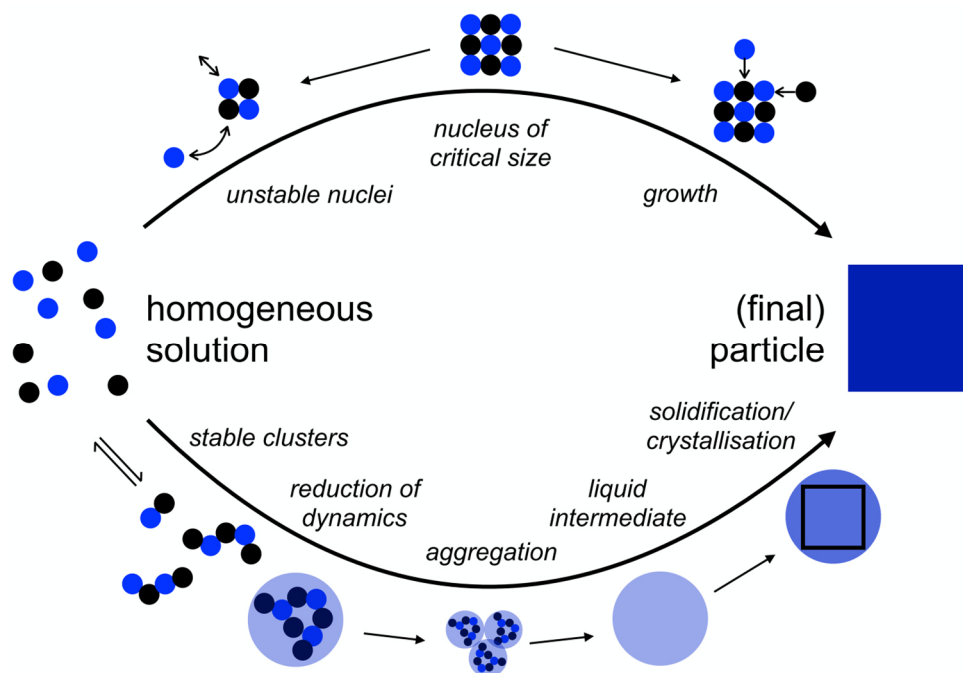
Figure 1.1   Illustration of classical nucleation theory (CNT, top) and the prenucleation cluster (PNC) pathway (bottom). For explanations refer to the text. Taken with permission from the author under terms of the CC-BY license.[11] Copyright 2018, MDPI.

Although CNT offers a quantitative and easy framework for nucleation, the experimental observations, such as nucleation rates, often differ by orders of magnitude from the calculated values.[12] This is likely due to drastic oversimplifications made in CNT in order to arrive at a quantitative description, particularly due to the "capillary assumption" that uses bulk material properties, such as solubility and interfacial energy, to describe nuclei smaller than 10 nm in size. While some systems can be described by CNT successfully,[13-14] the theory shows limited applicability to other systems. Especially in case of additive-controlled systems, the drastic effects of additives on the crystallization pathway cannot be explained by CNT, as the additives can only interact with the system in limited ways, i.e., reducing supersaturation by adsorption of ions or affecting interfacial tension by adsorption on the growing particle.

Due to these discrepancies, new models for nucleation and growth have been developed. In general, these assume the participation of non-monomeric species in the nucleation pathway, and are described as "nonclassical nucleation" theories.[15] One particularly relevant pathway is the prenucleation cluster (PNC) pathway, which was mainly developed from experimental investigations on $CaCO_3$ formation.[8] The PNC pathway exhibits strong explanatory power for

mineral systems and beyond,[16-17] especially when recent quantitative refinements of the model are considered.[18]

The PNC pathway nucleation model is based on the involvement of thermodynamically stable prenucleation clusters (PNCs) in the phase separation process (Figure 1.1, bottom).[19] The clusters are in equilibrium with individual ions and possess a polymer-like structure (so-called "dynamically ordered liquid-like oxyanion polymers" or DOLLOPs)[20] with a size of a 1-2 nm.[21] Upon increase of supersaturation, these chain-like structures develop a higher internal coordination, resulting in the decrease of cluster dynamics, finally resulting in the conversion of solute clusters to phase separated nanodroplets of a dense liquid phase (DLP).[22] This is also described as liquid-liquid phase separation (LLPS). In the following stages, these nanodroplets aggregate to reduce interfacial energy resulting in the formation of aggregates of several 100 nm in size.[11] Starting from this liquid mineral phase, several pathways have been observed toward formation of the actual crystal, involving additional intermediates such as amorphous species.[23]

1.1.2   Liquid-like mineral precursor phases

While the presence and participation of PNCs in the mineral formation process has been intensely discussed in the last years,[24-26] the presence of (dense) liquid mineral phases has been much less debated. Viscoelastic mineral precursor phases, often described as "liquid" or "liquid-like" precursors, were first described by Gower et. al. in the end of the 1990s for calcium carbonate formation in presence of poly(aspartic acid).[27-28] At the time, it was suggested that the polymer is essential for the formation of the liquid mineral, therefore the phase was described as "polymer-induced liquid-precursor" (PILP). However, later it was revealed that in polymer-free systems the phase separation also takes place via LLPS.[22, 29-32] The dense liquid mineral phase can be described as a water-rich amorphous mineral phase (recent estimates propose 7 water molecules per Ca^{2+} in the precursor),[33] which therefore possesses liquid-like properties. In addition, it was proposed that bicarbonates play a structural role in the (additive-free) calcium carbonate dense liquid phase,[31, 33-34] already hinting towards the complex interactions involved during the formation of the DLP. Stabilizing and achieving controlled crystallization of the mineral DLP is of particular interest for materials scientists, as the liquid-like properties allow the formation of new crystalline minerals possessing non-equilibrium morphologies and are very effective regarding infiltration of small pores, allowing the synthesis of porous or convoluted mineral structures.[35]

1.1.3   Transformation of precursor phases to crystalline minerals

Starting from the DLP, several pathways for the formation of crystalline minerals have been observed. In most systems, (hydrated) amorphous calcium carbonate (ACC) is detected as intermediate, which can be formed by dehydration of the DLP, while the precise transformation mechanism is still unclear.[36] It needs to be mentioned that hydrated ACC also possesses gel-

like properties up to a certain degree,[37] and that there is a continuous transition from the initially liquid-like precursor to the solid (gel-like) amorphous intermediate. In general, the water content and properties of ACC are highly dependent on the synthesis conditions resulting in a wide range of water contents of ACC.[38-39]

The transformation of ACC into crystalline minerals can in principle take place via two different ways: via dissolution-recrystallization or via a solid-state transformation process.[36] In most aqueous systems the ACC will dissolve and release ions that participate in nucleation of the crystalline phase, if the solution becomes supersaturated, or in crystal growth processes.[40] In this case, the dissolution kinetics of the ACC particles determine the local supersaturation and thereby affect the crystallization kinetics of the newly formed phase.

In case of solid-state transformation, dehydration of the ACC has to occur before crystallization, which can be achieved via external stimulation such as high temperature[41-44] or electron beam radiation.[39] Again, the resulting crystalline structure, i.e., crystalline polymorph, and the crystallite size can be tuned via the stimulus, as different stimuli cause different transformation kinetics of the ACC.[36] Regarding the solid-state transformation process it is especially intriguing that ACCs with different short-range order ("proto-structure") exist, that is, the calcium carbonate system exhibits amorphous polymorphism (polyamorphism).[45-46] Due to the structural similarity of the precursor phases to crystalline minerals, polymorph control may be achieved by the controlled synthesis and crystallization of the proto-structured amorphous intermediates. As described before, according to the PNC pathway the proto-ACCs are formed from the DLP which is itself formed from PNCs. This means that controlling the structure of PNCs can potentially help in achieving polymorph control for the formed minerals, especially as it has been shown that PNCs and small clusters can already possess such proto-structures.[47]

In combination with the possibility to control the morphology and macroscopic structure via the liquid-like properties of precursor phases, the strategy of controlling the crystallization starting from early precursor phases becomes a powerful approach towards synthesis of new materials. The big challenge in employing this strategy is the instability of the liquid-like precursors and amorphous intermediates and the limited understanding on how their structure and transformation to crystalline phases can be controlled. One promising approach is to seek inspiration in nature, where astonishing crystallization control in biomineralization is achieved via the participation of additives during the phase separation process.

1.2   Additive-Controlled Crystallization

In a broad sense, most crystallization processes occur in presence of additional species that can affect the crystallization. Usually, ionic species are present in the solution, for example in seawater,[48] or in the form of counterions during *in vitro* approaches.[49] In the case of calcium carbonate formation, it is known that metal ions, especially Mg^{2+}, have a strong effect on the stability of amorphous intermediates and can affect the formed crystalline polymorph.[50-52] In

addition to ions, arguably the most important species that can affect crystallization processes are macromolecules, especially in biomineralization.[53] Macromolecules are incorporated as organic components in most biominerals, which can therefore be described as hybrid materials. The composite nature leads to superior properties of these materials, for example in nacre, in which the organic matrix can function as an "adhesive" between aragonite platelets, which leads to remarkable thoughness.[5, 54] In addition, it was discovered that by using certain macromolecules, for example mollusk shell macromolecules[55] or coral acid rich proteins,[56] it is possible to control the ratio of formed $CaCO_3$ polymorphs. Understanding how macromolecules, or in general organic additives, can affect the crystallization and form distinct polymorphs is very promising for applications in material synthesis, as the toolbox of organic chemistry can be used to synthesize specifically designed additives for crystallization control.[57-58] The strong effect of macromolecules on the mineral formation pathway is already employed in industrial applications in the use of polycarboxylates, e.g., poly(acrylic acid), as scale inhibitors.[59-61]

1.2.1 Relevance of polycarboxylates in biomineralization

The macromolecules that build the organic matrix in biominerals are usually proteins, polysaccharides and lipids.[10] In general, the organic matrix is composed of soluble and insoluble components. In case of calcium carbonate biominerals, the soluble components are acidic macromolecules that are often rich in aspartic[55, 62-65] and glutamic acids,[66-70] and in many cases also contain polysaccharides.[53, 71-72] For example, glycoproteins of scallops contain around 20% aspartic acid,[73-74] while aspartic acid residues account for up to 60% of the protein aspein, which occurs in the pearl oyster *Pinctada fucata*.[75-76] Numerous investigations have been performed on biominerals to elucidate the mechanisms of biomineralization.[4] Thereby, it is assumed that the insoluble matrix can act as scaffold to determine where minerals are deposited, while the soluble macromolecules play a key role in controlling the nucleation and morphology of the biominerals. It was assumed that stereospecific interactions of the organic matrix with the growing crystal are responsible for the influence of organic additives on the morphology of the mineral, resulting in the characteristic "molded" non-equilibrium morphologies in biominerals.[6, 77] One key interaction was described as the selective adsorption of negatively charged macromolecules on specific crystallographic facets, thereby altering the crystal morphology.[65] In addition, it was discovered that organisms form amorphous calcium carbonates,[67, 78-80] for example during the mineralization of sea urchin spicules,[81-82] which can then act as precursor phases for more stable, crystalline polymorphs. It was shown that macromolecules play a key role for stabilizing ACC and governing the transformation of precursor species,[72, 83] while inhibiting the formation of crystalline polymorphs.[84] Interestingly, differences between aspartic acid-rich and glutamic acid-rich proteins were detected, although their chemical structure is quite similar. Thereby, in corals, glutamic acid-rich proteins are upregulated at the beginning of the crystallization pathway when ACC is formed, while at later

stages, during the formation of crystalline $CaCO_3$, the concentration of aspartic acid-rich proteins is increased.[56] Recently, there have also been reports of the relevance of liquid precursors to biomineralization in sea urchins that showed transformation to single crystalline calcite with complex morphology.[85] Due to similarity of the liquid precursors detected in the sea urchin to artificial polymer-stabilized liquid precursors, it is assumed that acidic macromolecules also play a key role in the stabilization and controlled crystallization of the this phase in biomineralization.[35] Although the biomineralization research field advances rapidly,[86] a full picture of the mechanisms governing biomineralization is still missing. Like in most biological systems, molecules, processes, and parameters involved are of high complexity. Therefore, *in vitro* investigations have been performed to gain a more fundamental understanding of the effects of macromolecules on calcium carbonate formation.

1.2.2   Effects of macromolecules on calcium carbonate crystallization *in vitro*

To gain insight into the interactions of acidic macromolecules on mineralization processes, synthetic poly(aspartic acid)s and poly(glutamic acid)s are often used to emulate the role of glycoproteins associated to biomineralization processes. In these *in vitro* approaches, the polymers show a strong inhibiting effect on the formation of crystalline calcium carbonates, with poly(aspartic acid)s showing a stronger inhibition compared to poly(glutamic acid)s.[87-88] If crystalline polymorphs are formed, it was observed that vaterite formation is promoted in the presence of the polymers.[89] Another effect was the stabilization of ACC, with increasing polymer concentration resulting in an increasing stabilizing effect.[90] Especially in combination with Mg^{2+} ions, the polymer additives show a strong stabilizing effect on amorphous intermediate species.[52, 91] Although these systems are much simpler compared to biomineralization environments, and in all systems large effects of polymers can be detected, the precise mechanism of crystallization inhibition and polymorph control remains to be elucidated. Usually additive adsorption on ACCs, followed by an interplay of dissolution-reprecipitation and pseudomorphic transformation processes is used as explanation, while the transformation is highly dependent on chosen parameters, such as polymer chain length, concentrations, and pH value.[90, 92-94]

According to CNT macromolecules can influence the crystallization in essentially two different ways: reduction of supersaturation by binding monomeric species or altering interfacial tension of the crystal by adsorption on the growing mineral phase.[11] The adsorption of monomeric species, in case of mineral formation the adsorption of ions, is of key relevance to technological applications of polyelectrolytes as additives for wastewater treatment.[95-96] Differences in the ion binding process have also been proposed as one explanation for the different effects of poly(aspartic acid)s and poly(glutamic acid)s on mineralization.[97] However, these additives show large effects on the crystallization already in distinctly substoichiometric amounts,[87, 98] therefore the sole reduction of supersaturation cannot explain nucleation inhibition. The

adsorption of polymer additives on distinct crystal facets based on interfacial matching, on the other hand, can affect the rates of crystallization for different polymorphs and crystal facets, resulting in different polymorph ratios.[65, 99-100] Nevertheless, explanations regarding the observed effects of the polymer additives on liquid-like precursors and amorphous intermediates are difficult to rationalize based on the notions of CNT.

Evaluating additive-controlled mineralization processes from the viewpoint of the PNC pathway provides many more interaction possibilities between the additives and the distinct precursor species occurring in the mineralization process (Figure 1.1, bottom). While no effects of the acidic macromolecules on PNCs or the locus of the binodal limit of LLPS have been detected so far,[22, 98, 101] numerous effects on liquid precursor and amorphous intermediate species have been observed. For example, it was shown that certain additives strongly interact with structural water in the amorphous phase, thereby affecting its mobility or suppressing dehydration, which in turn has effects on the ACC stability.[36, 102-104] Arguably the most interesting effect of the additives, however, is their stabilizing effect on liquid-like minerals.

1.2.3   Stabilization of liquid-like precursor phases by polymer additives

The stabilizing effect of additives on liquid-like mineral precursors was first described by Laurie Gower in the end of the 1990s, when "molded" calcium carbonate structures were observed in mineralization experiments in presence of poly(aspartic acid).[27-28] At that time, these structures were described as "polymer-induced liquid-precursors" (PILP), however, as already discussed above, later research revealed that these liquid-like mineral precursors are also formed in absence of polymers and that these structures are therefore polymer-stabilized rather than polymer-induced.[22, 31] Due to the similarity of the structures observed by Gower to the non-equilibrium morphologies observed in biominerals, it was assumed that liquid-like precursors play a key role in biomineralization.[35] Indeed, it was recently shown that liquid-like precursors participate in the biomineralization process in sea urchins.[85] Stabilization and controlled crystallization of liquid-like precursors also showed great potential for material synthesis due to complex morphologies accessible by this method.[105-107]

The formation of minerals via the polymer-stabilized liquid precursor can be described as a colloid assembly and transformation (CAT) process,[35] with the key steps involving assembly (fusion) of the polymer-stabilized viscoelastic (liquid-like) precursor colloids followed by their pseudomorphic transformation (crystallization) into the final solid matter. The detailed composition of the precursor phase and stabilization mechanism by the polymers are difficult to investigate because of the instability of the liquid-like precursor.[108] In general, it is assumed that the polymers kinetically stabilize the liquid-like precursor, and that a high degree of hydration, which correlates with the amount of incorporated polymer, is key for the liquid-like properties.[108] In addition, it has been reported that bicarbonates are accumulated in this phase, which might play an important role in its stabilization.[31] Recently, this view, and the relevance

of LLPS in the phase formation process, has been challenged and the PILP phase was described as consisting of 2 nm ACC particles that are cross-linked by polymer.[109] However, these results remain debated and illustrate the difficulties in investigating the properties that are actually inherent to the polymer-stabilized precursor phase.

1.3   Methodology: Using Potentiometric Titrations to Investigate the Early Stages of Crystallization

Potentiometric titration is a powerful tool to investigate crystallization processes.[110] The method was first described by Gebauer et. al. for the calcium carbonate system,[19] and is based on the slow mixing of dilute salt solutions, e.g. addition of calcium chloride solution into sodium carbonate solution, while the pH is kept constant by automatic addition of acid or base. By the addition of the solutions the system is slowly driven into supersaturation until phase separation occurs, while different parameters and concentrations are recorded *in situ* by potentiometric electrodes. The main advantage of this method is the ability to work at precisely controlled conditions, especially pH values, and the possibility to gain insights into the entire mineralization process, starting from the undersaturated solution up to the final crystalline particles. In *in situ* investigations using potentiometric electrodes, the dynamics of the species in the solution remain largely unaffected. The titration also allows isolation of mineral samples at distinct and well-defined stages along the crystallization pathway. These samples can then be analyzed using *ex situ* techniques, such as Fourier-transform infrared spectroscopy (FTIR) and scanning electron microscopy (SEM). *In situ* analysis by potentiometric titration coupled with sample isolation and *ex situ* characterization is a powerful strategy to investigate phase separation and material formation processes. This way, insights into the formation of numerous minerals could be gained, such as carbonate minerals,[111] phosphates,[112] oxalates,[113] hydroxides[114] and sulfates.[115] In addition, slightly modified titration-based methods were used to characterize phase separation of pharmaceutical compounds[116], metals[117] and metal oxides.[118-119]

To investigate $CaCO_3$ crystallization by potentiometric titration, dilute $CaCl_2$ solution is dosed into dilute sodium carbonate solution, with the pH held constant by automatic counter-titration of NaOH or HCl, respectively (Figure 1.2a). The development of the calcium activity is recorded by a calcium ion selective electrode (ISE), and optionally the turbidity of the solution can be tracked by an optrode. Using appropriate calibration procedures,[120] the measured calcium activities can be converted to (free) calcium concentrations, allowing for quantitative determinations. In a basic experiment, a linear increase of the free calcium concentration up to critical supersaturation is detected, followed by a drop indicating nucleation of a solid (Figure 1.2b, black curve). Then, a plateau in free calcium concentration is detected that is governed by the solubility product of the most soluble solid phase.
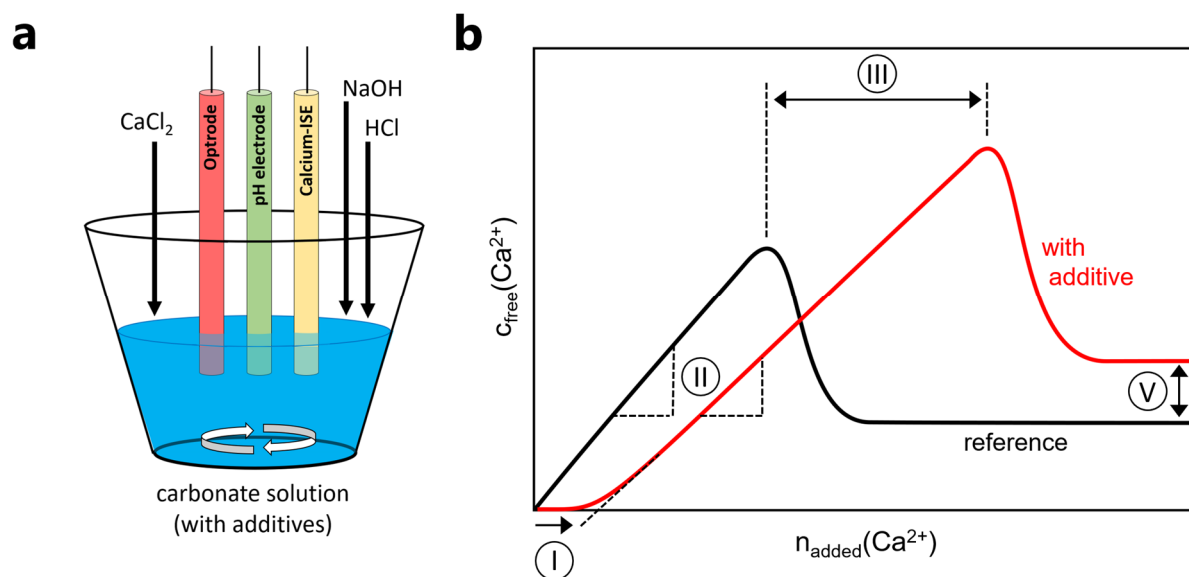
Figure 1.2 Experimental investigation of additive effects by potentiometric titration.
a) Illustration of the experimental setup for titration experiments. Dilute $CaCl_2$ solution is added into pure carbonate buffer (reference experiment) or to carbonate buffer with additives. The pH is kept constant by automatic addition of acid or base and during the addition, parameters are recorded *in situ* by electrodes. **b)** Exemplary development of free calcium concentration during additive-free reference experiments (black) and experiments with additive (red). Interactions of the additive with species along the PNC pathway (Figure 1.1, bottom) result in distinct changes visible in the titration curves. Please refer to the text for explanations.

The titration procedure is especially powerful for investigating the effect of additives on the crystallization process.[98] Thereby, the same experimental setup is used and additives are added to the carbonate solution. Then, the data recorded in presence of additives is compared to a polymer-free (reference) experiment, allowing the identification of different types of interactions (Figure 1.2b, red curve). In this way, changes in the initial offset of the curve indicate calcium ion binding by additives (type I);[121] changes in the slope of the curve in the prenucleation regime indicate interactions with prenucleation clusters (type II);[19] shifts in the maximum of the curve indicate nucleation inhibition (type III) and changes in the plateau of free calcium concentration detected after the drop indicate the presence of different species in the post-nucleation regime (type V). There are additional additive effects that are not directly visible in the titration experiments, e.g., face-specific adsorption of additives on crystals or effects on the oriented attachment of nanoparticles,[98] and additional characterization techniques have to be employed for further insights.

If we compare the scope of this experimental method to the numerous open questions regarding the effects of macromolecules on the mineralization (see section 1.2), it is evident that potentiometric titration is a powerful tool that can help to understand fundamental additive-mineral interactions, especially in the prenucleation regime. So far, there have been titration experiments performed investigating the effects of numerous additives on the $CaCO_3$

crystallization, among those the effects of amino acids,[122] small organic molecules and polymers,[98, 101, 115] carbohydrates,[123] and proteins.[124-125] Regarding polycarboxylates, it has been shown that poly(acrylic acid) shows a strong crystallization inhibition, with features indicating the stabilization of a dense liquid phase.[126] Investigations on poly(aspartic acid) showed strong inhibition, with significant stabilization of a more soluble phase in the postnucleation regime.[98] While the effects of the polycarboxylate additives have been evident in these titration experiments, as in experiments based on other methods, explanations for these effects are still missing, especially regarding the strong crystallization inhibition. It is therefore desirable to explore the fundamentals of additive-controlled $CaCO_3$ crystallization in a systematic and comprehensive way, especially in the view of the numerous advancements that have been made on the mechanisms of $CaCO_3$ crystallization in the past years.[16]

1.4 Scope of Thesis

The aim of this study was to gain insight into the fundamental interactions of polymer additives with the distinct stages along the calcium carbonate crystallization pathway. Thereby, calcium carbonate was chosen due to its crystallization pathway in absence of additives being rather well understood at this point, and its use as an established model system to explore mineral formation mechanisms in general. In order to investigate the calcium carbonate formation, potentiometric titration experiments were performed using selected, well-defined polycarboxylate additives, i.e., polymers with small polydispersities and similar chain lengths. A systematic strategy was chosen to investigate the additive-controlled crystallization by individually assessing the polymer effects at each stage of the mineral formation pathway, starting from interactions with ions and prenucleation clusters and later exploring the interactions with liquid-like, amorphous, and crystalline minerals. The polycarboxylates poly(aspartic acid) and poly(glutamic acid) were selected for this study, as they represent a simple form of the amino acid sequences occurring in proteins that are associated with calcium carbonate formation in biomineralization. In addition, poly(acrylic acid) is investigated to represent commercially used scale inhibitors. For these additives, strong effects on the calcium carbonate mineral formation pathway have been detected previously, however, the underlying interactions and mechanisms are still unknown. Recent advancements in the description of mineral precipitation, especially regarding the role of liquid-liquid phase separation and dense liquid phases challenge many of the previously described mechanisms of polymer-controlled crystallization, and it seems imperative to revisit the system from a new perspective.

First, the basic interactions of the polycarboxylates with calcium ions were studied. In a carbonate-free system and in absence of mineral formation, the adsorption of calcium ions by polycarboxylates with different chain lengths was quantified and tested against the Langmuir model, which is commonly used to describe ion adsorption by polymers. Understanding the basic mechanisms of the interaction of polymer additives with calcium ions and potential interactions with counter ions is crucial before moving on to more complex mineral systems. The corresponding results are shown in Chapter 2.

In the next step, carbonate ions were introduced in the system to investigate the effects of polymer additives on the mineralization process. Using potentiometric titration as basic tool, polymer effects on the early species of mineral formation were studied, while special focus was put on the strong inhibiting effect displayed by the additives at low concentrations. The key stages of mineral-additive interaction were then explored in more detail by isolation of mineral samples and performing *ex situ* characterizations using thermogravimetric analysis coupled with mass spectrometry and infrared spectroscopy (TGA-MS-IR), magic angle spinning nuclear magnetic resonance spectroscopy (MAS NMR) and conductive atomic force microscopy (C-AFM). The experimental insights and discussions are presented in Chapter 3.

In a separate part of this study, the question towards potential commercial uses of polymer-stabilized mineral precursors was addressed. Thereby, a novel synthesis method was developed to solve the previously existing problem of limited scalability of synthesizing liquid-like mineral precursors, which have been only available on milligram scales and could not be successfully isolated previously. The newly developed, specialized synthesis method allowed the use of high concentrations of starting solutions and production of the precursor phase on a gram scale. After optimizing the synthesis procedure by using selected organic and ionic additives, further investigations addressed the performance of the liquid-like calcium carbonate precursors for the synthesis of crystalline minerals in application-relevant systems. In addition, the effects of adjusting the used starting concentrations on the characteristics of the formed minerals were investigated. These investigations are shown in Chapter 4.

Finally, the effects of polymer additives on calcium carbonate crystallization were investigated with the widely used ammonia diffusion method (ADM). Focusing on poly(acrylic acid) as a model polymer, the changes in morphology and polymorph selection of the formed crystalline minerals was investigated. Using a previously established modified gas diffusion method with much shorter reaction time, the effect of additives on early stages, with focus on formation of liquid-like mineral precursor phases, was highlighted. Having a closer look at the polymer-free system with the method revealed the general importance of liquid-like mineral phases on $CaCO_3$ formation. The results are discussed in Chapter 5.

In summary, the main objectives of this work are:

- Examination of the adsorption of calcium ions by polycarboxylate additives in carbonate-free systems to gain mechanistic insights into the ion adsorption process

- Investigation of the interactions of polycarboxylates with different mineral species along the PNC pathway to identify the key interactions in the system

- Formulation of a mechanism that allows understanding the reasons for the strong nucleation and crystallization inhibition in presence of polycarboxylate additives

- Development of an experimental method that allows the synthesis of liquid-like mineral precursors on application-relevant scales

- Elucidation of the performance and the optimization of liquid-like precursors for mineral materials synthesis

- Exploration of additive effects on mineral precursors and crystalline minerals using gas diffusion experiments considering recent advancements in the understanding of nonclassical nucleation mechanisms

Chapter 2

On the Binding Mechanisms of Calcium Ions to Polycarboxylates: Effects of Molecular Weight, Side Chain and Backbone Chemistry

14

Record of Contribution

I performed all preliminary studies to the work, the majority of titration experiments, ITC experiments, polymer characterization as well as corresponding data analysis and evaluation, figure design and writing of the original manuscript draft. Krzysztof K. Malaszuk performed and evaluated additional titration experiments under my supervision and with my instructions. Prof. Dr. Christine Peter contributed with valuable ideas and discussions. Prof. Dr. Denis Gebauer developed the project idea and supervised the experimental work.

Publication

2.1 Abstract

We experimentally determined the characteristics and Langmuir parameters of the binding of calcium ions to different polycarboxylates. By using potentiometric titrations and isothermal titration calorimetry, the effects of side chain chemistry, pH value and chain length were systematically investigated using the linear polymers poly(aspartic acid), poly(glutamic acid), and poly(acrylic acid). We demonstrate that for polymers with high polymerization degrees, the binding process is governed by higher order effects, such as change of apparent pK_a of carboxyl groups, and contributions arising from the whole polymer chain while the chemistry of the monomer unit constituting the polymer plays a subordinate role. In addition, primary binding sites need to be present in the polymer, thus rendering the abundance and sequential arrangement of protonated and deprotonated groups important. The detection of higher order effects contradicts the assumptions posed by the Langmuir model of noninteracting binding sites and puts a question mark on whether ion binding to polycarboxylates can be described using solely a Langmuir binding model. No single uniform mechanism fits all investigated systems, and the whole polymer chain, including terminal groups, needs to be considered for the interpretation of binding data. Therefore, one needs to be careful when explaining ion binding to polymers solely based on studies on monomers or oligomers.

2.2 Introduction

The binding of divalent metal cations to polycarboxylates has been intensively investigated, as these processes occur in many areas of chemistry, biology and technology, e.g. in the removal of heavy metal ions from wastewaters[96, 127-128] or ion binding in metallopeptides in organisms.[129-130] Polycarboxylates can strongly adsorb on interfaces, rendering them important surface or crystallization modifiers.[96, 131-132] So as to enable the exploitation of the full potential of polycarboxylates in their respective technological applications, fundamental binding equilibria need to be well characterized as a first step to acquire a deeper understanding of the corresponding binding mechanisms.[133] On a molecular level, the binding of cations by carboxyl groups is entropically driven by releasing water molecules from the hydration shells of charged species.[95] Several theoretical models have been established to describe these binding processes, such as counterion binding and "site binding".[127, 134-136] The most commonly used model to describe experimental binding data is the Langmuir adsorption isotherm, which accounts for the dynamic equilibrium of adsorption and desorption.[137] Originally developed to describe gas-solid phase adsorption, the Langmuir isotherm has been successfully used to describe a wide variety of processes, and among them, ion binding in aqueous solutions.[138-141] Typically, Langmuir adsorption isotherms are determined by measuring adsorbent concentrations using atomic absorption spectroscopy (AAS),[131, 138-139, 142] high-performance liquid chromatography (HPLC)[140], photometric[141, 143] or gravimetric methods.[144] A different strategy is to make use of titration techniques, such as conductometric titrations[145], potentiometric titrations[95] or

isothermal titration calorimetry (ITC).[95, 146-148] The advantage of automated titration experiments coupled with *in situ* analytics is the relative ease to gather many data points compared to preparing individual samples as for non-titration-based methods. This guarantees a high quality of regression of experimental data with the respective model isotherms.

The binding of ions by peptides is a fundamental process occurring in biological systems, e.g., in signaling pathways, or biomineralization. Proteins or peptides containing charged aspartic and glutamic acid residues in the backbone often participate in binding processes via their carboxyl functions.[130] Aspartic and glutamic acid-rich peptides also strongly affect crystallization processes,[149] e.g., polymorph control during calcium carbonate formation and biomineralization.[28, 53, 55-56, 66, 90, 93, 98, 150-151] In this way, organisms can produce specific mineral polymorphs in target oriented ways by sequestering proteins.[55-56] In the case of ion removal from wastewaters and inhibition of industrial scale, the most investigated and large-scale manufactured polycarboxylate is poly(acrylic acid) (PAA). It is used as a water softener and commercial antiscalant,[135, 152-153] and also shows a strong effect on crystallization processes, such as stabilization of amorphous intermediates and distinct effects on the morphology of the formed crystals.[154-156] PAA can also be used to synthesize calcium carbonate-polyacrylate composite materials.[157] Again, the interaction of polymers with single ions is one of the underlying processes in aqueous systems. Therefore, investigating and understanding the interactions of polycarboxylates with free calcium ions is of fundamental importance. Previous studies indicated a strong dependence of the Ca^{2+} binding to PAA on the polymer chain length,[146] indicating that several dissociation constants are necessary to model Ca^{2+} binding to polyaspartate,[158] and that chelating effects are present in aspartate and glutamate monomers and dipeptides.[159-160] However, comprehensive studies comparing various polymers with defined polymerization degrees, narrow polydispersities and at precisely controlled pH values are still missing. Indeed, due to the changing protonation state of the polymers, the binding mechanism is expected to be pH-dependent,[161] which has not been assessed in detail and for different polymers in previous work.

In this study, we used an advanced potentiometric titration assay to determine the binding characteristics of poly(aspartic acid)s, poly(glutamic acid)s and poly(acrylic acid). Polymers with the same chain lengths and narrow polydispersities were used to resolve the effect of chain length on the binding process. ITC in a pH-constant environment allowed us to complement the potentiometric titration data. Our results reveal a significant influence of the chain length on the binding characteristics and elucidate the performance of different polymer types in metal ion binding in precisely controlled conditions. This provides new insights into the mechanisms of polymer-based metal ion removal from wastewaters, crystallization inhibition, and beyond. Additionally, the presented experimental protocol can be used for a wide range of metal cations if respective electrodes are available.

2.3 Experimental Section

2.3.1 Materials

Poly(L-glutamic acid) sodium salt, ($M = 6700$ g/mol, PD = 1.03) and poly(L-aspartic acid) sodium salt, ($M = 7400$ g/mol, PD = 1.04) with polymerization degrees of 50 were purchased from Alamanda Polymers Inc. Poly(L-glutamic acid) sodium salt, ($M = 2900$ g/mol, PD = 1.1) and poly(L-aspartic acid) sodium salt, ($M = 3700$ g/mol, PD = 1.1) with polymerization degrees of 20 were purchased from Nanosoft polymers. Poly(acrylic acid), 2-(Dodecylthiocarbono-thioylthio)-2-methylpropanoic acid (DDMAT)-terminated, ($M = 6800$ g/mol, PD < 1.1) was acquired from Sigma-Aldrich. Molecular weights of the polymers were experimentally determined by ^{1}H NMR spectroscopy (see section 2.6.5 in the supplementary information (SI) of this chapter) and polymer polydispersities were taken from the data provided by the manufacturers (see section 2.6.6 in the SI), as we encountered difficulties in our investigations and received different polydispersities dependent on the method used. Ac-Asp-NH$_2$, Ac-Glu-NH$_2$, triaspartic acid and triglutamic acid were purchased from BACHEM AG. 1.0 M calcium chloride stock solution (Fluka) from Fisher Scientific and 0.01 M NaOH and 0.01 M HCl stock solutions from Alfa Aesar were used. Borate buffer solution (pH 10.0) was obtained from Sigma Aldrich.

2.3.2 Polymer purification

In titration experiments, interference of the polymers with the calcium ion selective electrode (Ca-ISE) was observed that led to an irreversible damage of the electrode, which then had to be replaced (see supplementary discussion in section 2.6.1). This is most likely due to fractions of polymers with a small molecular weight that can penetrate, poison, or clock the ion carriers within the membrane of the used Ca-ISE.[95] Although polymers with a narrow polydispersity were used, the presence of small fractions of low-molecular weight oligomers cannot be excluded. Therefore, before titration experiments, the polymers with molecular weights above 6 kDa were purified by diafiltration using a molecular weight cut-off of 3 kDa (Amicon Ultra-15, PLBC Ultracel-PL membrane). After two washing cycles using Milli-Q water, a 100 mg/L polymer stock solution was prepared and used for titration experiments. The purification procedure significantly improved data quality, indicating that the problems with the Ca-ISE were indeed most likely caused by small molecular weight compounds in the purchased polymers. The stock solutions were stored in a fridge and freshly prepared every two days.

2.3.3 Potentiometric titrations

A commercial automated titration setup (Metrohm Titrando) controlled by computer software (Metrohm tiamo 2.3) was used for the titration experiments. A titration device (905 Titrando) controlled three dosing units (800 Dosino) for the precise addition of dilute CaCl$_2$, HCl and

NaOH solutions. The calcium potential was monitored using a calcium ion selective electrode (Ca-ISE, Metrohm, No. 6.0508.110) and the pH was measured using a pH electrode (Metrohm, No. 6.0256.100). The internal reference electrode of the pH electrode was used as a reference electrode for the Ca-ISE. All solutions were prepared using Milli-Q water.

Calibration of the pH electrode was carried out once per week using pH buffers from Mettler Toledo with pH 4.01 (No. 51302069), 7.00 (No. 51302047) and 9.21 (No. 51302070). The Ca-ISE was calibrated by dosing a 10 mM $CaCl_2$ solution at a rate of 0.04 mL/min into 25 mL Milli-Q water at the same pH value as the one used in the experiment. Experiments at pH values higher than 6 were performed under a stream of H_2O-saturated N_2 to prevent in-diffusion of CO_2. The pH value was kept constant by automatic counter titration of 10 mM NaOH or 10 mM HCl. Due to possible damage of the electrode by exposure to the polymers, the Ca-ISE was calibrated before and after each measurement to ensure the reproducibility of the electrode signal after exposition to the polymers. The calibration was carried out for 60 min, and both the pH electrode and Ca-ISE were regenerated twice a week by stirring for 2 h in 100 mM HCl (pH-electrode) and 10 mM $CaCl_2$ (Ca-ISE), respectively.

Binding experiments were carried out by adding a 10 mM $CaCl_2$ solution at a rate of 0.04 mL/min into 25 mL of 50 mg/L (PAsp20, PGlu20, pAsp50, PGlu50, PAA, Ac-Asp-NH_2 and Ac-Glu-NH_2) or 200 mg/L (H-Asp-Asp-Asp-OH and H-Glu-Glu-Glu-OH) polymer solution at the desired pH value (pH 9, 7, 6, 5 and 3). Before titration experiments, the pH was set to the desired value by adding small amounts of 10 mM NaOH and 10 mM HCl. The pH was then kept constant during the experiments by automatic addition of 10 mM NaOH and 10 mM HCl. The experiments were stopped after 60 min and the electrodes were quickly washed using Milli-Q water to minimize the time exposed to polymers. At least three independent experiments were performed for each pH value and each investigated polymer type.

Any potential precipitation of the polymers upon calcium addition was tracked using an optrode (Metrohm, No. 6.1115.000) operated at a wavelength of 660 nm. During the titration experiment, no increase in turbidity could be observed for the investigated polymer concentrations (data not shown).

2.3.4 Determination of binding parameters

In order to calculate binding parameters by potentiometric titration, the measured free calcium potentials of the ISE need to be converted into calcium ion activities. It should be noted that contributions of the polymers to the ionic strength of the solutions can be neglected, and due to the same ionic strength in both calibrations and experiments, ion activity obtained from the ISE data can effectively be treated as free ion concentration $(a(Ca^{2+})c^0 = c_{free}(Ca^{2+}))$.[120] The calculated $\ln(a(Ca^{2+}))$ was plotted against the measured $U(Ca^{2+})$. Then, the relevant potential regime for each measurement (e.g., from -50 to -10 mV) was fitted with a linear function. The

experimentally measured potential was then used to calculate the calcium activity according to the Nernst equation, as described elsewhere:[120]

$$U(\text{Ca}^{2+}) = U_0 + \frac{RT}{2F} \ln(a(\text{Ca}^{2+})) \tag{2.1}$$

In some cases, especially for polymer measurements, the calibration was not perfectly linear in the relevant regime of $U(\text{Ca}^{2+})$, which was most likely caused by interactions with the electrode membrane or interference caused by the polymers (see discussion in SI section 2.6.1). In this case, a nonlinear calibration with the following empirical exponential function was performed:

$$a(\text{Ca}^{2+}) = \exp\left(A_1 \exp\left(\frac{U(\text{Ca}^{2+})}{t_1} \right) + A_2 \exp\left(\frac{U(\text{Ca}^{2+})}{t_2} \right) + y_0 \right) \tag{2.2}$$

Thus, five parameters were used for the fit of the calibration curve, instead of two parameters as for the linear approach. The nonlinear function yields a better fit of the curves and therefore prevents significant errors in the conversion from $U(\text{Ca}^{2+})$ to $a(\text{Ca}^{2+})$, especially for potentials where the electrode behavior is nonlinear (Figure S2.1a in section 2.6.1). The nonlinearity of the electrode was well reproducible within a day, and the nonlinear calibration thus provides a reasonable conversion from calcium potential to calcium activity. In the next step, the amount of bound calcium ions at each point in the titration experiment was calculated:

$$n_{\text{bound}}(\text{Ca}^{2+}) = n_{\text{total}}(\text{Ca}^{2+}) - V_{\text{total}} c_{\text{free}}(\text{Ca}^{2+}) \tag{2.3}$$

where $c_{\text{free}}(\text{Ca}^{2+})$ corresponds to the concentration of free calcium ions in equilibrium with the calcium ions bound to the polymer and was calculated from the measured calcium activities due to $a(\text{Ca}^{2+})c^0 = c_{\text{free}}(\text{Ca}^{2+})$ for the equal ionic strength in the calibrations and binding experiments. $n_{\text{total}}(\text{Ca}^{2+})$ is the total amount of calcium ions in the solution and was calculated using the dosed volume of $CaCl_2$ solution (and any additional volumes due to pH titration). The Langmuir binding model was applied to calculate the parameters of the binding process according to

$$n_{\text{bound}}(\text{Ca}^{2+}) = \frac{n_{\text{max}} K_L\, c_{\text{free}}(\text{Ca}^{2+})}{1 + K_L\, c_{\text{free}}(\text{Ca}^{2+})} \tag{2.4}$$

Plotting $n_{\text{bound}}(\text{Ca}^{2+})$ against $c_{\text{free}}(\text{Ca}^{2+})$ and fitting with the function $y = (Ax)/(1 + Bx)$ enables the determination of the Langmuir binding parameters, with n_{max} representing the maximum binding capacity and K_L being the binding equilibrium constant. Due to the high number of data points recorded in each titration experiment (more than 1000 points), no linearization of the Langmuir adsorption isotherms is necessary, which is favorable for data regression.[162] However, a linear correction was applied to the raw data, as a nonlinear slope was visible at the end of titration experiments (see supplementary discussion 2.6.2).

2.3.5   Binding of counterions

25 mL of a stirred 200 mg/L polymer solution was set to pH 9 using 10 mM NaOH. Then, 100 mM $CaCl_2$ solution was added with a rate of 0.01 mL/min and the pH was kept constant by automatic counter titration with 10 mM NaOH. The pH value, calcium ion activity, and chloride ion activity were recorded during the titration. Therefore, a chloride ion selective electrode (Metrohm, No. 6.0502.120) was employed, which was calibrated alongside the Ca-ISE. The pH was measured with a double junction pH electrode (Metrohm, No. 6.0269.100) using KCl as an inner electrolyte and KNO_3 as a bridge electrolyte. Before each measurement, the bridge electrolyte was replaced to ensure no leakage of chloride into the solution took place.

2.3.6   Isothermal titration calorimetry (ITC)

Isothermal titration calorimetry experiments were performed on a Malvern VP-ITC at 25 °C. Solutions with 50 mg/L polymer with a 1 wt-% borate buffer (pH 10.0) were prepared using Milli-Q water and set to pH 9 using 0.01 M HCl. The borate buffer was necessary to stabilize the pH value during the titration to achieve pH-constant conditions comparable to potentiometric titration experiments. The effect of the 1% borate buffer on the binding process was investigated by performing potentiometric titration experiments in buffer solution. The same conditions and parameters as those described in the previous section were used for the experiments, except that the 1% buffer solution was used for the Ca-ISE calibration, and that the pH was not kept constant in the binding experiment due to the sufficient buffer capacity. The results showed that a constant pH value during the experiments could be achieved (less than 0.05 pH units drift) and that no effect on the association constant K_a was observed. This is in line with literature binding constants of calcium in borate-polyhydroxycarboxylate systems, which are several orders of magnitude lower compared to the calcium-polycarboxylate binding investigated in this study.[163] However, roughly a 20% increase in n_{max} was observed in titrations with borate buffer (data not shown).

In ITC experiments, 1.5 mM $CaCl_2$ (2.5 mM for PAA) was titrated into the polymer solution at a stirring rate of 600 rpm and a reference power of 12 µCal/s at pH 9. Usually, 26 injections of 10 µL each were performed with a spacing of 200 s, with a 2 µL injection before the first injection. As reference experiments, titrations of $CaCl_2$ into the 1 wt-% pure buffer solution and the NaCl solution (the same ionic strength as the $CaCl_2$ solution) into polymer/buffer solutions were performed. The data points were processed using ITCsy (sedphat) and NITPIC (The University of Texas Southwestern Medical Centre) software. For evaluation, the reference experiments were subtracted, and the curves were fitted with a simple hetero association model ($A + B \rightleftharpoons AB$) in ITCsy, while the first 2 injections were not considered for the evaluation. From the sigmoidal fits the thermodynamic parameters of the binding process, ΔG^0, ΔH^0 and ΔS^0, were calculated according to standard procedures.[164-165]

2.4 Results and Discussion

2.4.1 Investigated polycarboxylates

In this study, we investigated the binding processes of calcium ions by selected polycarboxylates at different pH values. Polymers with a low polydispersity were chosen to determine the effects originating from differences in the polymerization degree and functional groups. A detailed overview of all investigated compounds is given in Table 2.1.

Table 2.1   Overview of compounds and their abbreviations (Abbr.) used in this study. In addition, polymerization degrees (DP_n), molecular weights (M) and polydispersities (PD) are provided. Polymer structures are shown with protonated carboxyl groups

Abbr.	Name	Chemical Structure	DP_n	M [g/mol]	PD
PAsp50	poly(aspartic acid) sodium salt		55[a]	7400[a]	1.04[b]
PAsp20			27[a]	3700[b]	1.10[b]
Asp3	triaspartic acid; H-Asp-Asp-Asp-OH		3	363	-
Asp1	aspartic acid monomer (protected); Ac-Asp-NH$_2$		-	174	-
PGlu50	poly(glutamic acid) sodium salt		45[a]	6700[a]	1.03[b]
PGlu20			22[a]	2900[a]	1.1[b]
Glu3	triglutamic acid; H-Glu-Glu-Glu-OH		3	405	-
Glu1	glutamic acid monomer (protected); Ac-Glu-NH$_2$		-	188	-
PAA	poly(acrylic acid)		91[a]	6800[a]	<1.1[b]

[a]Determined by ^{1}H NMR spectroscopy (see SI section 2.6.5).
[b]Determined by GPC, according to the manufacturer's certificate of analysis (see SI section 2.6.6).

It is known that the polymerization degree of an additive may have large effects on additive-controlled crystallization processes.[98] Therefore, we investigated poly(aspartic acids) and poly(glutamic acids) with different chain lengths (DP_n = 50 and 20) as well as the respective trimers (DP_n = 3) and monomers. The free acid groups of the terminal amino acid can also participate in the binding process, resulting in a bidentate binding of the ions. This contrasts with the amino acid repeating unit in a polymer chain, where two amino acids neighbor it. Therefore, the investigations with the monomers were carried out using protected amino acids, in which the terminal groups are chemically protected to create a similar chemical environment with regards to the amino acids in a peptide. In addition, all experiments were performed using a comparable ionic strength in the starting solution, as differences in ionic strength also affect the binding process (Figure S2.9).[166] The pK_a values of all polymers fall in a similar range and are therefore only considered qualitatively in the following discussion (see SI discussion 2.6.3).

2.4.2   Binding parameters from potentiometric titration

The Langmuir binding parameters were determined using potentiometric titration. A diluted solution of CaCl₂ was added to the polymer solution, while the pH was recorded and kept constant by automatic counter titration with NaOH. During the addition, the free calcium activity was recorded using an Ca-ISE, so the free and bound calcium concentrations could be precisely determined at each point in the experiment. At the beginning of the experiment, added calcium is bound to the polymer, therefore the increase in calcium activity is less than expected from the added amount of calcium. From the concentrations of bound and free calcium ions, the binding parameters can be calculated by fitting the experimental data with a Langmuir binding isotherm and a linear correction term due to non-zero slopes at the end of experiments:

$$n_{\text{bound}}(\text{Ca}^{2+}) = \frac{n_{\max} K_L\, c_{\text{free}}(\text{Ca}^{2+})}{1 + K_L\, c_{\text{free}}(\text{Ca}^{2+})} + K_{\text{corr}} * c_{\text{free}}(\text{Ca}^{2+}) \qquad (2.5)$$

where K_L represents the Langmuir binding constant, $n_{\max}$ is the maximum binding capacity, and K_{corr} is the linear correction factor. The linear correction term was introduced to account for the non-zero slope at the end of potentiometric titration (see SI section 2.6.2 and related discussions). This effect can be attributed to the interference of the polymers with the electrode and is not discussed further herein. The titration setup automatically maintains a constant pH value during the binding process and the pH-dependence of the binding parameters can be determined for PAsp50, PGlu50 and PAA, individually. In addition, PGlu20 was investigated to quantify the effect of different polymerization degrees. Experiments with PAsp20 are not shown due to the strong interactions with the Ca-ISE membrane, as no polymer purification was possible (see experimental section 2.3.2). Other experiments showed good reproducibility and the binding parameters were determined in the pH range from 3 to 9 (Figure 2.1 and Figure S2.10). All parameters determined by titration are listed in Table S2.2 in section 2.6.8 in the SI.
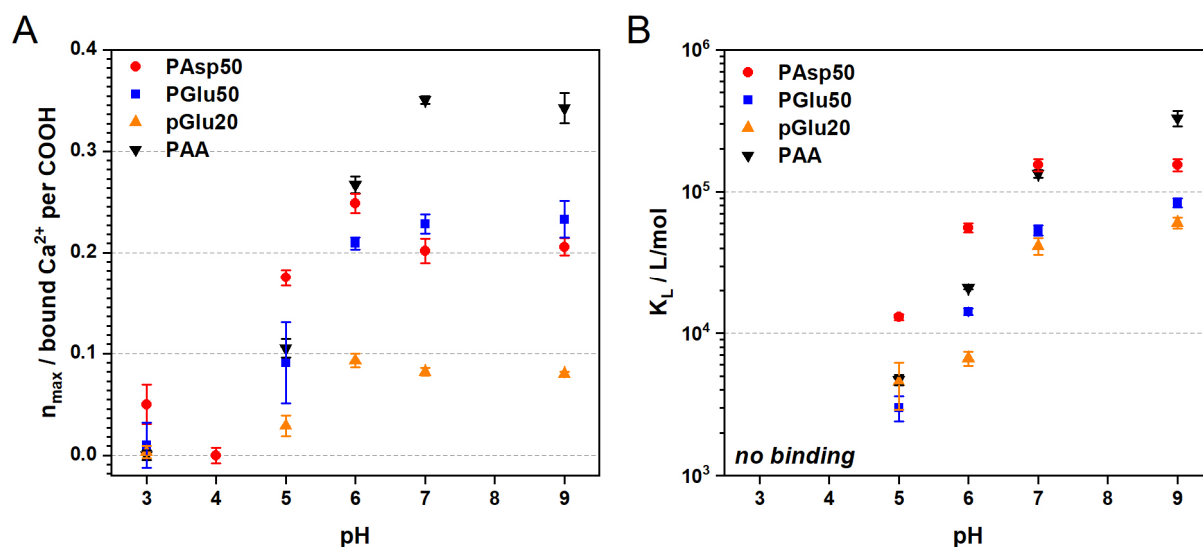
Figure 2.1 pH-dependence of binding parameters for different polycarboxylates. The Langmuir binding parameters **a)** n_{max} (maximum binding capacity) and **b)** K_L (Langmuir binding constant) are shown. To determine the Langmuir parameters, we used an additional linear correction term to account for non-zero slopes in bound calcium after the end of the experiments that are due to polymer interference with the Ca-ISE. Linear correction parameters K_{corr} are shown in Figure S2.11.

From the maximum binding capacity n_{max} (Figure 2.1a), it becomes evident that polymers with higher molecular weights possess increased binding capacity at all investigated pH values. At pH 7 and 9, PAA ($DP_n \sim 100$) exhibits the highest binding capacity with 0.35 bound Ca^{2+} ions per monomer segment, followed by PAsp50 and PGlu50 ($DP_n \sim 50$) with n_{max} around 0.20 to 0.25 followed by the shortest polymer PGlu20 ($DP_n \sim 20$) with $n_{max} = 0.07$. Remarkably, the binding capacities of pAsp50 and PGlu50 are very similar despite their different chemical structures, but significant differences for PGlu50 and PGlu20 are detected. This hints towards a binding mechanism that is determined by effects arising primarily from chain length, instead of being determined by the chemical structure of a monomer unit or a short segment of a chain. This could be possible through bidentate/polydentate binding in terms of intramolecular interactions of neighboring groups in the chain, polydentate binding by groups with larger spatial separation in one polymer chain, or intermolecular interactions. The decrease in binding capacity starting from pH 5 is qualitatively in line with the pK_a values of the polycarboxylates (see supplementary discussion 2.6.3), where an increasing degree of protonation corresponds to lower binding capacities. For all investigated polymers, almost no adsorption occurs at pH 3 ($n_{max} \approx 0$), implying that no Ca^{2+} binding is possible on predominately protonated chains. Due to the much higher abundance of protons at low pH values, Ca^{2+} ions and protons compete for binding sites.

The comparison of the Langmuir adsorption coefficients K_L of the three polymers (Figure 2.1b) indicates differences among the polymer types. In the whole pH range, the adsorption coefficients for PAsp50 are significantly higher than for PGlu50, while there is only little

difference between polymers with different chain lengths (PGlu50 vs. PGlu20). Therefore, in terms of the Langmuir adsorption coefficient K_L, differences in the molecular structure of the monomer units are relevant rather than polymerization degree. Again, for all investigated polymers, a lower pH value yields a lower binding constant. The adsorption coefficients of the polycarboxylates are in the order of 10^3 L/mol (pH 5) to 10^5 L/mol (pH 9), which is a moderate binding strength for a chelator. For comparison, the K_L value of the Ca^{2+} binding by EDTA ($3.8 \cdot 10^6$ L/mol at pH 7.4 in HEPES) is at least one order of magnitude higher.[146, 167] An interesting trend is visible for PAA, as for pH values lower than 7, the K_L is smaller than for PAsp50, while for pH 9, the binding constant is considerably higher. This can be understood considering the titration curves (Figure S2.12). At pH 9, almost quantitative binding at the beginning of the titration can be observed for PAA, while at lower pH values, the process can be described by Langmuir isotherms. Therefore, due to the non-Langmuir behavior at pH 9, the binding constant is not ideally represented and overestimated by the applied Langmuir fit. Several other binding isotherms were tested, but no isotherm can account for quantitative binding in the beginning of the titration. Therefore, the data for PAA at high pH has to be interpreted carefully. One explanation for the deviation from the Langmuir isotherm might be a different mechanism of binding at low binding coverage. In the beginning, PAA can strongly bind calcium, possibly by chelating and interactions of several carboxyl groups with one calcium ion. Later, at higher calcium loads, this mechanism might not be possible anymore due to interactions between calcium ions and could therefore start to follow a Langmuir type binding more closely. Alternatively, non-Langmuir behavior could be caused by phase separation in the system. Indeed, it was reported that precipitation of calcium-PAA coacervate takes place at a critical molar ratio of calcium and carboxyl groups of 0.3 to 0.4 at higher polymer concentrations.[95, 168] In the titration experiments, this critical ratio range theoretically occurs between 700 to 900 s, which corresponds to a free calcium concentration of 10 to 40 μmol/L (Figure S2.12). The potential precipitation of Ca-PAA coacervate was also experimentally assessed using a titration setup coupled with an optrode, however, no precipitation was visible (data not shown). This is potentially due to the lower polymer concentrations used in the experiments than in the other studies. Regardless of whether coacervate formation is taking place in the investigated system or not, significant differences in the PAA binding characteristics at high pH values compared to lower pH values, and compared to the other polycarboxylates, are evident.

In the neutral pH regime, the polycarboxylates are partially protonated and calcium ions can replace the protons of the polymer to bind to the carboxyl groups. Since protons are released during this process, they can be tracked by the amount of NaOH added during the titration to keep the pH constant (Figure 2.2a). At higher pH values, polymers are fully deprotonated and at low pH values, no binding takes place, resulting in a pH window at which a significant NaOH addition can be observed during the titration experiments. In our work, this effect was visible between pH 5 and pH 7. This additionally illustrates the broad range of pK_a values of the

polymers (see SI section 2.6.3) and the broad pH range, in which the polycarboxylates are partially protonated.
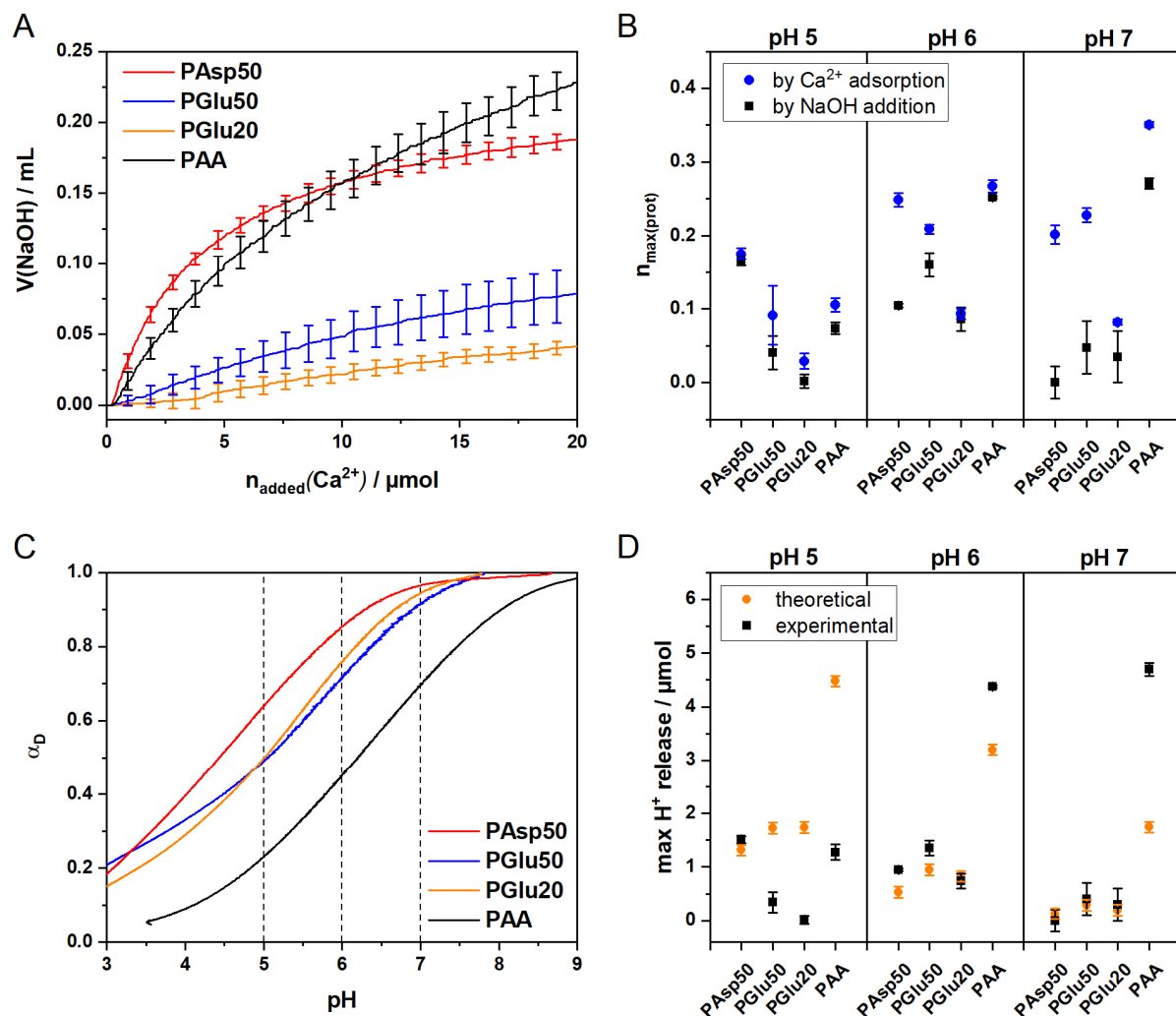

Figure 2.2   Insights into the binding process from proton release. a) Volume of NaOH added during the titration experiments at pH 5 for the different polymers. **b)** Calculated n_{max} from Ca^{2+} adsorption (bound Ca^{2+} per COOH) and $n_{max(prot)}$ calculated from the amount of the added NaOH solution (released H^+ per COOH). **c)** Dissociation degree α_D of polymers calculated from potentiometric titration data. **d)** Comparison of the theoretical maximum proton release upon binding calculated from the dissociation degree α_D in comparison with values calculated from $n_{max(prot)}$ from NaOH addition.

The amount of added NaOH was also fitted with a (linearly corrected) Langmuir isotherm, which allows to determine $n_{max(prot)}$ from the number of released protons. The parameter $n_{max(prot)}$, thus, allows us to determine the amount of calcium ions binding to protonated groups, which can be compared to the overall n_{max} for calcium binding determined by the calcium ISE (Figure 2.2b). At pH 5, for all investigated polymers, the amount of released protons is very similar to the amount of bound calcium, showing that essentially, for a calcium ion to bind to the polymer, a proton is released. At pH 6, PAA and PGlu20 show the same behavior, however, for PGlu50

and PAsp50, $n_{max(prot)}$ is lower than n_{max}, so a significant extent of binding occurs to deprotonated groups. Upon further increase of the pH value to 7, the amount of released H^+ becomes even smaller for the poly(amino acids); however, for PAA, a large release of protons is recorded, which seems to be difficult to rationalize. At pH 9, the polymers are essentially fully deprotonated, and no NaOH titration due to proton release was detected within experimental accuracy. Further insights into the different calcium ion/polymer systems can be obtained by comparing the number of released protons (i.e., the amount of added NaOH to keep the pH value constant) to the theoretical number of protons that the polymer can release at a given pH value. We have, therefore, calculated the dissociation degree of the polymers in dependency of pH (Figure 2.2c) using the pH titrations of the polymers (Figure S2.3).[169] The pH titrations show that the dissociation degree of PAsp50 is higher than that of PGlu50/PGlu20 at any given pH value. In principle, PGlu50/PGlu20 exhibits the same dissociation degree as PAsp50 at pH values that are higher by around 0.5 to 1 unit. This trend is also consistent with the difference in K_L from the binding experiments, with the pK_L of PAsp being roughly one pH unit shifted to lower pH values (Figure 2.1b). Although the pK_a values of the polymers exhibit a broad distribution, the apparent pK_a of PAsp is lower than that of PGlu, resulting in higher dissociation degrees at a given pH value and higher K_L.

From the individual dissociation degrees, the theoretical number of protons that can be released was calculated and compared to the detected number of released protons (Figure 2.2d). PAsp50 has a slightly lower number of protons that can theoretically be released at a given pH value compared to PGlu50/PGlu20, which probably lies within experimental certainty. In the case of PAsp50 at pH 5, essentially all H^+ are released during the binding process, resulting in a much higher n_{max} compared to the poly(glutamic acid)s, which can release protons only partially. The data for PAsp50 at pH 5 is very interesting; 60% of the carboxyl groups are initially deprotonated, and we determine a value for n_{max} corresponding to 0.2 bound calcium ions per carboxyl group. Theoretically, enough groups are deprotonated already from the beginning so that the calcium binding may occur exclusively at deprotonated groups, yet we detect that essentially all protons are released in the binding process. At pH 5, the binding of Ca^{2+} is directly coupled to the release of protons, while at lower pH values, at which the polymer is fully protonated, no binding is detected. This suggests that cooperative effects play a role in the binding process. Essentially, it appears that an initially deprotonated binding site is required to exist close to a protonated one, so that the initial calcium binding can occur, which then lowers the pK_a of the neighboring carboxyl group, leading to deprotonation. Upon further binding, the neighboring groups release their protons to bind more calcium. Alternatively, we can assume bidentate binding by neighboring groups or folding of the polymers. This trend is also visible at pH 7 (Figure 2.2d), where the polymers exhibit a deprotonation degree larger than 90%. Yet, we still detect full deprotonation of the polymers upon calcium binding. Although binding is also possible at fully deprotonated groups, i.e., at higher pH values, our results indicate that binding processes that lead to full deprotonation of the polymers are favorable.

In the case of PAA, higher experimental proton release than theoretically possible occurs at pH 6 and 7. The reason for this unphysical effect is unclear; however, taking the above-described effects of potential polymer precipitation and the very strong initial binding of calcium by PAA into account, we propose that complete deprotonation of PAA upon calcium ion binding occurs at all pH values. We attribute the additional unphysical proton release to interference of PAA with the pH electrode, e.g. due to precipitation of "sticky" Calcium-PAA precipitates on the electrode membrane which might affect its pH responsiveness and thereby the amount of added NaOH in the experiments. This might also explain the practically identical amount of NaOH addition detected at pH 6 and pH 7 for PAA, although the dissociation degree and the binding capacity are clearly different at these two pH values. We like to emphasize that this behavior was detected exclusively for PAA, and that in all other systems a good agreement between theoretical and experimental H^+ release was detected. We therefore argue that, except for PAA, extracting quantitative data from NaOH addition is reasonable.

Additional experiments at pH 9 using poly- and oligo(amino acid) compounds with different polymerization degrees were performed. Poly(aspartic acid) and poly(glutamic acid) 50mers, 20mers, unprotected trimers, and protected monomers were investigated (see Table 2.1). Relative binding capacities, i.e., bound Ca^{2+} per carboxyl group, and binding constants decrease for both polymers from 50mers to 20mers and for protected monomers, no binding was detected (Figure 2.3).

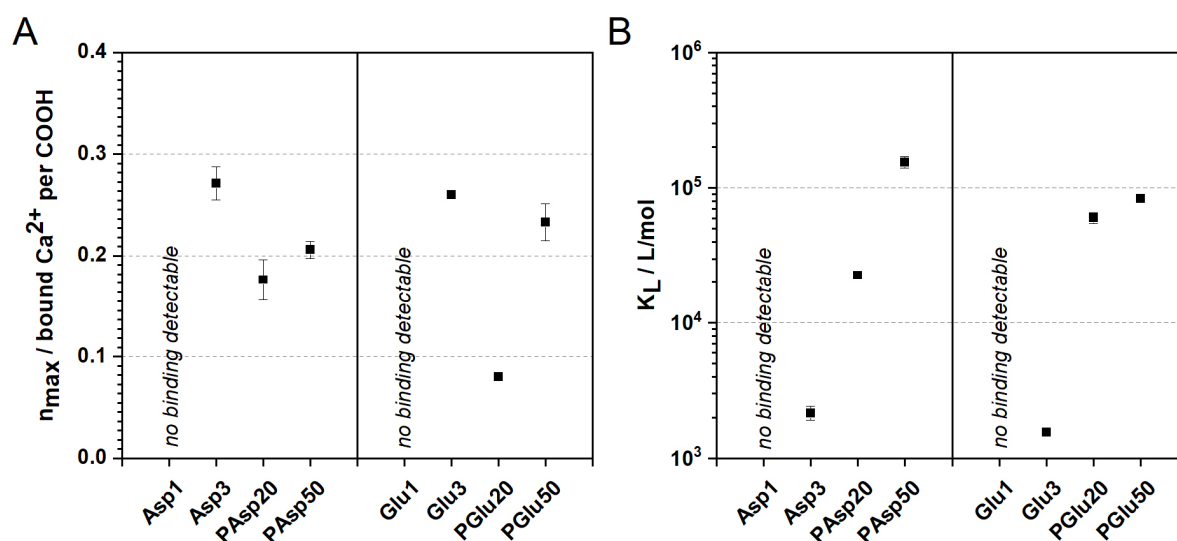**Figure 2.3 Dependency of binding parameters on the chain length of investigated polymers and oligomers at pH 9. a)** The maximum binding capacity n_{max} and **b)** the Langmuir binding constant K_L are shown. For protected monomers, no binding could be resolved for the used concentration (50 mg/L), likely due to too low association constants. Detailed binding parameters are given in Table S2.2.

The unprotected trimers show the highest relative binding capacity. However, due to the use of unprotected trimers, bidentate binding is possible at the terminal groups of the chain, resulting in the additional binding of calcium ions. Due to the short chains of the compounds, this leads to a higher n_{max} compared to the longer polymers. The difference in binding characteristic is also evident in the vastly different K_L values compared to those of the larger chain-length compounds. In addition, we do not detect calcium binding for (protected) monomers. This is probably due to too low concentrations used in the experiments and comparatively small association constants of monomeric amino acids.[170] It is evident that protected monomers exhibit considerably lower binding constants than the higher molecular weight compounds. The protection of the monomer was deliberately chosen to be closely related to the chemical environment of the monomer unit in a polymer chain, yet no binding can be detected for the monomers. The impact of the whole polymer chain on the binding mechanism is again evident from this set of experiments. In addition, it is very important to specify whether protected or unprotected monomers and oligomers are used to investigate effects of amino acids or polycarboxylates on ion binding processes or related phenomena.[97] Especially for short polymers or oligomers, characteristics of the terminal groups have to be specified. When we take a closer look at the difference between 50mers and 20mers, a striking feature is evident. In terms of n_{max}, PAsp20 possesses a higher binding capacity than PGlu20, while the K_L of PAsp20 is lower than that of PGlu20 (Figure 2.3a). These trends in n_{max} and K_L are opposite for 20mers compared to 50mers, implying different binding mechanisms for shorter polymers (and oligomers) compared to longer polymers.

2.4.3   Binding parameters from ITC

So as to complement the potentiometric titration experiments, isothermal titration calorimetry (ITC) experiments were performed to gain insight into thermodynamic parameters during the calcium binding process (Figure 2.4).[146] We can directly compare the parameters determined by ITC and potentiometric titration, as the ITC evaluation was performed using a model for simple hetero association, which assumes noninteracting binding sites according to the standard Langmuir model (Table 2.2).[165]

The ITC results show that the trends for binding stoichiometry n are consistent with the potentiometric titration, where a higher DP_n of polymers correlates with a higher n. In addition, the order of magnitude of K_L and the significantly higher adsorption coefficient for PAA at high pH values are confirmed by ITC. The determined binding characteristics of PAA are in excellent agreement with values reported in earlier studies.[146] However, some trends visible in the potentiometric titration cannot be reproduced by ITC, namely the higher K_L of PAsp50 compared to PGlu50 and PGlu20. At this point, it remains unclear why this effect cannot be reproduced, but we assume a systematic error upon ITC evaluation, as the ITC data evaluation is rather sensitive, especially regarding the determination of K_{ITC}, and depends on the chosen

software of evaluation, even if the same binding model is used. Indeed, the equations used for evaluations of ITC experiments are more complex than those for the Langmuir evaluation (see SI section 2.6.4), and in case of ITC, only around 25 data points are used for fitting in one experiment compared to over 1000 points in potentiometric titration experiments. Thus, the results seem to be influenced by the evaluation routine. Of course, differences in results from ITC and titration experiments could also be caused by interactions of polymers with the electrodes or effects of the buffer used in ITC experiments. Nevertheless, we can still confirm key findings of the potentiometric titration experiments: a strong influence of chain length on n_{max} and the order of magnitude of K_L as well as a significantly higher K_L value for PAA than for other polycarboxylates.
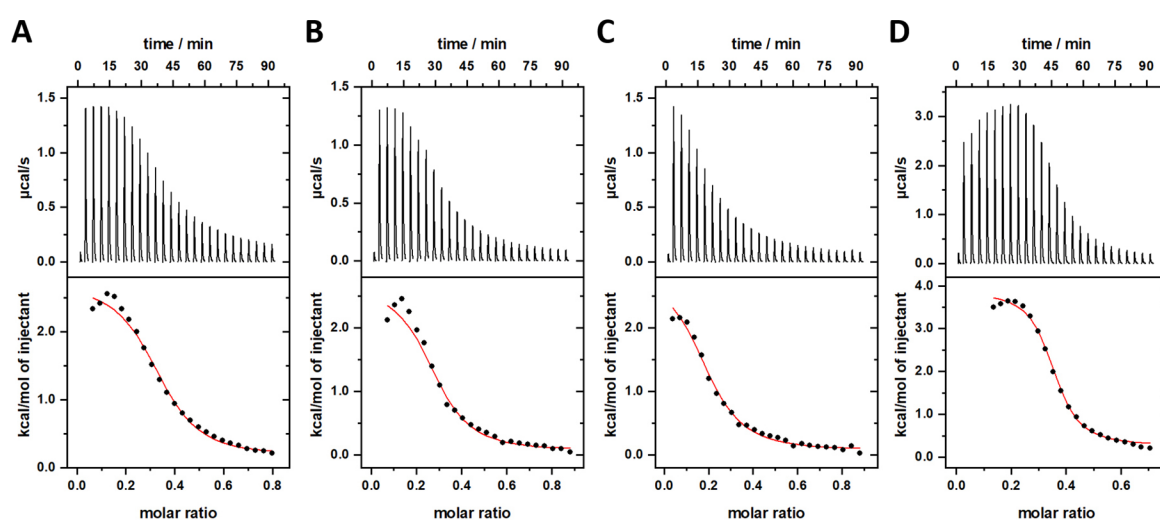

Figure 2.4 Isothermal titration calorimetry (ITC) experiments of calcium ion binding to polycarboxylates. a) PAsp50, **b)** PGlu50, **c)** PGlu20, and **d)** PAA. Reference titrations of Ca^{2+} into buffer and water into polymer solutions were subtracted for quantitative evaluations in order to account for heats of dilution, and isotherms were fitted with a model of simple hetero association ($A + B \rightleftharpoons AB$).

Table 2.2   ITC results for calcium ion binding to PAsp50, PGlu50, PGlu20 and PAA. ΔH^0: standard reaction enthalpy; ΔG^0: standard reaction Gibbs free energy; ΔS^0: standard reaction entropy; n: binding stoichiometry; K_{ITC}: association constant. The $\pm$ 1-σ-standard deviation of 3 ITC experiments is shown. In addition, the Langmuir binding parameters n_{max} and K_L determined by potentiometric titration (pH 9) are shown for comparison

	Isothermal titration calorimetry					Potentiometric titration	
	ΔH^0 [kJ/mol]	ΔG^0 [kJ/mol]	ΔS^0 [J/mol·K]	K_{ITC} [·10^3 L/mol]	n	K_L [·10^3 L/mol]	n_{max}
PAsp50	11.3 ± 0.8	-28.3 ± 0.3	133 ± 2	129 ± 15	0.33	155 ± 15	0.21
PGlu50	10.3 ± 0.2	-28.7 ± 0.3	131 ± 0.4	154 ± 18	0.29	84 ± 6	0.23
PGlu20	13.5 ± 1.9	-26.7 ± 0.3	135 ± 7	68 ± 7	0.17	61 ± 6	0.08
PAA	14.8 ± 0.7	-29.8 ± 0.4	150 ± 1	249 ± 44	0.35	330 ± 40	0.34

Thermodynamic parameters derived from ITC provide further insight into the binding energetics and therefore, the mechanisms underlying the binding process. The standard reaction enthalpy ΔH^0 thereby reflects the strength of the interactions of Ca^{2+} with the polymer, such as van der Waals interactions or hydrogen bonds, compared to the interactions existing with the solvent. On the other hand, the standard reaction entropy ΔS^0 reflects changes in conformational entropy of the polymer, such as loss of conformational freedom of the chain, or changes in solvation entropy, e.g., the release of bound water molecules into the bulk solvent upon binding.[171]

While no differences in thermodynamic data for PAsp50 and PGlu50 can be accurately detected in the experiments, differences between PGlu50 and PGlu20 are evident, namely lower K_{ITC} values for PGlu20. The difference in the Gibbs free energy ΔG^0 and therefore K_{ITC} can be attributed to the enthalpic contribution. ΔH^0 values reveal a more endothermic process for PGlu20, showing that Coulomb interactions, hydrogen-bonds or van der Waals interactions within the Calcium ion-bound polymer species are less favorable compared to the 50mers. As the polymer exists without specific secondary structures or conformations at high pH,[172-174] it is unlikely that the difference arises from differences in the pure-polymer water interaction in the starting solutions. This indicates that polymers with a shorter chain length cannot form hydrogen bonds, van der Waals, and Coulombic interactions upon binding of calcium ions as favorably as longer polymers investigated in this study. For the shorter polymer, the entropic contribution during binding is essentially the same as for the longer polymer chains (ΔS^0: 130 J/mol·K). The measured ΔS^0 also includes changes in conformational entropy of the polymers, effects of solvent restructuring, (de)protonation reactions, release of hydration waters and entropic effects due to varying numbers of particles.[175] It is impossible to isolate the term for conformational entropy from ITC experiments alone, as effects resulting from different polymer conformations could, for example, be also balanced by entropy gains resulting from solvent restructuring. However, it seems unlikely that these effects perfectly cancel out and we conclude that there is no detectable difference in entropic changes during binding in case of PGlu20 and PGlu50. Thus, even if higher-order effects such as folding of the polymer backbone upon binding come into play, it is unlikely that a rigid, folded structure is present in this binding motive (e.g., conformations similar to an alpha-helix), as this reduction in configurational entropy would result in large contributions to the measured entropies (on average -18 J/mol·K per amino acid).[176-177] If it is assumed that only the release of hydration waters and particles contributes to the measured entropic change, ΔS^0 corresponds to roughly $16R$, with R being the universal gas constant. This means that roughly 2 sodium ions and 8 hydrated water molecules are released into the bulk solvent upon binding one calcium ion, with each released ion/molecule contributing $3/2R$ in translational degrees of freedom to the entropy change.

We can conclude that the longer peptide chain yields a more exothermic and therefore energetically favorable binding of calcium ions, resulting in higher value of n_{max}. The effects

that cause stronger exothermic ΔH^0 for longer polymers cannot be precisely determined, however, it is unlikely that these effects and interactions are caused by functional groups in close distance in the chain, e.g., neighboring groups, as this would lead to no difference between 20mers and 50mers. The interactions occur between carboxyl groups at a significant distance (based on our results, likely more than 20 amino acids apart) in the polymer chain, originating from, e.g., folding of the polymer chain during the binding process, causing enthalpically favored interactions. We need to keep in mind that all evaluations were performed using the Langmuir binding model that assumes noninteracting binding sites and an entirely reversible binding process, which may impair the validity of the proposed mechanisms. Deviations from the assumptions made could also explain the deviations of experimental data from theoretical Langmuir isotherms (see above).

PAA shows even less favorable enthalpic interactions in the bound state; however, this is overcompensated by a much more favorable entropic contribution, resulting in an overall more exergonic binding process and thereby higher value of K_{ITC}. This can be explained by the increased release of hydration waters due to the higher binding capacity of PAA. A difference of 20 J/mol·K in ΔS^0 is detected in comparison to the polypeptides. This corresponds to 2-3 additionally released water molecules upon binding of one calcium ion compared to PAsp50, PGlu50, or PGlu20, which could be explained by a polydentate binding of PAA around calcium,[178] removing more bound hydration waters from Ca^{2+}. This is also consistent with the essentially quantitative binding detected at the beginning of potentiometric titration experiments for PAA, which is much stronger than can be rationalized by a binding mechanism giving rise to the Langmuir isotherm.

2.4.4   Binding of counterions

Different models have been proposed to explain the difference of binding in the case of poly(aspartic acid) and poly(glutamic acid), and among them is the binding of counterions. Using molecular dynamics simulations on penta-aspartic acid and penta-glutamic acid, Lemke et. al. showed that aspartic acid oligomers possess increasing ring strain upon chelation of calcium ions, while for glutamic acid oligomers, bidentate binding to calcium is causing less strain due to the longer side chain.[97] To release strain, counterions, such as chloride or carbonate ions, contribute to the binding mechanism in case of PAsp. In addition, even if bidentate binding takes place in the case of PAsp, the carboxyl groups cover a smaller angle due to the shorter side chains, resulting in increased space for counterions to bind to Asp oligomers in comparison to Glu oligomers. It was proposed that these reasons might explain the differences that PAsp and PGlu exert on mineralization processes. So as to investigate the predicted participation of counterions in the binding process, titrations with a chloride ion selective electrode were performed to detect the potential binding of chloride ions during the calcium binding process of PAsp50 and PGlu50 (Figure 2.5).
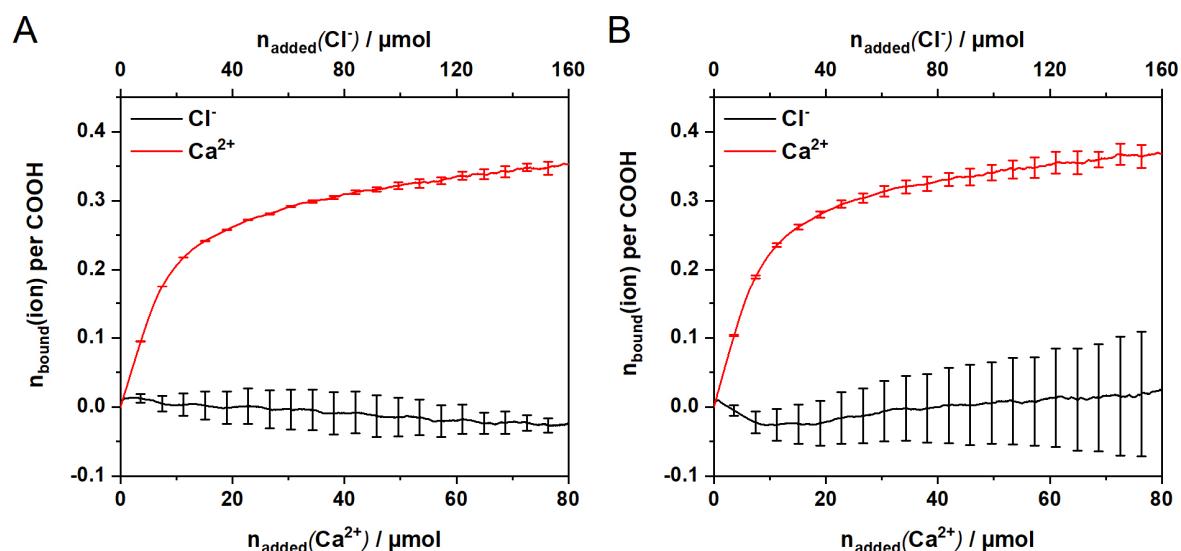
Figure 2.5   Binding of chloride and calcium ions during titration experiments. Experiments with **a)** PAsp50 and **b)** PGlu50 (200 mg/L) at pH 9 are shown. Note that $CaCl_2$ is added in the experiments, so twice the amount of chloride ions is added compared to calcium ions.

The titrations experiments confirm that no binding of chloride ions can be observed in the process, while calcium binding can be described by the Langmuir binding isotherms. In addition, the simulations suggest that the binding constant for calcium binding to PGlu is higher than to PAsp, as there is less ring strain in the system, allowing for favorable bidentate binding. This is contrary to our observations, as PAsp50 possesses a higher K_L in the investigated pH regime (Figure 2.1b). However, we need to keep in mind that the simulations were carried out using much shorter peptides, namely protected pentapeptides, while our primary experimental data was recorded for 50mers. Considering the experimental data for the shorter 20mers, the trends reverse, with PAsp20 showing a lower K_L compared to pGlu20 (Figure 2.3b), which is in line with the MD simulations. The molecular dynamics simulations also imply an increased binding capacity of PAsp, as one calcium per carboxyl group can be bound, and counterions could balance the resulting additional positives charges. For PGlu, the theoretical maximum binding capacity would be one bound calcium for every two carboxyl groups in a bidentate binding mechanism without counterion participation. Again, while for PAsp50 and PGlu50 the binding capacity is essentially the same within experimental accuracy, for the 20mers an increased binding capacity in case of PAsp20 is detected (Figure 2.3a). Although our titrations do not detect the participation of Cl⁻ ions in the binding process, we can confirm the predicted effects of the simulations for K_L and n_{max} for 20mers. As we are substantially below the binding of one Ca^{2+} per carboxyl group, the need for charge balancing by counter ions is not obvious. The necessity of counter ion participation in the binding process might be more pronounced for shorter peptides or oligomers, which might explain the better accordance of 20mers to simulations. The different trend for 50mers in the titration experiments seem to confirm the ITC results and point towards a distinct binding mechanism for longer chains. The binding in case

of longer chains is dominated by effects less dependent on the chemistry of the individual monomer unit. The results show that for polymers with high polymerization degrees, higher-order effects contribute to the binding process which cannot be resolved using simulations on oligomers with only several amino acid units or short polymers. However, the MD simulations help to understand the binding characteristics for shorter oligo- and poly(amino acids).

2.5 Conclusions

Systematic investigations of the binding of calcium ions by polycarboxylates for distinct side chain chemistries, pH values, and chain lengths reveal the role of complex mechanisms. No single uniform mechanism fits all investigated systems, and the whole polymer chain, including terminal groups, needs to be considered for the interpretation of binding data. Due to the potential backfolding of the polymer chain for increased polymerization degrees, it is insufficient to try to explain binding effects solely based on monomers and oligopeptide segments. Our experiments even reveal differences in the binding mechanism for 20mers compared to 50mers, with the longer chain resulting in significantly higher maximum binding capacities per carboxyl group.

The assessment of the proton release during the calcium ion binding process at different pH values provides further insights into the binding mechanisms (Figure 2.6). In the acidic pH regime, the polycarboxylates are predominately protonated. The abundancy of initial binding sites, i.e., deprotonated carboxyl groups, is very low, and no binding can occur (1). With increasing pH value, deprotonated carboxyl groups become more abundant, and calcium binding can start at these initial sites (2). Interestingly, protons are released upon further binding of calcium ions, indicating that the successive binding steps do not exclusively take place at deprotonated groups. In fact, we observe that almost all protons are released at pH values at which a certain amount of fully deprotonated groups would be present for further calcium binding. The total amount of released protons is dependent on the initial protonation degree of the polymer, with a lower pK_a value of the carboxyl groups in PAsp corresponding to lower amount of H^+ release (3) compared to PGlu with a higher pK_a value (4). That all protons are released upon calcium binding shows that the apparent pK_a value of the carboxyl groups is lowered, which has previously been reported in similar polypeptides and has been attributed to electrostatic or hydrophobic hydration effects.[179-180] Similar effects seem to play a role during the calcium binding to carboxyl groups, likely reinforced by conformational changes of the polymer chain. For PAA, an extremely high proton release is detected, possibly due to higher-order effects such as conformational changes or precipitation (5). In the basic pH regime, carboxyl groups are essentially fully deprotonated, and binding can take place up to n_{max} (6). The strong dependency of n_{max} on the polymer chain length also indicates the relevance of higher order effects, such as conformational changes of the polymer. For PAA, a very high K_L

value is observed, and the Langmuir isotherm does not appropriately describe the binding process, likely due to strong chelation effects and/or precipitation of a Ca-PAA coacervate (7).
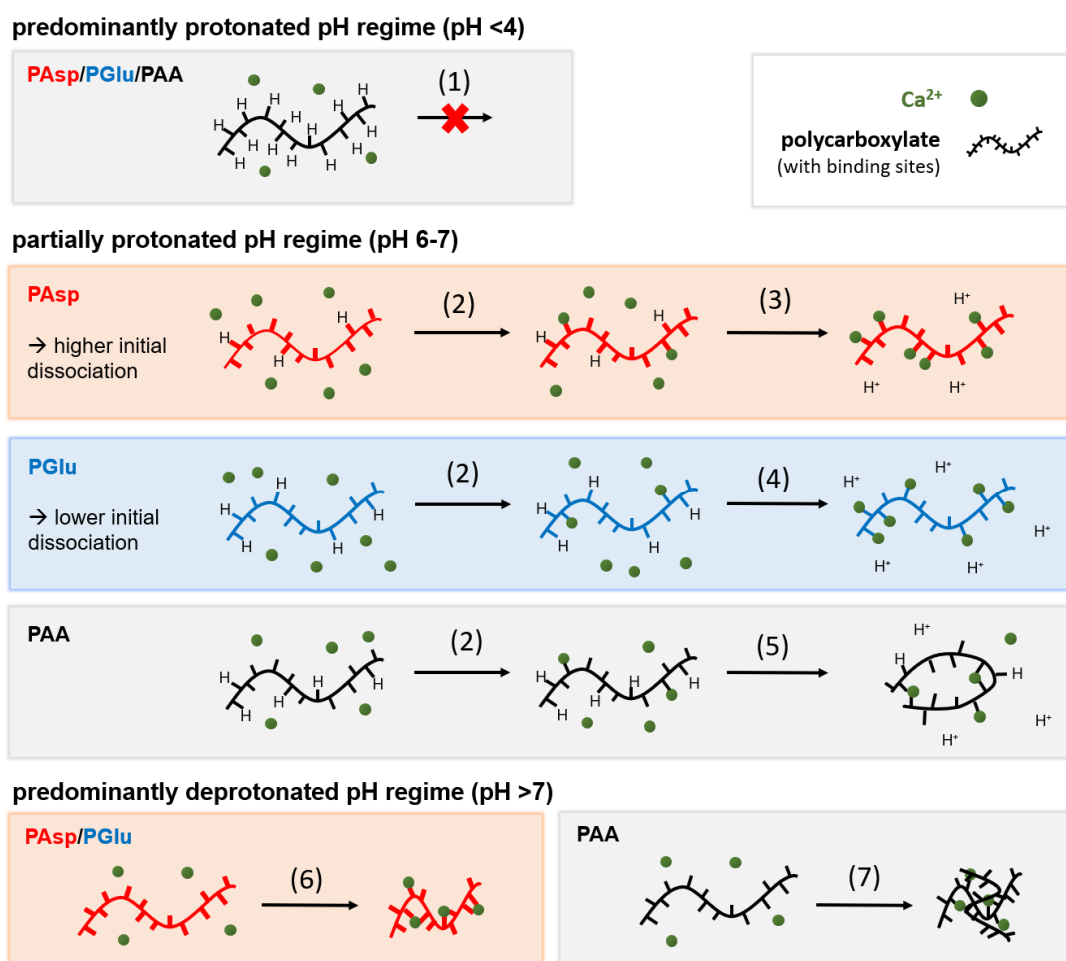

Figure 2.6 Schematic illustration of the calcium binding mechanisms by polycarboxylates at different pH values. For explanation, see text.

Although this work does not reveal how the coordination of calcium ions by the polymer precisely takes place, we demonstrate possible parameters affecting calcium binding processes. Simulations or investigations of short chains of amino acids seem to be insufficient to explain binding phenomena occurring in longer polymers, since the binding characteristics change at a certain chain length (in our experiments between 20 and 50 amino acids). At this stage, the chemistry of the individual repeating unit does not solely govern the binding process, and effects and interactions involving chemical groups located at larger distances in the chain, e.g. folding processes, come into play, which is also supported by ITC experiments. These effects also indicate that one needs to be careful using a pure Langmuir model, which assumes noninteracting binding sites, to describe the process of ion binding to polycarboxylates.

2.6   Supplementary Information

2.6.1   Working with calcium ion selective electrodes

Investigating polymer binding processes using an ion selective electrode leads to difficulties, as the ion selective electrode (Metrohm, No. 6.0508.110) can potentially be irreversibly damaged by small molecular weight polymers. Interactions and damage to the electrode is evident by nonlinear calibration experiments (Figure S2.1a) and an unusually steep slope in detected calcium potential in experiments, with a larger amount of calcium detected than added (Figure S2.1b).
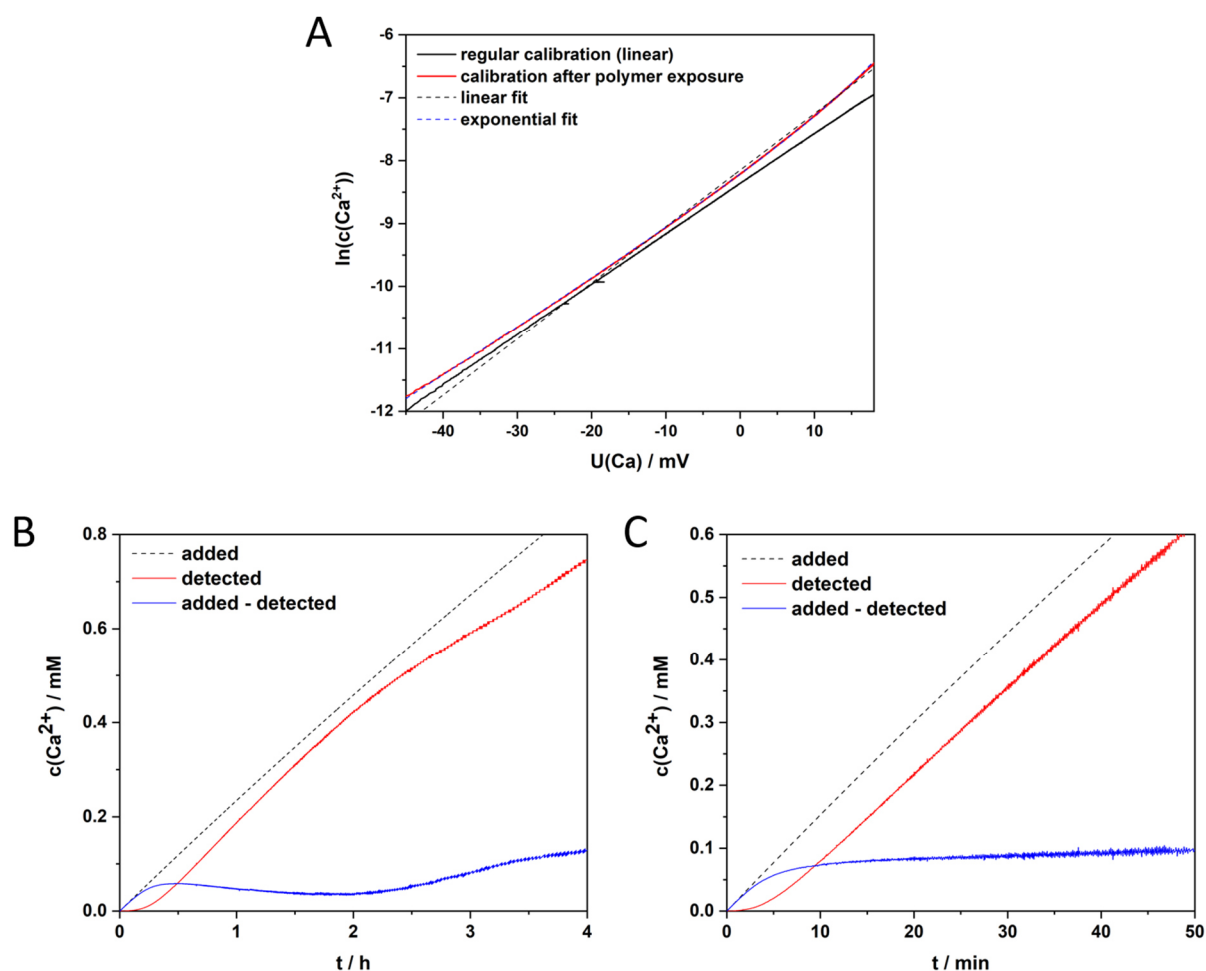

Figure S2.1 Experimental data showing interactions of polymers with the Ca-ISE. a) Comparison of regular, linear calibration data (black full line) and calibration data after exposure of the ISE to polymer (red full line). After polymer exposure, the data shows a nonlinear dependency of the measured potential from calcium concentrations and a linear equation cannot be used for fitting (black dashed line). Therefore, an exponential fit function was used that represented the calibration data very well (blue dashed line). **b)** Typical titration experiment with unpurified PAsp50 additive (50 mg/L, pH 9.0, addition of 10 mM $CaCl_2$ with 0.02 mL/min). **c)** Titration data after using purified PAsp50 and modifying the experimental procedure (50 mg/L, pH 9.0, addition of 10 mM $CaCl_2$ with 0.04 mL/min).

Due to these problems, quantitative evaluation of titration data is impossible, and several measures were applied to protect and restore the calcium electrode to ensure quantitative evaluation of results. These steps greatly improved data quality (Figure S2.1c) and can be applied for any system, in which interactions and damage of the (calcium) ion selective electrode is an issue:

1. Remove oligomers and additive with short chain length from solution, for example using diafiltration
2. Keep titration time short (< 60 min) to minimize interaction time with the membrane
3. Restore the calcium electrode by stirring several hours in 10 mM CaCl₂ solution
4. Perform calibration of the electrode *before and after each measurement*, to check for potential damage or change in calibration parameters. This allows determination of precise data, even if the precision of electrode changes in the long term
5. If calibration is non-linear but reproducible, use non-linear calibration for experiments

2.6.2   Application of Langmuir binding model

Comparison of the experimental titration data to the Langmuir model shows that the data is not appropriately represented by the Langmuir model (Figure S2.2, red curve). It is evident that the fit is overestimating the binding constant, due to the stronger curvature of the fitted curve compared to the experimental data. In addition, the experimental data does not approach a zero slope toward a saturation of the binding. This is especially evident for titration experiments at low pH values (pH < 5), where no initial binding process can be detected but an increase in bound calcium during the experiment is still visible (Figure S2.10a).
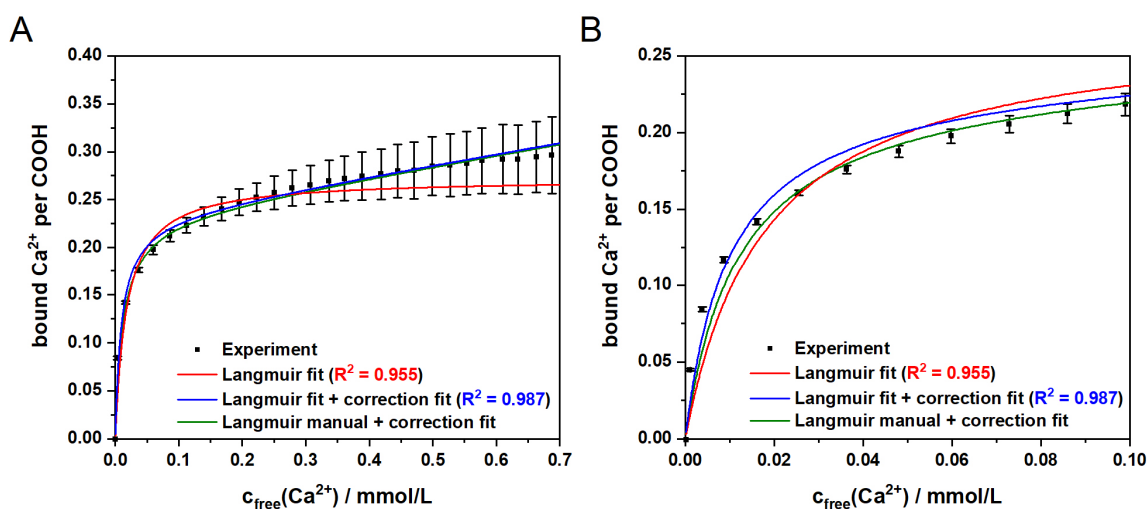

Figure S2.2 Comparison of experimentally determined titration data with theoretical binding models. The data for PGlu50 (50 mg/L) at pH 9 (every 60th data point is shown) with fitted binding isotherms are shown. **a)** Fits with 2 parameters (Langmuir isotherm, red) and 3 parameters (Langmuir and linear correction, blue), as well as the fit resulting from manual adjusted Langmuir parameters (green) are shown. **b)** Higher magnification of the beginning of the experiment. It is evident that the experimental data does not show pure Langmuir-type behavior.

This suggests that the binding consists of 2 separate processes, a Langmuir-type binding caused by calcium binding to carboxyl groups, and an additional contribution with linear increase in bound calcium. We contribute the linear increase to a measurement artifact of the ion selective electrode, as interactions of the polymer with the PVC membrane of the Ca-ISE are possible, which can affect the recorded calcium activities (see section 2.6.1).[95] Therefore, this study is focused on the Langmuir-type binding and the linear contribution is not further discussed.

To account for the linear deviation in the binding isotherms, an additional term for fitting experimental data was introduced, which includes all interactions that lead to a non-zero slope at the end of the binding process in the isotherms. The applied empirical correction features a linear relationship of bound species and free adsorbate concentration, resulting in the following fitting function for the experimental data

$$n_{\text{bound}}(\text{Ca}^{2+}) = \underbrace{\frac{n_{\max} K_{\text{L}} \, c_{\text{free}}(\text{Ca}^{2+})}{1 + K_{\text{L}} \, c_{\text{free}}(\text{Ca}^{2+})}}_{\text{Langmuir term}} + \underbrace{K_{\text{corr}} * c_{\text{free}}(\text{Ca}^{2+})}_{\text{linear correction}} \qquad (\text{S2.1})$$

with K_{corr} representing the slope of the linear correction term. The adjusted procedure resulted in improved fits, especially in the beginning of the binding process, where the deviation of experimental data and theoretical binding isotherm is significantly reduced (Figure S2.2b, blue curve). In the next step, the Langmuir parameters were further tuned manually to yield a better fit. This is necessary, as the points in the beginning of the experiments contain most of the information regarding the Langmuir adsorption constant K_{L}, and therefore need a higher weighting during the regression. We decided to account for this higher weighting of earlier data points by manually tuning the parameters K_{L} and $n_{\max}$ to yield acceptable fits, instead of defining complex "weighting functions". The manually adjusted fits yielded an acceptable agreement with experimental data over the whole experiment (Figure S2.2, green curve). However, at the beginning of the experiments, a slight deviation of experimental data and fits is visible, showing that the potentiometric titration data does not show ideal Langmuir-type behavior. The error bars for the Langmuir parameters (Figure 2.1 and Table S2.2) represent the range, at which the manual fits resulted in an acceptable representation of experimental data.

2.6.3   Acid dissociation constants of polycarboxylates

Experimental. To 10 mL of a stirred solution of 500 mg/L polymer, 0.1 M HCl was added with an addition rate of 0.01 mL/min. The pH was recorded using a pH electrode (Metrohm, No. 6.0256.100), calibrated once per week using pH buffers from Mettler Toledo with pH 4.01 (No. 51302069), 7.00 (No. 51302047) and 9.21 (No. 51302070). Titrations were performed under H_2O saturated N_2 stream to prevent in-diffusion of CO_2, which potentially affects measured pH values in the basic regime.

Results and Discussion. Polymers were analyzed using acid-base titration in order to determine respective pK_a values. Determination of pK_a values of polycarboxylates is difficult, as the titration curves usually show no clear point of inflection and can therefore only be modeled by several pK_a values.[181] This is also visible in our titration curves (Figure S2.3). Especially for PAsp50, no point of inflection is detected.
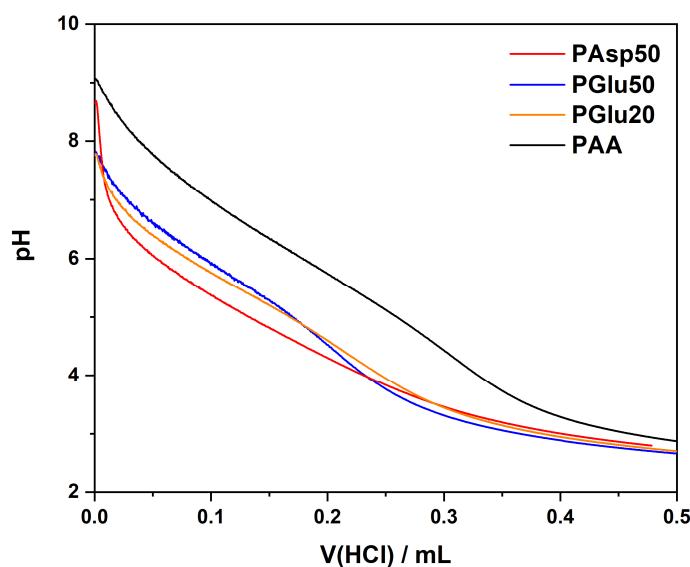

Figure S2.3 pH titration curves for polymers. Titrations were performed by addition of 0.1 M HCl to 500 mg/L polymer solution.

The determination of pK_a values of polycarboxylates is associated with several challenges, among which are effects of conformational changes of the polymer[182] or electrostatic interactions, due to which only apparent dissociation constants can be determined.[183-185] Therefore, usually the combination of several models is necessary to precisely determine pK_a values,[186] self-dissociation models are applied for interpretation of titration curves[187] or several pK_a values are used to model the titration curves.[158, 181] There are also studies that claim that pK_a for the polymer is similar to the one obtained for simple amino acids.[188] Due to these challenges in quantitative determination of pK_a values of polycarboxylates, we will focus on qualitative interpretations in this work. Qualitative comparison of our measured titration curves

(Figure S2.3) show good agreement with titration curves from literature.[169, 181, 187] For comparison, literature pK_a values of PAsp, PGlu and PAA are compiled in Table S2.1.

Concerning literature pK_a values of PAsp, we observe a rather broad range of determined values between 2.2 and 5.4. Values for PGlu and PAA also fall in this region. Due to the difficulties in the determination of these values mentioned before, these differences in pK_a values of the investigated polymers are not interpreted in detail. For potentiometric titration and ITC experiments performed at pH 9, full deprotonation of the carboxylic acid groups can be assumed, therefore, differences of binding parameters at high pH will not arise from the deprotonation degree of the carboxyl groups of the polymers. Also, at high or physiological pH values, secondary structures are usually not detected, and the poly(aspartic acid) and poly(glutamic acid) exist in a random coil conformation.[172-174] We will therefore not comment in the discussion on pK_a values for experiments in the basic regime. For interpretation of results at neutral or acidic pH values, however, the effects of protonation degree and secondary structures on the calcium binding process have to be kept in mind.

Table S2.1   Literature pK_a values for the investigated polymers. The corresponding ionic strength I during measurement and values of the degree of ionization/deprotonation α_D are stated as well

Polymer	pK_a	I / M	α_D
poly(aspartic acid)	3.73[188]	0.01	0.16 (at pH 3)
	5.3 to 2.4[158]	0.2	0.29 (at pH 2)
	5.4 to 2.2[181]	0.1	0.28 (at pH 3)
	4.78[189]	0.1	-
poly(glutamic acid)	4.375[182]	salt free	-
	4.07[190]	salt free	-
poly(acrylic acid)	4.3[169]	0.8	0 (extrapolation)
	4.5[169]	0.1	0 (extrapolation)
	5.28[183,a]	0.005	0 (extrapolation)

2.6.4   Comparability of binding constants

The binding constant determined by potentiometric titration via the Langmuir adsorption isotherm, K_L, and the binding constant determined by ITC, K_{ITC}, are calculated through different methods. To following calculations demonstrate that the constants can directly be compared, and no conversion factors are necessary:

a) Model for simple hetero association

For simplicity, 1:1 binding stoichiometry is assumed in the following. The equations describe the equilibrium of a binding process $M + X \rightleftharpoons MX$:

$$K_r = \frac{(MX)}{(X)(M)} \tag{S2.2}$$

with K_r representing the equilibrium constant and (X), (M), and (MX) representing concentrations of adsorbate (e.g. a metal ions), adsorbent (e.g. a macromolecule or a specific binding site) and the complex (e.g. metal ions bound to the binding site). The total concentrations of the reaction partners, X_{tot} and M_{tot}, can be calculated according to

$$X_{tot} = (X) + (MX) \tag{S2.3}$$

$$M_{tot} = (M) + (MX) \tag{S2.4}$$

Equations (S2.3) and (S2.4) can be solved for (MX) and (M) and substituted into eq. (S2.2) to yield an expression to describe the binding constant in terms of (X), X_{tot} and M_{tot}:

$$K_r = \frac{X_{tot} - (X)}{(X)\big(M_{tot} - X_{tot} + (X)\big)} \tag{S2.5}$$

b) Determination of K by ITC

In ITC experiments, effectively the differential heat during injections of adsorbate, dQ/dX_{tot}, is determined. This heat change dQ can be related to the change of (MX) concentration as

$$dQ = d(MX) * \Delta H^0 * V_0 \tag{S2.6}$$

with ΔH^0 representing the molar enthalpy of binding and V_0 the cell volume. From equations (S2.3) to (S2.5), $d(MX)/dX_{tot}$ can be calculated, resulting in the following expression:[164]

$$\frac{d(MX)}{dX_{tot}} = \frac{1}{2} + \frac{1 - \dfrac{1+r}{2} - \dfrac{X_r}{2}}{(X_r^2 - 2X_r(1-r) + (1+r)^2)^{\frac{1}{2}}} \tag{S2.7}$$

where $r = 1/(K_r M_{tot})$ and $X_r = X_{tot}/M_{tot}$. For evaluation of ITC experiments, usually dQ/dX_{tot} is plotted against X_{tot}/M_{tot} and fitted by the function

$$\frac{1}{V_0 \left(\frac{dQ}{dX_{tot}}\right)} = \Delta H^0 \left(\frac{1}{2} + \frac{1 - \frac{1+r}{2} - \frac{X_r}{2}}{(X_r^2 - 2X_r(1-r) + (1+r)^2)^{\frac{1}{2}}} \right) \tag{S2.8}$$

This allows determination of binding parameters and a binding constant according to eq. (2.4).

c) Determination of K by potentiometric titration and Langmuir binding isotherms

Potentiometric titration data was fitted using the Langmuir binding isotherm as described in eq. (2.4)

$$n_{bound}(Ca^{2+}) = \frac{n_{max} K_L c_{free}(Ca^{2+})}{1 + K_L c_{free}(Ca^{2+})} \tag{S2.9}$$

The parameters can be translated to the parameters used in the previous sections. Thereby, the amount of adsorbed adsorbate, $n_{bound}(Ca^{2+})$, can be expressed as

$$n_{bound}(Ca^{2+}) = c_{bound}(Ca^{2+}) * V = (MX) * V = (X_{tot} - (X)) * V \tag{S2.10}$$

and the maximum sorption capacity, n_{max}, as

$$n_{max} = c_{max} * V = M_{tot} * V \tag{S2.11}$$

Substituting equations (S2.10) and (S2.11) into eq. (S2.9) and using $c_{free}(Ca^{2+}) = (X)$ we get the expression

$$X_{tot} - (X) = \frac{M_{tot} K_L (X)}{1 + K_L (X)} \tag{S2.12}$$

Rearrangement of equation (S2.12) yields

$$K_L = \frac{X_{tot} - (X)}{(X)(M_{tot} - X_{tot} + (X))} \tag{S2.13}$$

which is the same expression as eq. (S2.5).

It is evident that constants determined by ITC employing a model of simple heteroassociation ("one set of sites") and constants determined by fitting Langmuir isotherms to titration data yield the same K. The ITC "one set of sites" model and the Langmuir adsorption model share

the same set of assumptions, i.e., noninteracting binding sites and same affinity of each binding site to the ligand. In this model, there is also no distinction of microscopic- and macroscopic binding constants, as only a single independent binding site is regarded instead of a macromolecule with multiple binding sites.[191]

2.6.5   Polymer characterization by NMR

a)   Experimental

^{1}H NMR spectra were recorded on a Jeol YH 400 MHz NMR spectrometer in D_2O (99.9 %) at 298 K. [1]H chemical shifts were referenced to the residual solvent proton signal (D_2O: 4.79 ppm).

b)   Determination of DP_n by NMR

The polymerization degree of the polymers was determined by end group analysis.

PAsp50, PGlu50, PAsp20 and PGlu20. Upon request, the manufacturers confirmed the presence of a primary amine as N-terminus end group, while the structure of the alkylamide on the C-terminus remained confidential. The N-terminus end group allowed determination of the polymerization degree, as the C_α proton in the amide backbone closest to this group (marked red in Figure S2.4 to Figure S2.7) possesses a different chemical shift compared to the other C_α protons in the amide backbone (marked blue in Figure S2.4 to Figure S2.7). The spectra can therefore be normalized on the C_α proton on the N-terminus (PAsp50/PAsp20: δ 4.22; PGlu50/PGlu20: δ 4.08) and the resulting intensity of the amide backbone Cα protons (PAsp50/PAsp20: δ 4.3-4.7; PGlu50/PGlu20: δ 4.2-4.4) corresponds to DP_n -1.

PAA. The PAA used in our study was DDMAT (2-(Dodecylthiocarbonothioylthio)-2-methylpropanoic acid) terminated. The polymerization degree can be determined by using the protons at the thiol-neighboring carbons (marked red in Figure S2.8) for normalization.

Determination of polymerization degrees by NMR spectroscopy corresponded to characterization provided by the manufacturing data sheets for PAsp50, PGlu50, PGlu20 and PAA (see SI section 2.6.6), while we detected a higher molecular weight for PAsp20.

c)   NMR Spectra

In the following, the experimental ^{1}H NMR spectra for PAsp50 (Figure S2.4), PGlu50 (Figure S2.5), PAsp20 (Figure S2.6), PGlu20 (Figure S2.7), and PAA (Figure S2.8) are shown.
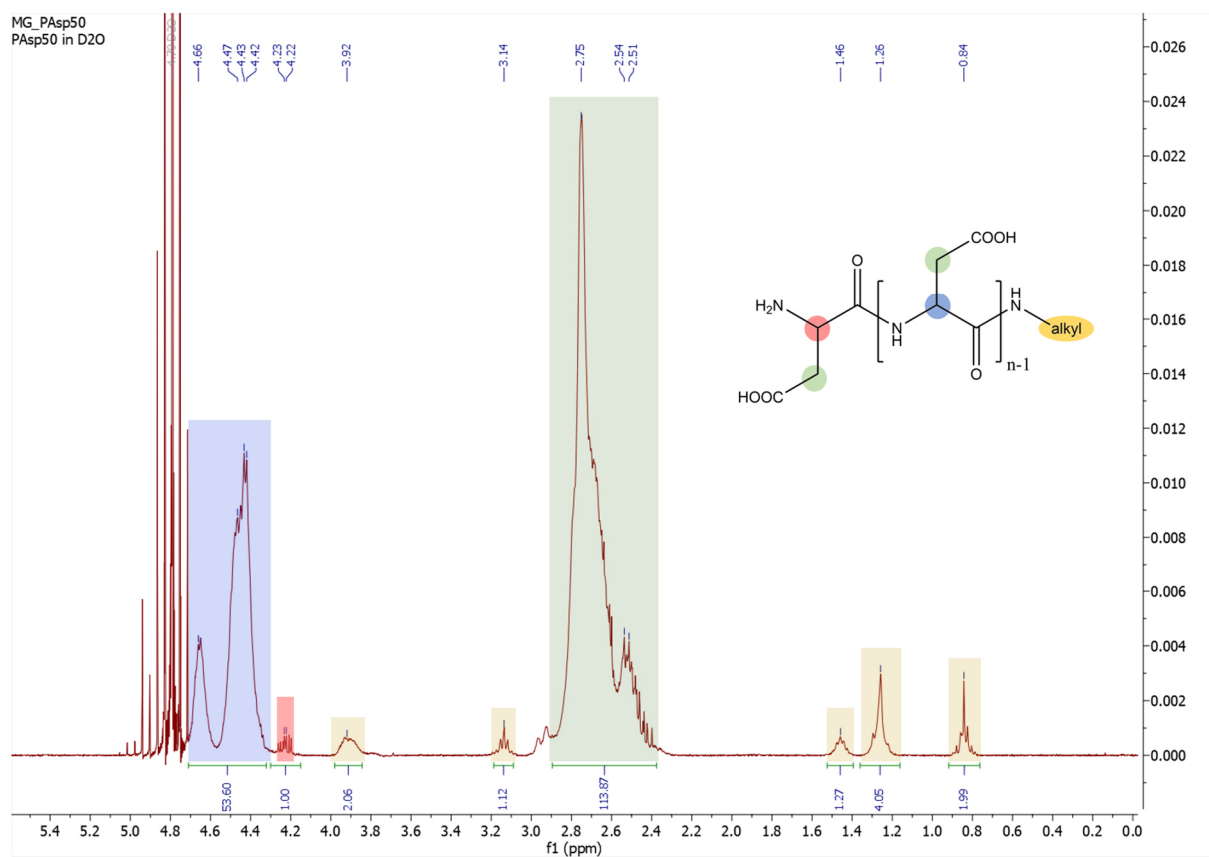
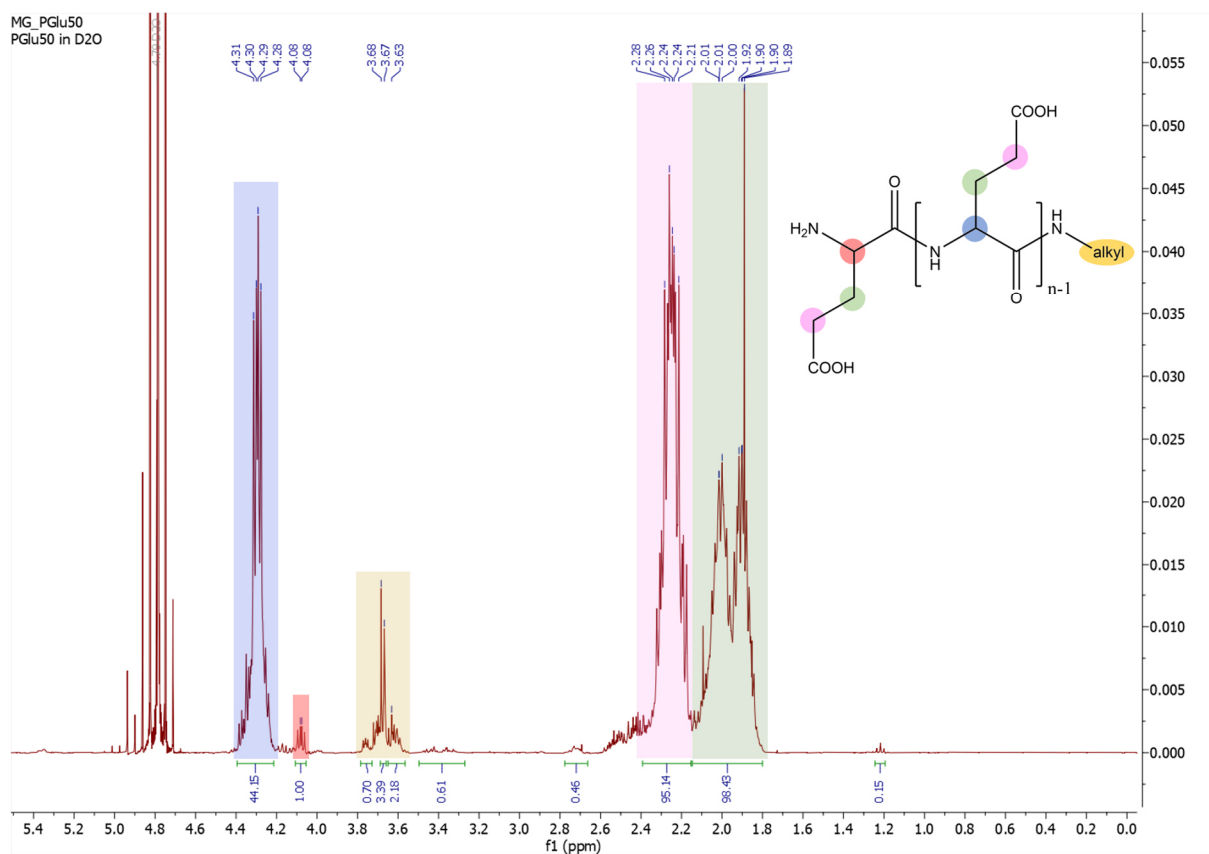**Figure S2.4** ^{1}H NMR spectrum (400 MHz, 298 K, D$_2$O) of PAsp50.

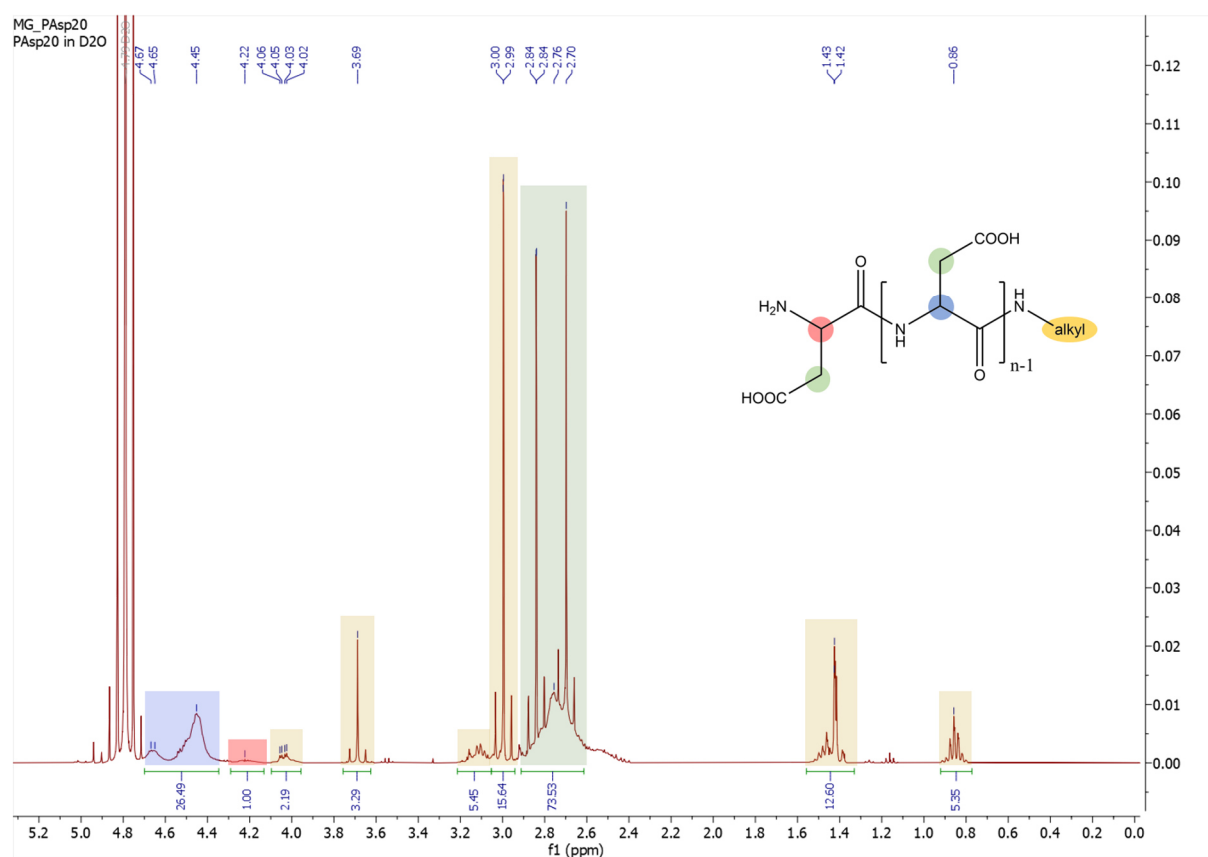**Figure S2.5** ^{1}H NMR spectrum (400 MHz, 298 K, D$_2$O) of PGlu50.

Figure S2.6 ^{1}H NMR spectrum (400 MHz, 298 K, D₂O) of PAsp20.
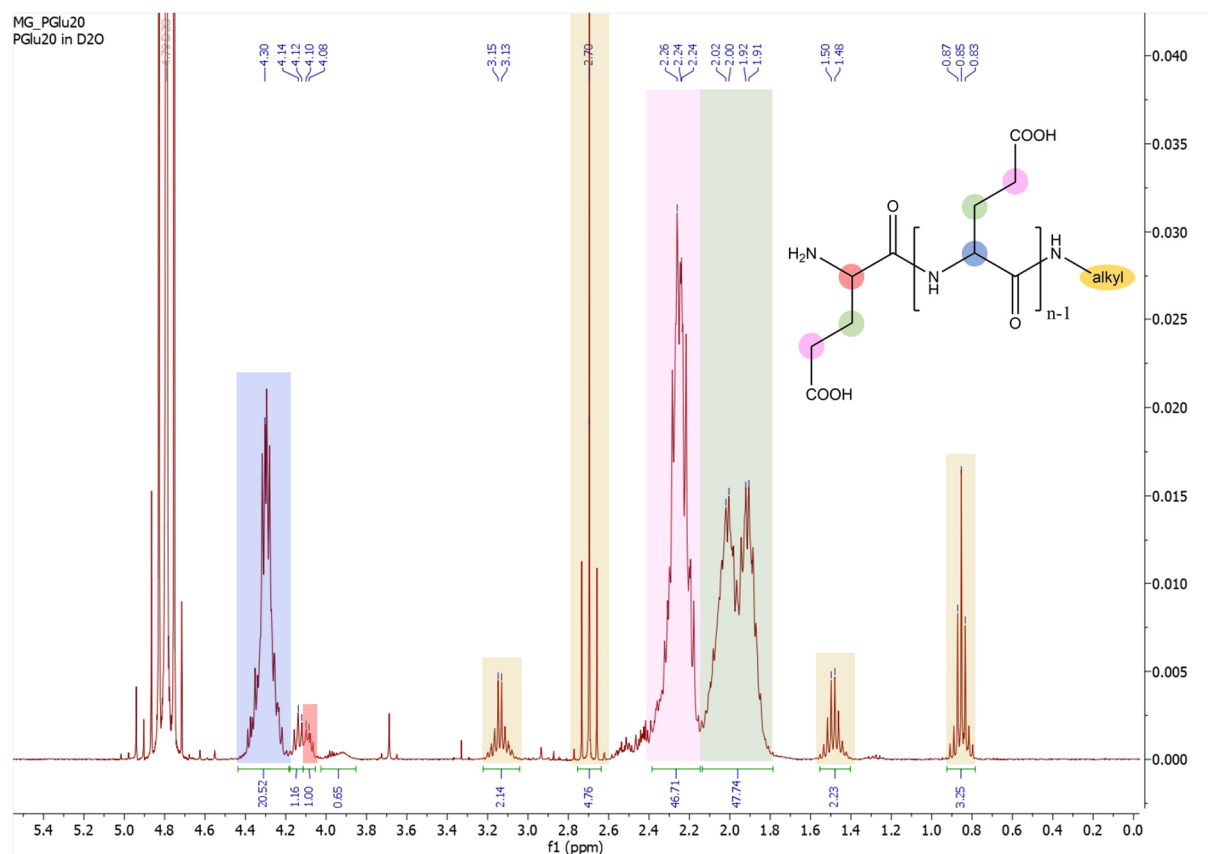

Figure S2.7 ^{1}H NMR spectrum (400 MHz, 298 K, D₂O) of PGlu20.
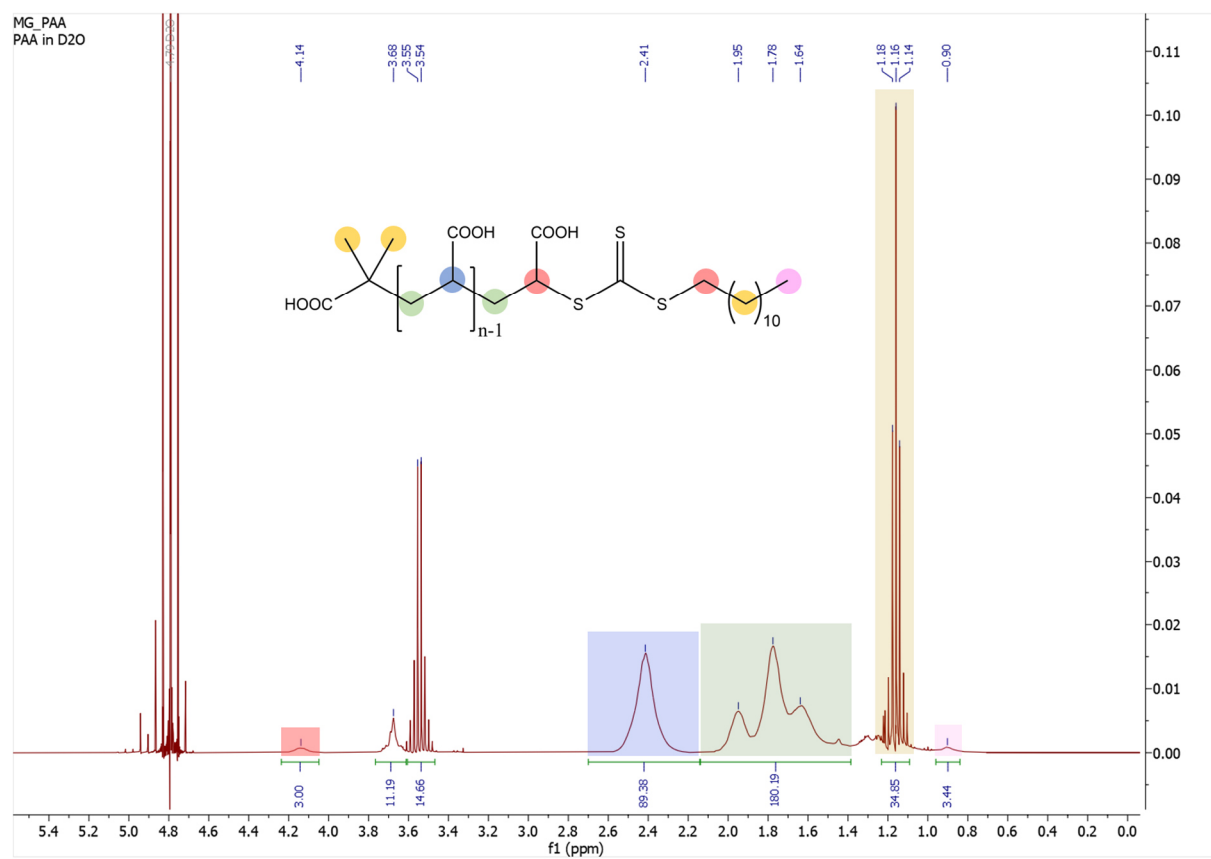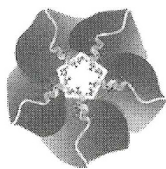
Figure S2.8 ^{1}H NMR spectrum (400 MHz, 298 K, D$_2$O) of PAA.

2.6.6   Polymer manufacturer's certificates of analysis

PAsp50 (Alamanda Polymers)

ALAMANDA
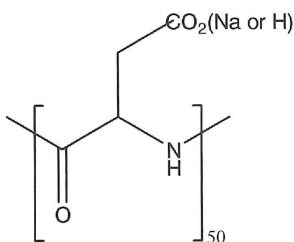P O L Y M E R S

☎ : 877-257-6597
🖷 : 256-489-4529
contact@alamanda-polymers.com

Certificate of Analysis

Chemical name: poly(L-aspartic acid sodium salt)

Catalog item: PLD_{50}, average MW 6800

Lot number: 000-D050-102

Manufacture date: 09/23/08
Retest date: 03/19/16

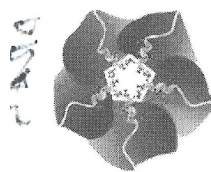| Appearance	Faint-yellow crystalline solid
Solubility	Clear solution at 50 mg/mL of water
Identify by NMR	Conforms
Quantitative analysis (%)	Na=14.8
PDI by GPC	1.04
MN by NMR	7500
DP_n by NMR	55

**Please store under the condition of flushing with argon
and protecting from light, and below -15°C.**

Signed by

03/21/16

Date

PGlu50 (Alamanda Polymers)

Certificate of Analysis

Chemical name: poly(L-glutamic acid sodium salt)

Catalog item: PLE_{50}, average MW 7500
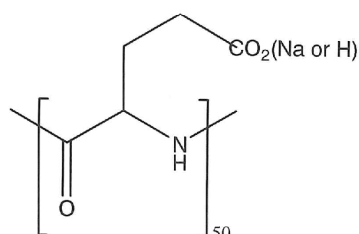
Lot number: 000-E050-105

Manufacture date: 06/23/15

Appearance	Faint-yellow crystalline solid
Solubility	Clear solution at 50 mg/mL of water
Identify by NMR	Conforms
Specific rotation $[\alpha]_D^{20}$	-55° (c=1, 0.2M NaCl)
Quantitative analysis (%)	Na=12.7
PDI by GPC	1.03
MN by NMR	6900
DP_n by NMR	46

**Please store under the condition of flushing with argon
and protecting from light, and below -15°C.**

Signed by

10/27/15

Date

PAsp20 (Nanosoft Polymers)

Functional Polymers & Copolymers
Your drug delivery solution-

CERTIFICATE OF ANALYSIS

Product Name: Poly(L-Aspartic acid sodium salt)20

SKU: 10970-2800; Item: Poly-L-Aspartic acid sodium salt (2800)

Structure:

n=20

Lot number: 10970020518   **Manufacture Date:** 05/18/2018

Appearance (color)	White to off-white
Appearance (form)	Crystalline Powder
Identity by NMR	Conforms
Molecular weight by GPC	~ 2600 Dalton
Polydispersity (Mw/Mn)	1.10

THIS PRODUCT IS FOR LABORATORY RESEARCH USE ONLY.

THIS PRODUCT SHOULD BE STORED UNDER NITROGEN OR ARGON AT LOW TEMPERATURE (-20°C).

THIS PRODUCT SHOULD BE KEPT AWAY FROM LIGHT.
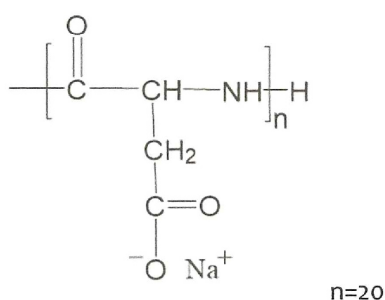
PGlu20 (Nanosoft Polymers)

NSP™
NANOSOFT POLYMERS

Functional Polymers & Copolymers
Your drug delivery solution-

CERTIFICATE OF ANALYSIS

Product Name: Poly(L-Glutamic acid)20

SKU: 10069-2500; Item: Poly-L-Glutamic Acid (2500)

Structure:

n=20
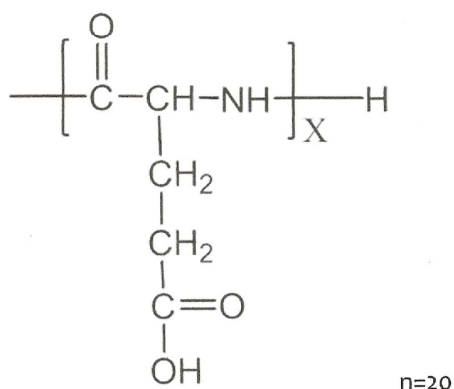
Lot number: 100690250227

Manufacture Date: 02/27/2018

Appearance (color)	White to off-white
Appearance (form)	Powder
Identity by NMR	Conforms
Molecular weight by GPC	~ 2500 Dalton
Polydispersity (Mw/Mn)	1.10

THIS PRODUCT IS FOR LABORATORY RESEARCH USE ONLY.

THIS PRODUCT SHOULD BE STORED UNDER NITROGEN OR ARGON AT LOW TEMPERATURE (-20°C).

THIS PRODUCT SHOULD BE KEPT AWAY FROM LIGHT.

PAA (Sigma Aldrich)

**SIGMA-ALDRICH**®

sigma-aldrich.com

3050 Spruce Street, Saint Louis, MO 63103, USA
Website: www.sigmaaldrich.com
Email USA: techserv@sial.com
Outside USA: eurtechserv@sial.com

Certificate of Analysis

Product Name:

Poly(acrylic acid), DDMAT terminated – average M_n 10,000, PDI ≤1.1

Product Number:	775843
Batch Number:	MKBN9467
Brand:	ALDRICH
Quality Release Date:	10 APR 2013
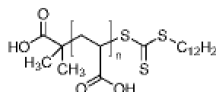
Test	Specification	Result
Appearance (Color)	White to Yellow	Light Yellow
Appearance (Form)	Powder	Powder
Infrared spectrum	Conforms to Structure	Conforms
Proton NMR Spectrum	Conforms to Structure	Conforms
Impurity by NMR	<10 %	< 10 %
diethyl ether		
Carbon		49.7 %
Specification: Report Results		
Poly Dispersity MW/MN	<1.1	< 1.1
Molecular Number by GPC	7000 - 9000	7871

Jamie Gleason

Jamie Gleason, Manager
Quality Control
Milwaukee, Wisconsin US

2.6.7   Supplementary figures
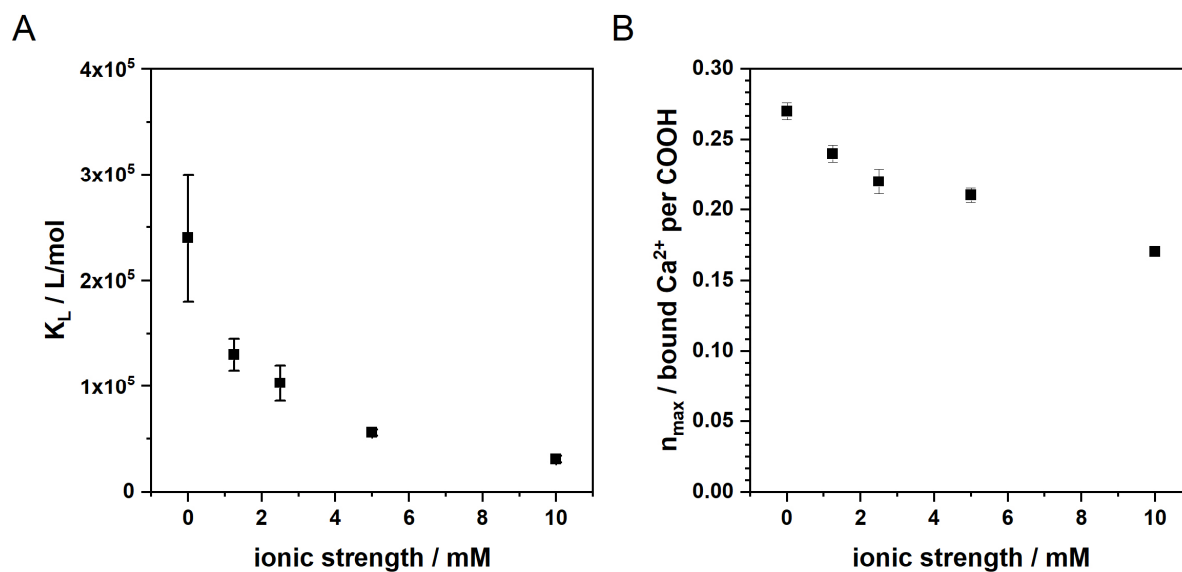
Figure S2.9 Effect of ionic strength on the binding parameters. a) K_L (Langmuir binding constant) and **b)** n_{max} (maximum binding capacity) for binding of Ca^{2+} on PGlu50 (100 mg/L) at pH 9 are shown. The experiments were performed using the same method as described in the experimental section, with additional NaCl (Carl Roth, >99.5%) added to the starting polymer solutions to adjust the ionic strength. It is evident that differences in ionic strength have a large effect on the determined binding parameters, with an increase in ionic strength resulting in a reduction of K_L and n_{max}.
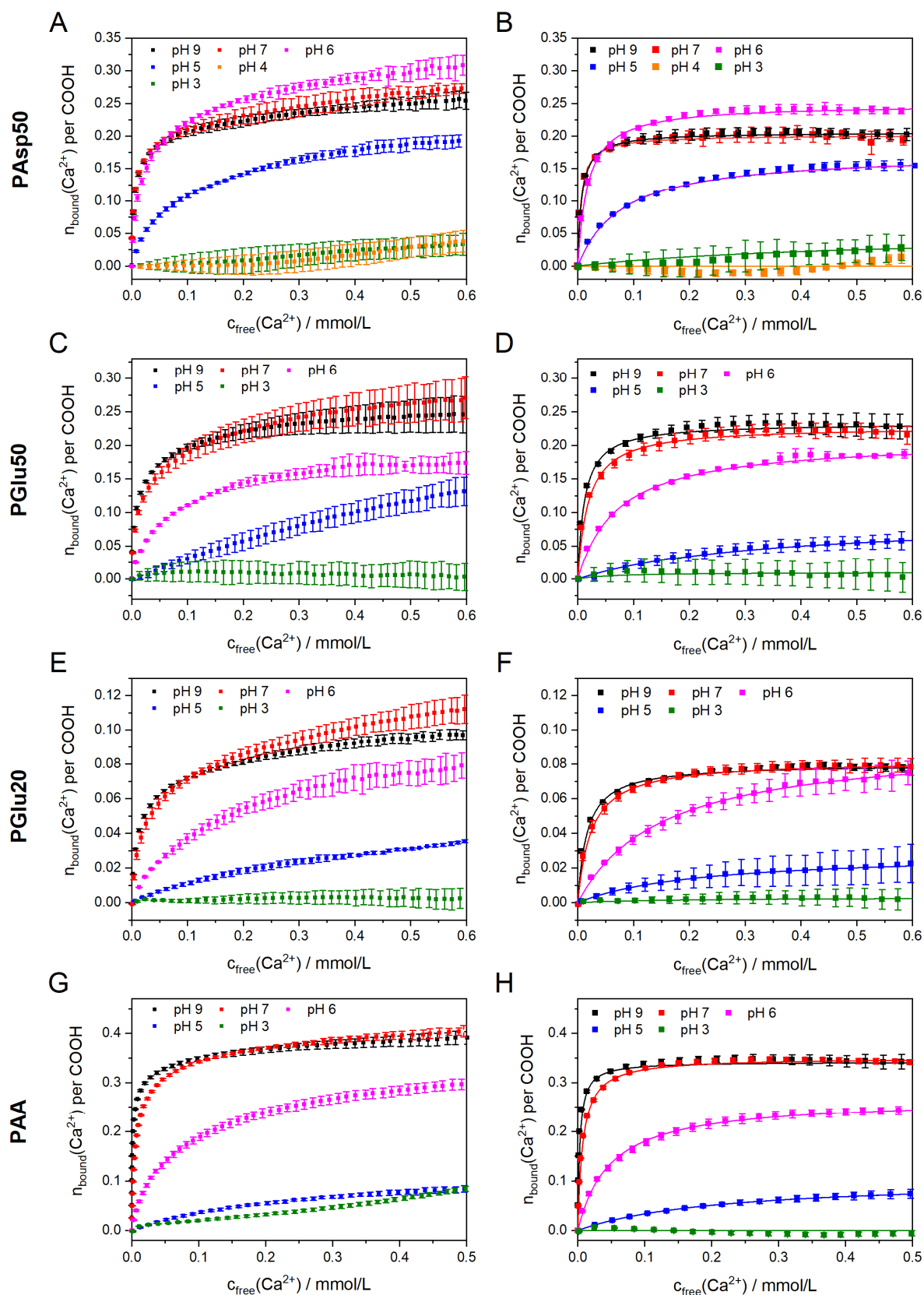
Figure S2.10   Raw data from titration experiments. The experimental raw data points (left column, every 30th data point is shown) and corresponding corrected data points (squares, right column, every 60th data point is shown) with corresponding Langmuir binding isotherms (lines, right column) for **a-b)** PAsp50, **c-d)** PGlu50, **e-f)** PGlu20 and **g-h)** PAA are shown. Error bars represent ± 1-σ-standard deviation of 3 independent titration experiments.
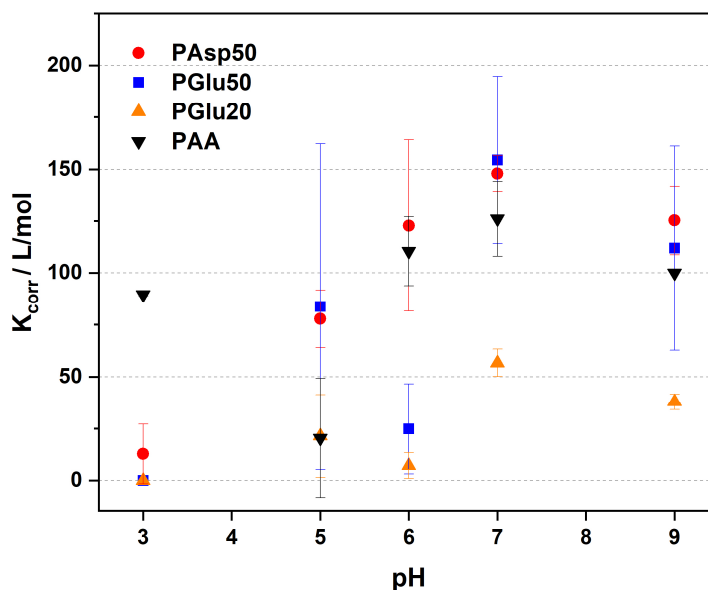
Figure S2.11   pH-dependence of the linear correction parameter K_{corr}.
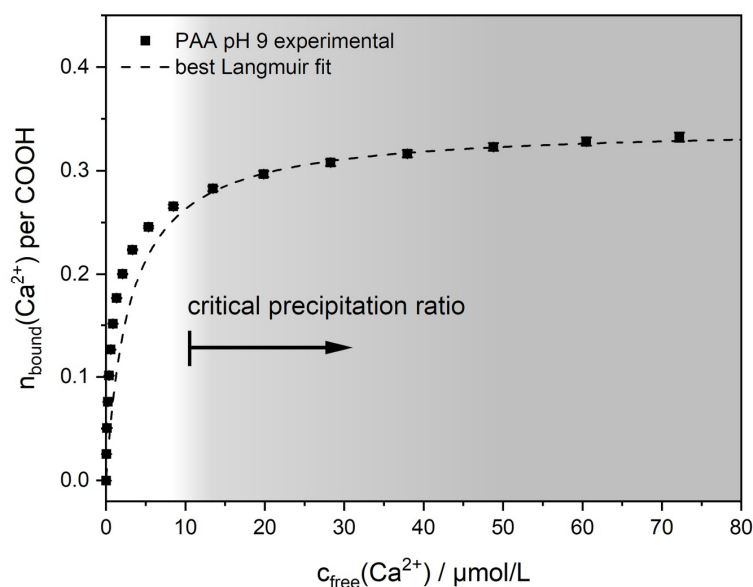
Figure S2.12   Background-corrected titration data for PAA at pH 9. The experimental data (squares, every 30th data point is shown) with the corresponding corrected Langmuir binding isotherm for PAA at pH 9 (see also Figure S2.10h) is shown. At the beginning of the experiment, binding takes place almost quantitatively and stronger as described by the Langmuir isotherm. The critical precipitation ratio is shown, at which precipitation of Calcium-PAA coacervate is expected.[95] It is evident that the experimental data cannot be fully fitted by a Langmuir binding isotherm.

2.6.8   Supplementary tables

Table S2.2   Binding parameters determined by potentiometric titration experiments using manually adjusted Langmuir fits

polymer	pH	K_L [$\cdot$ 10^3 L/mol]			n_{max}	K_{corr} [L/mol]		
	3	no binding			0.00	13	$\pm$	14
	5	13.0	$\pm$	0.7	0.18	78	$\pm$	14
PAsp50	6	56.0	$\pm$	4.0	0.25	123	$\pm$	41
	7	155	$\pm$	15	0.20	148	$\pm$	8
	9	155	$\pm$	15	0.21	125	$\pm$	17
PAsp20	9	22.4	$\pm$	1.1	0.18	103	$\pm$	33
Asp3	9	2.2	$\pm$	0.3	0.27	28	$\pm$	40
	3	no binding			0.01		0	
	5	3.0	$\pm$	0.6	0.09	84	$\pm$	78
PGlu50	6	14.1	$\pm$	0.7	0.21	25	$\pm$	22
	7	53.5	$\pm$	4.5	0.23	154	$\pm$	40
	9	84.0	$\pm$	6.0	0.23	112	$\pm$	49
	3	no binding			0.01		0	
	5	4.5	$\pm$	1.6	0.03	21	$\pm$	20
PGlu20	6	6.7	$\pm$	0.8	0.09	7	$\pm$	6
	7	41.5	$\pm$	5.5	0.08	57	$\pm$	7
	9	60.5	$\pm$	5.5	0.08	38	$\pm$	4
Glu3	9	1.55	$\pm$	0.05	0.26		0	
	3	no binding			0.00	89	$\pm$	1
	5	4.7	$\pm$	0.4	0.11	20	$\pm$	29
PAA	6	20.8	$\pm$	0.5	0.27	110	$\pm$	17
	7	134	$\pm$	8	0.35	126	$\pm$	18
	9	330	$\pm$	40	0.34	100	$\pm$	0

Chapter 3

Anti-Scaling Mechanisms Unveiled: Polycarboxylates Facilitate Bicarbonate Binding and Formation of Proton-Conductive Amorphous CaCO$_3$

Contents Chapter 3

Record of Contribution

I performed the majority of titration experiments, sample isolation and NMR sample packing and measurements of TGA-MS-IR and C-AFM as well as corresponding data analysis and evaluation, figure design and writing of the original manuscript draft. Johannes Rochau performed additional titration experiments and SEM and FTIR measurements of isolated samples in an internship under my supervision. Daniel Boemke as well as Eduard Groß performed additional titration experiments under my supervision and with my instructions. Dr. Venkata SubbaRao Redrouthu and Sanjay Vinod-Kumar conducted MAS NMR experiments and NMR data evaluation and provided valuable discussions. Dr. Guinevere Mathies supervised the NMR work and contributed with valuable ideas and discussions. Prof. Dr. Denis Gebauer developed the project idea and supervised the experimental work.

3.1 Abstract

CaCO$_3$ is the most abundant biomineral, and major constituent of incrustations forming due to water hardness. Great advancements have been made in understanding mineralization fundamentals in recent years, but in complex additive-controlled systems, a clear picture is still missing. Herein, we present a previously overlooked key aspect of additive-controlled CaCO$_3$ mineralization: pronounced bicarbonate binding even in basic conditions due to the presence of minor amounts of polycarboxylates. Significant amounts of HCO$_3^-$ ions are consequently incorporated in mineral precursor species and can also be detected in amorphous solids. Protons introduced by HCO$_3^-$ incorporation are highly mobile, and lead to ion conductivity in solid, polymer-stabilized amorphous calcium carbonate. This seems to play a key role for the strong crystallization inhibition by these additives and furthers the understanding of biomineralization and scale inhibition mechanisms.

3.2 Introduction

The mechanism of calcium carbonate (CaCO$_3$) formation has been of interest for many decades. This is not only due to its relevance in biomineralization processes,[4] geological phenomena or industrial applications, e.g., as filler or pigment. CaCO$_3$ also serves as a model system to investigate nucleation and crystallization phenomena in general. Several theories have been established, so as to describe the nucleation of mineral phases, ranging from classical nucleation theory to different, so-called "nonclassical" notions. Thereby, the prenucleation cluster (PNC) pathway, i.e., phase separation involving stable solute ion clusters,[19] has proven both its explanatory and predictive powers.[16] While the occurrence of liquid-like amorphous intermediates as precursors to crystalline CaCO$_3$ was proposed already two decades ago,[29] it was only recently that the liquid-liquid phase separation (LLPS) process was explored in more detail.[22] Liquid-like intermediates have been observed to occur in *in vitro* systems[154, 192] and biominerals.[85] Avaro et. al. presented the missing link between PNCs and these liquid-like intermediates and introduced a quantitative, "nonclassical" model to describe the phase separation process.[18] Further advancements have been made through uncovering the contribution of bicarbonate ions to CaCO$_3$ formation, showing that, at near-neutral pH values, HCO$_3^-$ ions are incorporated as a structural component in intermediate amorphous calcium carbonate (ACC), which might play a significant role in biomineralization in seawaters.[34]

Inspired by the progress made in the field of mineralization and fundamental phase separation mechanisms, we decided to explore additive-controlled systems in more depth, which are, owing to their high complexity and the numerous possibilities for interactions among the various chemical species occurring during the distinct mineralization stages, still poorly understood when compared to additive-free systems.[11] One of the most fascinating observations in additive-controlled CaCO$_3$ formation is the extremely effective crystallization inhibition by polycarboxylates, even in presence of minute concentrations of the additives.[98, 126]

Understanding the key interactions of polycarboxylates with the various species occurring along the mineralization pathway is not only relevant in terms of their application as commercial scale inhibitors but also crucial to better understand biomineralization mechanisms. This is because the soluble macromolecules associated with biomineral formation are often rich in aspartic- and glutamic acid residues.[55, 69] Polycarboxylates exhibit a strong stabilizing effect on liquid-like precursor and amorphous intermediate phases,[28, 35] while the stabilization is usually attributed to the adsorption of the additive molecules on the formed colloidal minerals, preventing their dissolution,[36, 93] or to the adsorption of calcium ions in the solution.[90] However, it is difficult to rationalize the strong crystallization inhibition in systems with highly substoichiometric, that is, almost "homeopathic" amounts of additives based on effects that would rather appear to rely on the presence of significant amounts of additive molecules. Some studies hinted toward the relevance of polycarboxylates in altering calcium (bi)carbonate ion association by modulating the pH value, resulting in the kinetic stabilization of a bicarbonate-rich mineral precursor.[31] However, even in systems employing precisely controlled higher pH levels and distinctly substoichiometric amounts of polycarboxylates, still a significant degree of inhibition can be detected.[98] So far, there seems to be no straightforward explanation for the effective inhibition of crystallization by polycarboxylates, suggesting that there is an "invisible" effect that has yet been overlooked.

In this study, we present a so far missing key for a better understanding of the polycarboxylate-controlled $CaCO_3$ system. Based on potentiometric titration, we investigated the pH-dependence of the effects of poly(aspartic acid) and poly(glutamic acid) on the early stages of $CaCO_3$ crystallization. Quantitative assessment of the bound species in the prenucleation regime reveals that significant amounts of bicarbonate ions are incorporated into the mineral precursor, while the extents of bicarbonate binding and crystallization inhibition are proportional. Compositional analysis of the isolated, polymer-stabilized ACC by means of thermogravimetric analysis coupled with mass spectrometry and infrared spectroscopy (TGA-MS-IR) confirms the presence of significant amounts of bicarbonate ions within the mineral phase through isotopic labeling. Complementary solid-state nuclear magnetic resonance (ssNMR) studies indicate that the protons introduced with the bicarbonate ions are highly mobile, leading to ion conductivity in the amorphous minerals, which is indeed confirmed by conductive atomic force microscopy (C-AFM). The polycarboxylate-facilitated bicarbonate binding in mineral precursors explains the strong inhibition of calcium carbonate crystallization by the additives, as a significant stoichiometric mismatch is introduced by the protons, which are furthermore mobile and may thus "poison" growth of emerging crystalline carbonate nuclei. These mechanistic insights can help to (i) gain a better understanding of biomineralization mechanisms, which take place at near-neutral pH in seawater in presence of much higher bicarbonate contents, (ii) further the understanding of the mechanisms and efficiency of commercial anti-scalants and (iii) potentially design new materials based on proton conductive amorphous minerals.

3.3 Experimental Section

3.3.1 Materials

All solutions were prepared using Milli-Q water that was degassed by bubbling N_2 through the solution overnight to remove dissolved CO_2. 20 mM $CaCl_2$ and 20 mM NaOH solutions were prepared by dilution of $CaCl_2$ stock solution (1.0 M, VWR, AVS Titrinorm volumetric solution) and NaOH stock solution (0.1 N, Carl Roth), respectively. Carbonate buffer solutions were freshly prepared before each experiment by dissolving Na_2CO_3 (Sigma-Aldrich, ACS grade, 99.95-100.05%) and $NaHCO_3$ (Sigma-Aldrich, ACS grade, >99.7%) in appropriate ratios for the desired pH value (pH 9.0, 9.4, 9.8 and 10.2). For ^{13}C enriched samples, $Na_2^{13}CO_3$ (99% ^{13}C, Cambridge Isotope Laboratories) and $NaH^{13}CO_3$ (99% ^{13}C, Cambridge Isotope Laboratories) were used. Prior to titration experiments, the pH values of the buffer solutions were adjusted by using small quantities of 0.1 N NaOH or 0.1 N HCl (Carl Roth), if necessary. For ionic strength corrected solutions, NaCl (Carl Roth, $\geq$ 99,5%) was used. Polymer stock solutions (100 mg/L) were prepared by dissolution of poly(L-aspartic acid sodium salt) (PAsp50, Alamanda Polymers, M = 7400 Da, PD = 1.04), poly(L-glutamic acid sodium salt) (PGlu50, Alamanda Polymers, M = 6700 Da, PD = 1.03), or poly(acrylic acid), 2-(Dodecylthiocarbono-thioylthio)-2-methylpropanoic acid (DDMAT)-terminated, (PAA, Sigma Aldrich, M = 6800 Da, PD < 1.1) in CO_2-free Milli-Q water. Characterization of polymer M and PD is shown in sections 2.6.5 and 2.6.6, respectively. The polymer stock solutions were stored at 5 °C and were used for no longer than 2 days. Prior to the preparation of PAsp50 stock solutions, the polymer was purified twice by diafiltration using a centrifugal filter device with a MWCO of 3 kDa (Merck Amicon® Ultra-15). This removes small molecular weight fractions from the polymer solutions that can penetrate the membrane of the calcium ion selective electrode (Ca-ISE) and therefore affect the recorded potential or damage the electrode.[121] Polymer containing carbonate solutions were freshly prepared before each experiment using polymer stock solution, Na_2CO_3 and $NaHCO_3$ in appropriate ratios.

3.3.2 Titration experiments

A commercial automated titration setup (Metrohm Titrando or Metrohm OMNIS) controlled by a computer software (Metrohm tiamo or Metrohm OMNIS) was used for the titration experiments. A titration device (905 Titrando or OMNIS Titrator) controls two dosing devices (800 Dosino or OMNIS Titration / Dosing Modules) for the precise addition of $CaCl_2$ and NaOH solutions. The calcium potential was monitored using a calcium ion selective electrode (Ca-ISE; Metrohm, No. 6.0508.110) and the pH was measured using a pH electrode (Metrohm, No. 6.0256.100). In addition, the transmission of the solution was measured with an optrode (Metrohm, No. 6.1115.000) using a wavelength of 660 nm. The inner reference system of the pH electrode was used as a reference electrode for the calcium electrode.

"Fingerprint" characterization of additive effects

Calibration of the pH electrode was carried out at least twice per week using pH buffers from Mettler Toledo with pH 4.01 (No. 51302069), 7.00 (No. 51302047) and 9.21 (No. 51302070). The Ca-ISE was calibrated at least once per day by dosing 20 mM $CaCl_2$ solution at a rate of 0.01 mL/min into 50 mL Milli-Q water at the same pH value as the actual experiment. For experiments with polymers, the Ca-ISE was calibrated before and after each measurement to confirm reproducibility of the electrode signal after exposition to the polymers and to exclude the possibility of damage to the electrode.[121] The calibration was carried out for 90 minutes. Both pH and calcium ion selective electrodes were regenerated twice a week by stirring for 2 hours in 100 mM HCl (pH electrode) and 100 mM $CaCl_2$ (Ca-ISE).

Titration experiments were carried out by adding 20 mM $CaCl_2$ solution at a rate of 0.02 mL/min (pH 9.0) or 0.01 mL/min (pH 9.4, 9.8 and 10.2) into 50 mL of 10 mM carbonate buffer at the desired pH value. All experiments were performed in a sealed beaked under N_2 shower, saturated with water vapor, to prevent diffusion of CO_2 into the solution. During the experiment, the pH was kept constant by automatic addition using 20 mM NaOH. Polymer containing experiments were performed in the same way using 50 mL of 10 mM carbonate solution containing 10 mg/L polymer. For each pH value and each polymer, at least 3 independent experiments were performed to ensure reproducibility.

After each titration experiment, the beaker and electrodes were washed two times using hydrochloric acid (3%, prepared by dissolution of 32% HCl, Carl Roth Rotipuran® p.a.) to remove traces of mineral precipitate of the vessel, electrodes, and dosing tips. After washing with HCl, the equipment was rinsed using Milli-Q water and dried with dust-free tissue paper.

Determination of bicarbonate binding

The electrode calibrations were performed in ionic strength adjusted solutions by dosing 20 mM $CaCl_2$ into 20 mL of 14.5 mM NaCl solution. Thus, actual ion products were determined from all experiments.[120] Titration experiments were performed using 0.01 g/L (PAA) or 0.1 g/L (PAsp50 and PGlu50) polymer concentrations at pH 9.8. The experiments were carried out by dosing 20 mM $CaCl_2$ with 0.01 mL/min into 20 mL of polymer containing carbonate buffer solution (10 mM carbonate concentration). The pH was held constant by addition of 10 mM NaOH and 10 mM HCl, respectively. The reaction vessel was flushed with N_2 for 10 min prior to the start of the experiment to remove CO_2 that could potentially diffuse into the solution. During the experiment, no N_2 shower was applied.

3.3.3 Isolation of pre- and postnucleation calcium carbonate samples

Sample isolation was performed according to a previously established protocol for amorphous calcium carbonate (ACC) isolation from titration experiments.[46]

Titration experiments were performed at pH 9.4 (see SI section 3.3.2 for titration experiments). At the desired time the sample was isolated by pouring the reaction solution (roughly 50 mL) into 1.5 L absolute ethanol (99.95%, VWR No. 20820.293) under vigorous stirring. After 30 min of stirring, the beaker was covered with parafilm and left standing for 90 min to let the particles sediment. Then, most of the ethanol was removed by decantation and the particles were isolated from the remaining solution (usually a few 100 mL) by centrifugation for 10 min at 7000 g. The particles were washed with 50 mL of ethanol followed by another centrifugation step. The procedure was repeated once more with ethanol and once with acetone (p.a. >99.98%, VWR No. 20066.296). Then, the particles were dried for 2 h at 40 °C in vacuum. The samples were stored in vacuum until characterization was performed. For samples isolated after 16 h, no quenching was performed, and the particles were directly isolated by centrifugation. The washing and drying steps were performed as described for ethanol quenched samples.

3.3.4 Preparation of ACC and polymer samples for *ex situ* characterization

Amorphous calcium carbonates (ACC) were synthesized according to the protocols presented by Gebauer et. al,[46, 193] using an automated titration setup (see section 3.3.2).[13]C enriched ACC samples were prepared in the same way as non-enriched regular ACC samples, but $Na_2^{13}CO_3$/ $NaH^{13}CO_3$ were used in for preparation of buffer solutions.

Pure ACC (Abbreviation: ACC). 2 L ethanol (99.9%, VWR No. 20820.293) were stirred in a plastic beaker. 50 mL of 50 mM $CaCl_2$ solution was added and after stirring for 2 min, 50 mL of 50 mM Na_2CO_3 solution was added. The beaker was sealed with parafilm and after stirring for 30 min, the stirrer was removed, and the beaker resealed. The beaker was left standing for 30 min, then the supernatant was decanted, and the remaining opaque sediment of ACC was isolated by centrifugation at 6000 g. The sediment was washed twice with 50 mL pure ethanol (VWR No. 20820.293), followed by 50 mL pure acetone (VWR No. 20066.296) and then stored in pure acetone. ATR-FTIR and TGA analysis of the product is shown in Figure S3.23 and Figure S3.24.

PAsp50-stabilized ACC (Abbreviation: PAsp50_ACC). 100 mM $CaCl_2$ solution were added at a rate of 0.01 mL/min into 150 mL of 10 mM carbonate buffer containing 0.1 g/L PAsp50 at pH 9.8. During the experiment, the pH was kept constant by automatic addition of 100 mM NaOH. The experiment was performed in a sealed beaker to prevent in-diffusion of CO_2. After 10,000 s, the reaction was stopped by pouring the reaction solution into 2 L of pure ethanol (99.9%, VWR No. 20820.293) that were stirred in a plastic beaker. The beaker was sealed with parafilm and after stirring for 30 min, the stirrer was removed, and the beaker resealed. The

beaker was left standing for 60 min, then the supernatant was slowly decanted, and the remaining opaque sediment of ACC was isolated by centrifugation at 6000 g for 15 min. The sediment was washed with ethanol (VWR No. 20820.293), followed by another centrifugation for 15 min. The procedure was repeated once more with ethanol and once with pure acetone (VWR No. 20066.296) and the ACC was dried and stored at 40 °C in vacuum. The synthesis yielded 20 mg of ACC per batch. The quality of the ACC was confirmed by ATR-FTIR spectroscopy. After each titration experiment, the beaker and electrodes were washed two times using acetic acid (10%) to remove traces of mineral precipitate of the vessel, electrodes, and dosing tips. After washing with acetic acid, the equipment was rinsed using Milli-Q water and dried with dust-free tissue paper. ATR-FTIR, TGA and MAS NMR analysis of the product is shown in Figure S3.23, Figure S3.24, and Figure S3.25, respectively.

PAsp50 calcium salt (Abbreviation: PAsp50_Ca). 76.0 mg of PAsp50 were dissolved in 40 mL of Milli-Q water. Then, 7.5 mL of 1.0 M $CaCl_2$ standard solution (VWR, No. 190646K) were slowly added to the stirred polymer solution, while the pH was monitored using a pH electrode (Metrohm No. 6.0256.100). The pH dropped from pH 9.5 to pH 8.2 during the addition of the calcium solution. The pH was then set to pH 10.0 by slowly adding 0.1 M NaOH standard solution (Roth, No. K020.1). After stirring for 5 min, the solution was added dropwise into 250 mL of a 1:1 (v/v) solution of absolute EtOH (VWR, ≥99.8%, AnalaR NORMAPUR® ACS) and absolute acetone (VWR, AnalaR NORMAPUR® ACS), which was stirred in a 1 L glass beaker. After stirring for 10 min, the cloudy white solid was isolated by centrifugation at 7000 g for 15 min. The obtained white sediment was resuspended in approx. 100 mL abs. EtOH and centrifuged again. This step was repeated one more time. Then, the product was dried at 40 °C in vacuum for 60 min. The synthesis yielded 78.1 mg of product. ATR-FTIR, TGA and MAS NMR analysis of the product is shown in Figure S3.23, Figure S3.24, and Figure S3.25.

Additional inductively coupled plasma optical emission spectrometry (ICP-OES) analysis was performed on a Spectro Arcos spectrometer. Samples were dissolved in 4% HNO_3 and measurements and calibrations were performed in 4% HNO_3. Calibration solutions for 5-point calibration (1 to 5 ppm) were prepared from Ca and Na standard solutions (1000 ppm ICP standard solutions, Carl Roth). For the pure PAsp50 (purchased as a sodium salt), a value of 0.65 bound Na^+ per carboxyl-group was determined by ICP-OES analysis. The PAsp50_Ca sample showed 0.38 Ca^{2+} bound per carboxy group, while no significant amounts of Na^+ were determined, confirming the successful ion exchange (data not shown).

Pure PAsp50 (Abbreviation: PAsp50). PAsp50 was used as purchased without further purification. If no experiments were performed, the salt was stored in inert gas atmosphere at -20 °C (for long term storage) or in vacuum (short term storage). ATR-FTIR, TGA and MAS NMR analysis of the product is shown in Figure S3.23, Figure S3.24, and Figure S3.25, respectively.

3.3.5 Sample characterization

TGA and TGA-MS-IR. Thermogravimetric analysis (TGA) was performed on a Netzsch STA 409 PC LUXX in oxidative atmosphere (Ar/O_2 80:20 v/v) and a heating rate of 5 K/min. Analysis of decomposition gases using mass spectrometry and infrared spectroscopy (TGA-MS-IR) was performed by coupling the TGA device with a Netzsch QMS 403 D Aelos mass spectrometer and a Bruker Invenio S FTIR spectrometer with an external gas cell. Before each measurement, the empty Al_2O_3 sample pan was heated to 1000 °C to remove any remaining impurities. Measurements were performed with at least 10 mg of sample and prior to TGA analysis, samples were dried at 40 °C in vacuum overnight to remove surface adsorbed water.

ATR-FTIR. Attenuated total reflectance Fourier-transform infrared (ATR-FTIR) spectroscopy was performed using a Bruker Tensor 27 or Bruker Vertex 70v spectrometer. Absorbance of the sample was measured from 4000 to 650 cm^{-1} with a resolution of 1 cm^{-1}. The samples were directly placed as a powder on the ATR unit for measurements.

SEM. Scanning electron microscopy (SEM) was performed on a JEOL JSM-6700F SEM. Samples were coated with a 5 nm thick layer of gold (Cressington 108auto) prior to analysis.

XRD. X-ray powder diffraction measurements (XRD) were performed on a STOE Stadi P diffractometer in transmission using Cu-Kα radiation ($\lambda = 1.54060$ Å, Generator: 40 kV, 30 mA) and a curved Ge (111) monochromator. Sample powders were fixed between X-ray amorphous foils for measurement.

AFM and C-AFM. Atomic force microscopy (AFM) and conductive AFM (C-AFM) was performed using a Park Systems NX 10 microscope in a glovebox in N_2 atmosphere. All measurements were performed using a CDT-FMR 10M_T conductive cantilever.

For sample preparation, a Si wafer (1x1 cm, Ted Pella) was coated with a 30 nm Au layer using a Cressington 108auto coater. Then, the wafer was coated with the sample dispersion (usually the ACC samples were obtained as dispersion in acetone after synthesis, see section 3.3.4) using a spin coater. Dependent on the concentration of particles, the spin coating process was repeated several times to deposit an appropriate number of particles. The Si wafer was then placed on the C-AFM sample holder disk and fixed with silver conductive paint to ensure good conductivity between the Au layer and the AFM holder (see Figure S3.7a in section 3.6.4). Prior to C-AFM analysis, the samples were stored in the glovebox lock in vacuum overnight to remove surface adsorbed water.

In AFM experiments, non-contact mode (NCM) was used to find suitable spots for C-AFM analysis. Then, C-AFM measurements were performed in spectroscopy mode using a sample bias from -1 to 1 V, while the cantilever was lifted between the measurement points. A set point value (pressing force for measurement) of 3 V and settling time of 500 ms was used. The detailed steps for evaluation of experimental data are described in section 3.6.4.

MAS NMR. Solid-state magic angle spinning nuclear magnetic resonance spectroscopy (MAS NMR) experiments were performed on a 400 MHz (9.4 T) Bruker Avance III 400 WB solid-state NMR spectrometer equipped with a Bruker 4 mm MAS HX probe (probe model: 4 mm PH MAS DVT 400W1 BL4 N - P / H CGR probe with gradient) at Larmor frequencies of 400.13 and 100.62 MHz for ^{1}H and ^{13}C, respectively. The spectra were acquired at 10 kHz spinning frequency and the sample temperature was maintained at 293 K using a Bruker VT unit (BCU-Xtreme). The nitrogen gas temperature was set to 263 K and the flow rate to 670 L/hr. Chemical shifts were referenced to TMS using adamantane as an indirect reference – the field was adjusted such that the ^{13}C low-field signal is observed at 38.48 ppm. ^{1}H-^{13}C cross polarization (CP) experiments on PAsp50 and ACC were done using a 90° ^{1}H pulse of 3 µs corresponding to a nutation frequency of 83.3 kHz. The contact time was 4 ms with an RF power of 75 W (48 kHz) on the ^{13}C channel and an optimized ramped power of 85 W (~70 kHz) on the ^{1}H channel. A heteronuclear decoupling with small phase incremental alternation with 64 steps (SPINAL-64) was used for proton decoupling during the acquisition. A recycle delay of 3 s was used for PAsp50/ PAsp50_ACC, and a recycle delay of 4 s was used for PAsp50_Ca.

3.3.6   Synthesis of reference samples for C-AFM measurements

Synthesis of gold nanoparticles. Au nanoparticles were synthesized according to the protocol by Huang et. al.[194], using a synthesis time of 6 h and were used as a conductive reference material for C-AFM investigations. After synthesis, the particles were washed several times with water to remove excess of CTAB from the particles. The particles showed an average size of 20 nm according to TEM (data not shown).

Synthesis of vaterite nanoparticles. Vaterite nanoparticles were synthesized according to the protocol by Tremel et. al.[195] and used as nonconductive mineral reference material for C-AFM investigations.

2.5 mmol of calcium chloride dihydrate (Sigma-Aldrich, ACS grade, >99%) were dissolved in 25 mL of ethylene glycol (>99%, Carl Roth) by ultrasonication (Elmasonic P, 80 kHz, 80% power, 40 °C, sweep mode) for 30 min. Then, a dispersion of 5 mmol sodium bicarbonate (Sigma-Aldrich, ACS grade, >99.7%) in ethylene glycol was added under stirring and the resulting dispersion was treated 30 min by ultrasonication (80 kHz, 90% power, 40 °C, sweep mode). The particles were isolated by centrifugation for 30 min at 7000 g and washed twice with Milli-Q water and once with ethanol (99.95%, VWR No. 20820.293). The product was stored in ethanol. ATR-FTIR characterization of the dried particles conformed to pure vaterite (data not shown).

3.3.7   Calculation of free ion products

For evaluation of the calibration of the Ca-ISE, $\ln(a_{\text{free}}(Ca^{2+}))$ was plotted against $U(Ca^{2+})$. Then, the relevant potential regime for each measurement (e.g. from -50 to -10 mV) was fitted linearly.

The experimentally measured potential can then be used to calculate the calcium activity according to the Nernst equation, as described elsewhere:[120]

$$a_{\text{free}}(\text{Ca}^{2+}) = \exp\left(\frac{2F(U_0 - U(\text{Ca}^{2+}))}{RT}\right) \tag{3.1}$$

In the following calculations, solutions were treated ideally, which is an acceptable assumption for the investigated concentration range, as demonstrated before.[120] To calculate the free ion product (corresponding to the ion activity product (IAP) if solutions are treated ideally), the concentration of free Ca^{2+} (determined from the Ca-ISE) was multiplied with the concentration of free carbonate ions.[19] The free carbonate concentration was calculated using a 1:1 binding ratio of calcium and carbonate according the following equation

$$c_{\text{free}}(CO_3^{2-}) = \frac{1}{V_{\text{total}}}\left(n_{\text{total}}(\text{carb}) - \left(n_{\text{added}}(\text{Ca}^{2+}) - n_{\text{free}}(\text{Ca}^{2+})\right)\right)$$
$$\cdot\left(\left(\frac{10^{-\text{pH}}}{10^{-10.33}}\right) + \left(\frac{(10^{-\text{pH}})^2}{10^{-6.35}\cdot 10^{-10.33}}\right) + 1\right)^{-1} \tag{3.2}$$

where $n_{\text{total}}(\text{carb})$ describes the total amount of carbonate species in the system (10 mM for standard experiments). Dilution effects during the experiments, e.g. during adjustment of initial pH value of the solution, were considered for the calculations.

3.3.8   Calculation of microscopic binding parameters of PNC association

Microscopic binding parameters of the multiple binding model used to describe PNC equilibria were calculated as demonstrated in the original work of Gebauer et. al.[19] Thereby, the microscopic number of calcium ions that bind a carbonate ion, x, and the microscopic binding equilibrium constant, K, are determined. For each measurement the $n_{\text{free}}(CO_3^{2-})$, $n_{\text{bound}}(\text{Ca}^{2+})$ and $c_{\text{free}}(\text{Ca}^{2+})$ data from the titration was fitted linearly in the prenucleation regime. The linear fits of $n_{\text{bound}}(\text{Ca}^{2+})$ and $c_{\text{free}}(\text{Ca}^{2+})$ were forced to intersect $y = 0$. This is necessary, because the electrode has a nonlinear behavior close to $c_{\text{free}}(\text{Ca}^{2+}) = 0$, which causes unrealistic values in this region, which in turn will result in a large error during the reciprocal plotting of the data in following steps of the evaluation procedure (eq. 3.3). The binding parameters x and K can then be calculated using a linear fit of the following equation:

$$1 + \left(\frac{n_{\text{free}}(CO_3^{2-})}{n_{\text{bound}}(\text{Ca}^{2+})}\right) = \frac{1}{x}\frac{1}{xK}\frac{1}{c_{\text{free}}(\text{Ca}^{2+})} \tag{3.3}$$

This procedure was repeated for each titration measurement and at least 3 independent titration experiments were evaluated. In case of experiments with polymers, the same method can be used, as the polymer concentrations used were very low (10 mg/L), and the error caused by calcium adsorption by the carboxyl groups of the polymer (Langmuir binding isotherm)[121] is within the experimental error of the experiment.

3.4   Results and Discussion

As discussed in detail in section 3.6.1 in the supplementary information (SI), the investigation of poly(aspartic acid) (PAsp50) and poly(glutamic acid) (PGlu50) in additive-controlled calcium carbonate formation using a previously established potentiometric titration procedure[98] reveals distinct effects. The arguably most interesting one is the strong inhibition of nucleation. This effect can be quantified using the so-called "scale factor" that describes the relative increase in calcium added until nucleation takes place compared to the additive-free reference experiment. Comparison of the pH-dependence of the scale factor for the polymers (Figure 3.1a) shows a stronger inhibition in presence of PAsp50 compared to PGlu50 at all investigated pH values, and in general, a strong pH-dependence of the scale factors is observed. While at pH 10.2, roughly 3 times stronger inhibition is detected for PAsp50 than in the reference, the scale factor even exceeds a factor of 10 at pH 9.0.

3.4.1   Polymers facilitate bicarbonate binding in mineral precursors

In search of mechanistic explanations for this strong inhibition and its pH-dependence, the pH titration data was quantitatively evaluated (Figure S3.14), in addition to the usually considered calcium ion selective electrode data. Interestingly, the prenucleation slope of the NaOH volume added to keep the pH value constant reflects the trend in scale factors, with the reference experiment showing the highest slope, followed by experiments in presence of PGlu50 and PAsp50 (Figure 3.1b and Figure S3.14b). From the NaOH addition, the removal of carbonate species from the buffer equilibrium upon addition of calcium due to ion association can be calculated. In polymer-free experiments, carbonate ions and calcium ions are bound in PNCs, resulting in the formal removal of carbonate ions from the buffer equilibrium ($HCO_3^- \rightleftharpoons H^+ + CO_3^{2-}$) and release of H^+ ions that are then neutralized by automatic NaOH addition. In previous polymer-free experiments, calcium and carbonate ions are essentially bound at a 1:1 binding ratio in the prenucleation regime above pH 9.0.[19, 34] Indeed, also here, if the amount of bound CO_3^{2-} (calculated from NaOH addition and buffer equilibria) is compared to the amount of bound Ca^{2+} (calculated from the Ca-ISE), the same values are obtained, confirming a 1:1 binding ratio for polymer-free reference experiments (Figure 3.1c). However, for experiments with polymers, NaOH addition is significantly lower than in the reference titration, while the amount of bound Ca^{2+} is affected less. The difference between bound carbonate calculated from NaOH addition and calcium binding (Figure 3.1c) can be explained by simultaneous binding of bicarbonate species in the prenucleation regime, while there is still Ca^{2+}-CO_3^{2-} association: Simultaneous binding of bicarbonate and carbonate ions causes some carbonate ions to be "invisible" to the NaOH addition, due to the properties of the buffer equilibrium. In fact, it can be shown that at the specific pH value considered here, the removal of 2.33 bicarbonate ions "masks" the binding of 1 carbonate ion, allowing the quantification of the amount of

bicarbonate binding from the recorded NaOH addition. The detailed calculations and reasoning for bicarbonate binding are discussed in section 3.6.3 in the SI.
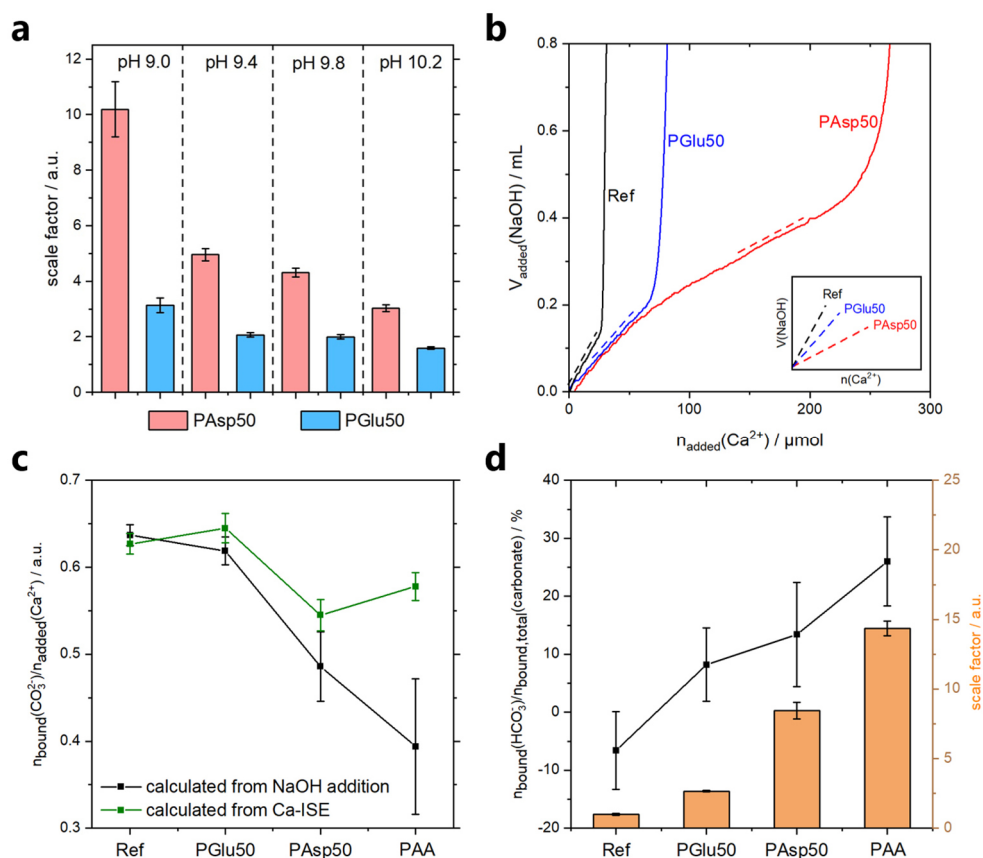

Figure 3.1 Potentiometric titration experiments in presence of polymer additives. a) pH-dependence of the scale factor (crystallization time relative to reference) for experiments containing 10 mg/L PAsp50 (red) and PGlu50 (blue). **b)** Amount of NaOH added in titration experiments at pH 9.0 containing 10 mg/L polymer. The dotted lines visualize the slope of added NaOH in the prenucleation regime close to nucleation. In experiments with polymer, the NaOH addition rate was significantly lower (see inset for easier comparison of slopes). **c)** Development of molar amount of bound CO_3^{2-} per added Ca^{2+} in the prenucleation regime for experiments containing 0.1 g/L (PAsp50 and PGlu50) or 0.01 g/L (PAA) polymer at pH 9.8. Values are calculated from the Ca-ISE (green) by assuming a 1:1 Ca^{2+}:CO_3^{2-} binding ratio and from the NaOH addition (black) by calculating the amount of bound CO_3^{2-} from changes in buffer equilibria. **d)** From the values shown in (c), the proportion of bicarbonate binding relative to the total amount of bound carbonate species (CO_3^{2-} + HCO_3^-) can be calculated (black). Error bars represent ± one standard deviation. The scale factors for each experiment are also shown (orange bars). The detailed calculations are described in section 3.6.3 in the SI.

The quantitative evaluation (Figure 3.1d, black data points) reveals considerable bicarbonate binding, amounting to around 15% relative to all carbonate species in the prenucleation regime for PAsp50 and around 25% for PAA. Remarkably, the order of the extent of bicarbonate binding (Ref → PGlu50 → PAsp50 → PAA, Figure 3.1d, black data points) corresponds to that observed in the scale factors (Figure 3.1d, orange bars). Indeed, the presence and relevance of

bicarbonate binding in a $CaCO_3$ dense liquid phase (DLP) was reported previously,[31, 196] however, the extent of bicarbonate binding reported therein could not be assessed. Here, bicarbonate binding upon the formation of a DLP, and its stabilization are in agreement with the stronger inhibition observed with decreasing pH values (Figure 3.1a) — lower pH corresponds to a higher fraction of bicarbonate present in solution. The bicarbonate binding seems to be facilitated by the polymer, having a stabilizing effect on the DLP. A potential explanation for this is the introduction of H^+ ions into the calcium carbonate DLP, thereby formally lowering local pH values and preventing the formation of solids, especially crystals. Here, calcium deficiency (relative to all carbonate species) within the DLP may hamper reaching the 1:1 stoichiometric composition required for the formation of crystalline calcium carbonates. How exactly the polymer can facilitate bicarbonate binding cannot be derived from this data, but it is likely to take place during coalescence and growth of the DLP droplets[11, 35] (see SI section 3.6.2 for a more in-depth discussion).

3.4.2 *Ex situ* characterization of polymer-stabilized ACC

To gain further insights into the polymer-stabilized DLP, samples were isolated by quenching the titration at pH 9.8 shortly before reaching the maximum in free ion products by pouring the reaction solution into a large excess of ethanol.[46] The quenching procedure causes rapid dehydration of the DLP, yielding the respective polymer-stabilized ACC sample (PAsp50_ACC), while the large excess of ethanol also prevents crystallization of the ACC. As shown in earlier studies,[46] quenching before the nucleation event leads to ACC nanoparticles with several tens of nm in size (see also Figure S3.10). The isolated sample was then characterized to explore, whether the bicarbonate binding detected in titration experiments can also be observed in the isolated solid ACC samples. Thermogravimetric analysis (TGA) of the ACC sample allows determining the contents of polymer and calcium carbonate, as the organic and inorganic compounds exhibit distinct decomposition characteristics. While ACC decarbonization takes place between 600-800 °C, the polymer shows a sharp (exothermic) decomposition at 300-400 °C, as visible from the pure ACC and PAsp50 reference TGA measurements (Figure S3.16). The PAsp50-stabilized ACC sample presents the characteristic ACC decarbonization at high temperature, as well as the sharp exothermic feature due to polymer decomposition (Figure 3.2a). The incorporation of significant amounts of polymer in the ACC sample is confirmed by ATR-FTIR investigations, as polymer vibrational bands are clearly visible in the PAsp50_ACC sample (Figure 3.2c). However, TGA also reveals a significant exothermic decomposition process occurring prior to polymer decomposition (Figure 3.2a, grey area). Analyzing the gases released during this decomposition process with mass spectrometry (TGA-MS) reveals H_2O and CO_2 release (Figure S3.17). This is expected for temperature-induced decomposition of bicarbonate ions, as the respective carbonate salt is formed upon release of H_2O and CO_2 (e.g., $2\ NaHCO_3 \rightarrow Na_2CO_3 + H_2O\uparrow + CO_2\uparrow$).
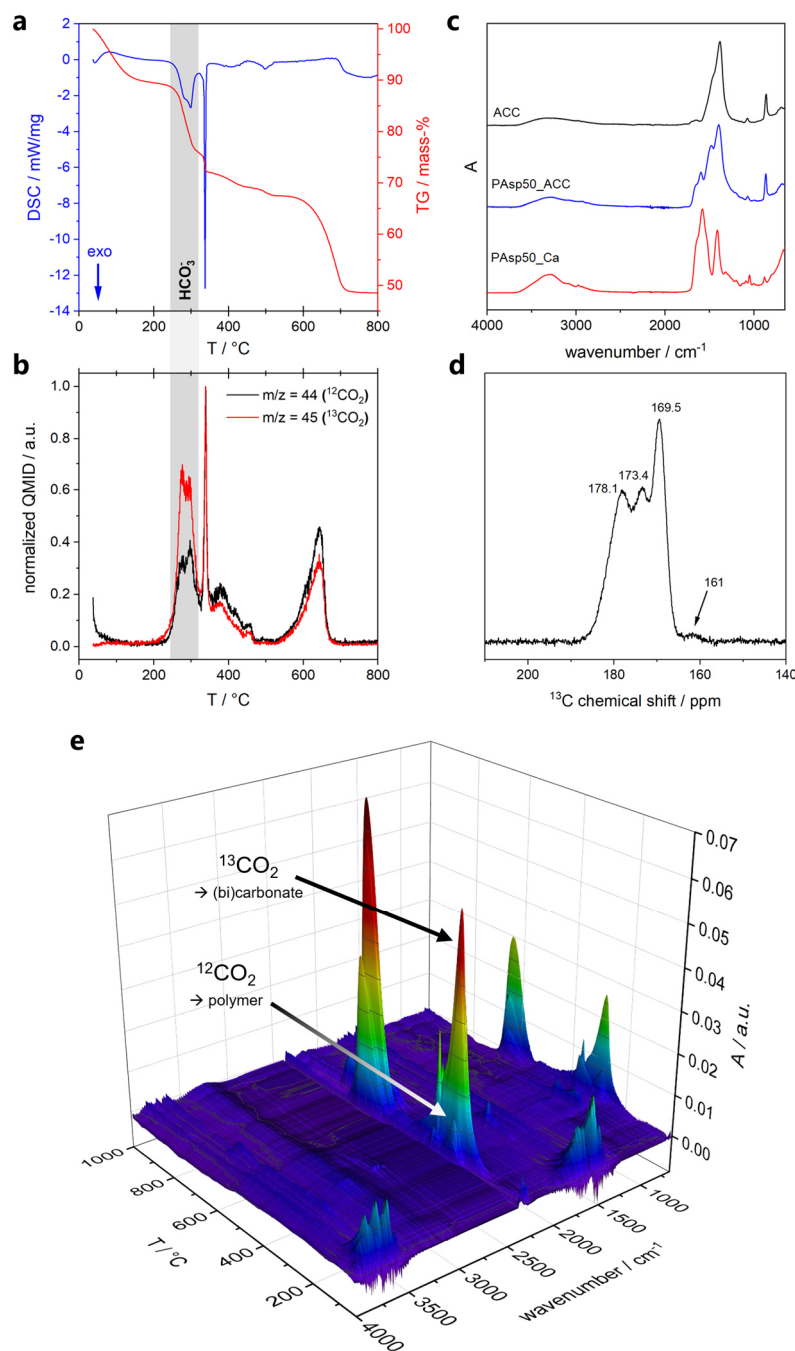
Figure 3.2 Characterization of isolated polymer-stabilized ACC. Characterization of isolated polymer-stabilized ACC. The sample was isolated from a titration experiment using 0.1 g/L PAsp50 at pH 9.8 by quenching the solution in ethanol (see section 3.3.4 in the SI). **a)** TGA (red) and DSC (blue) analysis. The exothermic decomposition of the bicarbonate species is highlighted in grey. **b)** Normalized QMID for TGA-MS measurement on the PAsp50_ACC sample using ^{13}C enriched carbonates in the titrations. Due to the natural abundance carbonate distribution in the polymer, released gases from polymer ($^{12}CO_2$; m/z = 44, black) and from mineral ($^{13}CO_2$; m/z = 45, red) can be distinguished, showing significant amounts of mineral decomposition below 300 °C (highlighted in grey). **c)** ATR-FTIR spectra of polymer-stabilized ACC sample, showing significant amounts of polymer incorporation. Pure ACC and PAsp50 calcium salt (PAsp50_Ca) are shown as reference (detailed FTIR spectra are shown in Figure S3.23). **d)** ^1H-^{13}C CP MAS NMR measurement, showing that almost no bicarbonate is detected (^{13}C: δ 161 ppm).[197] **e)** TGA-IR analysis of the ^{13}C carbonate enriched PAsp50_ACC sample confirms the strong $^{13}CO_2$ release from (bi)carbonate species at around 300 °C.

TGA-MS also indicates that polymer decomposition takes place, at least to some extent, at this temperature (Figure S3.17b), possibly triggering the decomposition of the bicarbonate species. On the other hand, polymer decomposition occurs in a similar temperature range and also results in the release of CO_2 and H_2O. Indeed, PAsp50 calcium salt shows vastly different decomposition characteristics when compared to PAsp50 sodium salt (Figure S3.17 and Figure S3.24), revealing additional decomposition stages, due to subsequent formation and decomposition of $CaCO_3$.[198] To elucidate, whether the observed process is due to mineral or polymer decomposition, ^{13}C enriched carbonates were employed in the synthesis of the polymer-stabilized ACC, allowing us to distinguish the CO_2 release arising from polymer decomposition ($^{12}CO_2$ release) from the decomposition of mineral (bi)carbonate species ($^{13}CO_2$ release). TGA-MS of the labeled sample clearly reveals a strong release of $^{13}CO_2$ prior to polymer decomposition (Figure 3.2b, grey area), indicating that significant (bi)carbonate decomposition takes place at this temperature. We also detect $^{12}CO_2$ in this temperature region, showing that some polymer decomposition takes place simultaneously, confirming the TGA-MS results discussed above (Figure S3.17b). The release of $^{12}CO_2$ at higher temperatures is then caused by decomposition of polymer carboxylate groups that are bound to Ca^{2+} in the ACC sample, forming $CaCO_3$ as an intermediate upon their decomposition (Figure S3.17d).[198] Additional TGA-IR characterization of the decomposition gases confirms the strong release of $^{13}CO_2$ around 300 °C (Figure 3.2e). The $^{13}CO_2$ release in this temperature range was only detected for the polymer-stabilized ACC sample synthesized by titration, and neither pure ^{13}C enriched ACC, pure polymer, nor a mixture of independently isolated polymer and ^{13}C enriched ACC did exhibit this characteristic release (Figure S3.18). Summarizing, the TGA-MS-IR study confirms the presence of bicarbonate species in the polymer-stabilized ACC sample. Importantly, the weight loss that can be assigned to the decomposition of bicarbonate species (~13% weight loss, corresponding to roughly 27% of bicarbonate present in the ACC, see Figure S3.18e) agrees with the amount detected in the pre-nucleation stage and bound in the the DLP in the titration experiments (Figure 3.1d). This suggests that bicarbonate bound within the DLP is indeed quantitatively transferred to solid ACC in the above-described quenching procedure. The exothermic decomposition of the bicarbonate species in polymer-stabilized ACC (Figure 3.2a) differs fundamentally from that of $NaHCO_3$, which exhibits endothermic decomposition (Figure S3.16d). In addition, no sodium-containing phase was detected in the XRD spectra of the product isolated after TGA (Figure S3.15), further confirming that no considerable $NaHCO_3$ coprecipitation took place upon the quenching and isolation of the ACC. It is possible that some sodium ions are incorporated within the ACC, e.g., for local charge balancing upon bicarbonate binding in the ACC and its precursors, however, if any, the amount should be low since we could not detect any sodium salts in the ACC (Figure S3.15).

MAS NMR experiments were performed to characterize the polymer-stabilized ACCs, especially in order to explore whether bicarbonate ions are a structural constituent of the mineral.[34] In ^1H-^{13}C CP MAS NMR studies, two polymer peaks arising from the carboxyl

carbons (C_γ) are visible in the carbonate region of the spectrum (Figure 3.2d). Thereby, one species corresponds to free carboxyl groups and the other to carboxyl groups bound to Ca^{2+} (Figure S3.25). Surprisingly, only a very small amount of bicarbonate ions can be detected (^{13}C, 161 ppm, Figure 3.2d, arrow), again confirming that no $NaHCO_3$ coprecipitation took place.

At first glance, the MAS NMR results seem to contradict the titration and TGA-MS-IR results, as only minor amounts of bicarbonate species are detected. A possible explanation for this seeming discrepancy is that protons possess significant mobility within the ACC, thus giving rise to ^{13}C chemical shifts distinct from established bicarbonate incorporation and potentially being more similar to carbonate chemical shifts. Distinct proton mobilities would also explain the regularly observed apparent inefficiency of MAS CP experiments in case of the polymer-stabilized ACCs (data not shown), which might explain the lower amount of bicarbonate ^{13}C detected by MAS NMR as calculated from titration and visible in TGA-MS-IR. However, a detailed NMR-spectroscopic exploration of this hypothesis is beyond scope of the present study.

3.4.3   Conductivity of polymer-stabilized ACC.

We decided to explore the mobility of protons in polymer-stabilized ACC by means of electrical conductivity measurements, as this phenomenon would render these amorphous minerals proton conductors, at least if mobility is not restricted within short-range ionic environments. Established methods to measure (single) particle conductivity usually include connecting the particles to electrodes.[199-201] However, the available methods are either not suitable for small sizes of particles (in our case, below 100 nm particle size) or only one particle can be measured at a time, resulting in poor statistics. We therefore developed a straightforward method for the qualitative assessment of conductivities of individual particles based on conductive atomic force microscopy (C-AFM). The method utilizes measurements in C-AFM spectroscopy mode, i.e., recording an I/V diagram, on individual particles. Thereby, it is important to record the distance of the tip to the substrate during the spectroscopy measurement to confirm that the tip is indeed in contact with a particle. The slope of the I/V diagram can then be compared to reference samples (conductive and non-conductive particles), to gain qualitative information on conductivity. The method allows measurements of a large number of particles starting from a size of a few nm. A detailed description of the method and data evaluation is provided in section 3.6.4 in the supplementary information. To validate the method, gold nanoparticles (as conductive reference particles) and vaterite nanoparticles (as non-conductive reference particles) were synthesized and investigated, showing that the difference in conductivity can reliably be determined above a distance of ca. 20 nm (Figure S3.19). The C-AFM experiments were performed in a glovebox in water-free atmosphere and samples were dried in vacuum prior to measurement to eliminate potential effects of surface-adsorbed water on the measured conductivities.
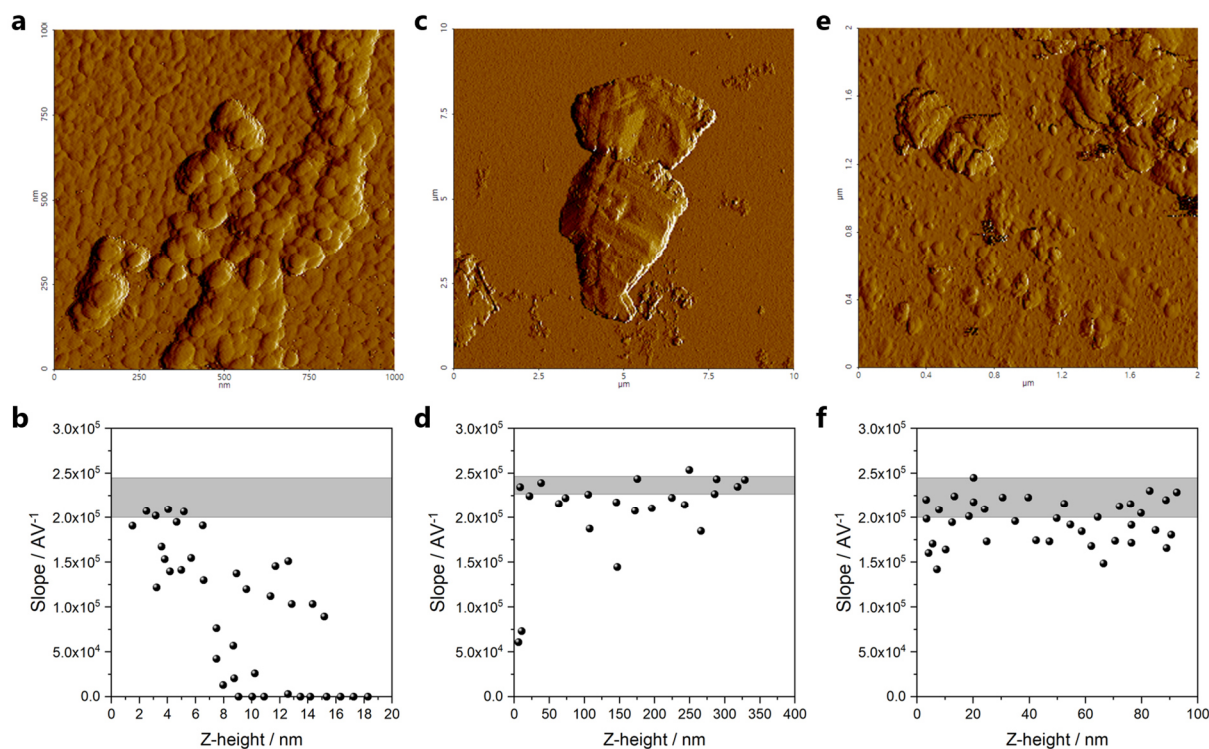
Figure 3.3   Measurement of conductivity of ACC particles using C-AFM. a) AFM amplitude map recorded in non-contact mode (NCM) during the investigation of a polymer-stabilized ACC sample (PAsp50_ACC). Individual ACC nanoparticles are visible. **b)** Results of C-AFM spectroscopy measurements of polymer-stabilized ACC of the area as shown in (a). The slope of the I/V diagram close to the origin is shown versus the Z-height of the respective measurement point. The grey part shows the standard deviation of 100 measurements on the gold wafer and is a measure for the highest conductivity that can be measured using this approach. **c)** NCM amplitude map for a different area of the same polymer-stabilized ACC sample showing a large structure of several µm in diameter and **d)** corresponding C-AFM results, showing good conductivity across a measurement distance of several 100 nm (more details are shown in Figure S3.22). **e)** NCM amplitude map for a polymer-free ACC sample and **f)** corresponding C-AFM results, showing good conductivity up to a Z-height of 100 nm (more details are shown in Figure S3.21).

Measurement of individual, sub-100 nm polymer-stabilized ACC particles showed indeed conductivity for a measuring height below 10 nm (Figure 3.3a and b), while above 10 nm, the conductivity (i.e., slope of the I/V diagram) gradually decreases to 0. This is because the increasing Z-height is caused by several particles lying on top of each other rather than particles with increasing size, as visible by the AFM height images (Figure S3.20), and obviously poor conductivity across grain boundaries. Due to limitations of the C-AFM measurements for Z-heights below 20 nm owing to leaking voltage, we thus cannot provide unambiguous evidence for conductivity of individual ACC particles at this point (see also Figure S3.21 and related discussions). However, we also detected larger structures in polymer-stabilized ACC samples (Figure 3.3c and d). These structures can be considered as dried residues of larger polymer-stabilized DLP species that had putatively formed in solution due to aggregation and partial coalescence of nm-sized ACC precursors before quenching. These structures have a

smooth surface and are different from loosely aggregated individual particles, appearing as a continuous phase. All of these structures exhibit electrical conductivity across length scales that are orders of magnitude larger than single ACC particles (Figure 3.3d), with the largest distance being almost 1 μm (Figure S3.22). Together with the above-discussed titration, TGA-MS-IR, and MAS NMR results, we attribute this electrical conductivity to originate from proton ionic conductivity, while the protons are introduced via bicarbonate binding in the initially formed DLP during the synthesis. ACC synthesized in absence of polymer exhibits the same behavior; loose agglomerates of particles are not conductive (Figure S3.21h and i), while larger, continuous structures are (Figure 3.3e and f). This indicates that also polymer-free ACC is formed via a bicarbonate rich dense liquid phase, albeit the total bicarbonate content is significantly lower than in polymer-stabilized ACC.[34]

3.5 Conclusions

Polycarboxylate additives strongly facilitate the binding of bicarbonate ions in an initially formed DLP, and corresponding protons are transferred to solid amorphous mineral precursors alongside additional carbonate ions upon their isolation. This effect seems to play a crucial role in additive-controlled mineralization. In light of the present results, the notions of the PNC pathway,[11] previously established for additive-free systems, can be extended for polycarboxylate-controlled scenarios, where interactions between polymers and bicarbonate ions play a central role at each step along the crystallization pathway (Figure 3.4). While our study does not provide a direct explanation for a mechanism how low amounts of polycarboxylates may facilitate considerable bicarbonate binding, several key insights have been obtained here. On the one hand, the binding of bicarbonate ions in the late prenucleation stage, in which aggregation and growth of DLP droplets occurs, effectively leads to the incorporation of protons and additional carbonate ions into the calcium carbonate phase, which thus becomes a calcium ion-deficient precursor. Upon transformation of the precursor to crystalline minerals, these protons must be excluded, posing a significant barrier for phase transformation. Due to their high mobility even in solid amorphous particles, protons may thus very effectively "poison" the growth of nascent crystalline domains: Release of protons upon crystallization can lower pH values near the crystalline nucleus, thereby dissolving the crystals. While further research is necessary to elucidate the process of bicarbonate release upon crystallization further, the sole detection of the presence of considerable amounts of protons within the DLP and solid ACC can explain the pronounced inhibiting effect of the polymers even for distinctly substoichiometric additive concentrations: The effect of polymers is essentially "leveraged" through bicarbonate ions. Considering biomineralization, such effects can be of even larger importance, as it takes place in seawaters at lower pH values than explored herein, and thereby at higher relative bicarbonate contents.

We believe that the crucial role of bicarbonate ions has not been discovered before due to the high mobility of the protons even in the solid state, which is putatively associated with structural water in the ACC. Due to this H^+ mobility, no "classical" bicarbonate ions are present in the mineral, making them hard to detect, especially via NMR techniques when chemical shifts of the distinct environments become too similar. In any case, the proton mobility gives rise to ion conductivity within ACC that can be observed as electrical conductivity in C-AFM, even across several 100 nm. Reference experiments on vaterite particles clearly show that the phenomenon is real. ACC therefore is a mineral ion conductor, which can potentially be used in electrochemical devices. Proton ion conducting materials are used as electrolytes,[202] proton exchange membranes,[203] for example in fuel cells, or touch panels,[204] illustrating the tremendous potential of this class of green materials. In future investigations, the potential use of ACC-based mineral proton conductors should thus be explored further.
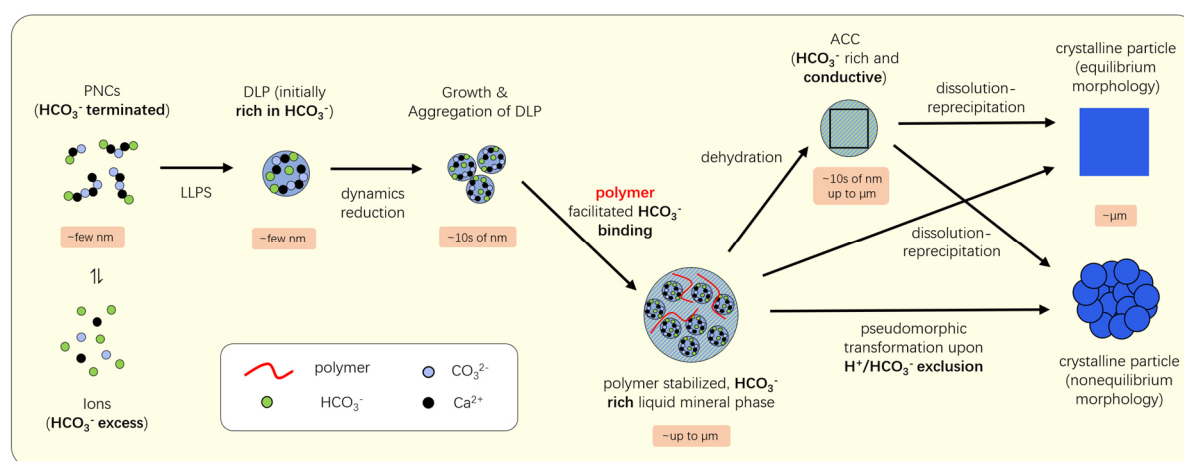

Figure 3.4   Prenucleation cluster pathway in presence of additives, underscoring the importance of bicarbonate ions in each step of the crystallization pathway. All results are in line with previously published results regarding mineral formation via the prenucleation cluster (PNC) pathway (Figure 1.1).[11] ***Ions:*** In the investigated carbonate buffer solutions, bicarbonate ions are the dominant carbonate species across the investigated pH range (pH 9.0 to 10.2; $pK_a = 10.33$).[19] Polycarboxylates can interact with the system by binding Ca^{2+} ions.[121] ***PNCs:*** In equilibrium with ions are prenucleation clusters, while bicarbonate ions can act as chain terminators for the growth of PNCs of DOLLOP structural form.[20] While, no effect of the polymers on PNC equilibria could be resolved in our titration experiments, at least for the investigated range of concentrations, the polymers could already facilitate bicarbonate binding in the clusters at this stage. ***DLP:*** Upon crossing the binodal limit for liquid-liquid phase separation (LLPS), the bicarbonate-terminated PNCs transform to nm size droplets of a dense liquid phase (DLP). The DLP is therefore initially rich in bicarbonate.[31, 34] In our experiments, there is no big difference in nucleation inhibition if the polymer is added before or after the LLPS (see section 3.6.2), suggesting that the key interaction for inhibition takes place at a later stage. This is in line with results showing that poly(aspartic acid) does not change the locus of the binodal limit.[22] ***DLP aggregation:*** In absence of additive, the DLP droplets aggregate to minimize their surface area by forming larger DLP droplets.[24] Polymers interact strongly with the growing DLP droplets, adsorbing on the droplets and stabilizing the growing phase. In the same step, bicarbonate is incorporated into the growing droplets, resulting in the differences of NaOH addition in the prenucleation regime and the strong influence of

the pH level (bicarbonate concentration) on the inhibition efficiency. A higher amount of bicarbonate binding corresponds to a kinetically more stable DLP. There is likely partial diffusion of bicarbonate and polymer into the (initially polymer-free) DLP droplets, as no structural differences are visible in SEM, forming a continuous polymer-stabilized liquid phase. This "inter-linking" of DLP droplets that are tens of nm in size by polymer strands also explains the often detected "granular" structure of minerals formed from polymer-stabilized structures.[205-206] *ACC:* Upon dehydration, the polymer-stabilized liquid phase transforms into solid amorphous calcium carbonates. The polymer-stabilized ACC exhibits a higher kinetic stability than the polymer-free ACCs. In addition, bicarbonate ions and polymer molecules are detected in the dried ACCs. The high amount of bicarbonate ions and polymer in the ACCs possibly explains their stability, as the protons (and polymer) have to be excluded to achieve the proper stoichiometry for crstallizing $CaCO_3$. ***Crystalline $CaCO_3$:*** While polymer-free ACCs mainly transform into crystalline $CaCO_3$ via dissolution-reprecipitation pathways, the polymer-stabilized DLP/ACC can also transform via pseudomorphic transformation, thereby forming structures with altered shapes and non-equilibrium morphologies.[35, 154] As mentioned earlier, the stoichiometric "mismatch" between the precursor and crystalline $CaCO_3$ is one reason for the increased kinetic stability of polymer-stabilized mineral precursors.

3.6 Supplementary Information

3.6.1 Discussion on basic titration experiments and polymer effects

In potentiometric titration experiments, dilute $CaCl_2$ solution is slowly dosed into a stirred solution of carbonate buffer and polymer, while the pH is kept constant by automatic addition of NaOH. During the process, parameters are recorded *in situ* using potentiometric electrodes, allowing to gain insights into the entire mineralization process, starting from the undersaturated solution up to the final crystalline particles. In addition, mineral samples can be isolated at distinct stages in the pathway and analyzed using *ex situ* techniques, such as Fourier-transform infrared spectroscopy (FTIR) and scanning electron microscopy (SEM). Using this approach and well-defined polycarboxylate additives, i.e., polymers with small polydispersities and comparable chain lengths (see also Table 2.1), the effect of polymers on the distinct stages along the $CaCO_3$ formation pathway can be systematically investigated.
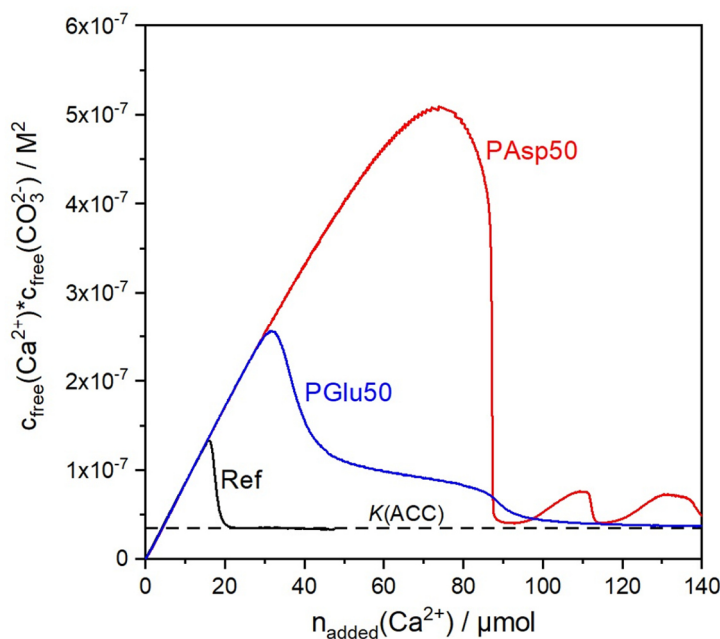

Figure S3.1 Exemplary titration curves of potentiometric titration experiments in presence of polymer additives. The development of free ion product during titration experiments without additive (black) and in presence of 10 mg/L PAsp50 (red) and PGlu50 (blue) is shown. Experiments were performed by dosing 20 mM $CaCl_2$ solution into 50 mL of 10 mM carbonate buffer at pH 9.4. The dotted line represents the solubility product of ACC formed after nucleation in the reference experiment. The curves are exemplary shown for pH 9.4, for full set of experiments see Figure S3.11.

As described in section 1.3 in the introduction, in titration experiments, the development of free calcium concentration is recorded by a calcium ion selective electrode (ISE) during addition of $CaCl_2$ solution into a polymer/carbonate solution. Then, the data recorded with additives in the carbonate buffer solution is compared to a polymer-free reference experiment, allowing the

identification of different types of interactions (Figure 1.2b). Analyzing the titration curves in this regard for poly(aspartic acid) and poly(glutamic acid) with a polymerization degree of 50 (PAsp50 and PGlu50) (Figure S3.1), it is evident that no calcium binding (type I) can be detected, due to the low additive concentrations used in the experiments (10 mg/L). However, although concentrations are very low, a strong inhibition of nucleation is detected (type III), with PAsp50 showing a stronger inhibition compared to PGlu50, as reported before.[87, 90, 98] Interestingly, no effect on PNC equilibria could be detected (type II), at least for the investigated concentrations, showing that the strong nucleation inhibition likely cannot be explained by (de)stabilization of PNCs or effects on PNC equilibria. After the maximum in the curves, the polymers also show a different behavior, with a phase of higher solubility product formed in presence of PGlu50 (type V), while in case of PAsp50, a product is formed with similar solubility as in the reference experiments, which, according to the solubility product, corresponds to amorphous calcium carbonate (ACC) formed at the respective pH value.[19, 22] Although there is no effect on the solubility product of the initially formed phase detected, in case of PAsp50 the free calcium concentration increases again before additional drops are detected. This indicates that the particle growth is inhibited after nucleation, presumably by adsorption of PAsp50 on the formed particles.[98] To investigate the species present at distinct points in the titration experiment, samples were isolated along the titration curve and characterized using FTIR spectroscopy (Figure S3.9) and SEM (Figure S3.10). Prior to the maximum in the titration curves, ACC particles are present with a size of less than 100 nm. The ACC particles then transform to crystalline $CaCO_3$ upon drop in calcium potential. In additive-free systems, this takes place by a dissolution-recrystallization process.[154] In all experiments, the first detected crystalline phase is detected at the maximum in the titration curve in the form of spherical vaterite particles (several 100s of nm in size). Without additives, these particles then transform to larger hexagonal vaterite crystals, which in turn (slowly) transform into the thermodynamically stable $CaCO_3$ polymorph calcite. In case of experiments with polymers, this transformation to calcite is not detected and the small spherical vaterite particles are stabilized, presumably by adsorption of the polymer onto the particles, as seen in the PAsp50 titration curves. In case of PGlu50, on the plateau with higher solubility after the maximum, there are small nanoparticles visible that can be identified as ACC according to FTIR (Figure S3.9f), showing the stabilizing effect of PGlu50 on ACC. This is reminiscent of biomineralization, as glutamic acid rich peptides are often associated with ACC, while peptides rich in aspartic acid are upregulated during formation of crystalline $CaCO_3$.[56] It is intriguing that PGlu50 shows a strong stabilizing effect on ACCs that remain stable even in presence of crystalline particles, while the nucleation inhibition, and therefore stabilization of liquid precursor and amorphous intermediate species in the prenucleation stage, is much stronger for PAsp50. Titration experiments at different pH values (Figure S3.11) reveal that at all investigated pH values the previously described trends are visible, with PAsp50 showing stronger crystallization inhibition, while PGlu50 possesses a stronger post-nucleation ACC

stabilization. Interestingly, this kinetic stabilization of ACC particles is stronger at higher pH values, visible by the plateau with higher solubility being present for a longer time. Even for PAsp50, at high pH (pH 10.2, see Figure S3.11d) a plateau becomes visible while at lower pH values (pH 9.0, see Figure S3.11a), the plateau for PGlu50 has almost disappeared. This effect could be caused by a dependence of stabilizing efficacy on ACC proto-structure.[46] Experiments performed with poly(acrylic acid) (PAA), reveal the same type of interactions, while they show the strongest inhibition of all investigated polymers (Figure S3.12). Although our further results focus on elucidating effects for PAsp50 and PGlu50 due to their relevance in biomineralization, we argue that the essential conclusions will be valid for PAA as well due to the similarity in the titration experiments.

As visible in Figure S3.1, the most interesting effect is the strong nucleation inhibition of the polymers ("scale factor") that also shows a strong pH-dependence (Figure 3.1a in section 3.4.1). It needs to be mentioned that there is also an increase in nucleation time in absence of additives if the pH value is lowered, as less carbonate is present in the carbonate-bicarbonate buffer equilibrium at a low pH values (4.4% CO_3^{2-} at pH 9.0 compared to 42.5% CO_3^{2-} at pH 10.2)[19] and more calcium needs to be added to reach a critical supersaturation. However, scale factors are reported relative to the reference experiment at the same pH value, and a clearly over-proportional increase in inhibition efficiency is detected for low pH values. The strong scale inhibition by polymers was previously attributed to the (colloidal) stabilization of liquid precursor phases, visible by the growth of precursor droplets.[101, 126] Indeed, this effect is also visible in our experiments, with the solution getting turbid before the maximum of free ion product is reached, indicating the formation of precursor droplets of a size detectable by the optrode (Figure S3.13). In fact, more elaborate titration experiments indicate that the main interaction of the polymers takes place with the dense liquid precursor (DLP) droplets by a complex interplay of surface adsorption and incorporation of the polymer into the bulk of the DLP (see discussions in section 3.6.2). Again, the early decrease in transmission is stronger at lower pH values (Figure S3.13), indicating that the increasing efficiency of scale inhibition at lower pH values is linked to the stabilization of the dense liquid precursor phase, and that elucidating the mechanism of this stabilization is key to understanding the extraordinary crystallization inhibition properties of polycarboxylates.

3.6.2   Advanced titration experiments

As described in section 3.6.1, the polymers interact strongly with the liquid mineral precursor droplets and stabilize them until they are large enough to be detectable by the optrode. Different types of interactions with the liquid precursor phase are possible, as the liquid phase goes through several stages along the PNC pathway.[11] It has recently been demonstrated that PNCs determine the characteristics of liquid-liquid phase separation (LLPS).[18] The droplets of the dense liquid mineral phase (DLP) directly result from the PNCs upon densification and reduction of dynamics, resulting in the formation of an interface. The initially formed nm-sized droplets then coalesce into larger liquid droplets that can reach several tens to hundreds of nm in size, with this process being driven by reduction of interfacial surface area. In the later stages of the crystallization pathway, the DLP droplets then dehydrate, densify, and solidify to amorphous mineral intermediates. The additives can potentially interact at all these stages, i.e., influence the structure (and stability) of the DLP by interaction with PNCs even before LLPS takes place, interact with the DLP droplets formed directly after LLPS, i.e., when they are still a few nm in size, or interact with already larger dense liquid droplets at the later stages. Furthermore, these interactions could take place on the surface of the droplets by adsorption of the polymer or in the bulk of the droplets.

To gain insights into this process, titration experiments were performed in which the polymer was added to a polymer-free system shortly before nucleation, i.e., shortly before the drop of calcium potential (Figure S3.2a). In this "late addition" experiment, the polymer is introduced into the system after LLPS has taken place[22] and already large DLP droplets are present. Considering this information, a drastic reduction of the inhibition efficiency would be expected, if the main interactions of the polymer take place at earlier stages along the mineralization pathway, i.e., interaction with PNCs or the DLP shortly after LLPS, as these species have already continued to grow to form larger species and are no longer present in their original state. The resulting curves show essentially the same behavior as titration experiments with the polymer being present from the beginning (Figure S3.2b vs. Figure S3.11b, scale factor comparison is shown in Figure S3.2f), with the same, if not even slightly pronounced, inhibition efficiency (Figure S3.2c). This shows that the main interaction responsible for the inhibition efficiency is likely not with PNCs or small liquid droplets, but rather with larger dense liquid droplets. As discussed for regular titration curves, no effects on PNCs are visible for the investigated polymer concentrations, as no differences in the prenucleation slopes are detected, which is in line with these results. This also fits to earlier results that showed that polymers do not affect the binodal limit for LLPS.[22] The interactions with these large liquid droplets (10s to 100s of nm in size) could take place via bulk interaction or on the surface of the droplets.[93]
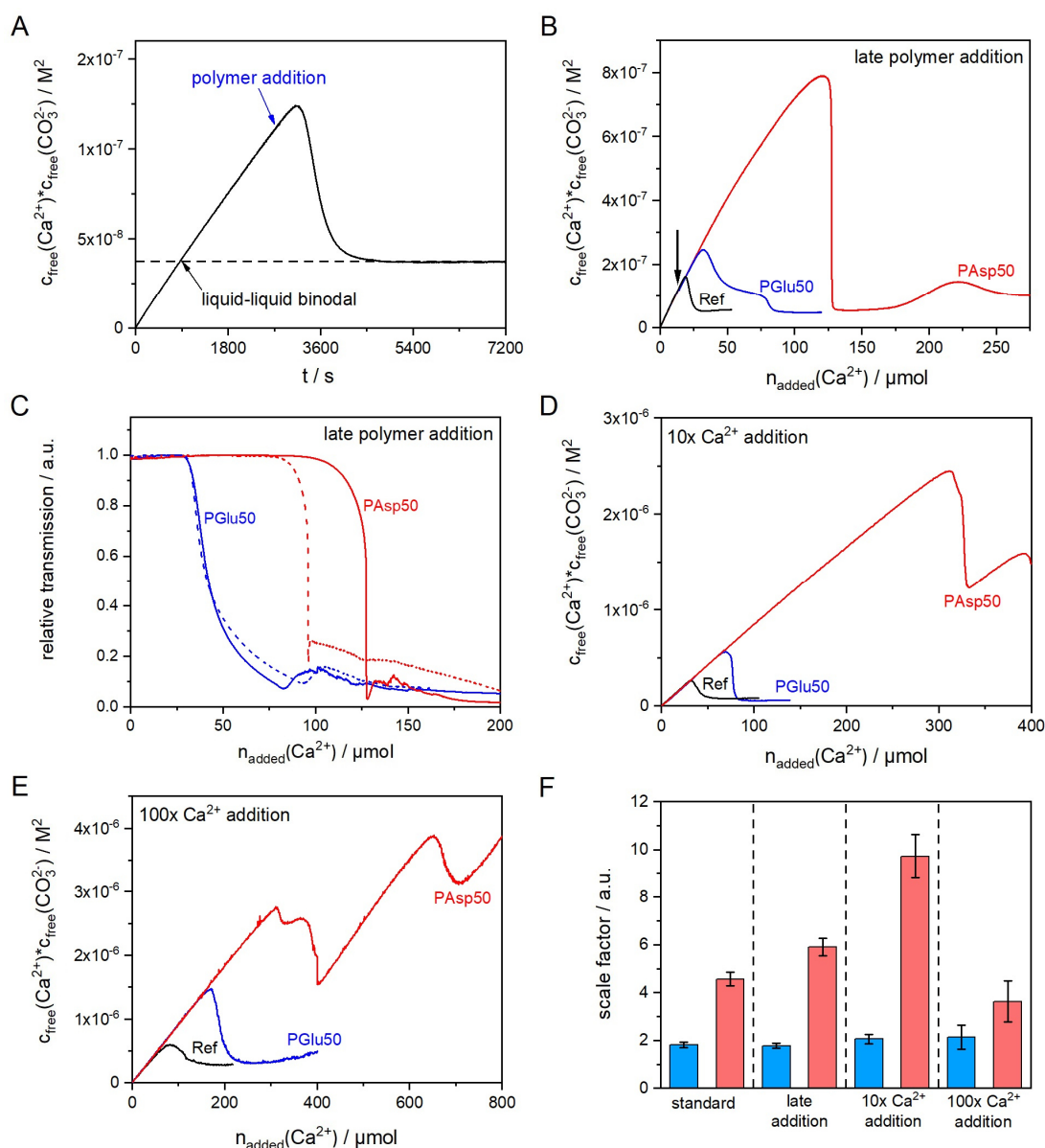
Figure S3.2 Modified titration experiments. a) Illustration of the principle of "late addition" experiments. From previous studies the locus of the liquid-liquid binodal can be determined, corresponding to the IAP of the formed ACC.[18, 22] The polymer can be added at a significantly later stage, after the binodal has been crossed. The polymer is added by injecting 0.25 mL of a concentrated polymer solution (2 g/L) with an Eppendorf pipette to the stirred, polymer-free carbonate solution (reference experiment). After mixing with the reaction solution, the polymer concentration is the same as in a regular experiment (10 mg/L), allowing the comparison of the experiments. **b)** Free ion product during "late addition" experiments at pH 9.4, showing essentially the same trend as for regular experiments, at which the polymers are present from the beginning (Figure S3.11b). **c)** Corresponding transmission signal measured by the optrode for late addition experiments (solid lines) and regular experiments (dotted lines). While PGlu50 shows essentially the same behavior in both experiments, an inhibition increase in the case of PAsp50 late-addition experiments is detected. **d)** In a different type of experiment, the addition speed of the CaCl$_2$ solution is changed, allowing to probe further into the binodal to access more hydrated ACCs.[18] The experiments with 10x CaCl$_2$ addition speed (0.1 mL/min) and **e)** 100x CaCl$_2$ addition speed (1 mL/min) show significant differences in the titration curves compared to regular experiments. **f)** Comparison of scale factors at pH 9.4 for regular experiments, late addition experiments and fast Ca^{2+} addition rate experiments (PAsp50 – red; PGlu50 – blue).

The decrease in transmission signal prior to the formation of crystalline particles in case of experiments with polymer, but not in absence of polymer (Figure S3.13) shows that the DLP droplets grow during the further evolution of the experiment, i.e., coalescence takes place. The stabilizing effect of the polymer therefore does not stop coalescence of the initially formed DLP, but rather stabilizes the larger droplets after coalescence. In the larger liquid phase formed from coalescence, the polymer is likely present in the bulk, as a strong type V interaction is observed for polymers, i.e., the solubility product after the titration is higher than for the reference experiments. This type V interaction is especially pronounced for PGlu50 but also for PAsp50 at high pH values (Figure S3.11), indicating that indeed the (bulk) structure of the formed products is different. ATR-FTIR suggests that this phase with higher solubility is ACC (Figure S3.9f), and the higher solubility product compared to ACCs formed in polymer-free experiments could be caused by a higher water content,[18] the incorporation of bicarbonate[34] or incorporation of polymer itself in the ACC structure.

To further support the notion of a "bulk interaction" motif of the polymers, titration experiments with faster $CaCl_2$ addition speeds were performed (Figure S3.2d and e), as a higher addition speed allows to reach further into the binodal before demixing takes place, therefore allowing to access less stable DLP droplets with higher water content.[18] These "fast calcium addition" experiments reveal a big effect on the scale factor (Figure S3.2f), with a 10x addition rate resulting in a strong stabilization by PAsp50 and 100x addition resulting in a destabilization compared to the regular addition experiment. Also at higher addition rates, a shoulder is formed for experiments with PAsp50 (Figure S3.2e). Interestingly, the data for PGlu50 shows almost no effect of the addition speed on the scale factor, but the type V interaction after the maximum seems to disappear. These strong effects of PAsp50 could be caused by changes in the size of the DLP droplets, affecting the efficacy of adsorption of polymer and stabilization of the formed aggregates. Alternatively, the structural differences of the DLP (more water content for faster addition rates) might hint towards a significant bulk interaction with the DLP, and the higher water content could lead to a favorable diffusion of PAsp50 into the DLP. The reduced scale factor at 100x addition rate might be caused by changes in the DLP structure upon approaching the spinodal limit, potentially causing unfavorable interactions or there is too little time for polymer adsorption to properly equilibrate.

3.6.3   Determination of bicarbonate binding

To calculate the amount of bound bicarbonate in the prenucleation regime, the amount of bound CO_3^{2-} determined from the Ca-ISE (by calculating Ca^{2+} binding and assuming a 1:1 binding ratio of bound CO_3^{2-} and bound Ca^{2+}) is compared with the amount of CO_3^{2-} binding "visible" to the pH electrode due to changes in the buffer equilibrium (Figure S3.3). Essentially, if bicarbonate binding takes place in addition to carbonate binding, the buffer equilibrium is shifted less and the change in pH value upon calcium addition/(bi)carbonate binding is reduced. Quantitative evaluation of these effects allows determining the amount of bicarbonate binding in the prenucleation regime.
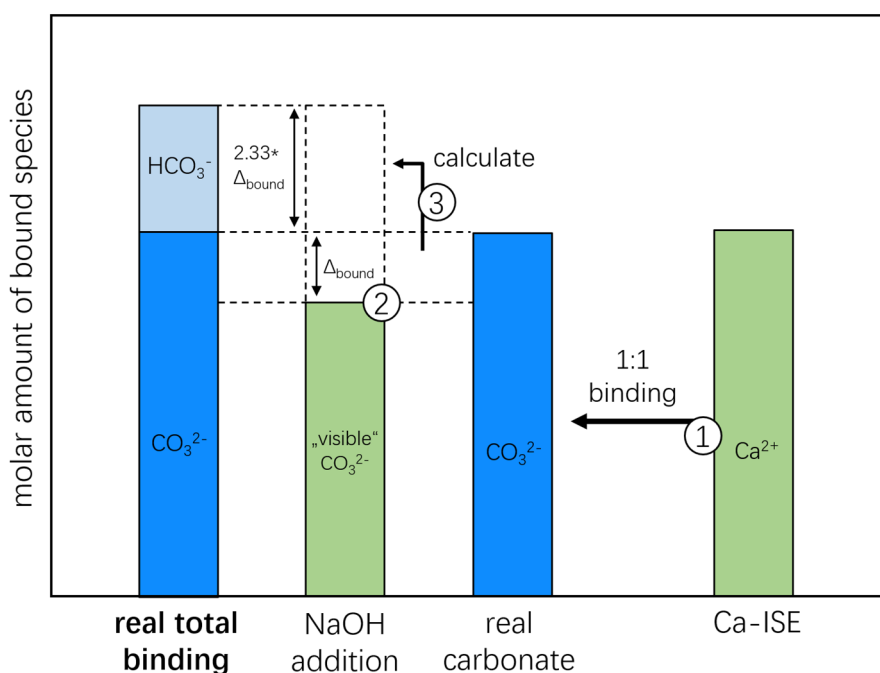
Figure S3.3 Strategy to determine bicarbonate binding. Molar amounts of bound species are shown and whether they can be determined directly from experimental measurements (green) or accessed from calculations (blue). In titration experiments, the amount of bound calcium can be determined directly from the measured calcium potentials from the Ca-ISE. Assuming a 1:1 binding ratio of CO_3^{2-} and Ca^{2+} (refer following text for justification of this assumption), the amount of bound CO_3^{2-} can be calculated from the amount of bound Ca^{2+} (1). Upon binding of CO_3^{2-}, the carbonate is removed from the buffer equilibrium ($HCO_3^- \rightleftharpoons H^+ + CO_3^{2-}$), resulting in the release of H^+ that are compensated by automatic addition of NaOH. Therefore, from the amount of added NaOH in the titration, the removal of CO_3^{2-} from the equilibrium can be quantified. As described in the results section 3.4.1 (see Figure 3.1c), there is a significant difference (Δ_{bound}) between this calculated value and the binding determined from calcium binding (2). The explanation for this difference is simultaneous binding of HCO_3^-, causing a reduced H^+ release if CO_3^{2-} is removed from the equilibrium upon binding to calcium. Quantitative evaluation shows that 2.33 mol HCO_3^- have to be bound to make 1 mol CO_3^{2-} "invisible" to the pH electrode. Using this value, the real binding speciation can be calculated (3).

Determination of bound carbonate via bound Ca^{2+}

Due to the difference in activity coefficients of HCO$_3^-$ and CO$_3^{2-}$ involved in the calculations, it has to be worked with actual concentrations, i.e., the solutions cannot be treated as ideal solutions. The free calcium concentration is accessible from the Ca-ISE, if the calibration is performed in ionic strength adjusted solutions.[120] The starting ionic strength of the regular experiments with 10 mM carbonate buffer at pH 9.8 was calculated using the Davies equation. The determined ionic strength of the solution is 14.5 mM, with the value only changing little during the first few hours of the experiments.

The ionic strength adjusted calibration of the Ca-ISE was carried out by dosing 20 mM CaCl$_2$ solution with 0.01 mL/min into 20 mL of 14.5 mM NaCl solution (see section 3.3.2). This way, the ion activity coefficient for Ca^{2+} ions was experimentally determined as $y(\text{Ca}^{2+}) = 0.63$ in the first 2 hours of each experiment, which is in good agreement with values determined in similar conditions.[24, 120] The free calcium concentration can then be calculated from the ion activities measured by the Ca-ISE according to:

$$c_{\text{free}}(\text{Ca}^{2+}) = \frac{a_{\text{free}}(\text{Ca}^{2+})c^0}{y(\text{Ca}^{2+})} \tag{S3.1}$$

According to earlier experiments,[19] a 1:1 binding ratio of calcium and carbonate in the prenucleation regime was determined for additive-free systems within experimental accuracy, while no bicarbonate association was detected. This can be explained by the 2 orders of magnitude smaller binding constant of Ca-HCO$_3^+$ (20 M^{-1}) compared to Ca-CO$_3^0$ (1700 M^{-1}).[34] The calcium-bicarbonate association only becomes relevant at pH values below pH 9.0 due to the low amount of carbonate present in the buffer equilibrium in this pH range. Our experiments are performed at pH 9.8 and using the ion association constants, a value 4.1% ± 4.4% of bicarbonate binding to calcium can be calculated, which is within the experimental accuracy of a 1:1 binding ratio determined via NaOH addition in earlier experiments[19] (see Figure 3.1e and f, reference experiments). Therefore, in our experiments, assuming a 1:1 binding ratio of calcium and carbonate in the prenucleation regime for additive-free systems is justified. The amount of bound carbonate according to the Ca-ISE can simply be calculated according to

$$n_{\text{bound,ISE}}(\text{CO}_3^{2-}) = n_{\text{bound}}(\text{Ca}^{2+}) = n_{\text{total}}(\text{Ca}^{2+}) - n_{\text{free}}(\text{Ca}^{2+}) \tag{S3.2}$$

with $n_{\text{total}}(\text{Ca}^{2+})$ being accessible via the known values of calcium concentration and addition rate and $n_{\text{free}}(\text{Ca}^{2+})$ being accessible from the detected concentrations by the Ca-ISE and the total volume of the solution. Dilution effects of the addition of CaCl$_2$ and NaOH solutions need to be considered for the evaluations.

These calculations are straight forward for additive-free systems, however, in presence of polymer additives, the binding of Ca^{2+} to carboxyl groups needs to be considered, as this will

affect the 1:1 binding assumption. One possibility is the determination and subtraction of the binding isotherm,[121] however due to potential coupled equilibria of free Ca^{2+} ions that are binding to carbonate and polymer at the same time, it is very difficult to isolate the two binding processes. Therefore, only the later stages of the titration experiment are considered, at which the initial (Langmuir) binding of Ca^{2+} to the carboxyl groups is not relevant (Figure S3.4). In addition, only the slope of the titration curve was considered, thereby eliminating the effect from Ca^{2+} binding to carboxyl groups on the total amount of bound Ca^{2+} species.
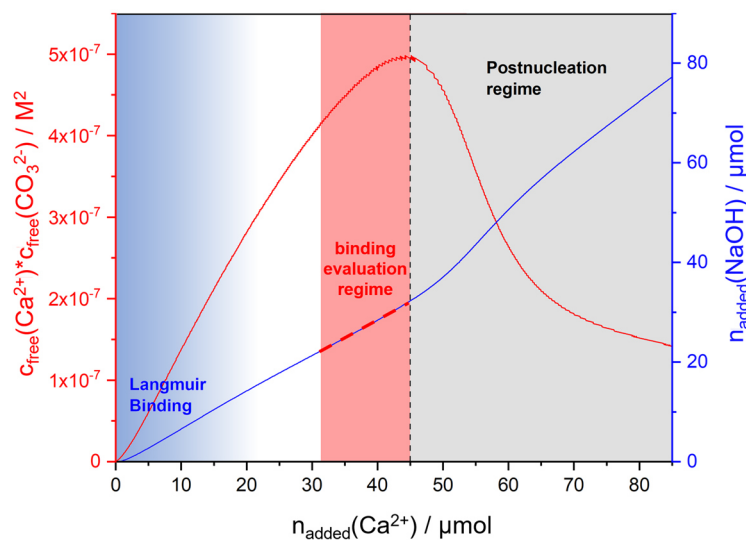
Figure S3.4 Relevant regime in titration experiments to determine bicarbonate binding. In the beginning of the experiments, Ca^{2+} is bound in PNCs as well as to the polymer carboxyl groups. The binding to the polymer groups cannot be unambiguously isolated in the calculations, therefore the beginning of the titration (area highlighted in blue) was not considered for evaluation. In the later stages of the experiment, crystallization takes place (highlighted in gray). Therefore, only the late part of the prenucleation regime (highlighted in red) was considered for binding evaluation. Calculations were performed using the slope of NaOH addition and Ca^{2+} binding, respectively.

Determination of "visible" bound carbonate via NaOH addition

It is possible to determine the amount of bound CO_3^{2-} from the addition of NaOH in pH constant experiments, as the carbonate buffer equilibrium is shifted upon removal of carbonate ions. However, the quantitative evaluation of NaOH data is quite challenging, as already small changes in the environment, e.g., caused by CO_2 in-diffusion into the NaOH solution, can introduce a large error into the measurements. Indeed, while determinations using NaOH addition rates have been performed before,[19] there have also been reports claiming that determinations using amounts of added NaOH are not sufficiently accurate to quantitatively determine binding speciations.[24] In the following, a strategy for quantitative evaluation of experiments involving NaOH addition is presented. The strategy involves evaluation of the NaOH addition from calibration experiments (dosing $CaCl_2$ into water) and polymer-free reference experiments (dosing $CaCl_2$ into carbonate buffer) to extract parameters to correct

experiments performed in presence of polymers. In the first step, the slope of added NaOH in calibration experiments (Figure S3.5a, black curve) was subtracted from the NaOH addition for reference experiments (Figure S3.5a, red curve). This way, the amount of NaOH added to neutralize the added $CaCl_2$ solution is subtracted, leaving only NaOH addition due to changes in carbonate buffer equilibrium.
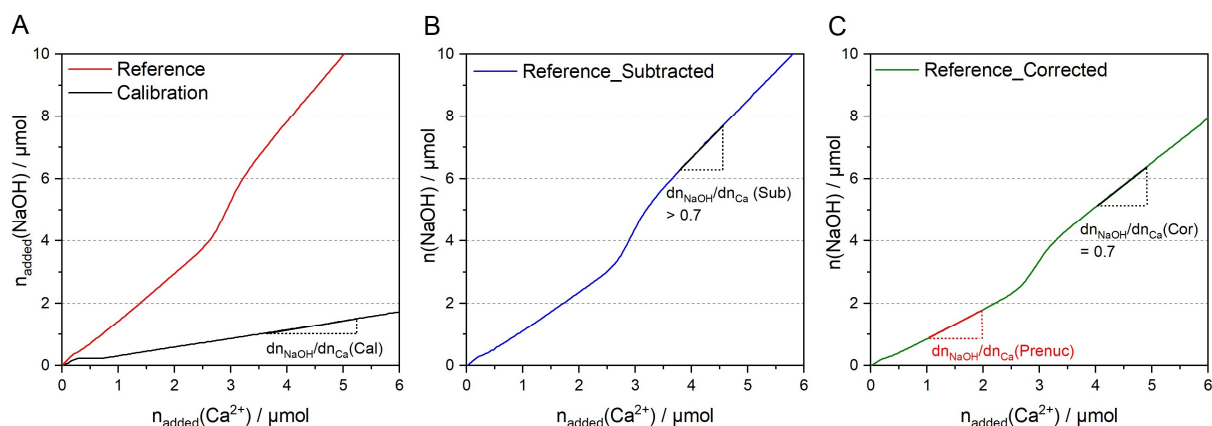

Figure S3.5 Strategy for determinations using NaOH addition. a) From a polymer-free reference experiment (red), the slope of the calcium calibration experiment (black) is subtracted to yield **b)** a corrected reference curve (blue). This curve can be multiplied by a "correction factor" to adjust the postnucleation slope to the theoretical value. **c)** From this corrected curve (green), the prenucleation slope (red slope) can be evaluated to determine prenucleation binding characteristics.

From the resulting data after subtraction (Figure S3.5b), the postnucleation slope (molar amount added NaOH per added molar amount of $CaCl_2$) can be evaluated. In the postnucleation regime for reference experiments, all added calcium is binding to carbonate (particle growth) and 1:1 binding takes place. Therefore, the determined slope can be corrected by multiplying the whole curve with a "correction factor", so the post-nucleation slope equals the theoretical value of 0.7 mol NaOH added per mol bound CO_3^{2-} (see next paragraph for calculation). This "correction factor" is accounting for all effects that lead to a "nonideal" behavior of the NaOH detection in our experiments, for example:

-   neutralization of CO_2 present in the experiment, e.g. due to in-diffusion
-   measurement error in preparation of NaOH solution
-   temperature differences
-   changes in ionic strength

Using this "internal" calibration for calculations involving NaOH addition, we can improve the data quality significantly. From the corrected NaOH additions (Figure S3.5c) we can now determine the slope of added NaOH in the prenucleation regime and calculate the amount of bound CO_3^{2-} that is "visible" to the pH electrode.

For experiments with polymer, due to interactions of the polymer with the formed $CaCO_3$ particles in the postnucleation regime, it is not possible to determine the "internal" correction

factor from the postnucleation slope of the same experiment. Therefore, the slope factor from at least 6 reference experiments was averaged and used for correction of the polymer experiments. All conditions (especially the used NaOH solutions) were kept constant during performance of reference and polymer experiments. As described earlier, only the middle part of the titration curves was used for evaluation (Figure S3.4), and the same part of the curves was used as for the determinations from the Ca-ISE. As result, a slope (added amount of NaOH per added amount of CaCl$_2$) in the prenucleation regime is obtained that can be converted to the amount of (apparently) bound carbonate, as described in the following paragraph.

Determination of amount of bound bicarbonate

As shown in Figure S3.3, for polymer experiments the values of CO$_3^{2-}$ binding determined by the Ca-ISE and determined via the NaOH addition are different. This difference Δ_{bound} can be calculated according to:

$$\Delta_{bound} = n_{bound,ISE}(CO_3^{2-}) - n_{bound,NaOH}(CO_3^{2-}) \qquad (S3.3)$$

The Δ_{bound} can be used to calculate the amount of bicarbonate binding in the system. Therefore, it needs to be determined, how much H$^+$ is released upon shift in equilibrium, if one CO$_3^{2-}$ ion is removed from the buffer equilibrium and how much H$^+$ is consumed, if one HCO$_3^-$ is removed from the equilibrium. The removal of one carbonate ion (in terms of total concentrations) from the buffer equilibrium causes the relative ratio of carbonate and bicarbonate to change, i.e., a perturbation is caused (Figure S3.6a). As the pH is held constant, the equilibrium readjusts so the activity ratio stays constant. Note that the ratio is in terms of activities and can be calculated using the Henderson-Hasselbalch equation (determination of the activity ratio) and the Davies equation (determination of actual activities).

a Carbonate binding

	c / mM	a / mM			c / mM	a / mM			c / mM	a / mM
CO$_3^{2-}$	2.98	1.83	binding	CO$_3^{2-}$	1.98	1.22	readjust	CO$_3^{2-}$	2.68	1.65
HCO$_3^-$	7.02	6.22		HCO$_3^-$	7.02	6.22		HCO$_3^-$	6.32	5.60
	10 total	ratio 3.39			9 total	ratio 5.09			9 total	ratio 3.39

b Bicarbonate binding

	c / mM	a / mM			c / mM	a / mM			c / mM	a / mM
CO$_3^{2-}$	2.98	1.83	binding	CO$_3^{2-}$	2.98	1.83	readjust	CO$_3^{2-}$	2.68	1.65
HCO$_3^-$	7.02	6.22		HCO$_3^-$	6.02	5.33		HCO$_3^-$	6.32	5.60
	10 total	ratio 3.39			9 total	ratio 5.09			9 total	ratio 3.39

Figure S3.6 Changes in carbonate buffer equilibria. a) 1 mM carbonate is removed from a 10 mM carbonate buffer at pH 9.8. The equilibrium readjusts resulting in the release of 0.7 H$^+$. **b)** 1 mM bicarbonate is removed from a 10 mM carbonate buffer at pH 9.8. The equilibrium readjusts resulting in the consumption of 0.3 H$^+$.

It is evident that 0.7 mM bicarbonate transform to 0.7 mM carbonate and 0.7 mM H$^+$, if 1 mM carbonate is removed from the buffer equilibrium (Figure S3.6a). In the same way, it can be calculated that the removal of 1 mM bicarbonate results in the consumption of 0.3 mM H$^+$ (Figure S3.6b).

Therefore, 0.7 mM/0.3 mM = 2.33 times more protons are generated for the binding of one carbonate than are consumed during the binding of one bicarbonate ion. This means that it is necessary to bind 2.33 bicarbonate ions to make the binding of one carbonate ion "invisible" to the pH electrode. From this relation, we can use Δ_{bound} to determine the bicarbonate binding according to

$$n_{bound}(HCO_3^-) = 2.33\Delta_{bound} \tag{S3.4}$$

with $n_{bound}(HCO_3^-)$ describing the bound bicarbonate ions in the system in the prenucleation regime. In this way, the relative amount of bound bicarbonate from the total amount of bound species can be calculated according to

$$n_{bound}(HCO_3^-) = \frac{2.33\Delta_{bound}}{3.33\Delta_{bound} + n_{bound,NaOH}(CO_3^{2-})} \tag{S3.5}$$

As only the slopes of the titration data are evaluated, the quantities stated in eq. (S3.5) are usually per added amount of Ca^{2+}.

3.6.4　Determination of single particle conductivity using C-AFM

Experimental strategy

To measure particle conductivity by C-AFM, the sample (usually stored as dispersion in acetone) was spincoated on a gold coated Si wafer that was then placed on the AFM holder and fixed using Ag conductive paint (Figure S3.7a), as described in experimental section 3.3.5.

In most works, nanoelectrodes are used to determine singly particle conductivity, with the particles being firmly connected to the electrodes.[199-201] In C-AFM however, the particles are not connected to the substrate and several difficulties can arise during conductivity measurement. For example, it was observed that during recording of a "conductivity map" in contact mode, the particles were pushed to the side by the AFM tip instead of being measured. We therefore decided to use non-contact mode (NCM) to look for interesting sample details and perform the conductivity measurements in the "spectroscopy mode", i.e., the tip is moved to the desired spot and then approached to press on the particle, followed by recording a current/voltage (I/V) diagram of this point. Using this strategy, the main difficulty is the apparent blindness during the measurement, as there is a time difference between recoding the NCM AFM image and the measurement of the I/V diagram. It is therefore difficult to know, if a certain sample detail was actually hit by the AFM tip. This is especially challenging as we are interested in recording very small (<100 nm) particles. Combined with the particles lying loose on the wafer, the following problems could occur:

- The tip pushes the particle aside and the substrate is measured instead.
- The stage has a slow drift and until the spectroscopy measurement is started the particle has moved to a different position, causing it to not be measured.
- The particle is measured but sticks to the tip after measurement (tip poisoning), thereby introducing an error in the following measurements.
- The tip is hitting the particle but during the measurement the particle is lost, e.g. electrostatic interactions cause the particle change position or the strong current causes damage or decomposition of the particle.

To solve these issues, we have recorded the Z-height of the tip during the whole spectroscopy measurement. In this way, it can be tracked whether a particle is hit and if the particle undergoes changes during the measurement. In the following, as example is presented to explain this process. First, a NCM image to select an interesting sample detail is recorded (exemplary shown in Figure S3.7b). Then, spectroscopy measurement is performed on points across the image (usually a 20 x 20 grid is selected, Figure S3.7c). On every point, an I/V diagram is recorded while the Z-height of the tip is recorded in parallel. If the measurement was successful, there is no change in Z-height during measurement (Figure S3.7d). However, as already visible in the NCM height image (Figure S3.7b), the structure shown as example is prone to moving. This is also visible during the spectroscopy measurement, as the Z-height decreases around 10 nm

during the measurement of a different point (Figure S3.7e). We would therefore regard the second measurement (Figure S3.7e) as invalid. In addition, as many points on the wafer/substrate are measured, the actual height of the sample detail can be calculated by the Z-height-difference between measurements on the wafer and on the sample detail. Usually we are interested in smaller particles than those shown in Figure S3.7, therefore before and after a measurement on a particle the wafer is measured, allowing us to check for changes of the wafer conductivity to exclude potential tip poisoning.
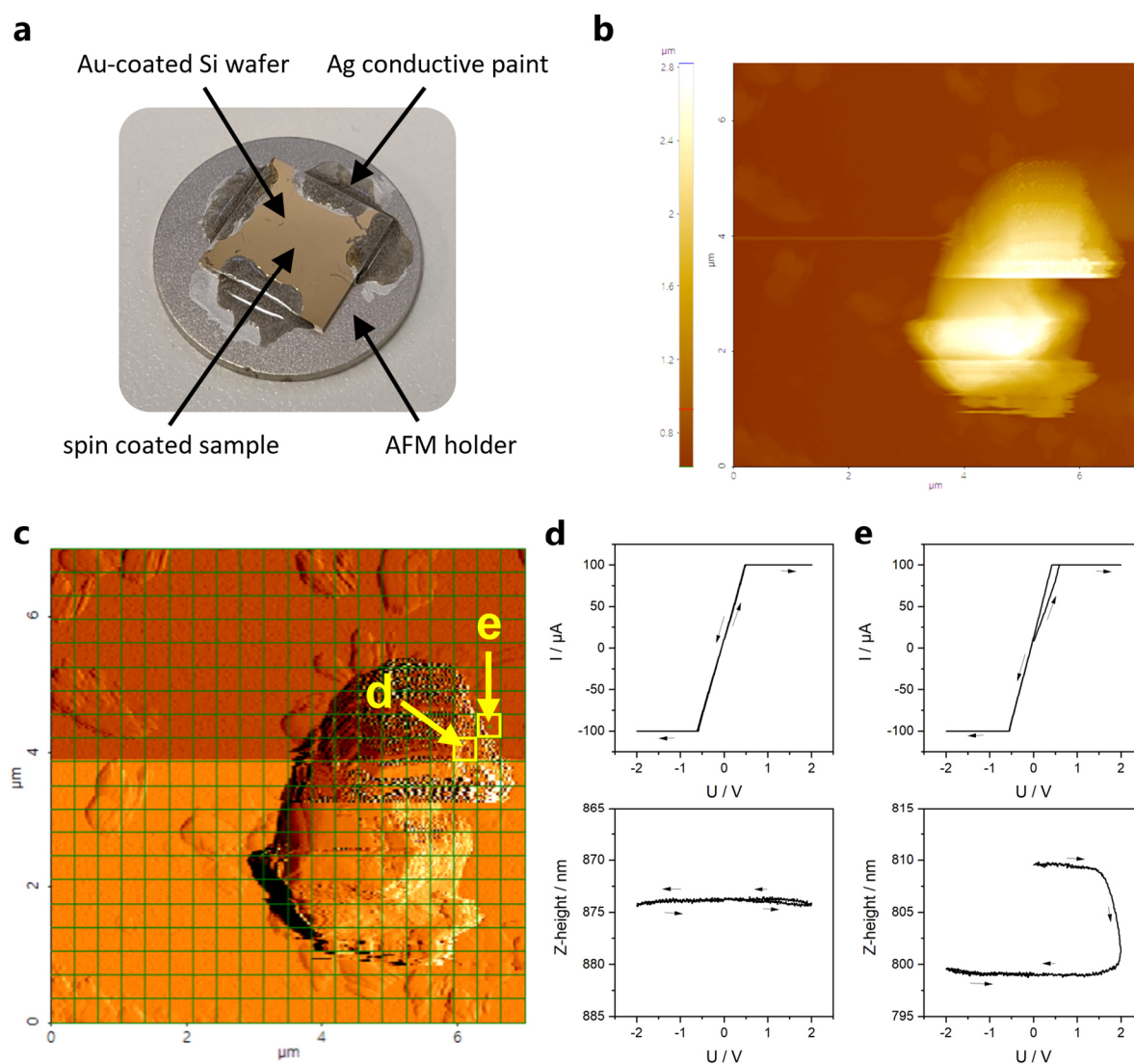
Figure S3.7 Experimental determination of particle conductivity using C-AFM. a) Picture of the prepared sample on the AFM sample holder. **b)** Non-contact mode (NCM) height image of an agglomeration of gold nanoparticles. From the steps in the image it is already evident that the particle moved during recording of the NCM image. **c)** NCM amplitude image with 20 x 20 grid for I/V spectroscopy measurements. Two points are highlighted, whose spectroscopy results are exemplary shown. **d)** Example for a I/V measurement (top) for a conductive particle. The maximum current was limited to ±100 µA. During the whole voltage screening, the Z-height (bottom) did not change, showing that no movement of the particle took place. **e)** I/V (top) and Z-height/V (bottom) diagrams for a point at which particle movement was detected. At the end of the measurement, the Z-height is 10 nm lower than at the beginning.

Evaluation of C-AFM data

In the following, evaluation of the data of C-AFM measurements is demonstrated for a sample of ACC nanoparticles. In the first step, AFM is performed in NCM to select a proper position for the C-AFM measurement, i.e., significant amounts of sample are present in the mapped region. After a detailed NCM map is recorded, the measurement mode is changed to C-AFM spectroscopy mode, and the spots for measuring the I/V diagrams are selected. Usually, a 20 x 20 grid is chosen for analysis (Figure S3.8a) and 3 measurements across the grid are performed. After the data is recorded, the Z-height measured at the beginning and end of each measurement is analyzed, allowing to determine the "baseline" of Z-height of the wafer/substrate. Then, the spots at which a particle was hit, visible by an increase in Z-height, can be identified (Figure S3.8b). The method allows to look at particles, or more precisely: Z-height offsets, down to an order of a few nm. Due to uneven surface of the wafer and the limited resolution of the AFM, the experimental Z-height measurement uncertainty is in the range of 2 nm. Therefore, data points with a Z-height difference of at least 2 nm relative to the wafer are selected for further analysis (Figure S3.8c, marked points) while it is paid attention that the end Z-height is similar to the starting Z-height, i.e., that there was no movement of the particle during the measurement. Usually, the selected data points correspond well to the features visible in the NCM image (Figure S3.8d), however, in some cases, there can be differences due to a small drift in the position of the wafer during the several hours of measurement time (e.g., point 84 in Figure S3.8d: no particle is detected in NCM image, but spectroscopy measurement clearly shows an Z-height offset). In the last step, the I/V diagrams of the selected points are analyzed and the slope close to the origin of the graph (-0.2 V to 0.2 V) is determined. A higher slope of current vs. applied bias corresponds to a higher conductivity (Figure S3.8e). For the final plots, this slope is plotted vs. the Z-height (relative to the level of the wafer) for each data point. In addition, points on the Au-coated substrate can be evaluated as a reference for the maximum detectably conductivity in the experiments.

As references, we performed measurements on conductive (Au) and non-conductive (vaterite) nanoparticles (Figure S3.19), confirming that it is possible to determine conductivity of nanoparticles down to a size of 20 nm by this method. Below 20 nm, the conductivity seems to increase for all samples, probably due to leaking voltage, demonstrating the limits for this method (Figure S3.21c and Figure S3.22a). However, above a Z-height difference of 20 nm, the method can reliably qualitatively determine the conductivity of nanoparticles. Due to the large amounts of data points analyzed in each measurement, the method has great potential to analyze conductivity of nanoparticles with better statistics compared to other available methods.
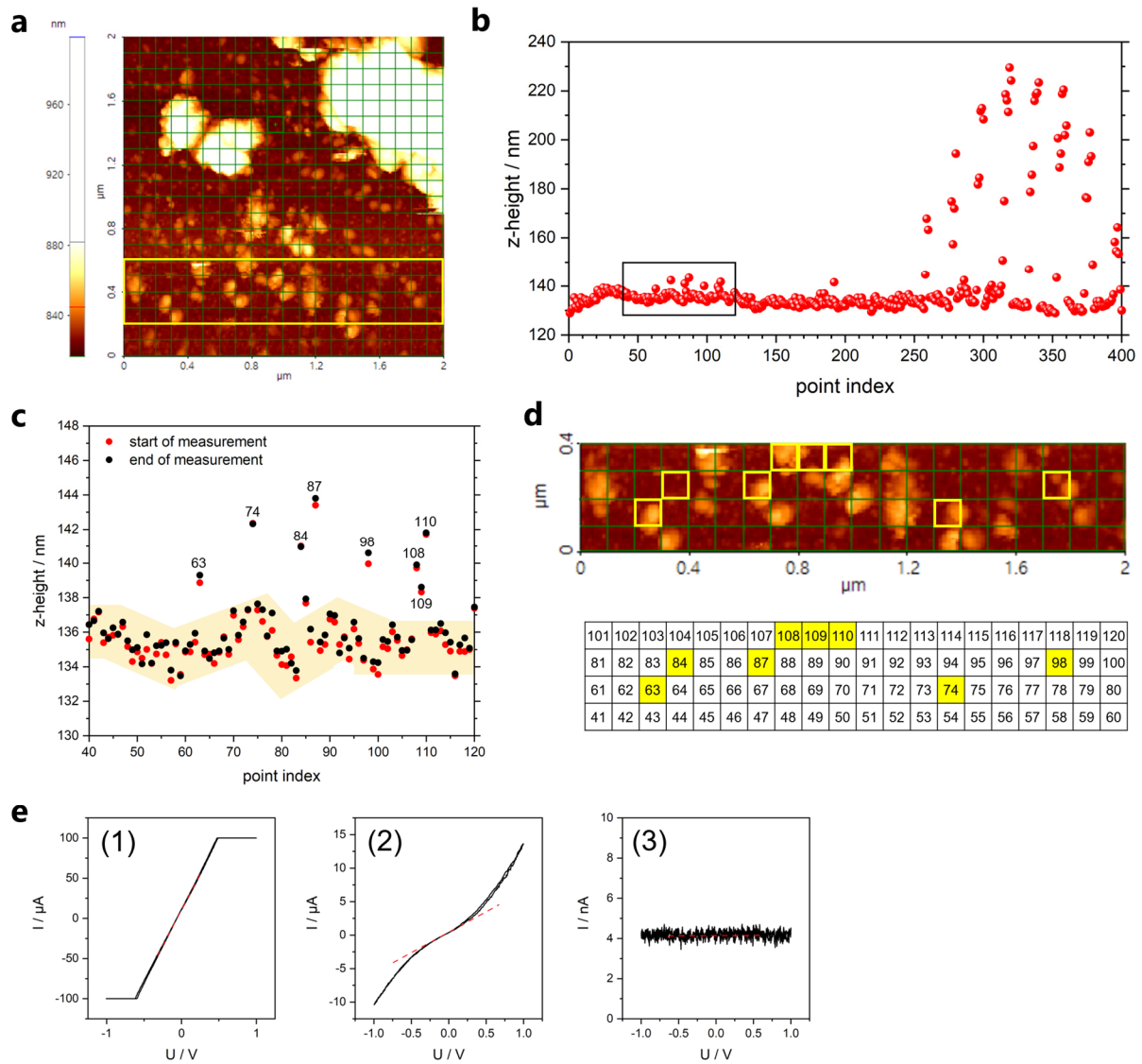
Figure S3.8 Evaluation of C-AFM measurements. a) Non-contact mode (NCM) height map for a spin coated sample of ACC particles. Overlayed on the height map the 20 x 20 grid is shown, indicating the points at which C-AFM spectroscopy measurements were performed. The region highlighted in yellow (point 40 to 120) was used to demonstrate data evaluation. **b)** Starting Z-height of the I/V measurements for each data point. The area highlighted in black corresponds to the area highlighted in (a). The larger particles visible in the top part of the height map in (a) are also visible by the large Z-height starting from data point 250. **c)** Zoom in the region from point 40 to 120. Data points with a difference larger than 2 nm from the measurements on the wafer (yellow area at a Z-height of ~ 136 nm) were used for further analysis, provided the Z-height did not change during measurement. The labeled points were selected for further analysis. **d)** Illustration of the correspondence of selected data points on the grid (bottom, yellow highlighted) to the position on the AFM height image (top, yellow highlighted). Not all particles visible in the NCM image were hit during measurement, e.g. point 81, resulting in less points selected for evaluation as visible in the height map. In addition, not every selected point corresponds to a visible particle in the height image, e.g. point 84, showing that the wafer might have shifted between acquisition of the NCM image and C-AFM spectra. **e)** I/V diagrams for a particle showing (1) good, (2) moderate and (3) no conductivity. The slope of the diagram was used for qualitative comparison of samples.

3.6.5   Supplementary figures
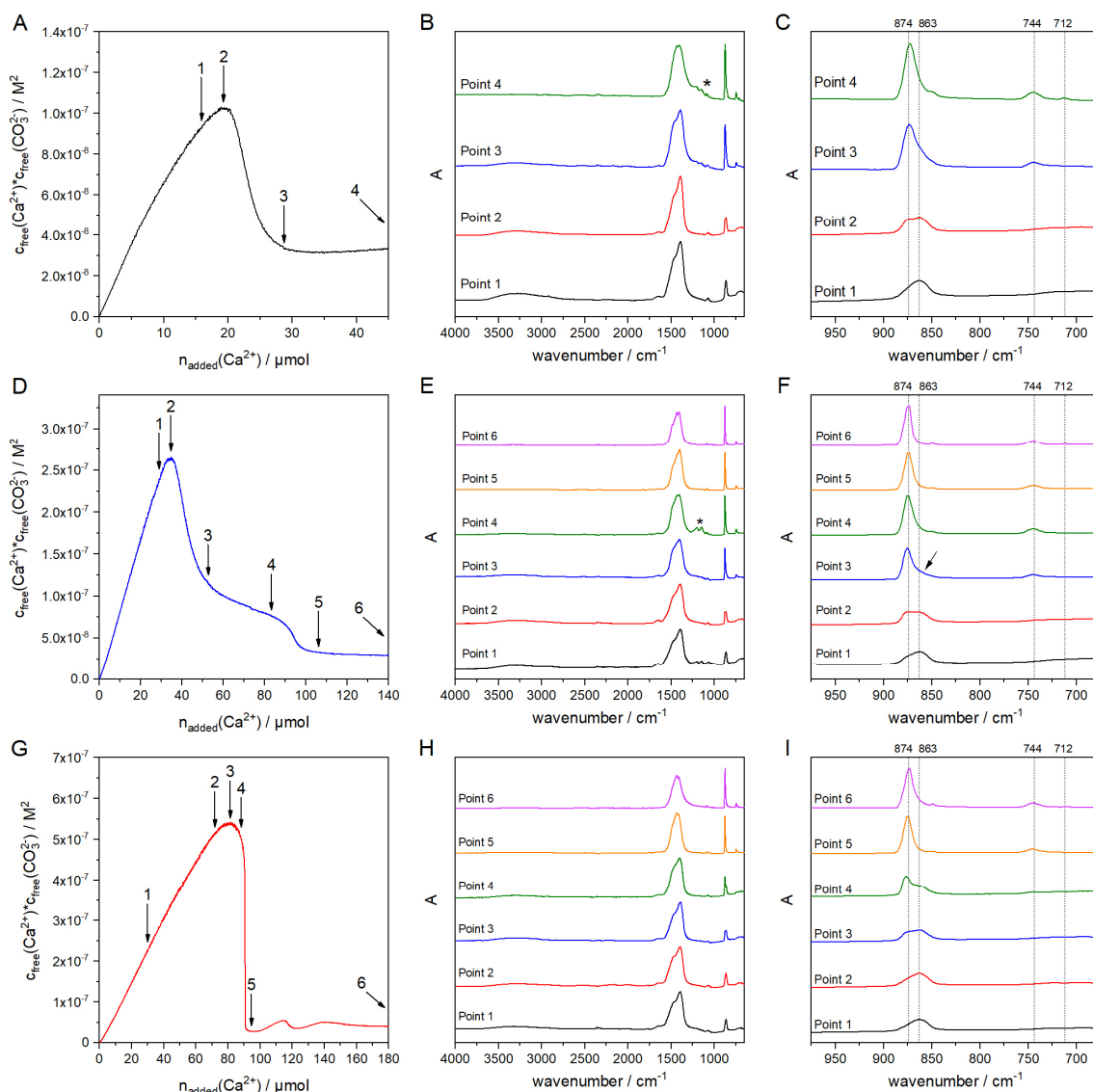
Figure S3.9 Isolation of samples at different stages in the titration. Titration experiments were performed at pH 9.4, using polymer concentrations of 10 mg/L. **a)** Reference titration curve. Arrows indicate points, at which samples were isolated (see experimental section 3.3.3). The last isolation (Ref: point 4; PAsp50/PGlu50: point 6) was performed 16 h after the nucleation point, corresponding to the addition of additional 400 µmol Ca^{2+}. **b)** ATR-FTIR spectra for the isolated samples. The asterisks indicate a small contribution from PTFE that was rubbed off from the PTFE stir bar. **c)** Magnification of the FTIR spectra in the range from 650 to 1000 cm^{-1}. The v_2 carbonate vibration can be used to distinguish crystalline (sharp band at 874 cm^{-1}) from amorphous CaCO$_3$ (broad band at 863 cm^{-1}). The crystalline polymorphs can further be distinguished by the vibrational bands at 712 cm^{-1} (calcite) and 744 cm^{-1} (vaterite).[46] The same analysis was performed for **d-f)** PGlu50 and **g-i)** PAsp50. For all samples, in the prenucleation regime, i.e., prior to the maximum in free ion product, ACC is present that transforms to vaterite upon drop in the free ion product. An interesting feature is the shoulder in the experiments with PGlu50 (point 3 and 4 in d). IR characterization shows a visible shoulder from ACC for this sample (arrow in f), confirming that significant amounts of amorphous mineral are present at this point. This shoulder has disappeared at point 5, in correspondence with a drop in free ion product in the titration (d), therefore, the phase with high solubility in titration experiments can be attributed to a (polymer-stabilized) amorphous phase.
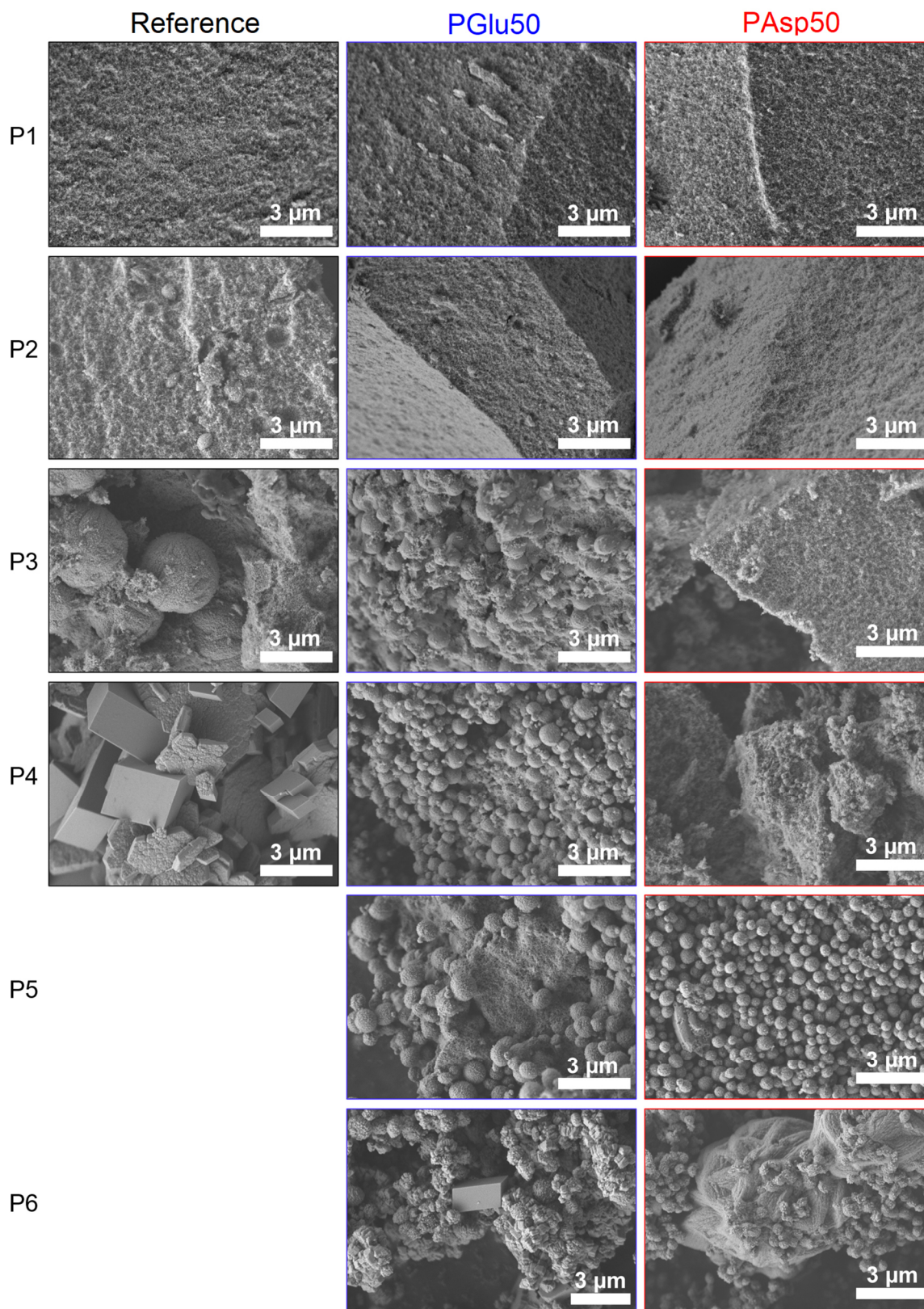
Figure S3.10   SEM investigations of isolated samples from titration experiments. Samples were isolated as shown in Figure S3.9. In the beginning of the titration experiments, ACC nanoparticles are visible that transform to spherical vaterite particles upon crystallization. For the samples isolated 16 h after nucleation, larger crystalline structures are visible, with drastic changes of particle morphology visible in presence of polymers. For PGlu50, small nanoparticles are also visible after nucleation (P3-P5), likely corresponding to the stabilized ACC phase detected by ATR-FTIR (Figure S3.9f, arrow).
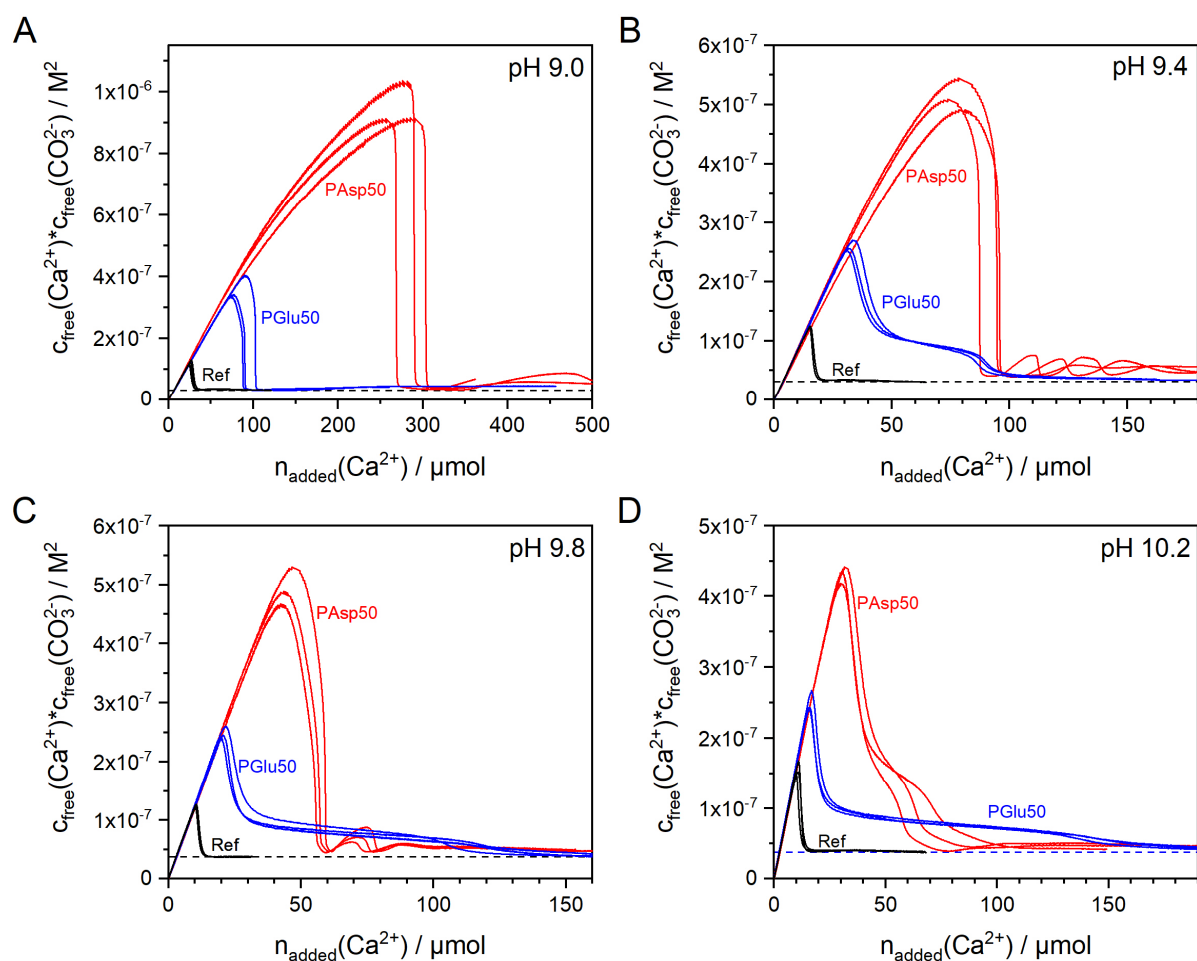
Figure S3.11   Titration experiments performed at different pH values. Experiments were performed by slowly dosing 20 mM $CaCl_2$ into a solution of 10 mM carbonate buffer and 10 mg/L polycarboxylate additive (PAsp50 - red; PGlu50 - blue). In addition, the reference experiment in absence of polymer (black) is shown. The experiments showed a good repeatability across the investigated pH values of **a)** pH 9.0 **b)** pH 9.4 **c)** pH 9.8 and **d)** pH 10.2. The dotted line indicates the solubility product of the ACC phase formed at each pH (pH 9.0/9.4: proto-calcite ACC; pH 9.8/10.2: proto-vaterite ACC).[19] Details for titration experiments are described in section 3.3.2.
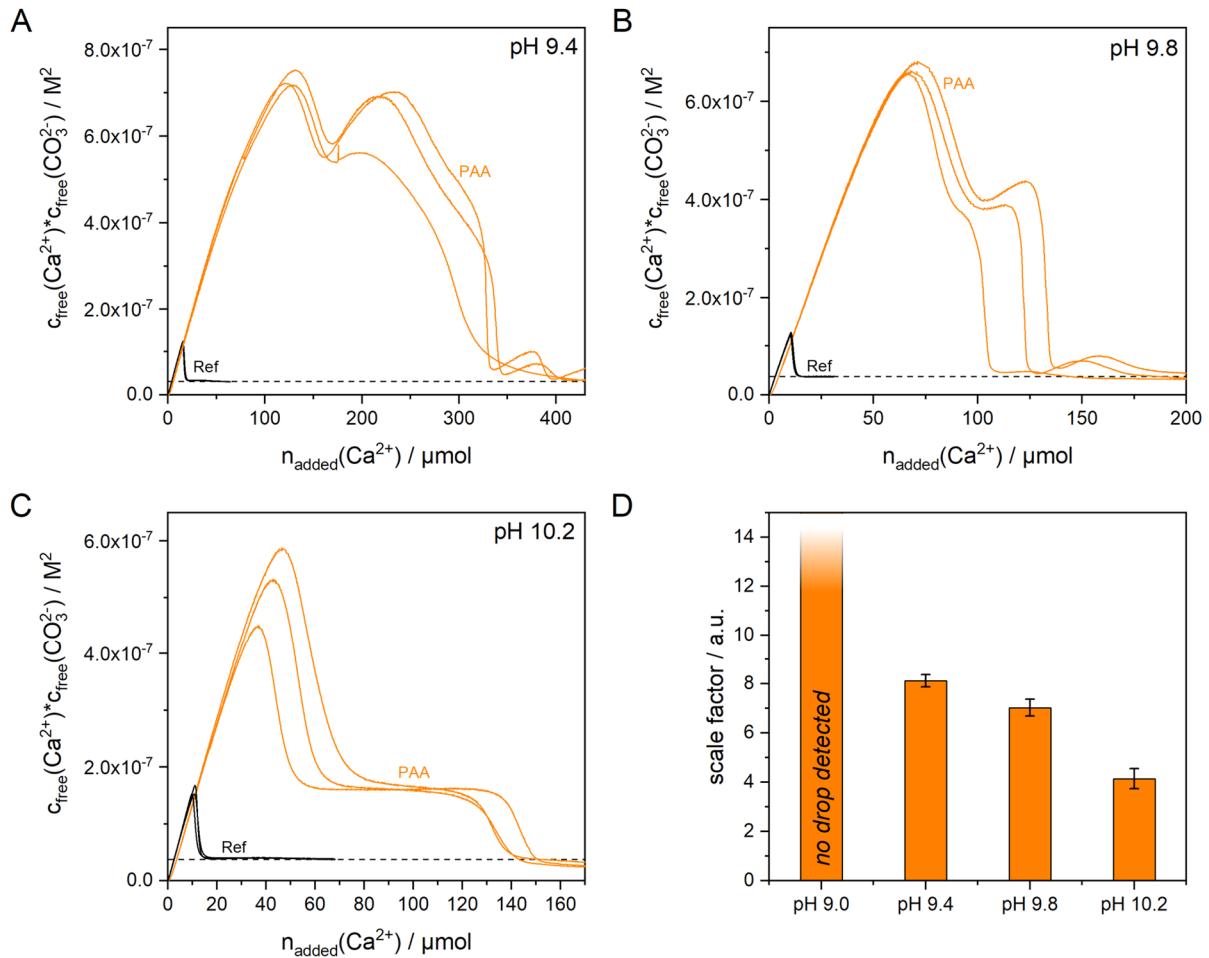
Figure S3.12 **Titration experiments with PAA.** Experiments were performed by slowly dosing 20 mM CaCl$_2$ into a solution of 10 mM carbonate buffer and 10 mg/L poly(acrylic acid) (PAA, orange). The reference experiment in absence of polymer (black) is shown as well. The experiments showed a good repeatability across the investigated pH values of **a)** pH 9.4 **b)** pH 9.8 and **c)** pH 10.2. The dotted line indicates the solubility product of the ACC phase formed at each pH (pH 9.0/9.4: proto-calcite ACC; pH 9.8/10.2: proto-vaterite ACC).[19] The experiments showed the same trends as for PAsp50 and PGlu50 (Figure S3.11), with increasing inhibition at decreasing pH values and the stabilization of a phase with higher solubility at high pH values. **d)** Quantitative evaluation of scale factors shows a stronger inhibition compared to PAsp50/PGlu50 (shown in Figure 3.1a). At pH 9.0, no drop was detected in the titration experiments. Details for titration experiments are described in section 3.3.2.
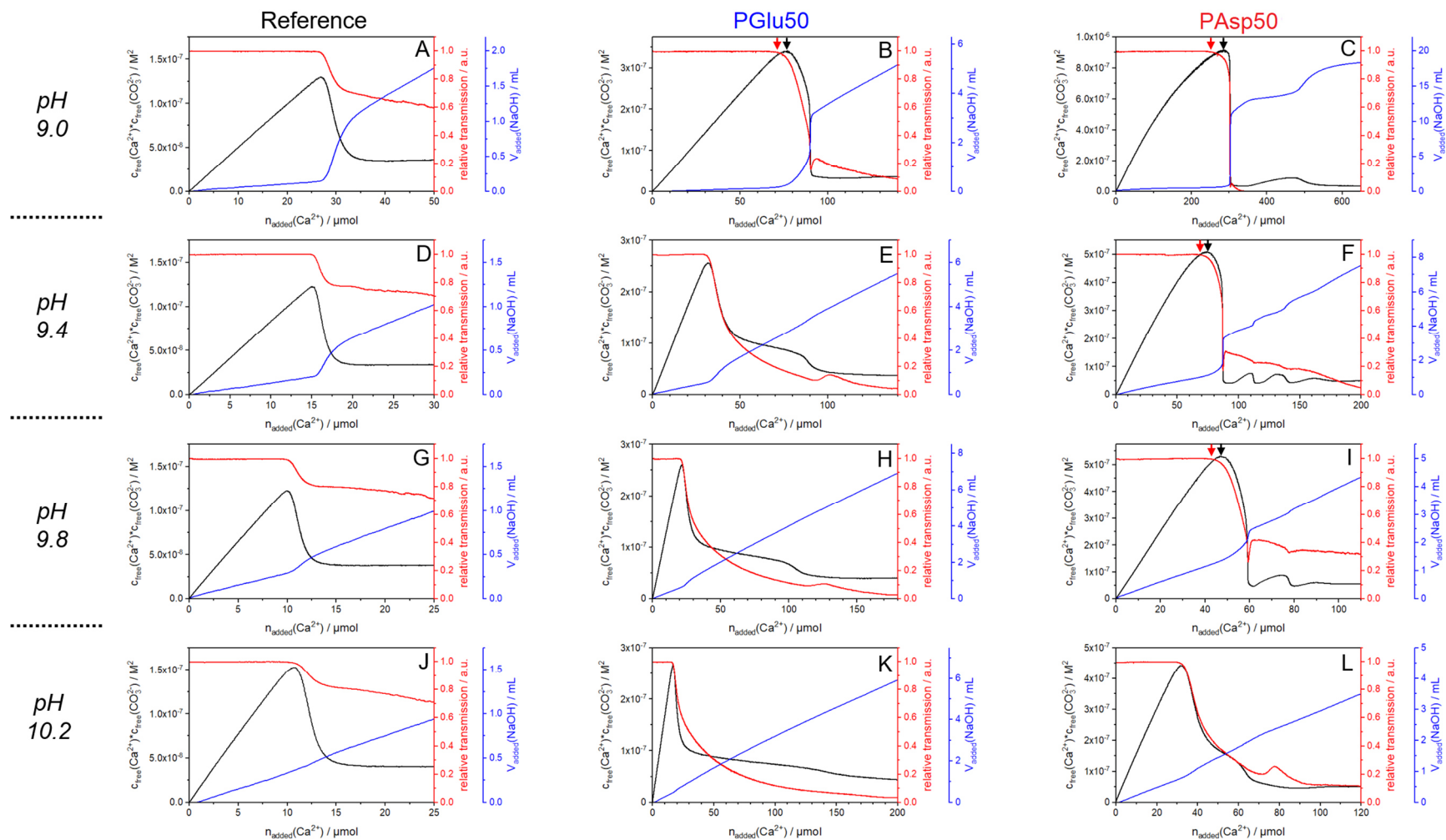
Figure S3.13   Additional data for titration experiments. Titration experiments for the polymer-free reference, PGlu50 and PAsp50 (10 mg/L polymer concentrations) are shown at **a-c)** pH 9.0, **d-f)** pH 9.4, **g-i)** pH 9.8 and **j-l)** pH 10.2. Experiments showed good repeatability (shown in Figure S3.11). In addition to free ion product (black), the development of transmission of the solution detected by the optrode (red) and the amount of added NaOH to keep the pH constant (blue) is shown. For polymer experiments at lower pH values, a difference between drop in transmission (red arrow) and maximum in free ion product (black arrow) is visible, indicating the stabilization of liquid precursor phases by the polymers.[101]
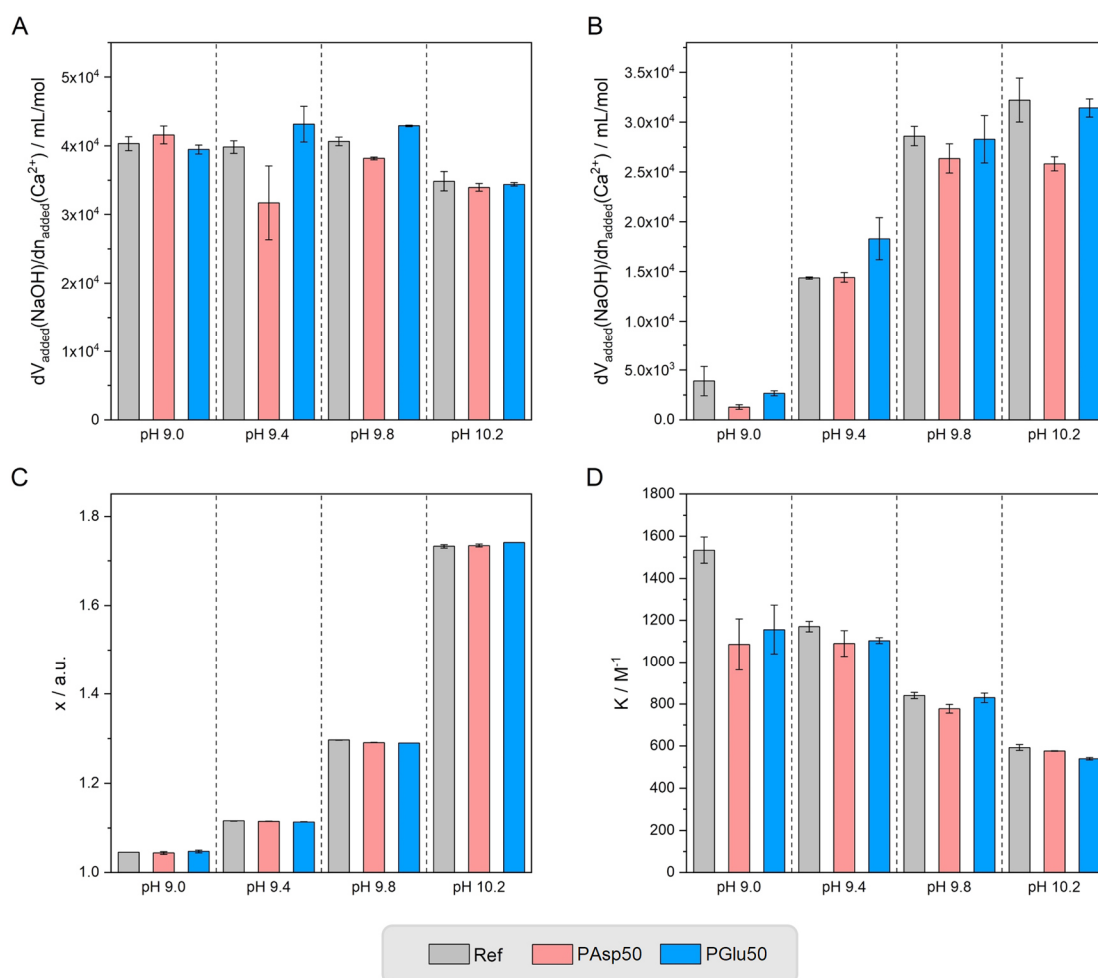
Figure S3.14   Quantitative evaluation of titration experiments. Titration experiments without additive (grey), 10 mg/L PAsp50 (red) and 10 mg/L PGlu50 (blue) were evaluated. Numerous parameters were compared to look for parameters that correspond to the strong polymer- and pH-dependence of nucleation inhibition (Figure 3.1a). **a)** The slope of molar amount of added NaOH per amount of added $CaCl_2$ for the postnucleation regime is shown. For reference experiments, only particle growth is expected at this stage, so similar values are expected across the pH range, i.e., the same amount of carbonate is removed from the buffer equilibrium per amount of Ca^{2+} added. **b)** Slope of molar amount of added NaOH per amount of added $CaCl_2$ for the prenucleation regime. Although evaluations of NaOH addition rates are challenging (see section 3.6.3) and low polymer concentrations of 10 mg/L were used, at three of four pH values (except pH 9.4) a trend in the slopes is visible. Thereby, the reference experiments usually show the highest slope, followed by PGlu50 and then PAsp50, corresponding to the same trend as detected for scale factors (Ref $\rightarrow$ PGlu50 $\rightarrow$ PAsp50). A lower slope of NaOH addition seems to correspond to a higher scale factor, which is especially evident at pH 9.0, at which the PAsp50 shows a high scale factor (Figure 3.1a) and a much lower slope in NaOH addition compared to the reference experiment (Figure 3.1b). The evaluation of microscopic binding parameters for PNC formation (see section 3.3.8) showed that the **c)** x (microscopic number of calcium ions that bind a carbonate ion) as well as **d)** K (microscopic binding equilibrium constant) did not depend on the polymer type or showed no clear effect correlating the binding inhibition. Additional parameters were quantitatively investigated, e.g., slope of free ion product in the prenucleation regime (not shown), but no effect directly corresponded to the trend of nucleation inhibition. Therefore, the NaOH addition in the prenucleation regime was the focus of further studies.
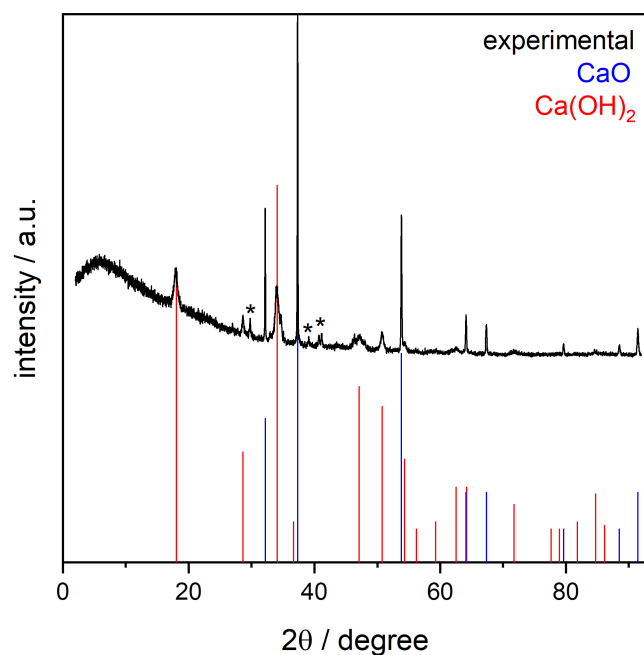
Figure S3.15   Investigation of the sodium content in polymer-stabilized ACC. After TGA analysis (oxidative atmosphere, heating to 1000 °C), the residue was investigated using XRD. No reflexes of sodium oxides were visible, while CaO and $Ca(OH)_2$ were detected as main components.[207-208] According to this data, the presence of sodium salts in the ACC sample, i.e., coprecipitated Na_2CO_3 or $NaHCO_3$, is unlikely. Asterixis correspond to reflexes that could not be assigned.
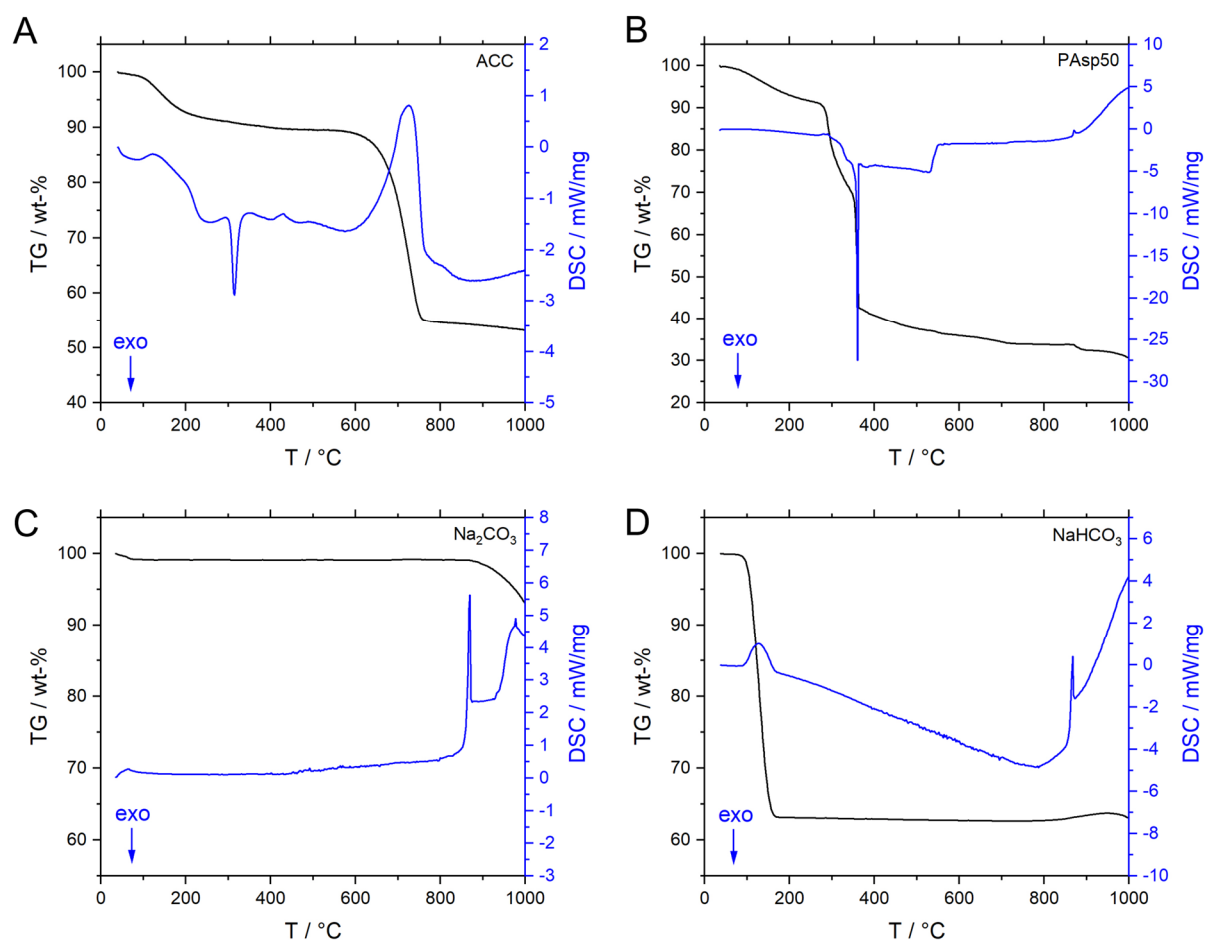
Figure S3.16   TGA and DSC analysis of selected samples. As reference for the polymer-stabilized ACC sample (PAsp50_ACC), pure ACC, pure polymer, and sodium (bi)carbonates were investigated using TGA (black lines) and DSC analysis (blue lines). For measurements, oxidative atmosphere (Ar:O_2 80:20 v/v) was used. **a)** Pure ACC shows initial water loss (<200 °C), followed by exothermic ACC crystallization (~320 °C) and final decarbonization (600-750 °C) to form CaO ($CaCO_3 \rightarrow CaO + CO_2\uparrow$). **b)** Pure PAsp50 shows a similar water loss at the beginning (<200 °C) followed by strong exothermic polymer decomposition (300-360 °C). As the purchased PAsp50 is a (partial) sodium salt, there is still mass from sodium oxide left at the end of the measurements. **c)** Na_2CO_3 shows no weight loss in the initial stages of the experiment. At ~900 °C, the melting point is reached, visible by an endothermic signal in DSC. Finally (>900 °C), decomposition takes place ($Na_2CO_3 \rightarrow Na_2O + CO_2\uparrow$). **d)** $NaHCO_3$ shows an endothermic decomposition at ~180 °C, releasing CO_2 and H_2O (2 $NaHCO_3 \rightarrow Na_2CO_3 + H_2O\uparrow + CO_2\uparrow$).[209] As Na_2CO_3 is formed in this step, the curves then follow the Na_2CO_3 decomposition characteristics (as shown in c).
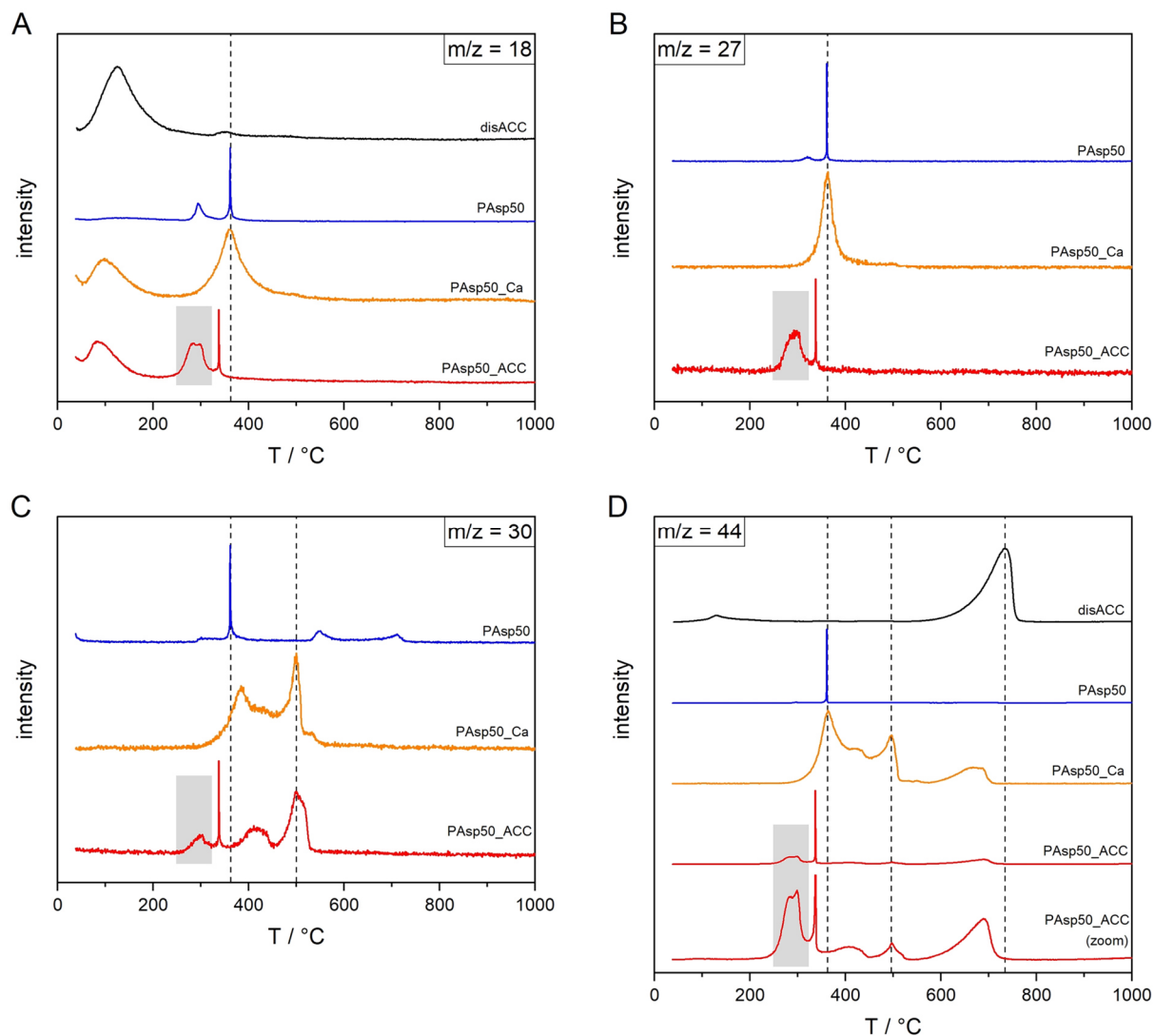
Figure S3.17   TGA-MS analysis of polymer-stabilized ACC and reference samples. The gases released upon decomposition in TGA are analyzed by mass spectrometry. As references for the polymer-stabilized ACC (PAsp50_ACC, red), the TGA-MS data for pure ACC (ACC, black), pure polymer (PAsp50, blue) and polymer calcium salt (PAsp50_Ca, orange) are shown. The PAsp50_Ca sample was synthesized as reference closer resembling the polymer in the mineral phase, i.e., with Ca^{2+} bound to polymer carboxyl groups, as the purchased PAsp50 is a (partial) sodium salt (synthesis of the samples is described in section 3.3.4). The curves for m/z with significant amounts of gases detected are shown. **a)** Results for m/z = 18 (release of H_2O). In addition to the initial release of surface adsorbed and loosely bound water (<200 °C), polymer decomposition (360 °C, dotted line) also results in the release of H_2O. Interestingly, there is a significant broadening for PAsp50_Ca compared to the PAsp50 (sodium salt). The sharp polymer decomposition is also visible in PAsp50_ACC, however, in case of PAsp50_ACC, a significant release of water is detected prior to the polymer decomposition (250-350 °C, highlighted in grey). As water is released during the decomposition of bicarbonate species (see Figure S3.16d), this fits to the presence of bicarbonate in the stabilized ACC. **b)** Results for m/z = 27 (release of HCN or $H_2C=CH$).[210] The released gases are an indication for polymer decomposition, with nitrogen of HCN arising from the polymer backbone (amide bonds). The sharp polymer decomposition (dotted line) is again visible in all samples, however in PAsp50_ACC, there is significant polymer decomposition detected before the sharp peak (250-350 °C, highlighted in grey). The width and temperature range of this decomposition corresponds well to the detected H_2O release (as shown in a). This indicates that the

decomposition of the (polymer-stabilized) bicarbonate species in the ACC structure is triggered by polymer decomposition and/or *vice versa*. **c)** Results for m/z = 30 (release of NO, H_2CO, C_2H_6 or $HC=NH_2$). In this case, a strong difference between PAsp50 and PAsp50_Ca is detected, while in PAsp50_ACC, features from both samples can be recognized (dotted lines). This shows that in the polymer-stabilized ACC sample, aspartic acid segments similar to PAsp50_Ca, i.e., with Ca^{2+} bound to the carboxyl group, and segments similar to PAsp50, i.e., carboxyl groups not bound to Ca^{2+}, are present. In addition, a composition prior to the sharp polymer decomposition is detected (highlighted in grey), confirming the partial destabilization of the polymer by presence of (bi)carbonate species. **d)** Results for m/z = 44 (release of CO_2). At temperatures of 650-750 °C, $CaCO_3$ decomposition takes place ($CaCO_3 \rightarrow CaO + CO_2\uparrow$), as visible for the pure ACC sample. PAsp50 is showing the familiar sharp decomposition peak, while for PAsp50_Ca, several stages of CO_2 release are detected. Especially interesting is the CO_2 release above 600 °C for PAsp50_Ca, showing that decomposition of COO-Ca groups proceeds via the formation of $CaCO_3$ as an intermediate.[198] The slight temperature difference for the $CaCO_3$ decomposition between the samples can be explained by the limited high-temperature accuracy of the TGA device. For PAsp50_ACC, an overlap of all characteristic signals in reference samples can be detected (dotted lines). In addition, a strong CO_2 release is detected prior to polymer decomposition at 250-350 °C (highlighted in grey) that we attribute to the decomposition of bicarbonate species in the ACC. Although the strong release of H_2O and CO_2 in this region fits to the decomposition of bicarbonate species, presence of bicarbonate cannot be unambiguously confirmed from this data. As discussed earlier, a strong interaction of PAsp50 with calcium (and carbonate species) is detected (as visible in b), so the polymer decomposition characteristics could be changed, resulting in the early release of CO_2 and H_2O. Therefore, additional TGA-IR characterization on ^{13}C enriched samples was performed (Figure S3.18).
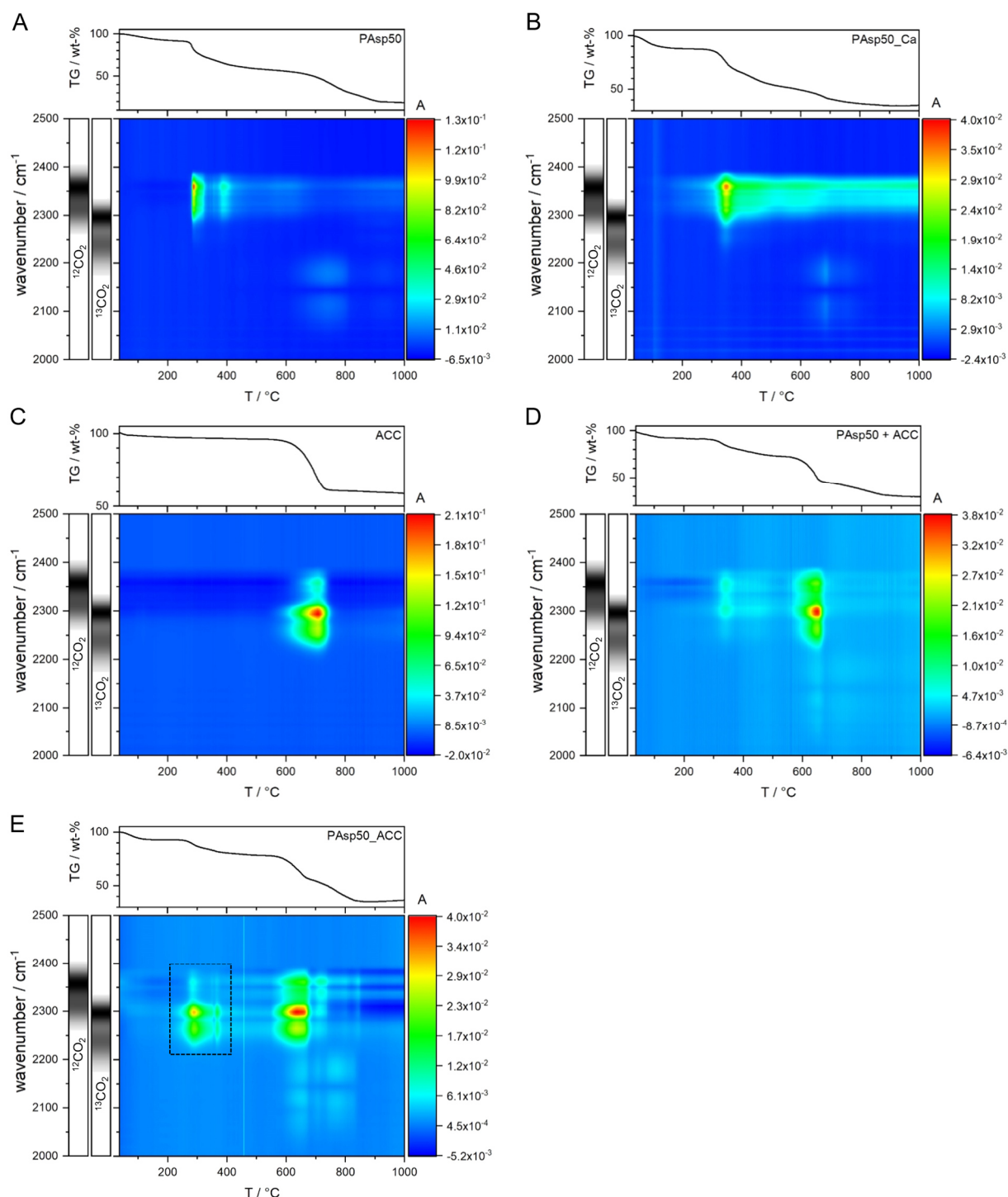
Figure S3.18   TGA-IR analysis of polymer-stabilized ACC and reference samples. In addition to mass spectrometry (Figure S3.17), the released gases were analyzed with FTIR spectroscopy to further investigate the structure of the polymer-stabilized ACC sample. Especially the characteristics of the strong CO_2 release for PAsp50_ACC at around 250-350 °C (Figure S3.17) is of interest, as we propose that this is caused by the bicarbonate species in the sample. Therefore, ^{13}C enriched carbonates (99% ^{13}C) were used in the titration experiments, effectively labelling all mineral carbonate species. Simultaneously, regular PAsp50, i.e., possessing natural abundance of ^{13}C (99% ^{12}C), was used. In this way, the CO_2 species released during sample decomposition can be distinguished by FTIR spectroscopy, allowing us to determine at which temperatures polymer decomposition (release of mainly $^{12}CO_2$, $\nu \sim 2275\text{-}2400 \text{ cm}^{-1}$) and decomposition of mineral carbonate species (release of mainly $^{13}CO_2$,

$\nu \sim 2200\text{-}2325$ cm^{-1}) take place. Herein, the depicted plots show a "top view" on the 3D TGA IR data (3D data of PAsp50_ACC is shown Figure 3.2c) for the relevant range of wavenumbers for CO_2 detection. **a)** Pure PAsp50 polymer shows strong release of $^{12}CO_2$ upon its decomposition at around 300 °C while for **b)** PAsp50_Ca the $^{12}CO_2$ release is broader and also takes place at higher temperatures due to the strong interactions of the polymer with Ca^{2+} and formation of $CaCO_3$ as an intermediate (as described in Figure S3.17d). A small release of $^{13}CO_2$ is detected as well, as there is still 1% ^{13}C (natural abundance) present in the polymer. In addition, release of CO species ($\nu \sim 2000\text{-}2200$ cm^{-1}) is detected above 600 °C, however this shall not further be discussed here. **c)** Pure ^{13}C enriched ACC shows the characteristic $CaCO_3$ decomposition and $^{13}CO_2$ release starting from 600 °C. In this case, a small amount of $^{12}CO_2$ is detected, as the (bi)carbonates used for preparation of the sample are "only" 99% ^{13}C enriched. **d)** A sample was prepared by mixing the previously discussed samples of pure ^{13}C enriched ACC and pure PAsp50 (50:50 w/w), which can be used as a reference of a mineral sample with significant amounts of polymer present in the sample. At 300 °C, only $^{12}CO_2$ is released from the polymer decomposition and starting from 600 °C, both $^{12}CO_2$ and $^{13}CO_2$ are released. Thereby, $^{12}CO_2$ arises from the $CaCO_3$ intermediate formed upon decomposition of the polymer,[198] while $^{13}CO_2$ is released from the $CaCO_3$ species formed from ACC crystallization. **e)** The polymer-stabilized ACC sample synthesized in titration shows a striking difference compared to the simple mixture of ACC and polymer. This time, starting at 250 °C, the main release is $^{13}CO_2$ (dotted box), showing that indeed the decomposition of mineral, i.e., (bi)carbonate species, is taking place at this temperature. This also excludes other side reactions that might be responsible for the weight loss in this temperature range, such as formation and decomposition of Ca-polymer coacervate type species, Ca-ethanolate species formed during quenching of the sample in ethanol or weight losses due to (calcium)hydroxide coprecipitation and decomposition, as all these compounds do not involve the release of $^{13}CO_2$ upon decomposition.[211] Also, simple (co)precipitation of $NaHCO_3$ can be excluded due to the exothermic decomposition characteristics of this bicarbonate species (see Figure 3.2a, in contrast to the endothermic decomposition of $NaHCO_3$ as shown in Figure S3.16d). In addition, no $NaHCO_3$ was detected in MAS NMR (Figure 3.2d), and no sodium oxides were detected in XRD analysis of the precipitate formed after TGA (Figure S3.15).

The difference of PAsp50_ACC (e) and the simple mixture of ACC and PAsp50 (d) confirms that bicarbonate is incorporated into the ACC in the titration experiments during formation of calcium carbonate, while this process is facilitated by PAsp50. The weight loss from this bicarbonate species is 13.7% (Figure S3.24b), and assuming decomposition of bicarbonate species according to: $2\ HCO_3^-$ (122 u $\leftrightarrow$ 100%) $\rightarrow CO_3^{2-} + H_2O\uparrow + CO_2\uparrow$ (60 u + 18 u$\uparrow$ + 44 u$\uparrow$ $\leftrightarrow$ 49% + 15%$\uparrow$ + 36%$\uparrow$) one can see that twice the amount of bicarbonate is present in the sample compared to the detected weight loss due to release of H_2O and CO_2. According to this calculation, $2 \cdot 13.7\% = 27\%$ bicarbonate is present in the sample. As visible in the TGA-MS data, likely some PAsp50 decomposition is taking place in this temperature range as well (Figure S3.17b), potentially triggering or being triggered by bicarbonate decomposition, so the actual amount of bicarbonate in the sample is (slightly) less than 27%. In any case, the significant amount of bicarbonate detected in PAsp50_ACC roughly fits to the values of bicarbonate binding predicted by titration experiments (Figure 3.1d).
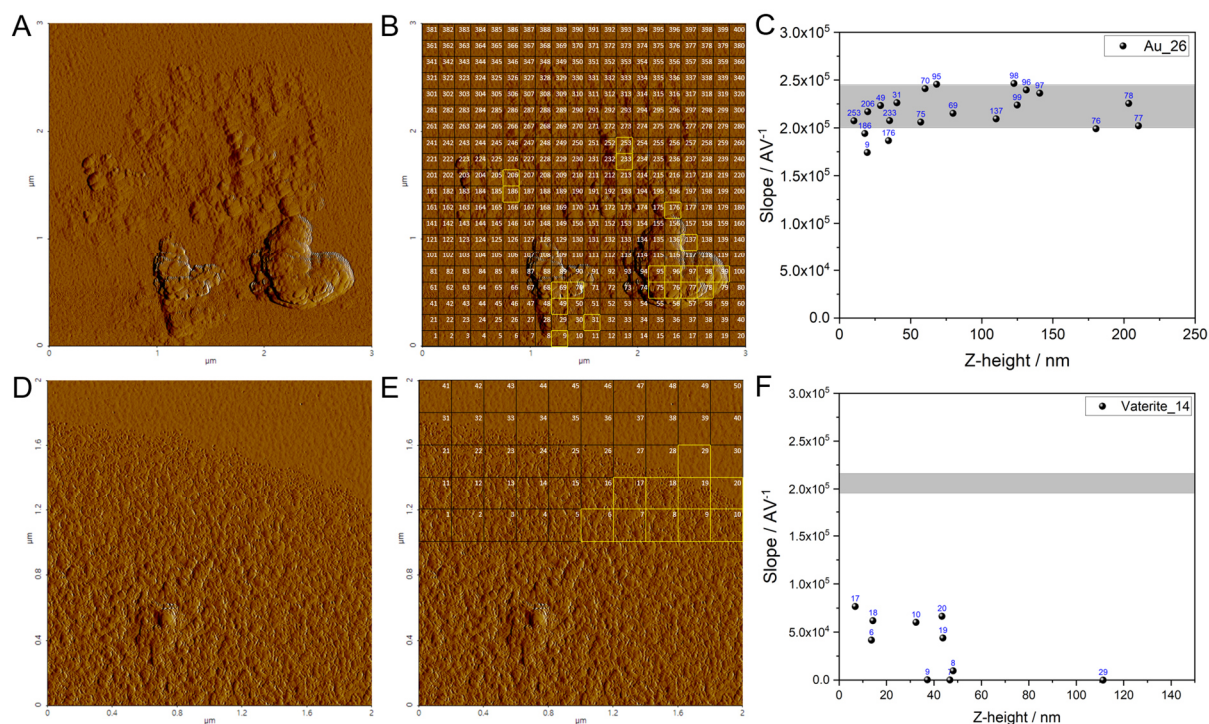
Figure S3.19   C-AFM investigation of reference samples. Determination of particle conductivity was carried out as described in section 3.6.4. For method validation, conductive and non-conductive nanoparticles were investigated (synthesis see section 3.3.6). **a)** Non-contact mode (NCM) amplitude map of a measurement of Au nanoparticles and **b)** amplitude map overlayed with the 20 x 20 grid of points measured in spectroscopy mode. In yellow, the data points considered for evaluation are highlighted. **c)** Plot of measured slope of the I/V diagram for each selected data point in dependence of the starting Z-height of the spectroscopy measurement. The area highlighted in gray corresponds to the average value determined for measurements on the Au substrate (standard deviation of at least 30 evaluated points), indicating the maximum conductivity that can be determined. It is evident that Au particles show good conductivity (similar to the Au substrate) over the whole range of measured Z-heights. **d-f)** Corresponding measurements on vaterite nanoparticles as reference for non-conductive CaCO$_3$ nanoparticles. The results show that the particles possess a lower conductivity compared to the wafer, however still a non-zero slope is detected for particles smaller than 40 nm. This might be due to leakage current across the extremely small Z-heights. Therefore, attention needs to be paid for evaluating particles with Z-height below 40 nm.
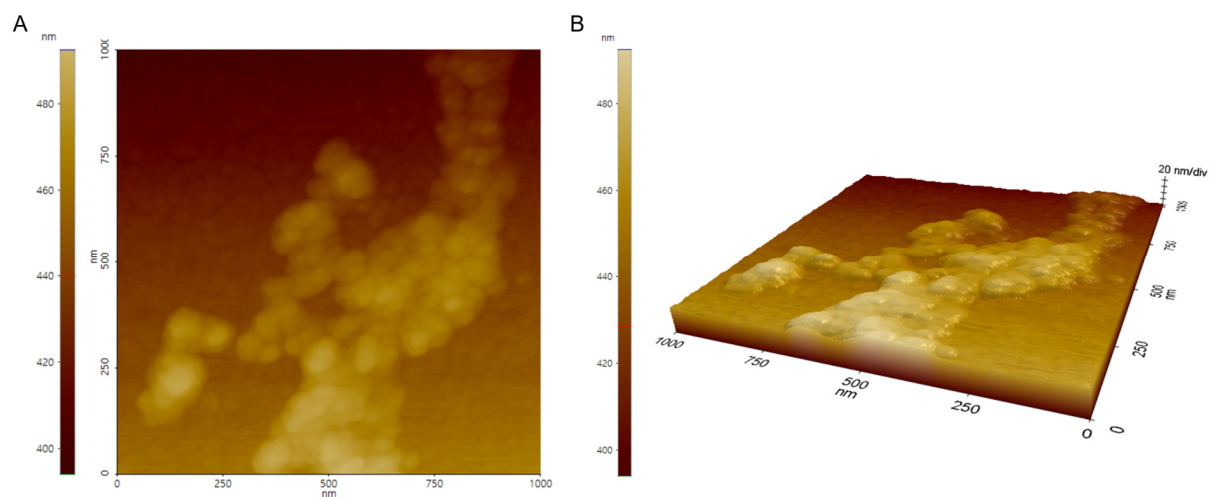
Figure S3.20   AFM height map of polymer-stabilized ACC particles. The image was recorded in non-contact mode (NCM) and shows the same area used for C-AFM investigations (discussed in Figure 3.3a,b and Figure S3.22a-c). **a)** AFM height map, showing individual ACC particles and agglomeration of particles. **b)** 3D visualization of the area, using isotropic axis scaling. Due to the gel-like properties of (polymer-stabilized) ACC, the particles spread on the substrate upon precipitation and drying, resulting in an oblate structure.[154] Therefore, although the individual particles show a size of 20-50 nm in top view (a), they possess a height of significantly less than 20 nm.
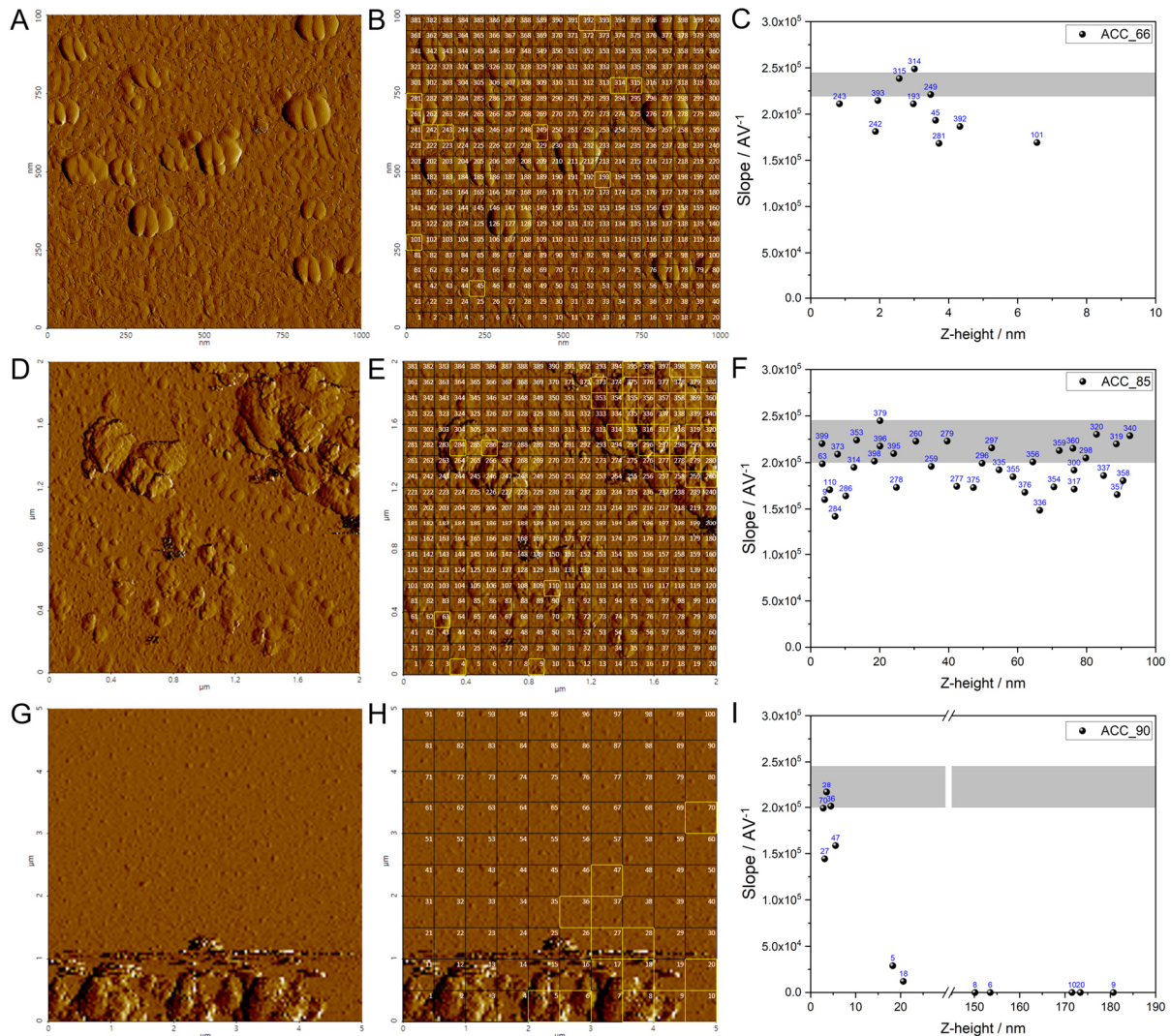
Figure S3.21   C-AFM investigation of polymer-free ACC particles. The conductivity of ACC nanoparticles (prepared according to section 3.3.4) was determined. **a)** NCM amplitude map of a measurement of ACC nanoparticles distributed on the substrate. The particles on the wafer show a diameter of 20-50 nm. **b)** Amplitude map overlayed with the grid of points measured in spectroscopy mode. In yellow, the data points considered for evaluation are highlighted. **c)** Plot of measured slope of the I/V diagram for each selected data point in dependence of the starting Z-height of the spectroscopy measurement. The area highlighted in gray corresponds to the average value determined for measurements on the Au substrate (standard deviation of at least 30 evaluated points), indicating the maximum conductivity that can be determined. Interestingly, although the particles show a diameter of 20-50 nm, the Z-height detected during measurement was less than 5 nm for most measurements, showing that the particles are deformed when precipitated on a wafer due to their gel-like properties, as detected for similarly prepared samples before (see also Figure S3.20).[154] This is also evident by the anisotropic, elongated shape of the particles due to the forces present during spin-coating the particles. In addition, it is possible that the AFM tip is penetrating into the particles when approaching for C-AFM spectroscopy measurements. Due to the high voltage applied (up to 2 V) we cannot exclude leaking voltage at Z-heights below 20 nm, especially considering the results for non-conductive vaterite reference nanoparticles (Figure S3.19f). We therefore decide not to comment on measurements with Z-heights below 20 nm. **d-f)** Corresponding measurements for a different area of the ACC sample, this time showing presence of larger particles. Interestingly, the pure ACC structures show good conductivity across all measured points, similar to the conductive Au reference sample (Figure S3.19c).

g-i) Corresponding measurements for another area on the sample, showing the presence of even lager structures, with Z-heights above 100 nm. This time, the conductivity rapidly decreases for increasing Z-heights, and already at 20 nm, there is no conductivity detected. This is in contrast to the measurements discussed before (in d-f). In fact, for all investigated areas of the sample, one of the two different trends was visible. Either high conductivity up to a Z-height of 100 nm or rapid decrease to 0 within a Z-height of 20 nm. We attribute this to different types of ACC structures present. If only a loose aggregation of nanoparticles is present, there is no conductivity detected, as several nanoparticles are present between the AFM tip and the substrate and conductivity on the surface of the particles is very low, especially if the particles are not in proper contact. That the particles are in loose contact is also visible from the "glitches" in the amplitude map (g), indicating movement of particles during NCM measurement. The other case is the presence of large, continuous ACC structures. These could be either formed by dehydration of a large-scale liquid mineral phase, as detected for polymer-free ACCs before,[154] or by the fusion of liquid-like (viscoelastic) ACC particles.[37] In either case, a continuous ACC structure will have much better contact with the wafer and no grain boundaries across the structure, resulting in better conductivities.
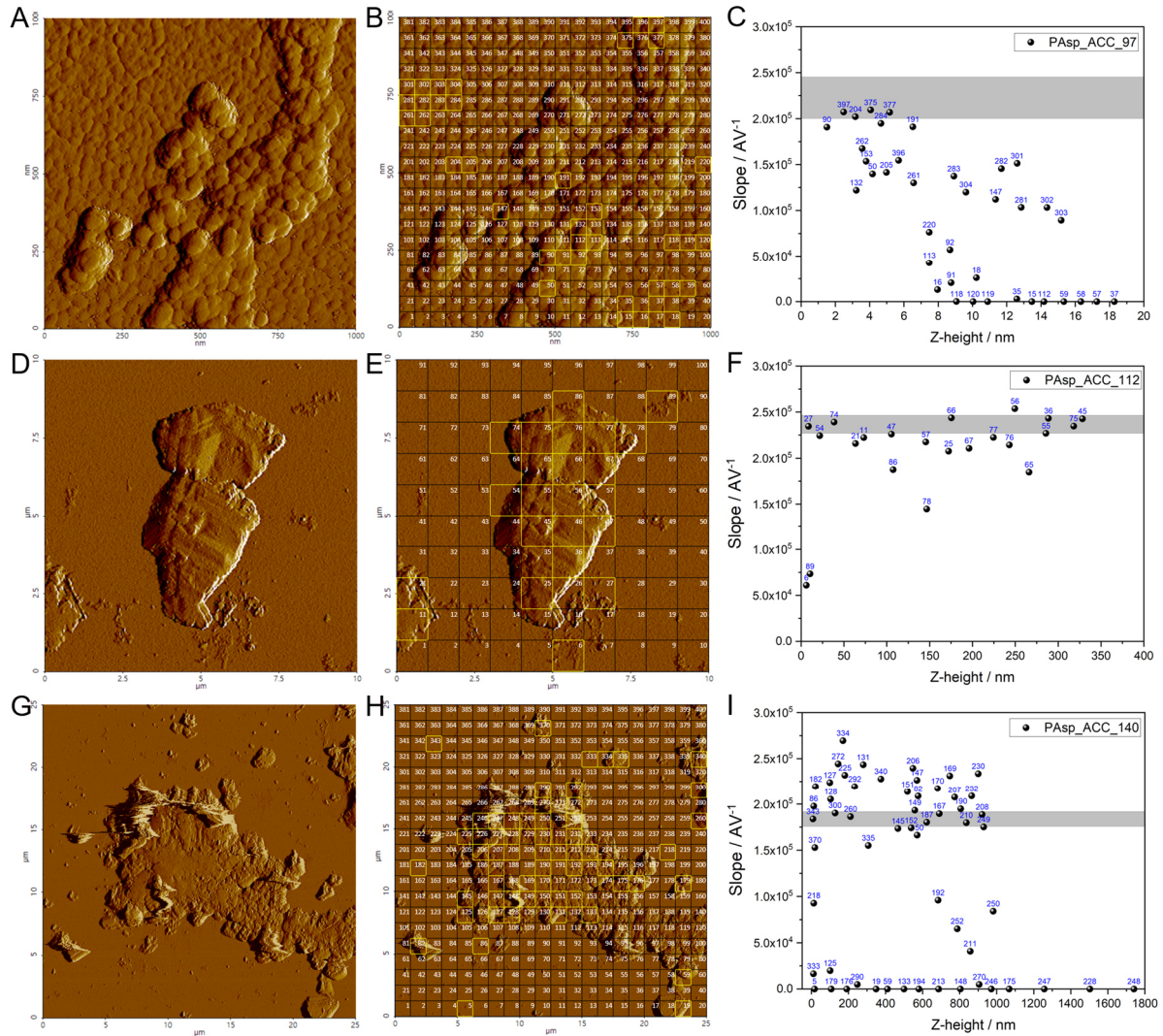
Figure S3.22   C-AFM investigation of polymer-stabilized ACC particles. The conductivity of the PAsp50-stabilized ACC particles (PAsp50_ACC, prepared according to section 3.3.4) was determined. **a)** NCM amplitude map of a measurement of PAsp50_ACC nanoparticles distributed on the wafer. **b)** Amplitude map overlayed with the grid of points measured in spectroscopy mode. In yellow, the data points considered for evaluation are highlighted. **c)** Plot of measured slope of the I/V diagram for each selected data point in dependence of the starting Z-height of the spectroscopy measurement. The area highlighted in gray corresponds to the average value determined for measurements on the Au substrate (standard deviation of at least 30 evaluated points), indicating the maximum conductivity that can be determined. As discussed in Figure S3.21, below 20 nm leakage current likely plays a role, so it cannot be commented on the conductivity of individual PAsp50_ACC nanoparticles. **d-f)** Corresponding measurements for a large ACC structure. These structures are the remaining of the µm size polymer-stabilized liquid precursor droplets that were causing the decrease in transmission in the titration experiments (see Figure S3.13). Surprisingly, these structures survived the quenching procedure. The ACC shows good conductivity for Z-heights over 300 nm. **g-i)** Corresponding measurements for an even larger PAsp50_ACC structures showing good conductivity across a Z-height of almost 1 µm, demonstrating that PAsp50_ACC shows conductivity on a scale well beyond nm range.
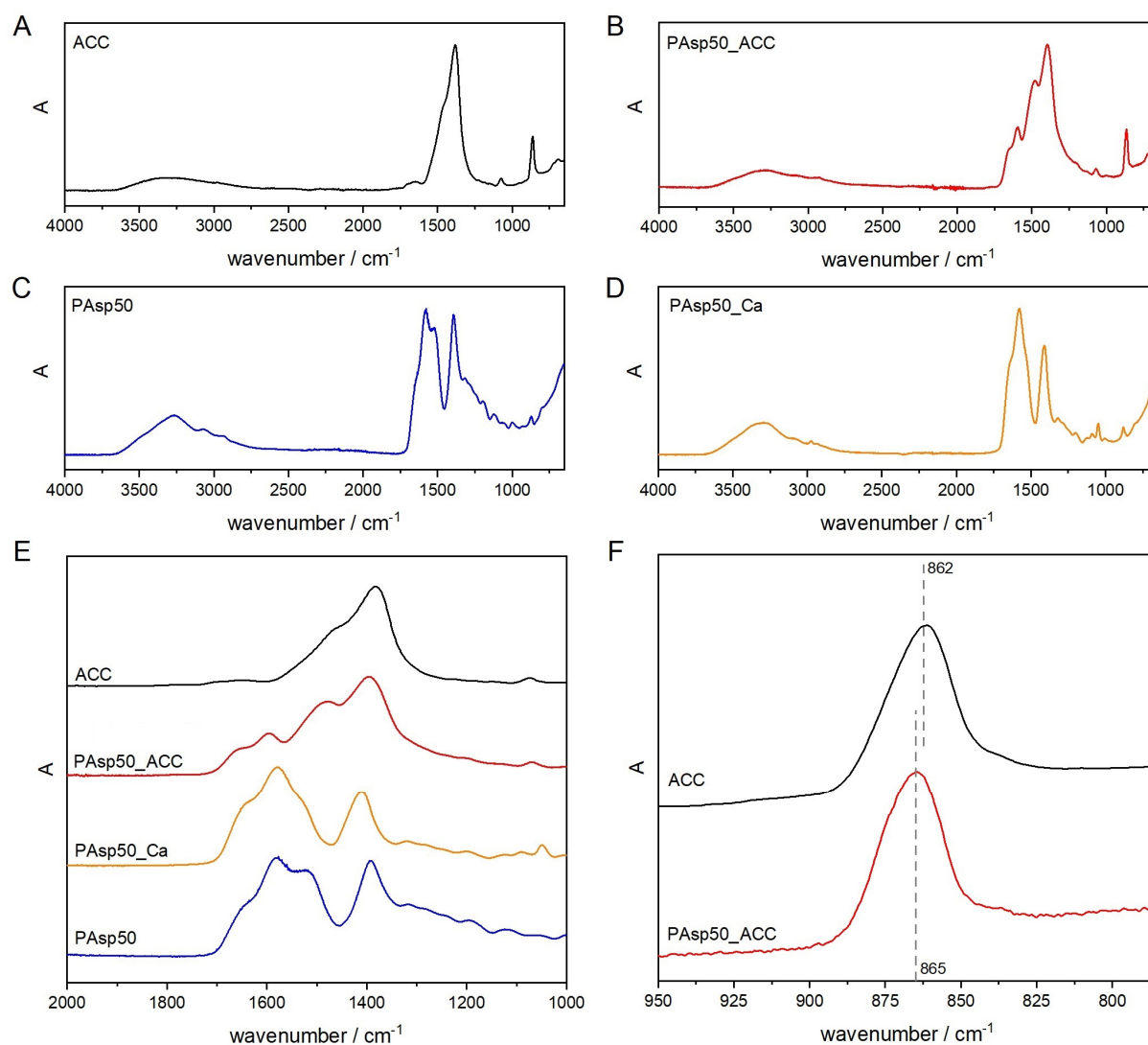
Figure S3.23   ATR-FTIR characterization of polymer and ACC samples. For all samples, the IR spectra of non-^{13}C enriched samples are shown. **a-d)** Individual IR spectra for each sample. **e)** Characteristic vibrations from PAsp50/PAsp50_Ca are visible in the spectra of the polymer-stabilized ACC sample (PAsp50_ACC). **f)** The calcium carbonate samples are amorphous, as visible be the broad vibrational band at around 863 cm^{-1}. The slight difference between the PAsp50_ACC sample (865 cm^{-1}) and the pure ACC samples (862 cm^{-1}) results from different ACC proto-structures.[46] Thereby, the prepared (disordered) ACC shows similar spectrum to proto-calcitic ACC.[212]
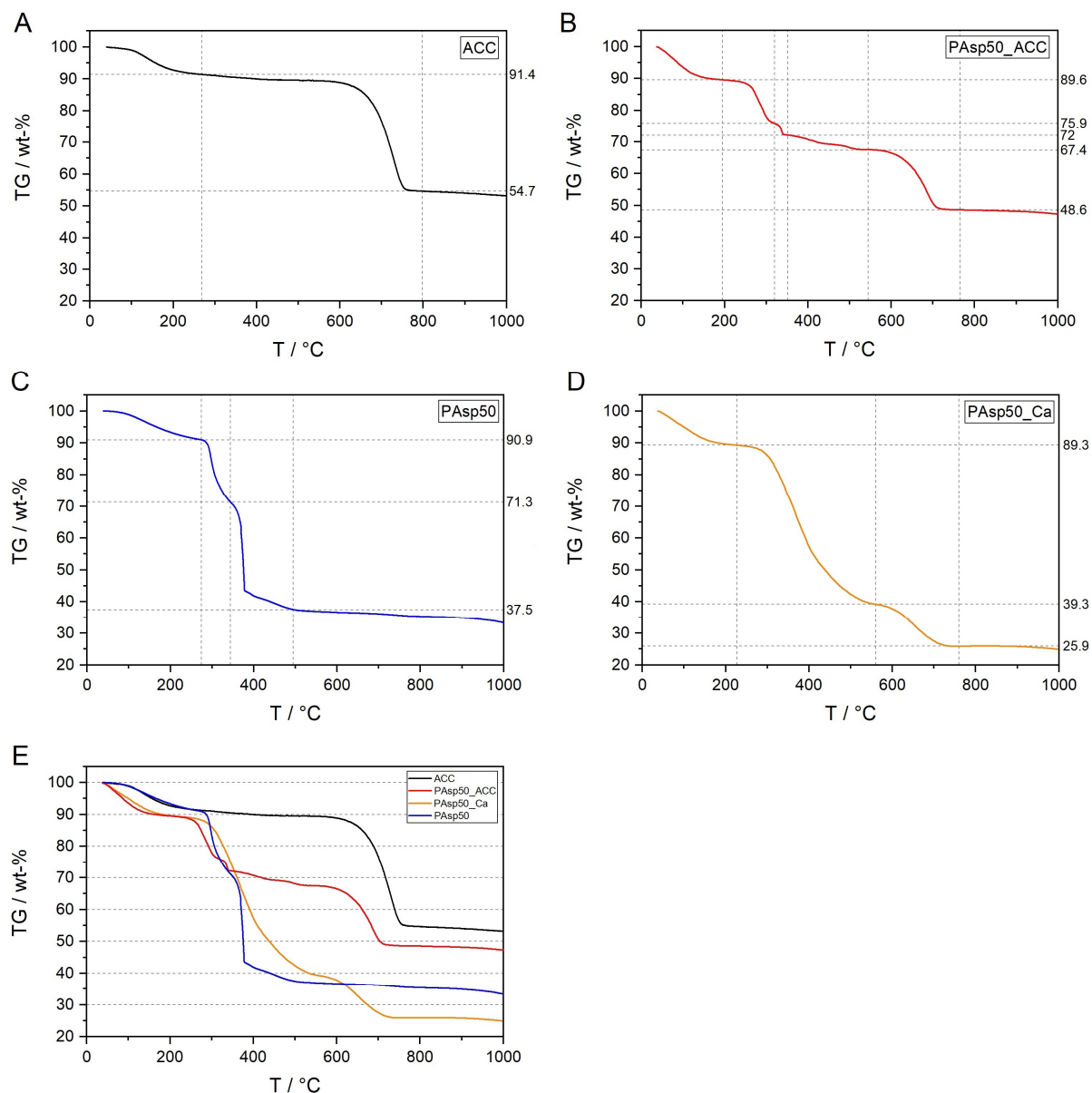
Figure S3.24　TGA characterization of polymer and ACC samples. All measurements were performed in oxidative atmosphere (Ar:O_2 80:20 v/v) and all samples were dried at 40 °C in vacuum prior to measurement to remove surface adsorbed water. **a-d)** Individual TGA thermograms for each sample. No significant differences in the thermograms for natural abundance and ^{13}C enriched samples were detected. **e)** Overlay of all thermograms of samples, showing the high amount of bicarbonate and polymer present in PAsp50_ACC (in comparison to pure ACC), which fits to FTIR analysis (Figure S3.23e).
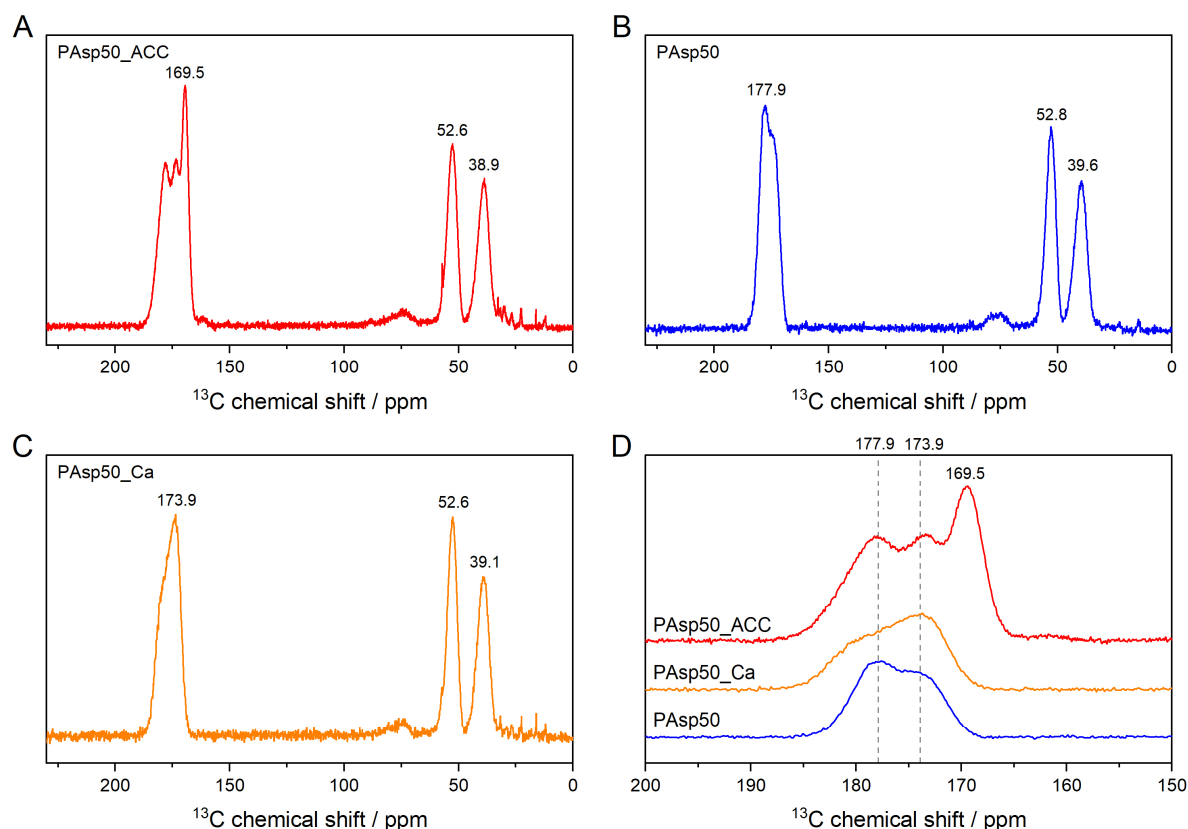
Figure S3.25 **^{1}H-^{13}C CP MAS NMR measurements of polymer and ACC samples.** The spectra for **a)** PAsp50_ACC, **b)** PAsp50 and **c)** PAsp50_Ca are shown. **d)** Overview of the carbonate region of all samples. All spectra were recorded using 10 kHz spinning frequency. The detailed acquisition and processing parameters for ^{1}H-^{13}C CP MAS NMR measurements are described in section 3.3.5. It is evident that several carboxylate species are detected for PAsp50 and PAsp50_Ca samples, indicating the effect of calcium binding on the shielding of the respective carbons. In PAsp50_ACC, several polymer carboxylate species were detected, indicating the presence of carboxylate groups with different chemical environments. The carbonate chemical shift in PAsp50_ACC (169.5 ppm) fits to the reported shift of pvACC,[46] which is expected as sample isolation (see section 3.3.4) was performed at pH 9.8, which was used to synthesize pvACC in earlier studies.[46] Due to the instability and rapid crystallization of (polymer-free) ACC in MAS NMR studies, no spectrum was obtained for pure ACC. No strong bicarbonate peak (161-164 ppm) was detected in PAsp50_ACC.

Chapter 4

Bottling Liquid-like Minerals for Advanced Materials Synthesis

Contents Chapter 4

Record of Contribution

I performed the majority of titration experiments, mineralization experiments, AFM experiments as well as corresponding data analysis and evaluation, figure design and writing of the original manuscript draft. Sina Nolte, Katharina M. Stock and Kristina Kebel performed additional titration and mineralization experiments, including SEM analysis under my supervision and with my instructions. Prof. Dr. Denis Gebauer and I developed the project idea. Prof. Dr. Denis Gebauer supervised the experimental work.

Publication

This chapter was submitted for publication in 2022.

In addition, a patent application was filed by Maxim B. Gindele and Prof. Dr. Denis Gebauer based on the result of this chapter.

4.1   Abstract

Materials synthesis via liquid-like mineral precursors has been studied since their discovery almost 25 years ago, because their properties offer several advantages, e.g., the ability to infiltrate small pores, the production of non-equilibrium crystal morphologies or mimicking textures from biomaterials, resulting in a vast range of possible applications. However, the potential of liquid-like precursors has never been fully tapped, and they received limited attention in the materials chemistry community, largely due to the lack of efficient and scalable synthesis protocols. Herein, we present the "scalable controlled synthesis and utilization of liquid-like precursors for technological applications" (SCULPT) method, allowing isolation of the precursor phase on a gram scale, and we demonstrate its advantage in the synthesis of crystalline calcium carbonate materials and respective applications. The effects of different organic and inorganic additives, such as magnesium ions and concrete superplasticizers, on the stability of the precursor phase and mineralization allow optimizing the process for specific demands. The presented method is easily scalable and therefore allows synthesizing and utilizing the precursor on large scales. Thus, it can be employed for mineral formation during restoration and conservation applications but can also open up pathways toward calcium carbonate-based, CO_2-neutral cements.

4.2   Introduction

In the last decades, the effects of global climate change have become evident, e.g., by an increasing rate of large-scale forest fires and droughts. There is consensus that climate change is mainly caused by anthropogenic emissions of greenhouse gases, while CO_2 is considered to be the main contributor to global warming.[213] In recent years, finding approaches to reduce anthropogenic CO_2 emissions has therefore been a key strategy in fighting climate change.[214] Besides the energy production and transportation sectors, industry is one of the main sources of global CO_2 emissions.[213, 215] Especially the cement manufacturing process has a significant contribution,[216] with some estimates attributing up to 5% of global CO_2 emissions to cement production.[217] Portland cement is one of the main components of concrete, the most widely used material on the planet, and improving cement sustainability is therefore a possible key towards reducing global CO_2 emissions.[218] One strategy is utilizing alternative materials to produce cements, such as calcium carbonate-based cements, especially when combined with carbon capture and storage (CCS) technologies.[219-221] In comparison to other alternatives, calcium carbonate cements can be produced without decarbonization, thereby eliminating the main source of CO_2 during the cement manufacturing process.[222] Common methods for the synthesis of calcium carbonate cements are based on mixing solid amorphous calcium carbonates (ACC) with crystalline ones. Due to the lack of crystallization control during the cementation process, however, the resulting cements are microporous, show poor mechanical

properties[219] and due to the difficulty in stabilizing the amorphous phase, are difficult to synthesize on an industrial scale.[223]

One promising solution to overcome these limitations of carbonate-based cementitious materials is, in our opinion, the polymer-induced liquid-precursor (PILP) process, an alternative crystallization pathway discovered by Laurie Gower in the late 1990s.[27-28] A PILP phase is essentially a polymer-stabilized, highly hydrated amorphous mineral precursor phase that, due to the high water content, possesses a viscoelastic (often also referred to as "liquid-like") consistency. This viscoelastic consistency can be used to "mold" crystal structures via a so-called colloid assembly and transformation (CAT) process.[11, 35, 105] In this process, the liquid-like mineral droplets (colloids) can coalesce, thereby forming non-equilibrium structures, followed by a pseudomorphic amorphous-to-crystalline transformation, yielding crystalline minerals. In addition, the liquid-like properties allow the mineral precursor to infiltrate small cracks and pores, which is useful not only for the synthesis of biomimetic materials,[35, 224] but also for stone restoration and conservation applications, where infiltration and penetration of cracks and pores is favorable.[225] In the following, we will use the term "liquid-like precursor" to describe the highly-hydrated polymer-stabilized viscoelastic amorphous mineral precursor phase.

For essentially any commercially viable and practical application, easy, cheap, and large-scale synthesis of the liquid-like precursor phase is required. Until today, the synthesis is mostly based upon so-called gas diffusion techniques, where CO_2 is released by a carbonate source, commonly ammonium carbonate, followed by diffusion of CO_2 and NH_3 into a solution of calcium ions and small amounts of polycarboxylates, usually poly(aspartic acid) or poly(acrylic acid).[28, 226] After sufficient in-diffusion of CO_2, the mineral precursor precipitates in the form of micron sized droplets, yielding a few mg of product after several hours of reaction time.[108] Another possibility is the slow mixing of dilute solutions containing calcium ions with polycarboxylate and (bi)carbonate. In this case, it will also take several weeks to yield product even on a mg scale.[206] The dilemma of either synthesis strategy is that it is impossible to simply increase the concentrations of the solutions, as this would result in immediate precipitation of crystalline calcium carbonate (if Ca^{2+} and CO_3^{2-} concentrations are too high relative to the polymer concentration)[105] or of Ca-polymer coacervates (if Ca^{2+} and polymer concentrations are too high relative to the carbonate concentration).[168] Even if close attention is paid to avoid the precipitation of Ca-polymer coacervate phases, there is the risk of forming solid and unreactive ACC-polymer composite materials if the concentrations used are too high.[157, 193, 227] These composite materials do not possess liquid-like properties and also do not transform into the crystalline minerals due to their high polymer contents. It is thus evident that the previously used synthesis methods are of highly limited practical use, as only small amounts of minerals can be synthesized. Also, the reaction times for liquid precursor production via available synthesis methods take days (gas diffusion) or weeks (mixing of dilute solutions), rendering the

isolation of the precursor species prior to crystallization challenging. This has further hindered the utilization of liquid-like mineral phases in technological applications.[206, 228] Due to the above-mentioned limitations of the available synthesis methods, the full potential of liquid-like mineral precursors in material synthesis has remained largely untapped in the past 25 years since their discovery.

We present an approach to synthesize liquid-like mineral precursors that uses highly concentrated starting solutions, thereby overcoming the limitations of previously known synthesis methods. We named the process "**s**calable **c**ontrolled synthesis and **u**tilization of **l**iquid-like **p**recursors for **t**echnological applications" (SCULPT). The SCULPT method allows scalable production of liquid-like mineral precursor, e.g. using an automated titration essay,[98] which can then be isolated and used for material synthesis based on the CAT process. In SCULPT, the concentrations of all species in the reaction solution can be precisely controlled by tuning starting concentrations and addition speeds. In this way, precipitation of side products, such as crystalline $CaCO_3$, Ca^{2+}-polymer coacervate or ACC-polymer composite material is prevented, and a concentrated dispersion of the liquid-like mineral precursor is obtained. The product can be isolated by centrifugation and applied to different substrates followed by controlled transformation of the precursor to yield the respective crystalline minerals. Additional additives, such as superplasticizers or metal ions, can be added during the synthesis to further tune the stability and properties of the precursor phase. The method yields several grams of liquid-like mineral precursor within a few hours, with the product then being stable against crystallization for several hours, allowing for the utilization of the unique viscoelastic properties of the precursor for different applications. Not only does this allow, for the first time, isolating the liquid-like precursor phase prior to crystallization, but also working with the precursor phase in application-relevant amounts as well as testing its performance in material synthesis, e.g., in the formation of "molded" crystalline minerals and mineral coatings. Additional advantages of SCULPT are the easy *in situ* investigation and quantification of experimental conditions using potentiometric electrodes, such as pH value and free ion concentrations, and quantifying the effect of additives on the stability of the precursor phase. In our view, SCULPT significantly extends the toolbox of mineral synthesis approaches and will help overcoming practical problems in mineral synthesis, from built heritage conservation to CO_2-fixating cementitious materials.

4.3   Experimental Section

4.3.1   Materials

All solutions were prepared using Millipore water. Solutions of $CaCl_2$ and $MgCl_2$ were prepared by dissolution of $CaCl_2$ dihydrate (Sigma-Aldrich, ACS grade, >99%) and $MgCl_2$ hexahydrate (Sigma-Aldrich, ACS grade, >99%). NaOH solutions were prepared from NaOH stock solution (1.0 M, Carl Roth). Sodium carbonate solution was prepared by dissolution of Na_2CO_3 (Sigma-

Aldrich, ACS grade, 99.95 - 100.05%). Poly(acrylic acid) (PAA) solution was prepared by dissolution of PAA partial sodium salt (Aldrich, M = 5,000 g/mol and M = 100,000 g/mol). Superplasticizers (FLUP® PCE-375 by Backstein; Pantarhit® RC550 and Pantarhit®(FM) by Ha-Be Betonchemie), gypsum (MEYCO moulding gypsum) and calcite crystals (optical calcite, Janine & Marc Köpke GbR) were purchased from commercial suppliers.

4.3.2   Synthesis of mineral precursor

A commercial automated titration setup (Metrohm Titrando) controlled by a computer software (Metrohm tiamo) was used for performance of titration experiments. A titration device (905 Titrando) is controlling four dosing devices (800 Dosino) for the controlled addition of solutions of $CaCl_2$, NaOH, Na_2CO_3 and PAA, respectively. The calcium potential was monitored using a calcium ion selective electrode (Metrohm, No. 6.0508.110) and the pH was measured using a pH electrode (Metrohm, No. 6.0256.100). In addition, the transmission of the solution was measured with an optrode (Metrohm, No. 6.1115.000) using a wavelength of 660 nm. The pH electrode was used as a reference electrode for the calcium electrode. The solution was stirred using an overhead stirrer (Metrohm, No. 2.802.0020). Calibration of the pH electrode was carried out at least twice a week using pH buffers from Mettler Toledo with pH 4.01 (No. 51302069), 7.00 (No. 51302047) and 9.21 (No. 51302070). The calcium ISE was calibrated by dosing 20 mM $CaCl_2$ solution with 0.01 mL/min into 50 mL Millipore water at the same pH value as the experiment.

In the following, the procedure for a standard precursor synthesis experiment is presented. The detailed conditions for all experiments discussed in this work are summarized in Table S4.1. Solutions of Na_2CO_3 (0.75 M), $CaCl_2$/$MgCl_2$ (0.5 M/0.025 M) and PAA (10 g/L) were added with rates of 0.1 mL/min into 50 mL of PAA solution (1 g/L) at pH 10.65. Prior to each experiment, the pH of this PAA starting solution was adjusted to pH 10.65 using 1 M NaOH. The experiments were performed in a sealed beaker under N_2 shower to prevent in-diffusion of CO_2. During the experiment, the pH value was kept constant by automatic addition of 0.5 M NaOH, and the maximum possible stirring speed of the overhead stirrer (without introducing air bubbles) was used. The experiments were carried out for 5.5 h (33 mL of each solution added), before the vessel was full and the product was isolated. After each titration experiment, the beaker and electrodes were washed two times using acetic acid (10%, prepared by dissolution of glacial acetic acid) to remove traces of mineral precipitate from the vessel, electrodes, and dosing tips. Afterwards, the equipment was rinsed several times with Millipore water and dried using dust-free tissue paper.

4.3.3   Isolation of mineral precursor

The mineral precursor was isolated by immediate centrifugation (15 min at 7000 g) after the titration was stopped. After discarding the mother solution, a gel-like, white precipitate was obtained that became a viscous liquid when it was stirred with a spatula. From one titration experiment, 10-15 g of concentrated mineral precursor dispersion were obtained. The product can directly be applied or be treated with an ultrasonic spear (Bandelin Sonopuls UW3100) for 2 min (at 20% power) to further reduce viscosity of the dispersion before application.

4.3.4   Mineralization experiments

To produce mineral layers, 0.3 to 0.5 mL of the precursor dispersion were placed on a calcite single crystal wafer (5x5 mm). The wafers were stored in a closed petri dish to prevent evaporation of the solution. After the desired reaction time (usually 3 h, check Table S4.2 for specific reaction times), the wafers were removed from the chamber, washed with Millipore water (to remove non-fused droplets) and dried on air for 1 d.

To produce mineral coatings on seed crystals, small calcite crystals (roughly 0.1 to 2 mm in size) were added directly to 5 mL of precursor dispersion in the centrifuge tube. The centrifuge tube was closed to prevent the dispersion from drying. After the desired reaction time, the particles were washed with water in an ultrasonic bath, the solution decanted and the crystals isolated by filtration, followed by drying on air for 1 d.

To produce mineral molds, 3-5 mL of the precursor dispersion were added on a regular German 50 ct coin. The coin was placed in a vessel with fitting diameter so that a layer of 0.5 to 1 cm of precursor dispersion was covering the coin. The vessel was covered with parafilm to prevent evaporation and left standing for 24 h. Then, the parafilm was removed and the dispersion slowly dried on air for 3 d. In some cases, the mineral mold separated from the coin in the drying step, while in other cases the mineral was removed from the coin using a spatula.

4.3.5   Material characterization

Attenuated total reflectance Fourier-transform infrared (ATR-FTIR) spectra were recorded using a BRUKER Tensor 27 or Vertex 70v spectrometer. Scanning electron microscopy (SEM) and energy dispersive X-ray spectroscopy (EDX) was performed using a JEOL JSM-6610 SEM, while HR-SEM analysis (Figure S4.6d,e and Figure S4.10) was performed using a JEOL JSM-6700F SEM. Samples were coated with a 5 to 10 nm thick layer of gold (Cressington 108auto) prior to SEM analysis. Light microscopy images were recorded using a Keyence VHX-600 Digital Microscope equipped with a VHZ100UR Zoom Lens. Thermogravimetric analysis (TGA) was performed on a Netzsch STA 409 LUXX in O_2 atmosphere with a heating rate of 5 K/min. Atomic force microscopy was carried out on a Park Systems NX 10 microscope equipped with a PPP-NHCR cantilever in non-contact mode.

4.4 Results and Discussion

4.4.1 SCULPT

SCULPT is based on an automated titration setup to simultaneously mix concentrated solutions of $CaCl_2$, Na_2CO_3, poly(acrylic acid) (PAA) and NaOH (Figure 4.1a) in a specific and controlled manner. The special procedure allows using much higher concentrations than previously, avoiding any side reactions, and was optimized as shown in Figure S4.1. Thereby, all reactants are separated at the beginning of the experiment and are mixed directly in the reaction vessel in appropriate ratios, which prevents the precipitation of side products. In addition, the use of potentiometric electrodes allows the *in situ* detection of parameters such as pH value and calcium activities.
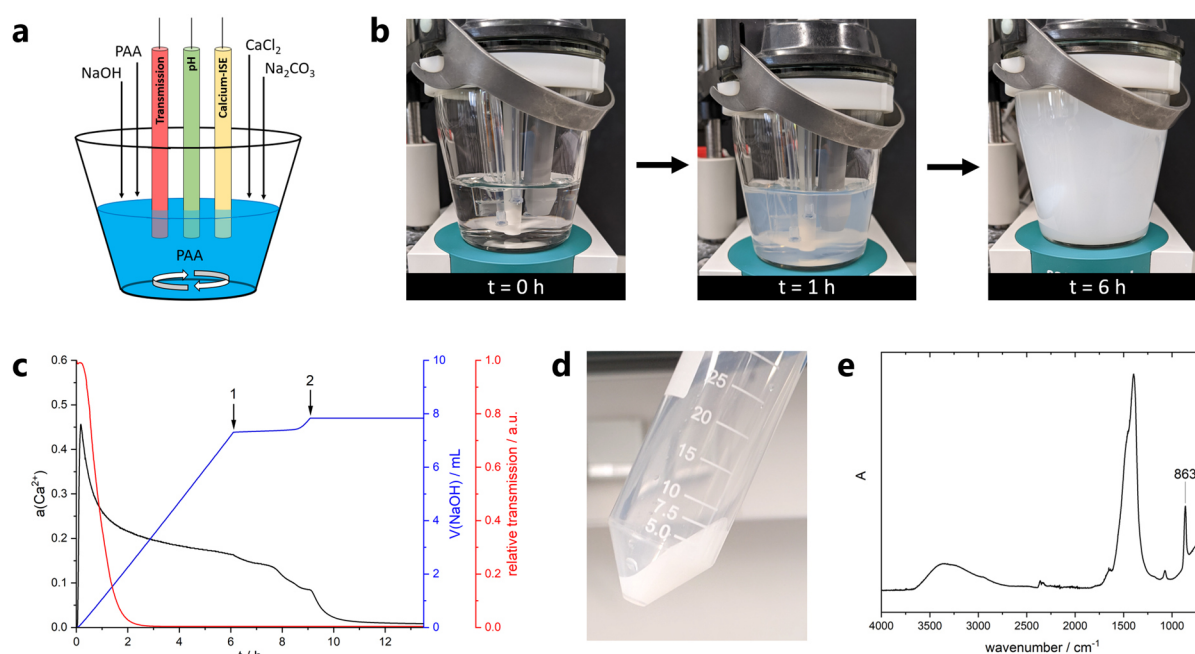
Figure 4.1 Synthesis of liquid-like mineral precursor. a) Scheme of the automated titration setup for SCULPT. Concentrated solutions of $CaCl_2$ (0.5 M), Na_2CO_3 (0.75 M) and PAA (10 g/L) are added at a constant rate (0.1 mL/min) into dilute PAA solution (1 g/L) under vigorous stirring, while the pH is kept constant at pH 10.65 by automatic addition of NaOH (0.5 M). Parameters such as pH, Ca^{2+} activity and transmission of the solution are recorded by potentiometric electrodes. **b)** Visual changes during the addition of the solutions. After 1 h, a visibly turbid dispersion is formed and after 6 h, when the reaction vessel is filled up, the dispersion is highly turbid. **c)** Data recorded by potentiometric electrodes during the addition of the solutions. The transmission of the solution/dispersion (red), Ca^{2+} activity (black) and volume of added NaOH solution so as to maintain a constant pH value (blue) are shown. After 6 h (point 1), the beaker is filled up and the addition of the solutions is stopped. The reaction can be further tracked, and crystallization is evident by a decrease in Ca^{2+} activity and an increase in NaOH addition (point 2). **d)** After the addition is finished (point 1 in c), the product can be isolated by centrifugation, resulting in several grams of a highly viscous dispersion of dense liquid precursor. **e)** ATR-FTIR spectroscopy of the dried product. The broad ν_2 vibration at 863 cm^{-1} confirms the formation of ACC.[78] The detailed conditions for the experiments are listed in Table S4.1.

In this way, properties of the formed mineral phases, such as the solubility product, can be quantified. Furthermore, it is possible to determine the point of crystallization of the precursor phase, allowing to estimate its kinetic stability. The ratios of added Ca^{2+}, CO_3^{2-} and PAA are similar to previous liquid-like precursor syntheses,[28] however, SCULPT allows using up to 3 orders of magnitude higher concentrations. Solutions are added under vigorous stirring at rather slow rates (0.1 mL/min), preventing the formation of concentration gradients. After 6 hours of reaction time the reaction vessel is filled up (Figure 4.1b) and the synthesis is complete. During the addition of the solutions, the calcium ion selective electrode (ISE) allows determining the activity of calcium ions in the solution, which, after phase separation, is governed by the solubility product of the most soluble solid phase present in the system. Indeed, phase separation occurs upon the drop in the calcium activity after reaching a maximum in the very beginning of the SCULPT experiment. The formed phase is characterized by a comparatively high calcium activity and is stable for several hours (Figure 4.1c, black curve), however, without reaching a constant value, i.e., establishment of a solubility threshold. From quantitative evaluation of the measured calcium potential, the equilibrium ion activity product of the liquid-liquid coexistence in the mother solution can be estimated (Figure S4.2), revealing much higher values than reported for solubilities of crystalline or (solid) amorphous calcium carbonates.[19, 229] This is expected for an amorphous liquid-like precursor.[18] Upon crystallization of the amorphous precursor, a drop in the calcium potential is visible due to the formation of the more stable solid phase, even though quantitative data suggests that small amounts of the most soluble form of solid ACC persist (Figure S4.2).[19] The crystallization point is also detectable via an increase in the NaOH addition rate, required to maintain a constant pH, due to the larger amount of carbonate ions bound from the buffer equilibrium upon crystallization (Figure S4.1). During the addition of the solutions in the SCULPT method, no sudden increase of NaOH addition occurs, corroborating that the precursor is amorphous (Figure 4.1c, blue curve). The amorphous character of the precursor was further confirmed by isolating species along the titration followed by characterization using ATR-FTIR spectroscopy (Figure S4.3), which clearly showed the difference to previously reported ACC-PAA composite materials ("mineral plastics").[157] In parallel to the addition of the reactant solutions, the turbidity of the solution was measured and showed a rapid decrease during the first 3 hours of the experiment (Figure 4.1c, red curve) due to the formation of a visibly turbid dispersion (Figure 4.1b). This is caused by the formation and growth of mineral precursor droplets of several μm in size, according to light microscopy (Figure S4.4). After the reaction vessel is filled up (roughly after 6 h, Point 1 in Figure 4.1c), the resulting product can be isolated by centrifugation to obtain a highly concentrated dispersion of precursor droplets, possessing a gel-like consistency (Figure 4.1d). Interestingly, the product appears to be highly viscous directly after centrifugation but liquefies after manipulation with a spatula (Figure S4.16). In total, 10-15 g of product can be isolated from one experiment on lab scale (using a 150 mL beaker). After liquefying, the product can be applied to substrates or filled in templates to produce minerals, as demonstrated

below. If the product is dried in vacuum directly after centrifugation, amorphous calcium carbonate is obtained, as evident from the IR spectrum of the dried residue (Figure 4.1e). No polymer bands are visible in the IR spectrum, showing that the main product of the reaction is no Ca-PAA coacervate, but calcium carbonate mineral. The formation of Ca-PAA coacervates is a valid concern when high concentrations of Ca^{2+} and PAA are used,[95] and we indeed observe coacervate formation if no carbonate sources are used in the experiment. However, these Ca-PAA precipitates are vastly different from the liquid-like precursors formed in SCULPT (Figure S4.5). Similarly, the formation of ACC-PAA composite materials as side products is of concern. If the concentrations of the polymer are significantly increased, we indeed observe the formation of a transparent ACC-polymer composite material with similar properties as other ACC inorganic-organic composites (Figure S4.6).[157, 193, 227] However, these materials do not transform into crystalline calcium carbonates, even if suspended in water for extended periods of time, and shall therefore not be discussed further. To conclude, at properly selected experimental conditions, SCULPT yields a concentrated dispersion of liquid-like precursor droplets on a gram scale, which can be used to synthesize crystalline minerals, as shown below.

4.4.2   Effect of additives

A key advantage of SCULPT is the quantification of the stability of the liquid-like precursor phase, i.e., monitoring the time required until crystallization occurs. This is important as the precursor loses its liquid-like properties in the subsequent stages of mineralization when dehydration and crystallization take place. Therefore, there is a limited time for application in which the viscoelastic properties of the precursor phase can be exploited. To estimate this time for a given system, SCULPT can be used, but without isolating the product. In this case, except for the addition of NaOH to keep the pH value constant, no further solutions are added, while stirring is continued and parameters are continuously recorded by the electrodes (Figure 4.1c). The crystallization of the precursor phase is then evident by a drop in the Ca^{2+} activity and an increase in the NaOH addition (Figure 4.1c, point 2, see also Figure S4.3). This strategy is especially useful to investigate the effect of altered conditions, e.g., changes in the concentrations of added solutions, or the effects of additives on the stability of the precursor phase.[98] At standard SCULPT reaction conditions (Figure 4.1), the precursor dispersion was stable for 2-3 h after the addition was stopped (Figure 4.1c, time between point 1 and 2). This stability is too low for most practical purposes, as only a few hours are available to apply the product until crystallization occurs and the advantageous liquid-like properties are lost. To solve this issue, additives can be used to increase the kinetic stability of the system. It is known that Mg^{2+} ions can stabilize ACC, especially if combined with polycarboxylates.[52, 91, 224] Therefore, $MgCl_2$ was added to the $CaCl_2$ solution, and the resulting effect on the stability of the precursor phase was explored, as well as changes in PAA concentration (Figure 4.2a).
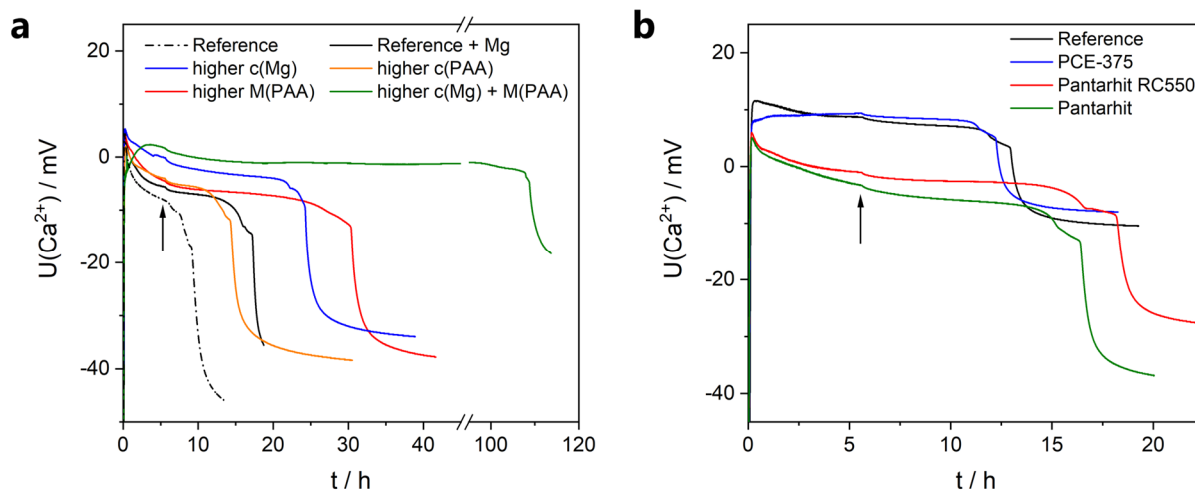
Figure 4.2 Effects of additives on the stability of mineral precursor. a) Titration curves for different ratios of Mg^{2+} and PAA concentrations in the added solutions. The reference conditions are shown in Figure 4.1c, using 10 g/L PAA with M = 5,000 g/mol in the added solution. Conditions for the shown curves are as follows: Reference + Mg: addition of 25 mM Mg^{2+} (5 mol-%) to the Ca^{2+} solution; higher c(PAA): 12.5 mM Mg^{2+} / 20 g/L PAA; higher M(PAA): 25 mM Mg^{2+} / 10 g/L PAA with M = 100,000 g/mol; higher c(Mg): 50 mM Mg^{2+} / 5 g/L PAA; higher c(Mg) + M(PAA): 50 mM Mg^{2+} / 5 g/L PAA with M = 100,000 g/mol. **b)** Titration curves for experiments with additional plasticizer in the starting solution. The initial concentration of plasticizer was 4 g/L in all experiments. In all experiments, dosing of solutions was stopped at 5.5 h (arrow), and data was recorded until crystallization took place. Detailed conditions for titrations are shown in Table S4.1.

It is evident that changes in the Mg^{2+} concentration have a larger effect than changes in the concentration of the polymer; with increasing Mg^{2+} concentration, we observe a strong increase in the kinetic stability of the precursor. Already the addition of 25 mM MgCl$_2$ to the CaCl$_2$ solution (corresponding to 5 mol-% Mg^{2+} relative to the amount of Ca^{2+}) was sufficient to increase the precursor stability from 2 h to 7 h, with 2 mol-% Mg^{2+} being incorporated in the mineral after crystallization (Table S4.2). Interestingly, this value is close to the Mg^{2+} content found in biominerals, such as sea urchin spines.[230] Using PAA with higher molecular weight (M = 100,000 g/mol) also results in a strong stabilization. However, the viscosity of the product also increased drastically, and usually no liquification of the gel-like product (as shown in Figure S4.16) was observed, hence compromising the liquid-like character. Therefore, although the stability of the precursor phase was lower, PAA with shorter chain length (M = 5,000 g/mol) was used for further experiments. TGA analysis of the isolated, crystallized products shows that roughly 2-5 wt-% of the polymer is present in the product (Table S4.2). This reveals that in terms of practical applicability, changing conditions and using additives affects not only the kinetic stability of the precursor phase, but the properties of the product during application and crystallization must be considered as well. Indeed, as already mentioned, the maximum kinetic stability can be reached when concentrations of polymer are drastically increased, up to the point where no more crystallization takes place due to formation of ACC-PAA composite materials (Figure S4.6). For the synthesis of liquid-like mineral precursor, it is however

favorable to reduce the polymer content as much as possible, as polymers and other organic impurities can only be incorporated into crystalline $CaCO_3$ to a limited extend and will be excluded during the crystallization of the precursor phase (Figure S4.7).[37, 231] Exclusion of the polymer from the growing crystalline phase will result in the enrichment of the surrounding solution in polymer, which in turn will affect the efficiency of precursor fusion and crystallization.

Another difficulty in materials synthesis from liquid precursor is the formation of cracks during drying and crystallization of the precursor phase (Figure S4.6) due to the high amount of water present in the product. Therefore, as in the case of cement pastes, superplasticizer was added to the initial solution to reduce the water content while preserving workability of the product.[232] Several commercial plasticizers based on poly(carboxylate ether) or lignosulfonates were investigated with respect to their stabilizing efficiency and effect on the water content in the product (Figure 4.2b). Addition of PCE plasticizers showed little effect on the stability of the precursor phase, while Pantarhit caused a slight stabilization. However, the addition of PCE based plasticizer (concentration of 4 g/L in the initial solution) resulted in a reduction of the water content to 45% if multiple centrifugation steps were performed, which represents a significant improvement compared to plasticizer free products that usually contain up to 80% water after centrifugation, independent of the number of centrifugation steps (Table S4.2). Therefore, in addition to using 5 mol-% Mg^{2+}, PCE based plasticizer was added to the titration experiments to synthesize an optimized precursor phase.

4.4.3   Material synthesis from liquid-like mineral precursor

Using the optimized reaction conditions, the application and material synthesis aspect was investigated. Again, it should be underscored that the SCULPT product is a highly concentrated dispersion of μm-sized amorphous mineral droplets in a salt-rich mother solution. As described earlier, the product can be directly dried to yield (solid) ACC, given that the time for drying is quicker than the time for crystallization of the precursor. However, starting from this ACC product, no large-scale minerals can be obtained due to the change in density from ACC ($\rho = 1.62$ g/cm^3) to calcite ($\rho = 2.75$ g/cm^3),[233] resulting in crack formation during transformation of ACC. Therefore, an advantageous strategy is to let the assembly and crystallization of the precursor droplets happen directly in the solution (Figure S4.9). Thereby, the droplets sediment and coalesce due to their liquid-like properties, resulting in the formation of larger mineral structures. In the same step, crystallization can take place yielding mineral structures without the problem of crack formation, as only small parts of the mineral crystallize at a time and potential ion-by-ion growth can fill interstitial spaces, similar to a recently reported growth mechanism for coral skeleton formation.[234] In addition, once crystallization has started, the growing crystalline structure can function as a substrate for further crystal growth, while

polymer and plasticizer, which are not fully incorporated into the crystal (Figure S4.7), are directly excluded and released into the mother solution at each step of crystallization. This way, formation of "pockets" of released additives are prevented and the formation of a solid mineral structure is possible. This strategy of crystallization in solution is in principle similar to the "conventional" gas diffusion-based synthesis of mineral using liquid-like precursors according to the colloid assembly and transformation process.[35] Contrary to gas diffusion, however, in our experiments all droplets are present from the beginning, instead of being formed slowly during the gas diffusion process. While this is a much faster protocol for mineralization, one needs to pay attention to the stability of the droplets. If no coalescence takes place, the droplets will eventually dehydrate and crystallize in their dispersed state, losing their liquid-like properties. The following sedimentation will then lead to lose aggregates of crystalline $CaCO_3$ particles, which is evident by the difference in surface morphologies of mineral structures for increasing reaction times (Figure S4.8). So as to obtain smooth mineral structures, the reaction has to be stopped before crystallization of the dispersed precursor droplets takes place. As described earlier, it is possible to estimate the stability of the precursor from the titration experiments, with the precursor usually being stable for several hours (Figure 4.2). After the desired reaction time, the remaining solution can be discarded and the product washed and dried, yielding the crystalline mineral (Figure S4.9). Using this strategy, we demonstrate several possibilities for material synthesis from liquid-like precursors in the following.

One possibility is to use the precursor to synthesize mineral coatings on calcite crystals. The mineralization on top of existing mineral structures is relevant for applications in restoration and conservation, e.g. in the restoration of marble structures. Small calcite crystals of several hundred µm in size were added to the precursor dispersions and mineralized. An even coating formed by the mineralized layer was visible in light microscopy (Figure 4.3a). SEM investigation of the surface shows that the layer was indeed formed by coalescence of precursor droplets, as still some semi-spherical features of individual droplets are visible (Figure 4.3b), while only minor cracks from drying occur on the surface. The observed mineral coatings look very similar to coatings formed by liquid-like precursors reported earlier,[206] which shows that our synthesis strategy can indeed produce results up to literature standard, with the ability to produce several orders of magnitude more of the precursor phase, in terms of quantity, rendering it practically usable in the first place. In several instances, SEM investigations of the dried specimens showed smooth structures formed by coalescence of the once liquid-like droplets (Figure S4.10), which are similar to recently reported structures occurring in biomineralization involving liquid-like precursors.[85] Occasionally, solid mineral structures without involvement of seed crystals were observed (Figure S4.11).
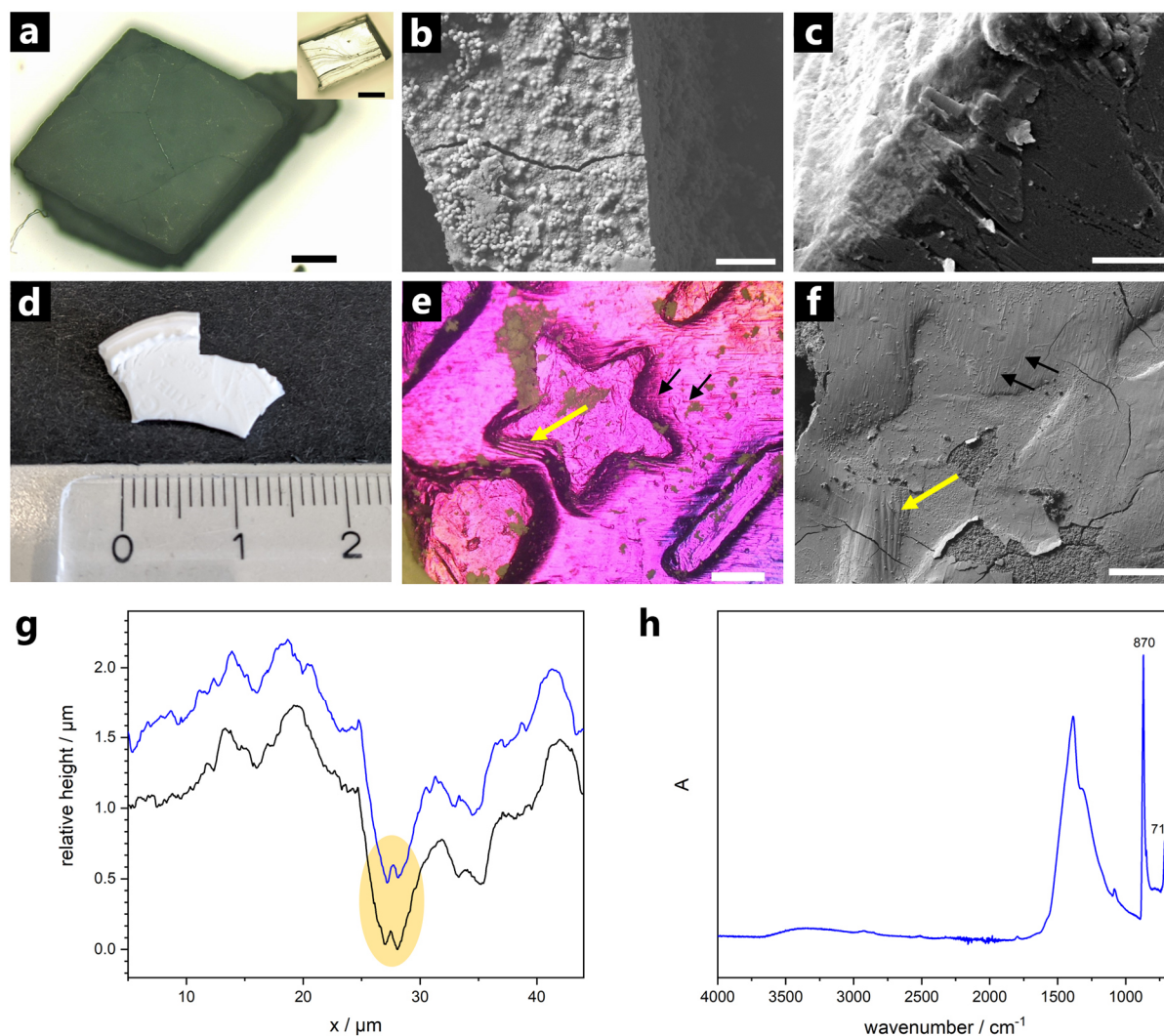
Figure 4.3 Application and material synthesis using liquid-like precursor. Calcite seed crystal covered with a layer mineralized from liquid SCULPT precursor. In the small inset, an uncovered calcite crystal is shown. Scale bars are 500 µm. **b)** SEM micrograph of a coating on a seed crystal formed by fusion of liquid-like precursor droplets. Scale bar is 10 µm. **c)** Cross section of a solid mineral layer formed on a calcite wafer. The layer shows even fusion of particles and a smooth surface. Scale bar 5 µm. **d)** Calcite mineral stamp of a coin with visible embossing. **e)** Light microscopy image of the surface of the coin after removing the molded mineral. Characteristic steps from the manufacturing process of the coin (yellow arrow) and scratches on the surface of the coin (black arrows) are highlighted. Scale bar is 250 µm. **f)** SEM micrograph of the mineral stamp, showing that the structures in from the coin shown in (e) are well reproduced. Scale bar 200 µm. **g)** Comparison of AFM line scans across a scratch on the coin and the corresponding imprint of the mineral mold. The yellow area highlights the resolution of a sample detail of a height of 80 nm. Raw data of the AFM scans is shown in Figure S4.15. **h)** ATR-FTIR spectrum of the mineral mold. The characteristic vibrations at 870 cm^{-1} and 712 cm^{-1} show the formation of calcite. Detailed conditions are summarized in Table S4.2.

In addition to seed crystals, we also used calcite wafers (5 x 5 mm in size) as template for the formation of mineral coatings. In these experiments, the coatings deposited on the calcite templates usually showed a thickness of several µm, based on the use of 0.5 mL of precursor

dispersion that was placed on top of the substrate (Figure 4.3c and Figure S4.8). The mineralized layers were strongly attached to the seed crystal, and it was not possible to remove the layers from the substrate once deposited. In fact, treatment of the coated wafers using ultrasonication resulted in the substrate being damaged, while the mineralized layer remained attached (Figure S4.12). These results demonstrate promising characteristics in using the precursor dispersion for mineral conservation and restoration applications, for which a strong adhesion of the mineralized layers is favorable.

The main advantage of using liquid-like precursors in the synthesis of minerals is their ability to infiltrate small pores or matrices, thereby enabling the production of structures that are inaccessible by conventional mineralization procedures. For example, commercial products for restauration of minerals are based on dispersions of calcium hydroxide particles of several hundreds of nm in size in ethanol.[235-236] It is easy to see that these conventional mineralization solutions based on (solid) particles are limited in their infiltration efficiency as soon as the dimensions of the template reach the dimensions of the particles, while a liquid, or liquid-like, precursor can easily "flow" into fine cracks. If we think of this "molding" of crystalline structures, the possible resolution and details should be much higher using a liquid-like precursor compared to (solid) particle-based approaches, which also will only produce an agglomeration of particles instead of an extended solid mineral structure. To demonstrate the use of liquid-like mineral precursors in these types of applications we placed the dispersion on a coin to test the efficacy of the precursor to infiltrate into the stamping and cracks on the surface of the coin. By letting the precursor droplets coalesce and crystallize, a "molded" mineral reflecting the features on the surface of the coin can be produced. In this way, molded minerals on a length scale of cm were produced (Figure 4.3d). Comparison of features embossed in the coin, e.g. 1 mm sized stars (Figure 4.3e), with the produced mineral mold (Figure 4.3f) showed that the structure was well reproduced. In addition, details such as characteristic steps arising from the manufacturing process of the coin (Figure 4.3e and f, yellow arrows and Figure S4.13) and even smaller scratches on the surface of the coin (Figure 4.3e and f, black arrows) were visible in the molded mineral material. The produced mineral stamp has a much higher resolution than achieved by the conventional mineral molding process using gypsum, which is limited to a scale of several tens of μm (Figure S4.14). To estimate the resolution of our mineral cast, atomic force microscopy (AFM) was used to compare a scratch on the coin with its counterpart on the molded mineral (Figure S4.15). Comparison of line scans across the scratch (Figure 4.3g) showed that features of less than 100 nm were resolved. Again, it needs to be mentioned that the investigated "molded" minerals are crystalline calcium carbonate, as revealed by the ATR-FTIR spectrum (Figure 4.3h). The manufacturing of crystalline minerals with the presented resolution visualizes the potential of material synthesis from liquid-like precursor phases, e.g., regarding nanofabrication of minerals or new classes of mineral molding formulations with resolutions close to that of PDMS stamps.[237]

4.5 Conclusions

We have demonstrated a scalable experimental method to synthesize a liquid-like mineral precursor phase. The synthesis strategy solves the previously existing limitations of the available synthesis methods for liquid mineral precursors. Using the presented method, already on lab scale several grams of precursor phase can be synthesized within several hours, and SCULPT can be transferred to industrial scales in a straightforward manner. The titration-based method was also used to estimate the stability of the precursor and tune its stability by adding magnesium ions, while the workability of the product was improved by using superplasticizer. The liquid-like properties of the precursors synthesized using SCULPT can be used for material synthesis of different kinds of mineral materials with distinct applications, e.g. the following minerals that were observed in this study:

i.   Crystalline, solid $CaCO_3$ materials, having applications in restoration formulations,[238] and potential for use in calcium carbonate-based cements[221]

ii.   "Molded" $CaCO_3$ minerals, having applications as high-resolution mineral molding formulation or for the synthesis of biomimetic materials[35, 105, 239]

iii.   Crystalline $CaCO_3$ coatings with (or without) hierarchical ordering, having applications in soil-stabilization,[206] films for biomedical materials,[240] or coatings for oil-water separation[241]

iv.   Polymer-ACC composite materials, having applications as sustainable "mineral" plastics,[157] protective packaging,[242] or glassy functional materials[227]

v.   Polymer-stabilized ACC materials or coatings, having applications as precursor for single crystals,[37, 43] precursor for inorganic monoliths[243] or precursor for thin $CaCO_3$ films[244]

vi.   Spherical Calcite particles with narrow size distribution, having applications as filler or reinforcing materials[245] or drug delivery materials[246]

Our work enables the use of liquid-like precursor phases for material synthesis on application-relevant scales, possessing relevance for use in stone restauration, production of mineral molds, mineral coatings, as well as showing promise to produce mineral materials for construction chemistry, e.g. towards the development and improvement of calcium carbonate based, CO_2-fixating concretes.

4.6 Supplementary Information

4.6.1   Supplementary figures
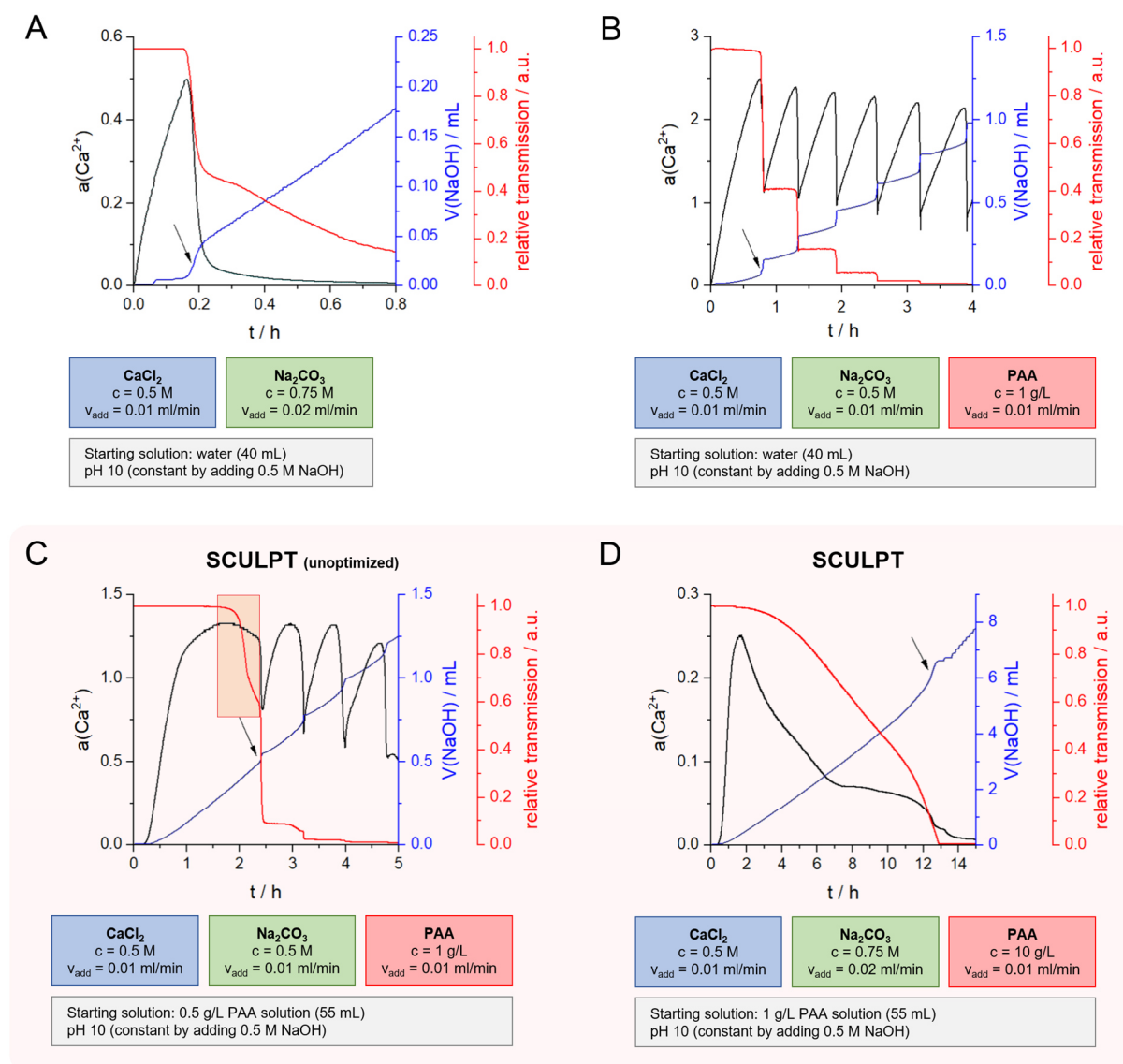
Figure S4.1 Development of the SCULPT method for liquid-like mineral precursors. The method is based on potentiometric co-titration.[101] **a)** In a standard experiment, solutions of $CaCl_2$ and Na_2CO_3 are dosed into Millipore water at a constant pH value. The pH value is held constant by the automatic addition of NaOH solution. During the titration, the free Ca^{2+} potential is recorded using a calcium ion selective electrode, and the measured potentials can be converted to Ca^{2+} activities by electrode calibration.[120] The results show a typical LaMer type titration curve,[19] with the Ca^{2+} activity (black curve) increasing until critical supersaturation is reached (at 0.2 h) and the Ca^{2+} activity then dropping to a level corresponding to the solubility product of the formed mineral. Upon the drop in Ca^{2+} activity, i.e., formation of crystalline $CaCO_3$, a decrease in transmission of the solution (red curve) is detected due to particle formation. In addition, an increase in NaOH addition (blue curve, arrow) is detected due to the rapid removal of carbonate ions from the buffer equilibrium upon crystallization ($HCO_3^- \rightleftharpoons CO_3^{2-} + H^+$) and resulting release of protons that are then neutralized. **b)** If PAA is continuously added during the titration, a drastic change in the curves is visible. PAA and other polycarboxylate additives are known to have a strong effect on calcium carbonate formation, especially towards stabilizing liquid precursor

phases.[98, 126] In the titration, an inhibiting effect is detected, with the crystallization now taking place at 0.8 h, again visible from the increase in NaOH addition (arrow). Due to the inhibiting effect of PAA on the crystallization, the maximum Ca^{2+} activity is also increased, and more Ca^{2+} can be added before crystallization takes place. The step-like behavior after crystallization can be explained by additive adsorption on the growing particles.[98] **c)** If the concentration of PAA is further increased by adding PAA to the starting solution, the system is stable for even longer, with the crystallization now taking place after 2.5 h (arrow). Interestingly, although the time until crystallization is increased, the maximum of Ca^{2+} activity decreases significantly, indicating that more Ca^{2+} is bound in precursor structures. In addition, after the maximum of Ca^{2+} activity is reached, there is no sudden drop, but a regime at which Ca^{2+} activity stays at a high value. In this region, a decrease in transmission is also visible (red area), taking place before the formation of crystalline $CaCO_3$ which is indicated by an increase in NaOH addition (black arrow). We attribute the effects to the formation and growth of amorphous precursor droplets that grow to a size that can be detected by the optrode. The significant decrease in Ca^{2+} activity (compared to the titration in b) shows that a significant amount of Ca^{2+} is bound in these precursor species. The presented conditions can in principle be described as SCULPT, however further optimization can be performed to increase the amount of precursor formed. **d)** Further increasing the PAA concentration allows to further the growth of precursor droplets, i.e., SCULPT. The previously described trends are now more pronounced, with Ca^{2+} activity reaching a maximum, but after the maximum there is a long regime before crystallization takes place (at 13 h, black arrow). In addition, the maximum and average Ca^{2+} activity is even lower compared to the previous measurements, indicating that an even higher amount of Ca^{2+} is bound in precursors prior to crystallization. The decrease in transmission, i.e., the formation and growth of precursor droplets, is also much more pronounced, with growth now taking place for several hours. The presented method therefore allows the straightforward and effective stabilization of precursor species, with high amounts of calcium (and carbonate) ions bound in these structures. Detailed conditions for all experiments are summarized in Table S4.1.
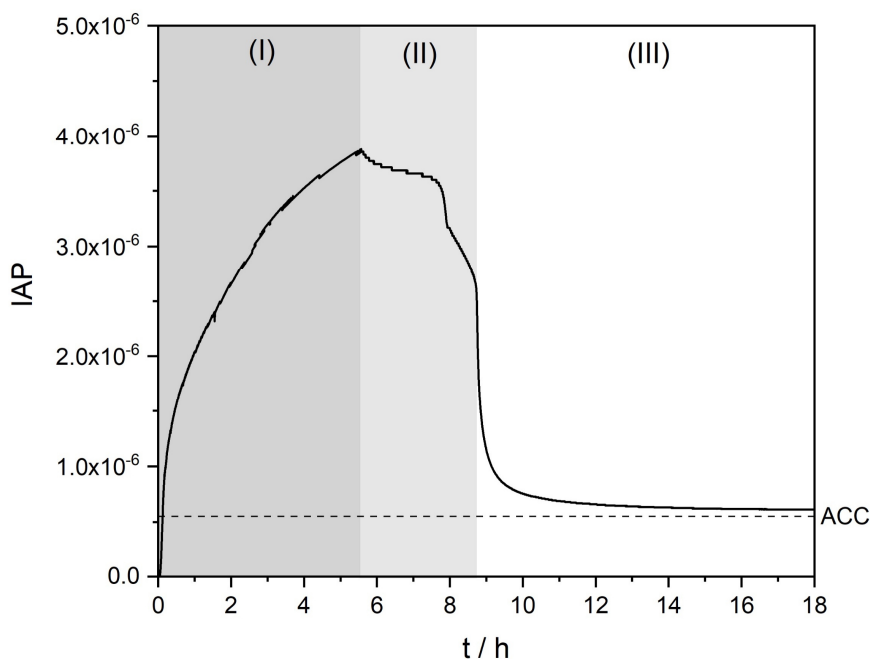
Figure S4.2 Evolution of the calcium carbonate ion activity product (IAP) during a typical SCULPT precursor synthesis experiment. The conditions for the experiment are shown in Table S4.1. In the titration experiment, solutions of $CaCl_2/MgCl_2$, Na_2CO_3 and PAA are added for 5.5 h into a dilute PAA solution until the reaction vessel is filled up (regime I). Then, the liquid precursor can be isolated by centrifugation, but here, the addition was stopped without isolation, and further data were recorded by the electrodes. The precursor dispersion is stable for a certain time (regime II) and eventually crystallizes (regime III), indicated by a drop in the Ca^{2+} activity, as described in Figure S4.1. Determination of IAPs in the present system is difficult, as the polymer, which is present in very high concentrations, can affect measured calcium potentials (see also discussions in section 2.6.1).[95, 121] In addition, from the data, it is not possible to directly determine the carbonate activity, so assumptions have to be made in order to estimate the IAP. The main assumption is 1:1 binding ratio of $Ca^{2+}:CO_3^{2-}$ in precursor structures, as earlier determined in additive-free systems.[19] This is indeed a rough assumption, as a part of the Ca^{2+} ions is bound by the poly(acrylic acid) and carbonate ions can be coordinated to Mg^{2+} ions. However, the amount of Ca^{2+} ions bound to PAA can be expected to be rather small compared to carbonate binding, as established in Figure S4.5. Based on these assumptions, the IAP in the mother solution during coexistence with the liquid precursor phase can be estimated to be on the order of 10^{-6}, which is at least one order of magnitude higher than the solubility of (solid) amorphous calcium carbonate (ACC) reported by Brečević and Nielsen (IAP of 10^{-7}, dotted line),[229] which according to Avaro et. al. is the upper limit of ACC solubility.[18] It was shown that less stable, more hydrated amorphous calcium carbonate species possess higher solubility products,[18] which suggests that in the presented titration experiment indeed a highly hydrated phase, i.e., liquid precursor phase, is formed initially, which continuously ripens towards solidification, thereby altering its composition, in turn changing the measured equilibrium IAP of the mother solution. Upon crystallization (regime III), full dehydration of the precursor species takes place and calcite is formed (Figure S4.3). We would therefore expect the IAP to drop to the solubility product of calcite (10^{-9}),[19] however, a significantly higher solubility product is detected, close to that of solid ACC formed via spinodal decomposition. Since the solubility product is governed by the most soluble phase in the system, the detected high solubility is likely due to persistent non-crystallized ACC or Ca-PAA coacervates being present in the system in regime III (potentially in rather low amounts that are too small to be detected by ATR-FTIR).
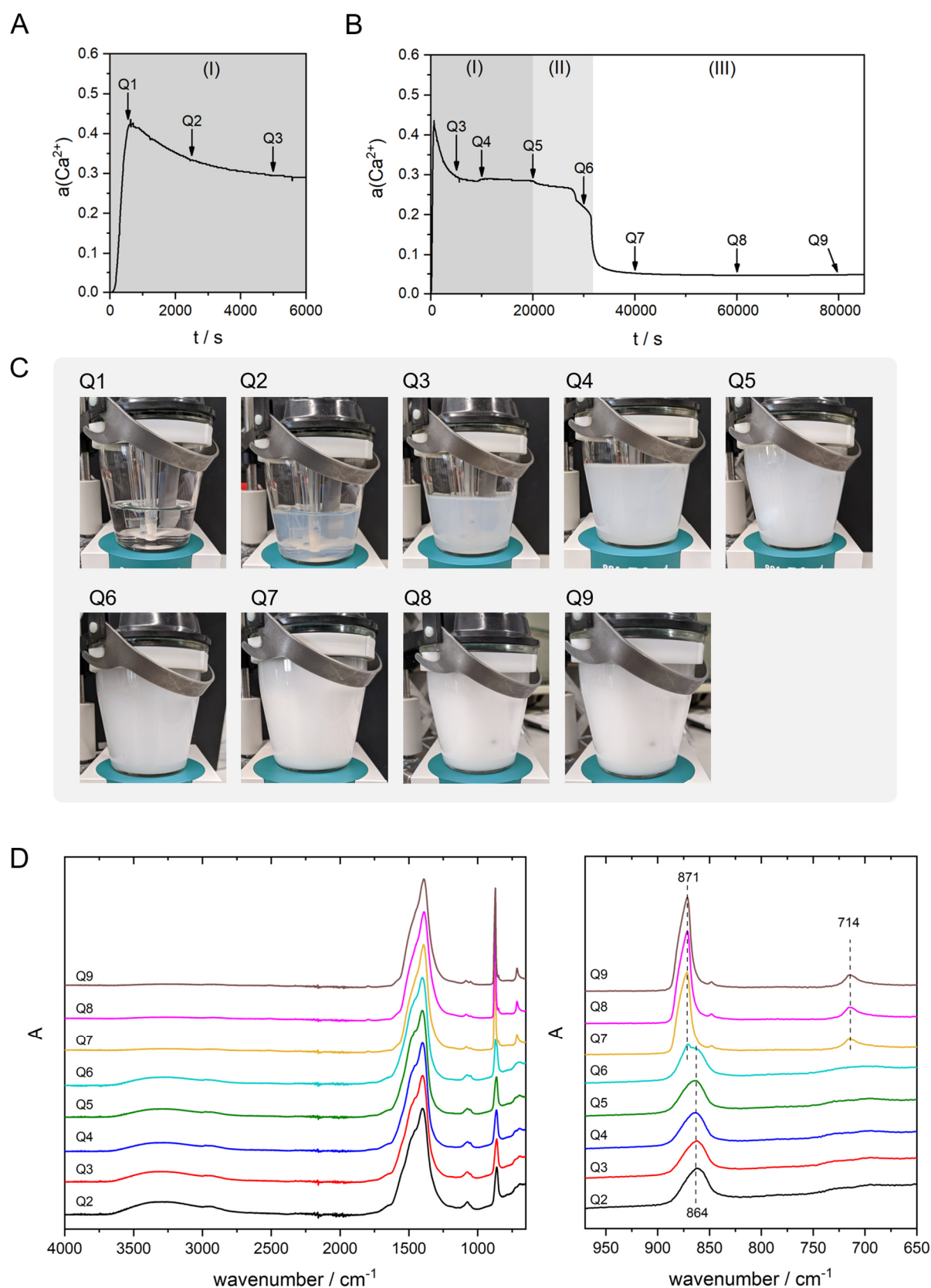
Figure S4.3 Isolation of mineral species during a SCULPT synthesis experiment. Experimental conditions are shown in Table S4.1. **a)** Evolution of Ca²⁺ activity in the first 6000 s of the experiment and **b)** over the entire duration of the experiment. Solutions are added until the vessel is filled up

(regime I, until 20000 s), followed by a stop of addition and further recording of data by the electrodes. The precursor dispersion is stable for a certain time (regime II) until crystallization takes place (regime III, at 32000 s). Points of sample isolation are marked by arrows: Q1 (500 s); Q2 (2500 s); Q3 (5000 s); Q4 (10000 s); Q5 (20000 s); Q6 (30000 s); Q7 (40000 s); Q8 (60000 s); Q9 (80000 s). **c)** Photos of the reaction vessel shortly before the samples are isolated. As confirmed by the optrode measurement (Figure 4.1c), the transmission of the solution decreases rapidly after the start of the experiment due to the formation of the liquid precursor droplets. **d)** ATR-FTIR characterization of the sample isolated at the different stages. The samples were isolated by centrifugation followed by washing with EtOH to prevent crystallization of amorphous species (at Q1, it was not possible to isolate a sample). Up until point Q5, at which product isolation takes place in SCULPT experiments, the droplets are amorphous, as indicated by the broad ν_2 vibration at 864 cm^{-1}.[18, 78] At point Q6, at which the drop in Ca^{2+} activity starts, transformation to crystalline CaCO$_3$ takes place, visible by the ν_2 vibrational band at 871 cm^{-1}. The formed crystalline polymorph is calcite (ν_4 vibration at around 714 cm^{-1}). In none of the spectra, vibrations from PAA are visible (see Figure S4.5e), showing that the main product is mineral precursor phase, and only minor amounts of PAA (and Ca-PAA coacervates) are present. The absence of PAA vibrational bands further confirms the distinct difference of the product formed in our titrations with previously reported PAA-ACC composite materials, which show clearly visible PAA vibrational bands in ATR-FTIR spectroscopy.[157]
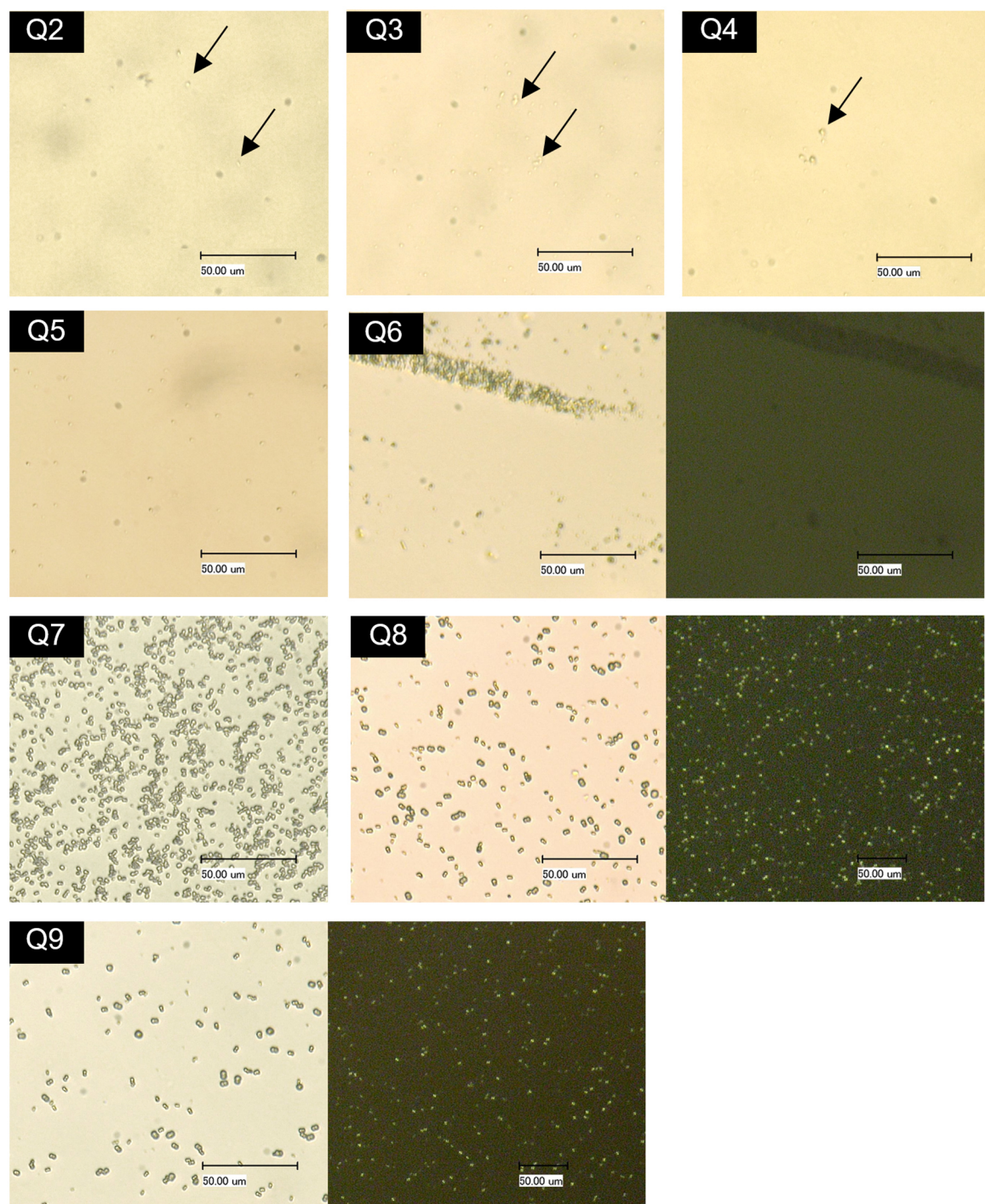
Figure S4.4 (Polarized) light microscopy investigations during different stages of a typical SCULPT synthesis experiment. Isolation of the samples is described in Figure S4.3 and experimental conditions are shown in Table S4.1. A few droplets of the reaction solutions (Figure S4.3c) were placed on a glass slide and investigated. When the solution turns turbid (Q2), particles/droplets with a size of several μm can be observed (arrows in Q2, Q3, Q4). At later stages, growth in particle size was detected. Polarized light microscopy (exemplary shown for Q6, Q8 and Q9; left image: parallel polarizers, right image: crossed polarizers) confirms results from ATR-FTIR (Figure S4.3d), with particles at Q6 still being largely amorphous and starting from Q7, crystalline particles being detected, as shown by the bright spots in polarized light microscopy images. Dark spots in the images (e.g. Q2, Q3, Q4) not marked by arrows can be attributed to measuring artefacts and impurities on the lenses of the light microscope.
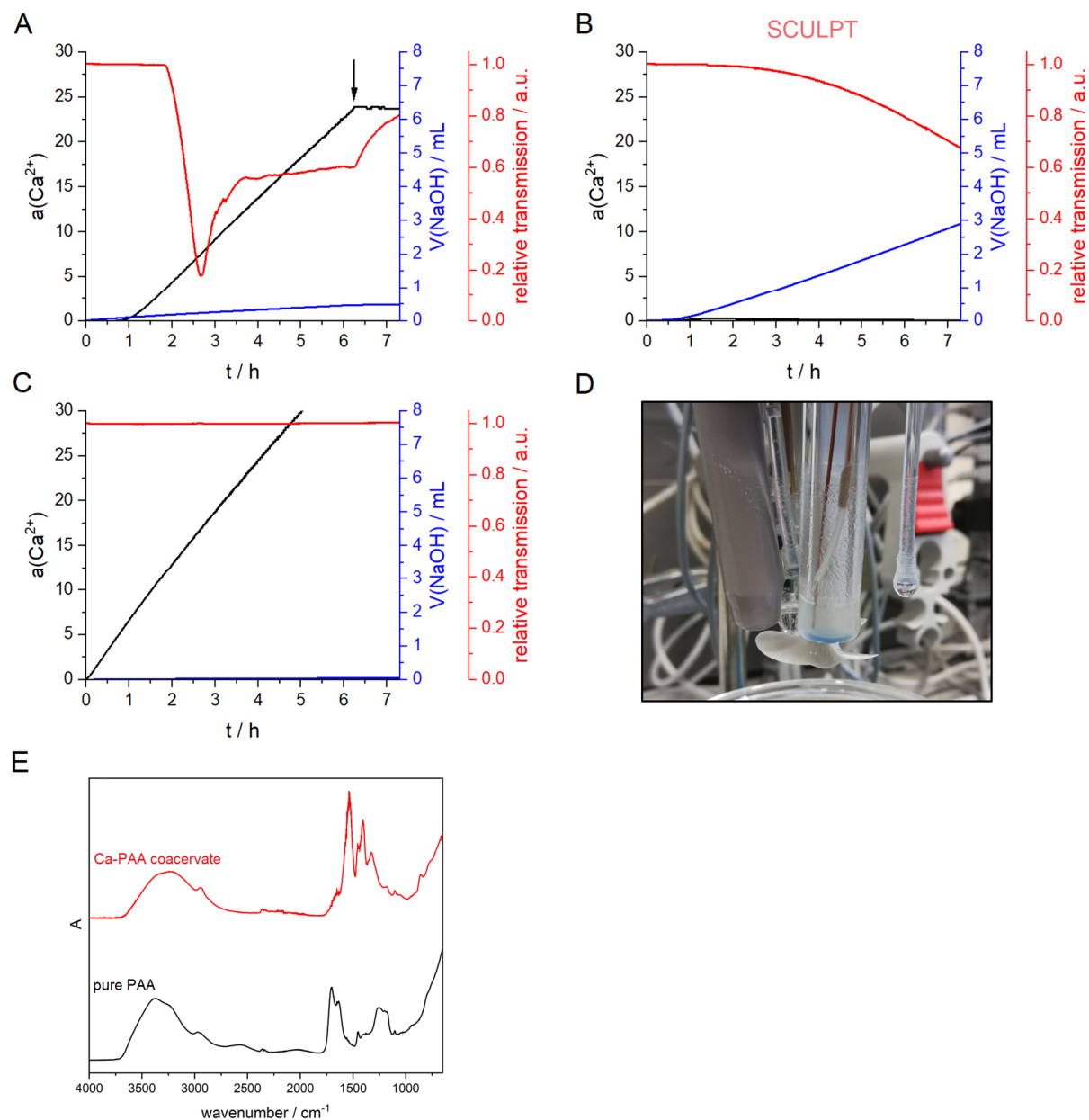
Figure S4.5 Titration experiments to investigate formation of Ca-PAA coacervates. The conditions for the experiments are show in Table S4.1. **a)** A titration experiment without the addition of carbonate is shown, i.e., $CaCl_2$ and PAA solutions are added at a constant rate at a constant pH value (pH 10.0) into dilute PAA solution. **b)** For comparison, a SCULPT precursor synthesis experiment and **c)** experiment of dosing calcium solution into water is shown. In contrast to the reference experiment of dosing calcium into water, in presence of PAA a drop in transmission is visible (a, red curve), caused by the precipitation of Ca-PAA species. Interestingly, the transmission increases again after a minimum is reached, as the precipitates quickly separate from the solution and stick to the glass walls and electrodes. This is also evident from the increase in transmission when the addition is stopped (a, arrow), and the remaining coacervate particles quickly separate from the solution, although the solution is continuously stirred. The Ca^{2+} activity (a, black curve), after an initial offset due to adsorption of Ca^{2+} by the carboxylate groups,[98] increases as well during the course of the experiment, as the added calcium exceeds the adsorption capacity of the newly added PAA. These trends are different from the SCULPT liquid-like precursor synthesis experiments. The Ca^{2+} activity is significantly lower in the SCULPT experiment (b, black curve), as most of the calcium is bound in the calcium carbonate mineral precursor structures. In addition, NaOH addition is higher in the synthesis experiments (b, blue curve), as

carbonate ions are bound in the precursor structures, causing the release of H^+ due to the shift in carbonate buffer equilibrium. **d)** Image of Ca-PAA coacervate sticking to the electrodes. The sticky precipitate is vastly different from the (non-sticky) gel-like precipitate obtained from mineral precursor synthesis experiments (Figure 4.1d and Figure S4.16). **e)** ATR-FTIR spectra of dried Ca-PAA coacervate isolated from titration (red) in comparison with pure PAA (black). The vibrational bands from PAA are visible in the spectrum of the Ca-PAA coacervate but are not detected in the regular mineral precursor synthesis experiments (Figure S4.3d). To conclude, it is evident that Ca-PAA coacervates show vastly different characteristics when compared to the product from SCULPT. The role of Ca-PAA coacervates is therefore negligible for this work.
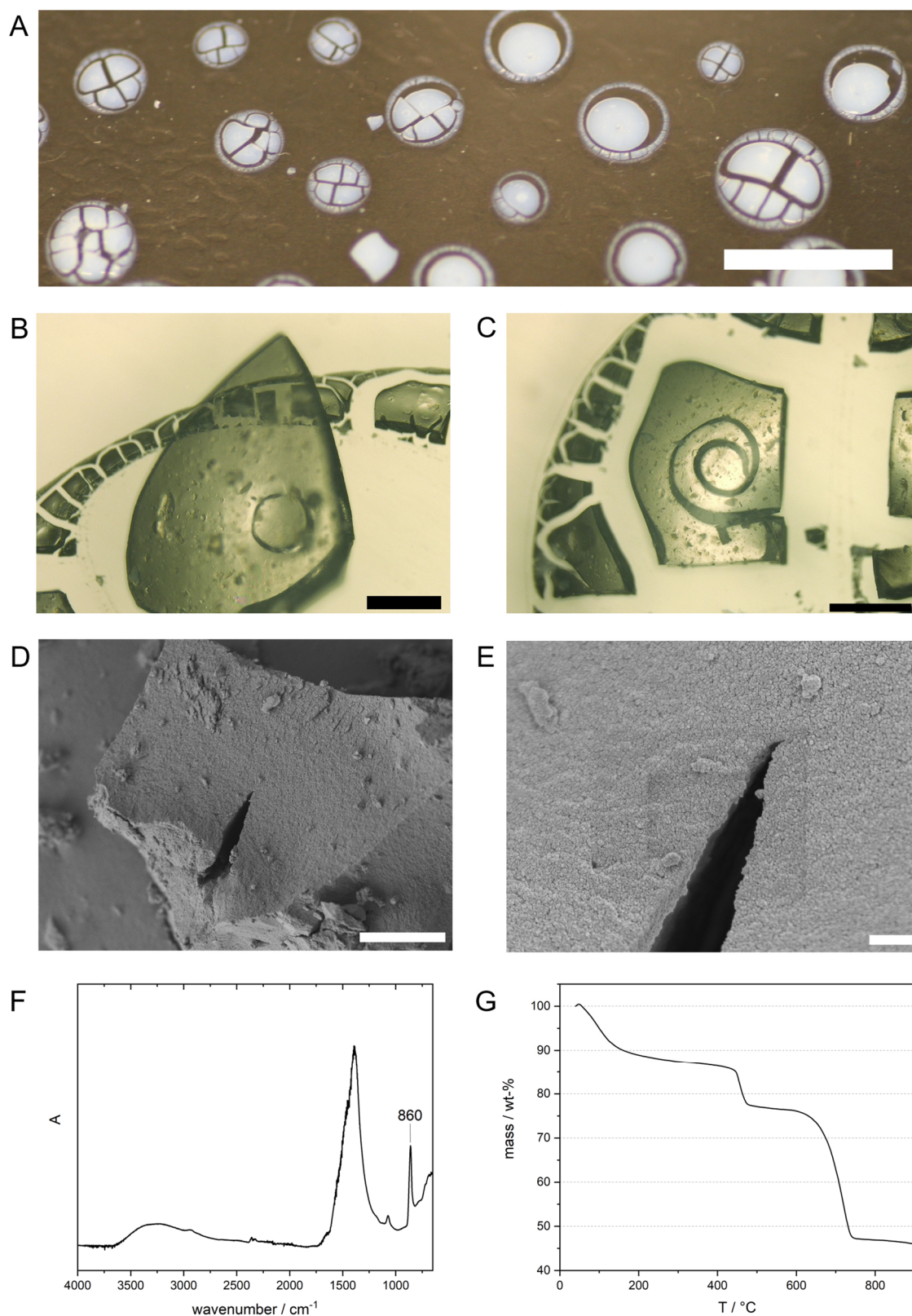
Figure S4.6 Synthesis and characterization of ACC-PAA composite materials using the presented titration method. In essence, if PAA concentrations are significantly increased in the synthesis protocol, a solid, transparent ACC-PAA composite material is obtained instead of the polymer-stabilized liquid-like mineral precursor phase. Conditions for the experiments are show in Table S4.2. Essentially, 4 times the polymer concentration of regular experiments was chosen to obtain the shown materials. **a)** Example image of dried droplets after the precursor dispersion was isolated from titration and placed drop-wise

on a glass slide. Cracks and volume reduction from the drying procedure are visible. Scale bar 1 cm. **b, c)** Light microscopy images of the transparent, plastic-like product. Scale bars 500 μm. **d)** SEM analysis of one particle. Scale bar 5 μm. **e)** SEM analysis at higher magnification, showing that the μm sized precursor droplets detected in the titration are no longer visible and fused to form a continuous structure. Scale bar 500 nm. Characterization of the product using **f)** ATR-FTIR confirms the amorphous character of the mineral components and **g)** TGA shows that roughly 10 wt-% of polymer is present in the sample, which is significantly higher than regular experiments for mineral precursor synthesis (Figure S4.7). The IR spectrum remained unchanged after storing the particles in water for 2 weeks, demonstrating the high stability of the ACC-PAA composite material. The inability of this material to crystallize illustrates the key difference of what we label as an ACC-PAA composite materials from the polymer-stabilized liquid-like mineral precursors that can be used for mineral material synthesis. As described in the results section, synthesis of (transparent) ACC-PAA composite materials or, in more general terms, ACC-organic composites have been described in literature before and shall not further be discussed here.[157, 227, 247-248]
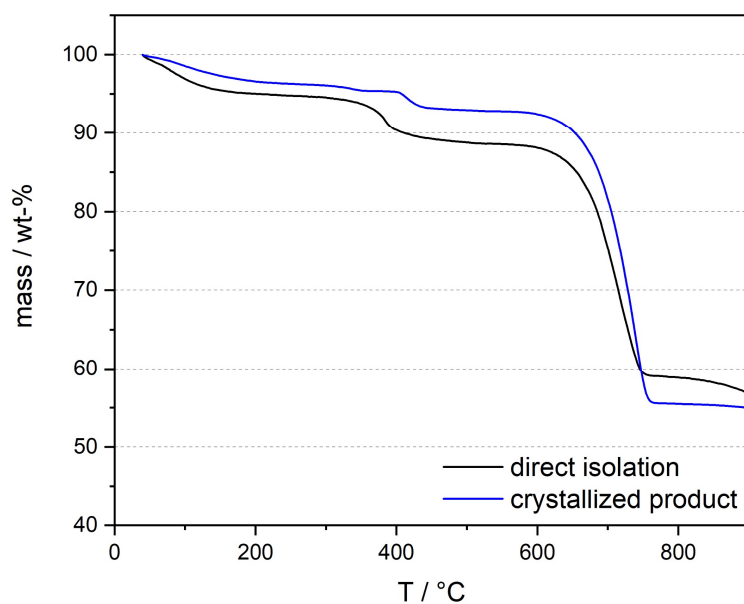
Figure S4.7 TGA characterization of CaCO₃ minerals. Thermogravimetric analysis (TGA) was carried out in oxidative atmosphere and conditions for sample synthesis are detailed in Table S4.2. Shown are the analyses of liquid-like mineral precursor dispersions directly dried after isolation, i.e., still in their amorphous state, (black) and the same sample after storing for 2 days in water, i.e., after crystallization, (blue). The initial weight loss (below 200 °C) can be attributed to loss of H_2O, which stems from structural or surface adsorbed water in ACC[249] or from water strongly bound by PAA that is present in the sample. The second step (300-500 °C) can be attributed to polymer decomposition and the final step (600-800 °C) arises from calcination, ($CaCO_3 \rightarrow CaO + CO_2\uparrow$). It is evident that in the crystalline sample less polymer is present compared to the amorphous sample. This shows that not all of the polymer is incorporated in the crystal structure and a significant fraction is excluded during crystallization. This excluded fraction of the polymer can further interact with other mineral phases in the system, which is also evident by the successive nucleation events in the titration curves (Figure S4.1b), as each nucleation event releases PAA that can then inhibit the next crystallization event. This observation poses a problem for material synthesis from liquid-like mineral precursors, as the expelled polymer can inhibit the crystallization of nearby mineral precursors, e.g. by affecting the local pH value or by adsorption on the droplets. It is therefore advantageous to use as little polymer as necessary for the mineral precursor synthesis to still guarantee the liquid-like properties of the minerals. Indeed, a compromise needs to be found between the kinetic stability of precursor phase (higher polymer content is advantageous), liquid-like properties of the precursor phase (higher polymer content is advantageous), and behavior of liquid-like precursor during crystallization and material synthesis (lower polymer content is advantageous).
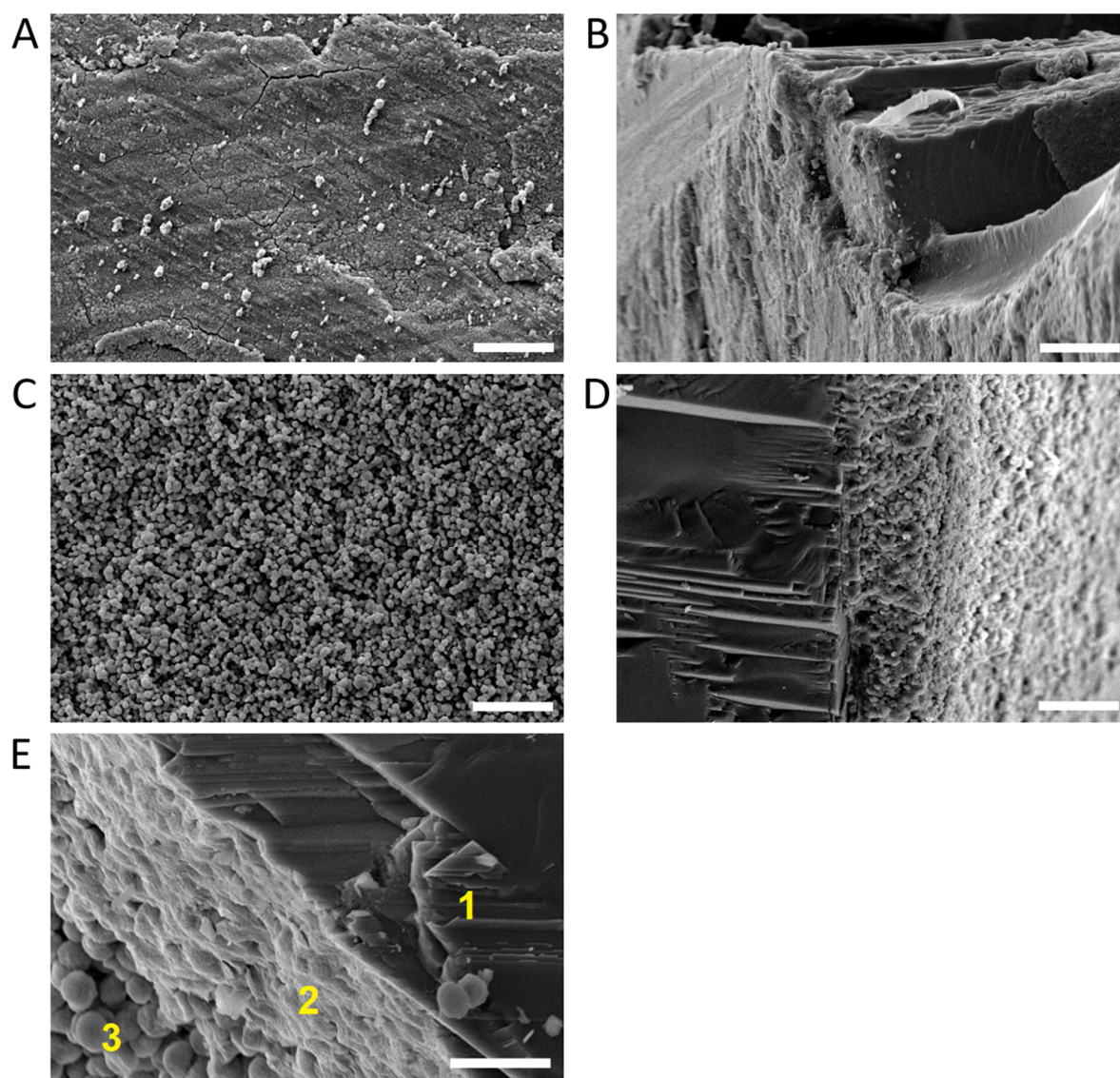
Figure S4.8 SEM micrographs of mineral layers formed on calcite wafers. For the experiments, 0.3 mL of precursor dispersion were placed on a calcite wafer (5 x 5 mm). **a)** If the precipitation is stopped before crystallization of the precursor droplets, in this case 3 h, a smooth layer of mineral has formed that **b)** is several µm in thickness. **c)** If the reaction is stopped after 6 h, partial crystallization of the droplets has started, and fusion is incomplete. Although the wafer was treated with ultrasonication after finishing the experiment, the surface is still rough and individual particles are visible. **d)** The thickness of the mineral layer has significantly increased to roughly 10 µm. **e)** Illustration of the transition from the calcite wafer (1) to fused zones (2) and partially fused zones (3). Scale bars are 10 µm (a to d) and 5 µm (e). Detailed conditions for all experiments are summarized in Table S4.2.
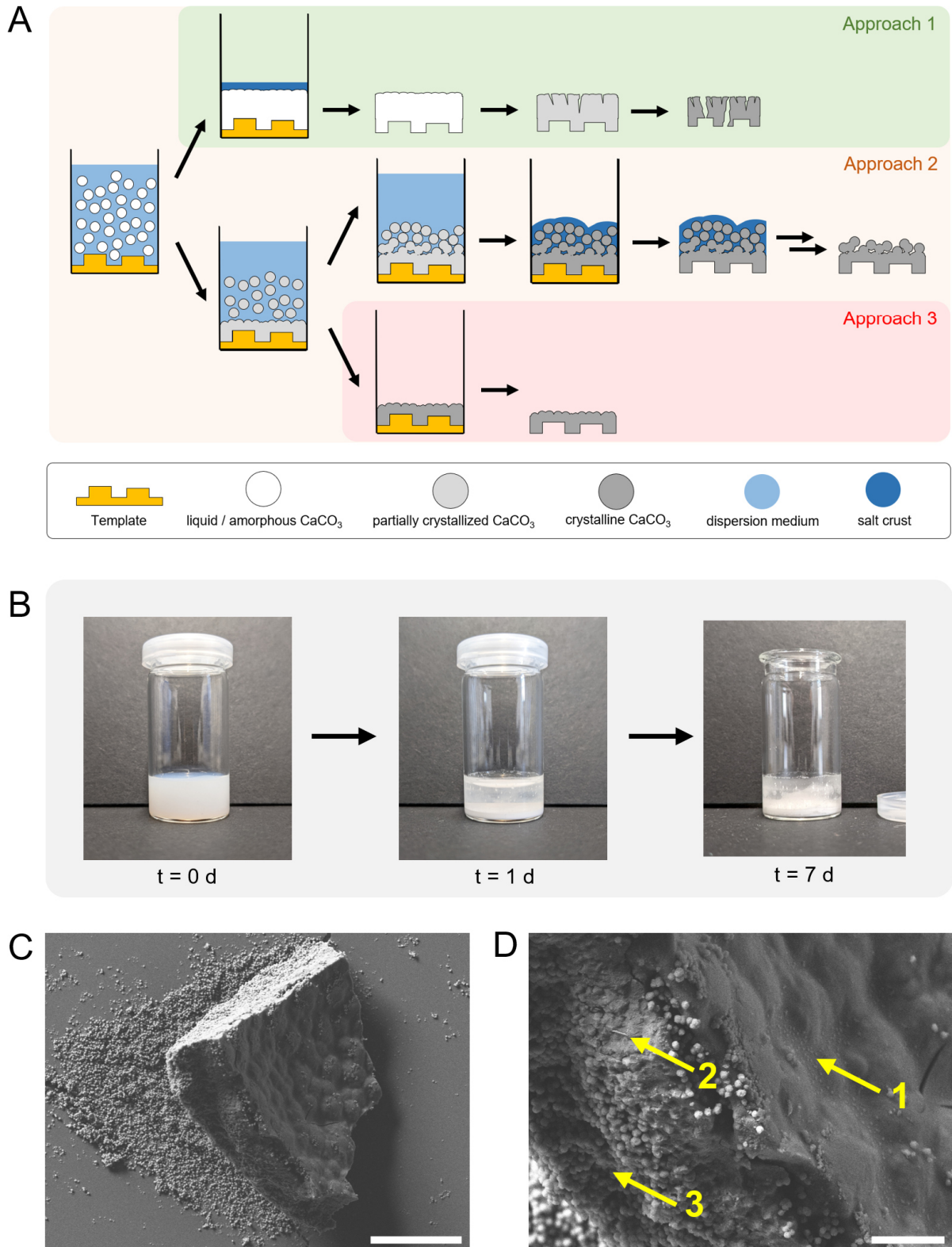
Figure S4.9 Illustration and discussion of different mineralization strategies using liquid-like mineral precursor. Three main synthesis strategies for formation of crystalline mineral are shown, starting from the highly concentrated dispersion of precursor droplets that was isolated by centrifugation. The straightforward method is the rapid drying of the solution, e.g., in vacuum or at increased temperatures (approach 1). The precursor droplets will fuse and form a "block" of amorphous mineral with a salt crust on top. The salt crust is formed due to the high salt/counterion concentrations still present in the mother solution of the precursor dispersion, originating from the highly concentrated

solutions added during SCULPT. The salt crust is water soluble and can be removed by washing with water, leading to the amorphous product. Due to the change in density (and resulting volume reduction) during transformation of amorphous to crystalline mineral it was not possible to transform the amorphous product into one "block" of crystalline mineral, and usually crack formation was observed (also see Figure S4.6a). As demonstrated in earlier studies, much more sophisticated conditions are necessary to synthesize crack-free (single) crystalline materials starting from (solid) amorphous precursors, e.g. patterning of crystals to release stress from volume reduction upon crystallization[37] or well defined temperature profiles during crystallization.[43] A better strategy for the synthesis of crystalline materials is therefore to not rapidly dry the dispersion but letting the droplets slowly sediment and crystallize (approach 2). Thereby, the droplets can still fuse, as long as they are in their liquid state. After fusion, crystallization can directly happen (especially if crystalline mineral is used as a template), thereby preventing crack formation. The crystalline layer can then grow by fusion and crystallization of individual particles, analogous to the gas diffusion-based PILP mineralization procedures.[28, 106] However, in contrast to gas diffusion the droplets are not freshly generated but exist all from the beginning, and eventually crystallization of the droplets in the dispersion will take place. The product will therefore have a gradient ranging from fully fused zones (at which the droplets were still in their liquid state) up to non-fused particles (droplets have already crystallized in dispersion prior to fusion). It is possible to remove the "loose" particles by ultrasonication, however usually still a rough surface is obtained due to only partially fused droplets (see also Figure S4.8). If the goal is to obtain a completely solid mineral it is therefore necessary to stop the experiment before (partial) crystallization of the dispersed droplets takes place (approach 3). The experiment can be stopped based on the stability of precursor droplets in solution, which can be estimated from the titration experiment. After the predetermined time, the solution can be discarded, thereby also preventing formation of a salt crust. This approach was used for most crystallization experiments. **b)** Images of sedimentation and drying of precursor dispersion according to synthesis approach 2. **c)** SEM micrographs of a mineral piece with salt crust synthesized from liquid-like precursor by drying the dispersion (scale bar 50 μm) and **d)** higher magnification of a cross-section of the piece (scale bar 10 μm). It is evident that the salt layer (arrow 1) is clearly separated by the mineral (arrow 2), with a visible gap in between. The salt crust can be easily removed by washing with water. Regarding the mineral, fused zones (arrow 2) and partially fused zones (arrow 3) are visible. Non-fused particles are visible as well below the large structure (in c). Conditions for the experiment to produce the depicted mineral are show in Table S4.2 (Exp. No. 10).
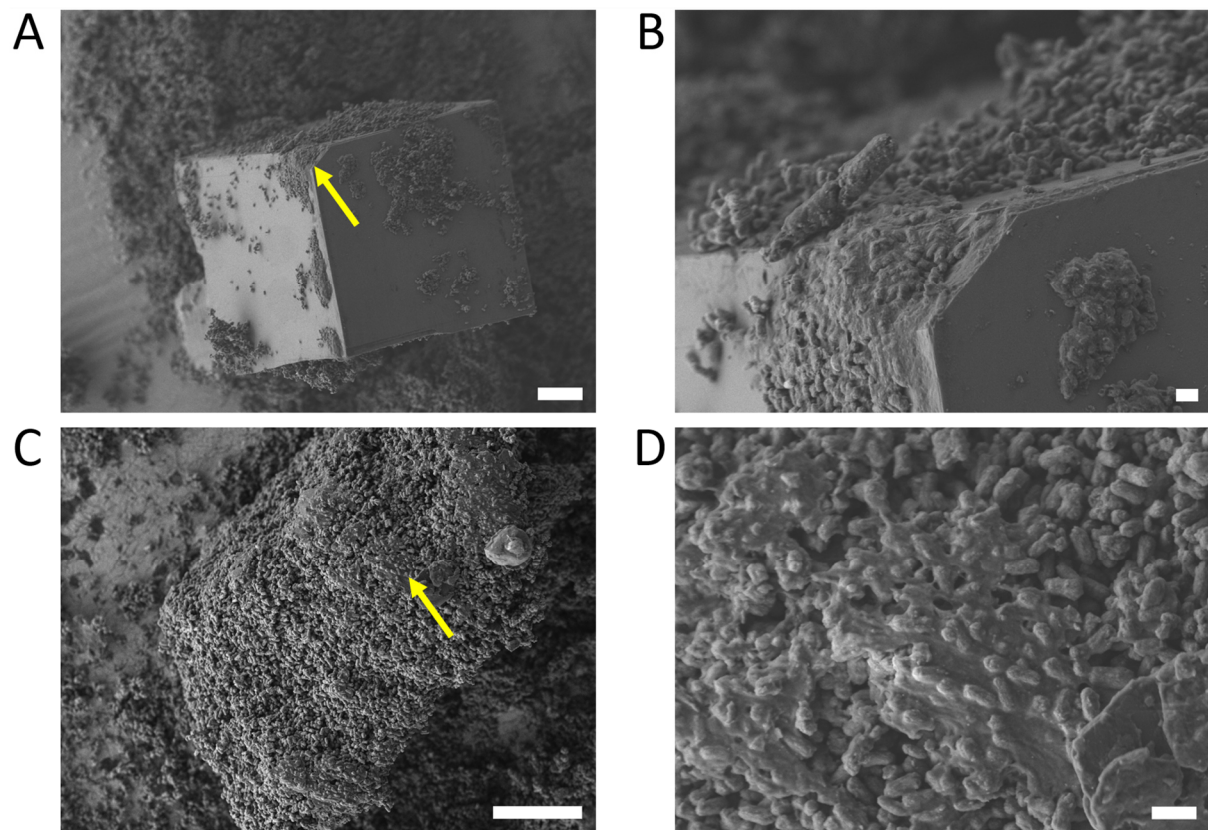
Figure S4.10   SEM micrographs of dried structures formed in mineralization experiments with seed crystals. Residues of fused liquid precursors were observed during the experiments. **a, b)** On partially coated calcite seed crystals, areas are visible at which droplets are fused together, illustrating their liquid-like properties. **c, d)** Observation of smooth structures formed on the surface of an agglomerate of precursor particles. The structures are similar to residues of liquid precursors involved during formation of biominerals[85] and nicely illustrate the liquid-like properties of the precursor-droplets. Scale bars are 10 µm (a,c) and 1 µm (b,d). Conditions for experiments are show in Table S4.2.
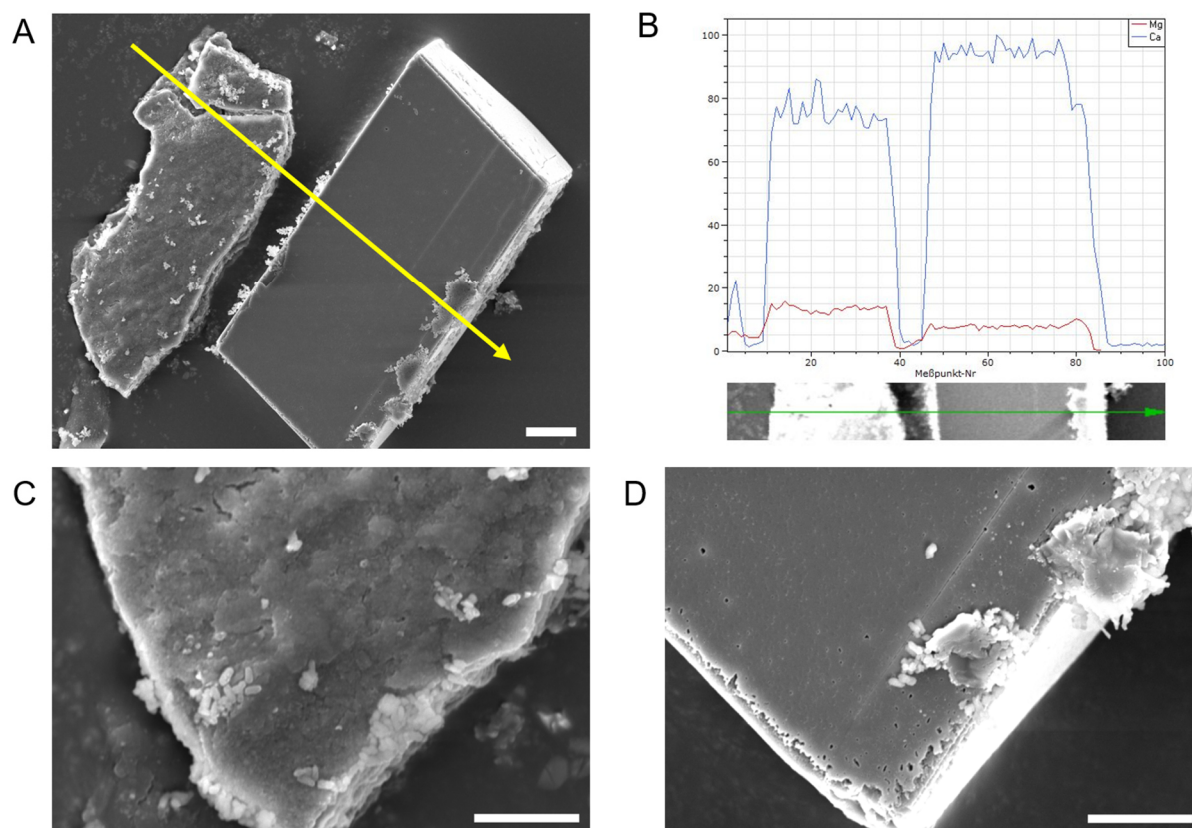
Figure S4.11   SEM micrographs of structures observed during material synthesis experiments from SCULPT precursors. a) Seed particle (right) covered with layer formed from fused precursor particles and a structure formed in absence of calcite seed (left) with a smooth surface. Scale bar 10 µm. **b)** EDX line scan across the structures (yellow arrow in a). Due to the use of Mg^{2+} in the synthesis of liquid-like mineral precursor (and the absence of Mg^{2+} in the calcite seed crystals) the Mg^{2+} content can be used to determine if structures were formed from the liquid precursor phase. EDX of the calcite crystal shows significant amounts of Mg^{2+}, confirming the presence of a smooth layer formed by the precursor phase on the surface. The structure on the left shows a higher $Mg^{2+}:Ca^{2+}$ ratio, indicating that the structure has indeed formed from the precursor phase. **c)** Higher magnification of the surface of the structure formed without seed crystal and **d)** layer formed by precursor particles on a calcite seed crystal (scale bars 5 µm). The structure without seed particle shows the great use of liquid-like mineral precursor for synthesizing mineral materials with smooth morphologies and in absence of seed crystals. Experimental conditions are show in Table S4.2.
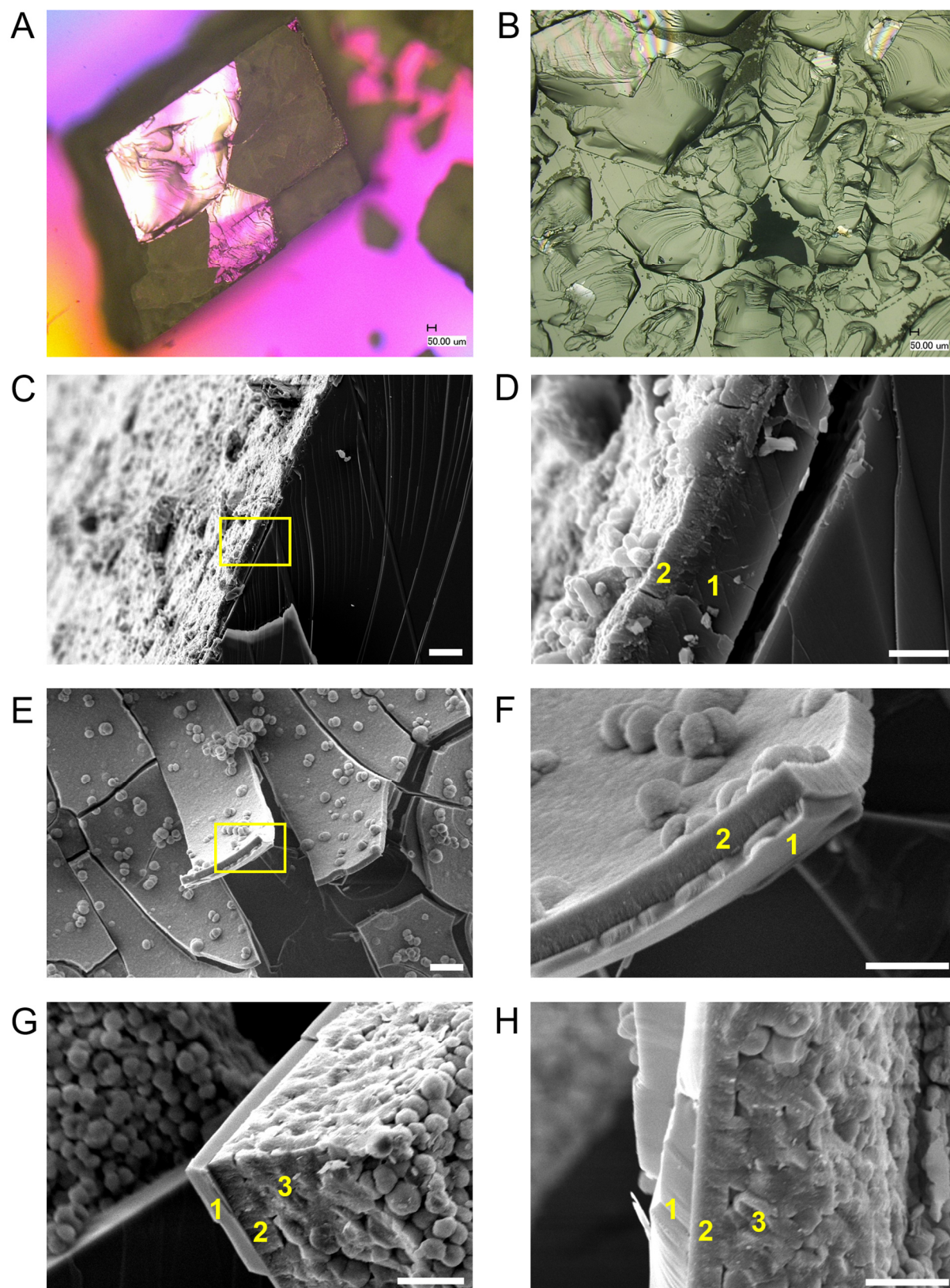
Figure S4.12   Investigation of calcite templates covered with a layer mineralized from the liquid-like precursor. a) Polarized light microscopy image of mineralized layer on a calcite seed crystal. To remove loosely attached particles from the surface of the seed crystal (see Figure S4.9), the crystals were treated in an ultrasonic bath. Usually, this process resulted in a rather smooth mineral coating of the crystal (see also Figure 4.3a). However, if the time of ultrasonication was extended, parts of the layer separated from the crystal, showing the single crystalline seed particle (light areas). **b)** The same

observation was also made on a larger 5 x 5 mm calcite wafer, where the mineralized layer could be almost fully removed after extended treatment in the ultrasonic bath. Interestingly, the surface of the parts at which the layer was removed are rough and the smooth calcite crystal facet from the original template were only visible in a few spots. The separation of the mineralized layer from the seed crystal was therefore closer investigated using SEM. **c)** SEM micrograph of a cross section of a mineralized layer on a calcite template and **d)** higher resolution (area highlighted in c). It is evident that the separation actually takes place in the calcite template (1), and the mineralized layer (2) stays attached to the template. This also fits to the observation in light microscopy (a, b), as the original calcite seed/template is damaged after the layer is removed and parts from the template are "ripped out". **e, f)** This effect was also visible in some samples without ultrasonic treatment, usually when higher concentrations of Mg^{2+}/polymer were used for the synthesis of the precursor. Interestingly, the mineralized layer (2) showed linear ordering perpendicular to the surface of the template (1), which was reported in $CaCO_3$ mineralization before.[206, 241] **g, h)** Indeed, upon close investigation of chips removed from the seed crystals this ordering was detected for a wide range of conditions. The ordered layer (2) is directly attached to the template (1) and usually areas without directional ordering (3) are observed as well. These results show that the mineralized layer is firmly attached to a crystalline mineral template. This is especially important in potential applications related to restoration, e.g. of marble, where a firm attachment of the deposited layer to the template is desired. Scale bars are c) 10 μm, d) 2 μm, e) 10 μm, f) 5 μm, g) 5 μm and h) 5 μm. Detailed experimental conditions are provided in Table S4.2.
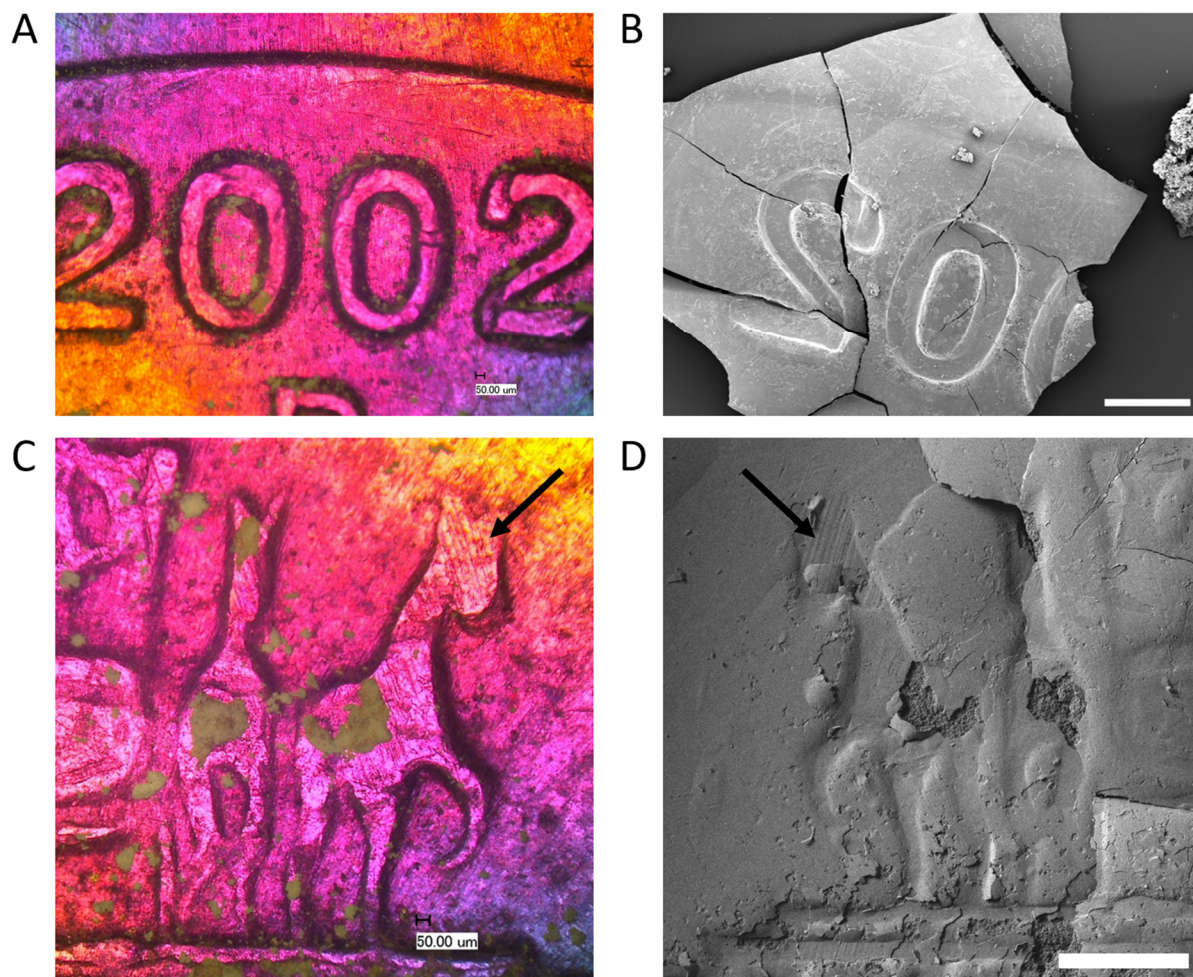
Figure S4.13   **Demonstration of use of precursor dispersion to produce mineral molds. a, c)** Light microscopy image of embossed structures on a coin (a: date of manufacturing of the coin, c: horse that is part of the "Quadriga" on top of the Brandenburg Gate embossed on the back of a German 50 ct coin) used as template and **b, d)** SEM micrographs of corresponding crystalline mineral "molds" synthesized via the liquid precursor phase. Scale bars in SEM micrographs are 500 μm. The mineral castings could be manufactured on mm² scale, and the embossing of the coin could be well reproduced. Even smaller features such as fine milling marks from the coin manufacturing process were well reproduced in the mineral casts (arrows in c, d). The cracks and damage visible in the mineral casts results from the removal of the mineral from the coin, as sometimes the mineral was sticking to the surface of the coin (also visible by the mineral residues left on the coin in a, c). Experimental conditions are shown in Table S4.2.
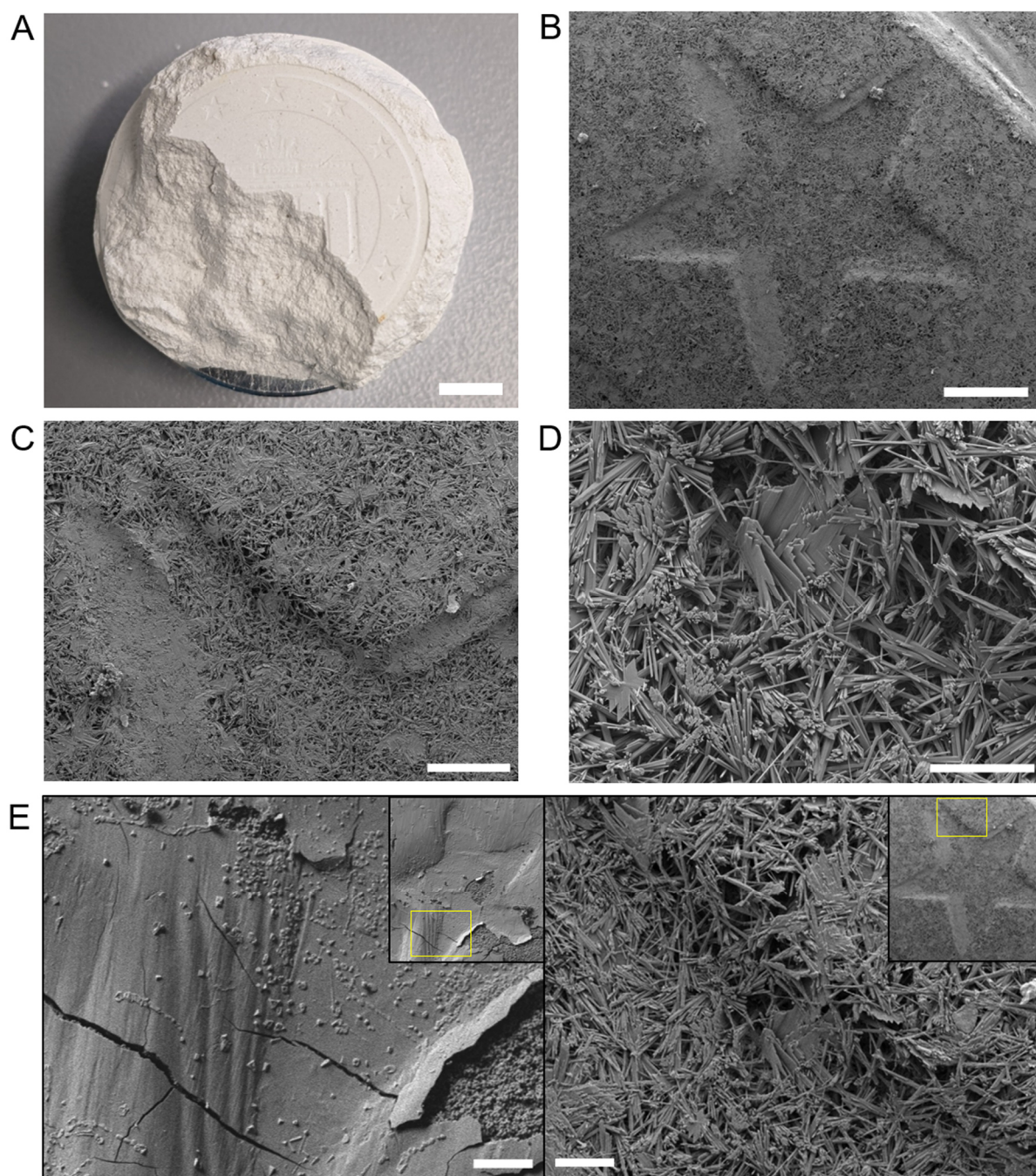
Figure S4.14 Manufacturing of a mineral cast of a German 50 ct coin using a commercial gypsum molding kit. a) Image of the gypsum cast. **b)** SEM image of a star in the gypsum cast and **c, d)** higher magnification of the surface structure of the cast. The gypsum crystals are clearly visible and lead to a rough surface of the cast. **e)** Comparison of calcium carbonate mineral cast produced from liquid-like precursor (left, see also Figure 4.3f) and gypsum mineral cast produced using a commercial gypsum molding kit (right). The same magnification is used to allow easy visual comparability. It is evident that a much higher resolution can be achieved using the liquid-like precursor-based molding procedure. While the possible resolution by the gypsum mold is limited to features on a scale of tens of μm, the resolution of the $CaCO_3$ mold is orders of magnitude higher, with even small scratches being resolved. Scale bars are a) 0.5 cm, b) 500 μm, c) 200 μm, and d,e) 50 μm.
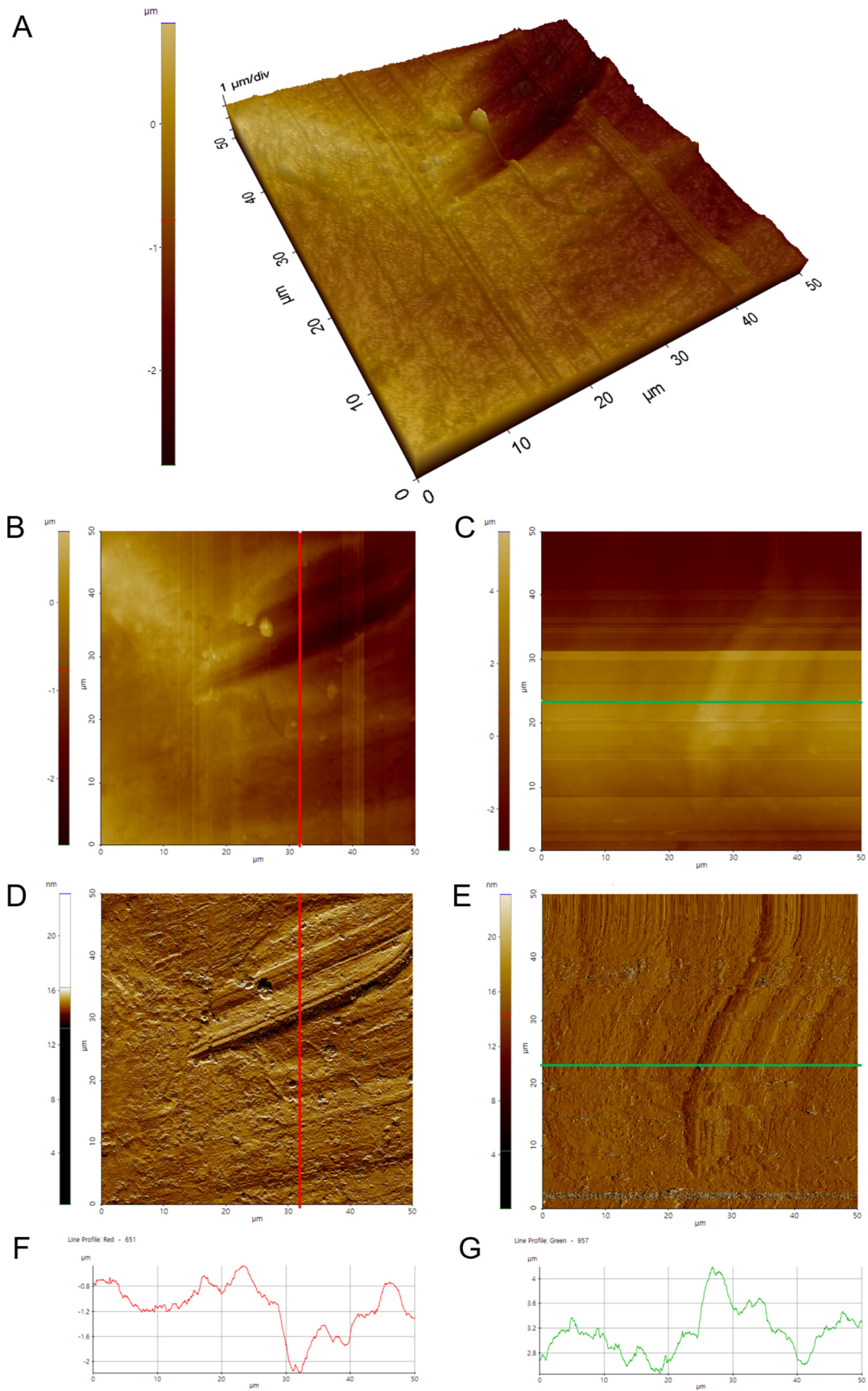
Figure S4.15   AFM investigations on mineral casts to investigate the resolution of the molding process. a) 3D atomic force microscopy (AFM) height scan and **b)** 2D height scan of a scratch on the surface of a 50 ct coin. **c)** 2D height scan of the corresponding feature on the mineral cast produced by

liquid-like precursor. **d, e)** Non-contact mode (NCM) amplitude scans of the areas are shown for better illustration of surface texture. The position of the performed line scans across the scratch/bump are indicated by red (coin) and green (mineral) lines. **f)** Raw data of AFM line scans across the scratch in the coin and **g)** across the bump in the mineral cast, respectively.
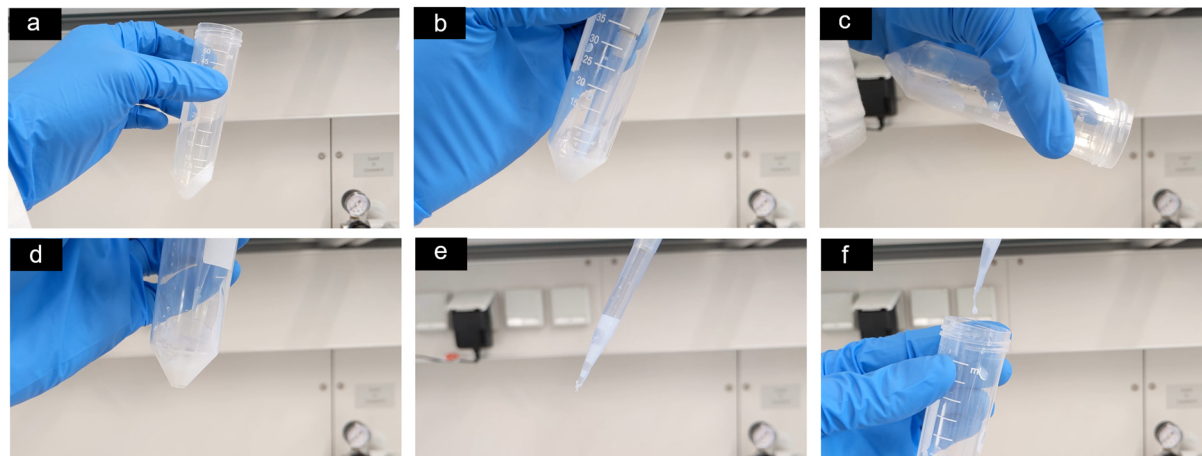
Figure S4.16   Handling and characteristics of the liquid-like mineral precursor dispersion isolated by centrifugation from titration procedure. The precipitate is initially solid, but liquifies when stirred. The precursor phase can then easily be applied, e.g. using an Eppendorf pipette. The images shown are taken from a movie that will be available as online supplementary material to the publication of this chapter.

4.6.2 Supplementary tables

Table S4.1 Experimental conditions for titration experiments. Exp. No.: Experimental Number; Fig.: Figure in which titration curves are shown; c: concentration; v: addition speed of solution; M: molecular weight; V_0: starting volume in the titration beaker. If materials were synthesized from the titration, all samples were isolated after 20,000 s by centrifugation (15 min at 7000 g). The standard conditions, which were used for the vast majority of mineral materials are listed on top (green)

Exp. No.	Fig. of titration curve	metal ion addition	NaOH addition	carbonate addition	PAA addition	PAA in starting solution	V_0 / mL	pH	plasticizer in starting solution
0	(Standard Conditions)	CaCl$_2$: $c = 0.5$ M MgCl$_2$: $c = 0.025$ M $v = 0.1$ mL/min	$c = 0.5$ M	$c = 0.75$ M $v = 0.1$ mL/min	$M = 5$ kDa; $c = 10$ g/L $v = 0.1$ mL/min	$M = 5$ kDa $c = 1$ g/L	50	10.65	PCE-375: $c = 4$ g/L
1	Figure 4.1b; Figure 4.1c	CaCl$_2$: $c = 0.5$ M $v = 0.1$ mL/min	$c = 0.5$ M	$c = 0.75$ M $v = 0.1$ mL/min	$M = 5$ kDa; $c = 10$ g/L $v = 0.1$ mL/min	$M = 5$ kDa $c = 1$ g/L	50	10.65	-
2	Figure 4.2a – Reference	CaCl$_2$: $c = 0.5$ M $v = 0.1$ mL/min	$c = 0.5$ M	$c = 0.75$ M $v = 0.1$ mL/min	$M = 5$ kDa; $c = 10$ g/L $v = 0.1$ mL/min	$M = 5$ kDa $c = 1$ g/L	50	10.65	PCE-375: $c = 4$ g/L
3	Figure 4.2a - Reference+Mg	CaCl$_2$: $c = 0.5$ M MgCl$_2$: $c = 0.025$ M $v = 0.1$ mL/min							
4	Figure 4.2a - higher c(Mg)	CaCl$_2$: $c = 0.5$ M MgCl$_2$: $c = 0.05$ M $v = 0.1$ mL/min			$M = 5$ kDa; $c = 5$ g/L $v = 0.1$ mL/min				
5	Figure 4.2a - higher c(PAA)	CaCl$_2$: $c = 0.5$ M MgCl$_2$: $c = 0.0125$ M $v = 0.1$ mL/min			$M = 5$ kDa; $c = 20$ g/L $v = 0.1$ mL/min				
6	Figure 4.2a - higher M(PAA)	CaCl$_2$: $c = 0.5$ M MgCl$_2$: $c = 0.025$ M $v = 0.1$ mL/min			$M = 100$ kDa; $c = 10$ g/L $v = 0.1$ mL/min				
7	Figure 4.2a - higher c(Mg) + M(PAA)	CaCl$_2$: $c = 0.5$ M MgCl$_2$: $c = 0.05$ M $v = 0.1$ mL/min			$M = 100$ kDa; $c = 5$ g/L $v = 0.1$ mL/min				
8	Figure 4.2b - Reference	CaCl$_2$: $c = 0.5$ M MgCl$_2$: $c = 0.025$ M $v = 0.1$ mL/min	$c = 0.5$ M	$c = 0.75$ M $v = 0.1$ mL/min	$M = 5$ kDa; $c = 10$ g/L $v = 0.1$ mL/min	$M = 5$ kDa $c = 1$ g/L	50	10.65	-
9	Figure 4.2b - PCE-375								PCE-375: $c = 4$ g/L
10	Figure 4.2b - Pantarhit RC550								Pantarhit RC550: $c = 4$ g/L
11	Figure 4.2b - Pantarhit								Pantarhit: $c = 4$ g/L
12	Figure S4.1a	CaCl$_2$: $c = 0.5$ M $v = 0.01$ mL/min	$c = 0.5$ M	$c = 0.75$ M $v = 0.02$ mL/min	-	-	40	10.0	-
13	Figure S4.1b	CaCl$_2$: $c = 0.5$ M $v = 0.01$ mL/min	$c = 0.5$ M	$c = 0.5$ M $v = 0.01$ mL/min	$M = 5$ kDa; $c = 1$ g/L $v = 0.01$ mL/min	-	40	10.0	-
14	Figure S4.1c	CaCl$_2$: $c = 0.5$ M $v = 0.01$ mL/min	$c = 0.5$ M	$c = 0.5$ M $v = 0.01$ mL/min	$M = 5$ kDa; $c = 1$ g/L $v = 0.01$ mL/min	$M = 5$ kDa $c = 0.5$ g/L	55	10.0	-
15	Figure S4.1d	CaCl$_2$: $c = 0.5$ M $v = 0.01$ mL/min	$c = 0.5$ M	$c = 0.75$ M $v = 0.02$ mL/min	$M = 5$ kDa; $c = 10$ g/L $v = 0.01$ mL/min	$M = 5$ kDa $c = 1$ g/L	55	10.0	-
16	Figure S4.2; Figure S4.3; Figure S4.4;	CaCl$_2$: $c = 0.5$ M MgCl$_2$: $c = 0.025$ M $v = 0.1$ mL/min	$c = 0.5$ M	$c = 0.75$ M $v = 0.1$ mL/min	$M = 5$ kDa; $c = 10$ g/L $v = 0.1$ mL/min	$M = 5$ kDa $c = 1$ g/L	50	10.65	PCE-375: $c = 4$ g/L
17	Figure S4.5a	CaCl$_2$: $c = 0.5$ M $v = 0.02$ mL/min	$c = 0.5$ M	-	$M = 5$ kDa; $c = 10$ g/L $v = 0.02$ mL/min	$M = 5$ kDa $c = 1$ g/L	55	10.0	-
18	Figure S4.5b	CaCl$_2$: $c = 0.5$ M $v = 0.01$ mL/min	$c = 0.5$ M	$c = 0.75$ M $v = 0.02$ mL/min	$M = 5$ kDa; $c = 10$ g/L $v = 0.01$ mL/min	$M = 5$ kDa $c = 1$ g/L	55	10.0	-
19	Figure S4.5c	CaCl$_2$: $c = 0.5$ M $v = 0.01$ mL/min	$c = 0.5$ M	-	-	-	55	10.0	-
20	titration curves not shown	CaCl$_2$: $c = 0.5$ M MgCl$_2$: $c = 0.025$ M $v = 0.1$ mL/min	$c = 0.5$ M	$c = 0.75$ M $v = 0.1$ mL/min	$M = 5$ kDa; $c = 5$ g/L $v = 0.05$ mL/min	$M = 5$ kDa $c = 1$ g/L	50	10.65	-
21	titration curves not shown	CaCl$_2$: $c = 0.5$ M MgCl$_2$: $c = 0.025$ M $v = 0.1$ mL/min	$c = 0.5$ M	$c = 0.75$ M $v = 0.1$ mL/min	$M = 5$ kDa; $c = 5$ g/L and $M = 100$ kDa; $c = 5$ g/L $v = 0.1$ mL/min	$M = 5$ kDa $c = 1$ g/L	50	10.65	PCE-375: $c = 4$ g/L
22	titration curves not shown	CaCl$_2$: $c = 0.5$ M MgCl$_2$: $c = 0.025$ M $v = 0.1$ mL/min	$c = 0.5$ M	$c = 0.75$ M $v = 0.1$ mL/min	$M = 5$ kDa; $c = 10$ g/L $v = 0.1$ mL/min	$M = 5$ kDa $c = 1$ g/L	50	10.65	PCE-375: $c = 15.6$ g/L
23	titration curves not shown	CaCl$_2$: $c = 0.5$ M $v = 0.05$ mL/min	$c = 0.5$ M	$c = 0.75$ M $v = 0.05$ mL/min	$M = 2$ kDa; $c = 10$ g/L $v = 0.2$ mL/min	$M = 5$ kDa $c = 1$ g/L	50	10.65	-
24	titration curves not shown	CaCl$_2$: $c = 0.5$ M $v = 0.05$ mL/min	$c = 0.5$ M	$c = 0.75$ M $v = 0.05$ mL/min	$M = 5$ kDa; $c = 10$ g/L $v = 0.2$ mL/min	$M = 5$ kDa $c = 1$ g/L	50	10.65	-

Table S4.2 Experimental conditions for mineral material synthesis. Fig.: Figure in which materials based on the listed conditions are shown; Synthesis Exp. No.: conditions used for synthesis of precursor dispersion as described in Table S4.1; ultrasonication: detail of ultrasonic treatment of precursor dispersion directly after centrifugation; water content: water content of precursor dispersion; precipitation time: time until individual experiment was stopped and minerals were washed (different types of mineralization experiments are described in experimental section 4.3.4). In addition, for selected samples the organic content and the amount of Mg^{2+} ions (relative to Ca^{2+}) in the final (crystalline) $CaCO_3$ mineral are shown

Fig.	Synthesis Exp. No. (Table S4.1)	ultra-sonication	water content / wt-%	precipitation / crystallization time	organic content (by TGA) / wt-%	Mg^{2+} content in product (by ICP-OES) / mol-%	comments
Figure 4.1d	0	-	81	-	-	-	-
Figure 4.1e	1	-	-	0 (directly dried in vacuum)	-	-	-
Figure 4.3a	8	2 min, 20% power	81	48 h (drying on air)	-	-	Calcite seed crystals placed in precursor dispersion
Figure 4.3b	20	2 min, 20% power	-	48 h	5	2	Calcite seed crystals placed in precursor dispersion
Figure 4.3c	21	2 min, 20% power	-	6 h	-	-	precursor dispersion was added on top of calcite wafer, 2 layers were applied
Figure 4.3d	7	2 min, 20% power	-	24 h in high humidity, then dried 3d on air	-	-	precursor dispersion was added on top of coin
Figure 4.3f-h	6	2 min, 20% power	-	24 h in high humidity, then dried 3d on air	-	-	precursor dispersion was added on top of coin
Figure S4.6b,c	23	-	-	0 (directly dried)	-	-	Experiment to investigate ACC-PAA composite material formation
Figure S4.6d-g	24	-	-	0 (directly dried)	10	-	Experiment to investigate ACC-PAA composite material formation
Figure S4.7	1	-	-	0 (black)	6	-	-
				24 h (blue)	3		
Figure S4.9b	0	-	-	-	-	-	Sample was directly placed in vessel after centrifugation and liquification
Figure S4.9c,d	20	2 min, 20% power	-	48 h, sample was dried on air	-	-	
Figure S4.8a,b	5	2 min, 20% power	-	3 h	-	-	precursor dispersion was added on top of calcite wafer
Figure S4.8c,d	5	2 min, 20% power	-	6 h	-	-	precursor dispersion was added on top of calcite wafer
Figure S4.8e	8	2 min, 20% power	-	40 h, sample was completely dry at isolation	-	-	precursor dispersion was added on top of calcite wafer
Figure S4.10a,b	22	2 min, 20% power	-	7 d	-	-	Calcite seed crystals placed in precursor dispersion, 2x centrifugation was performed
Figure S4.10c,d	8	2 min, 20% power	-	7 d	-	-	Calcite seed crystals placed in precursor dispersion
Figure S4.11	22	2 min, 20% power	-	7 d	-	-	Calcite seed crystals placed in precursor dispersion, 2x centrifugation was performed
Figure S4.12a	8	2 min, 20% power	-	48 h (drying on air)	-	-	Calcite seed crystals placed in precursor dispersion
Figure S4.12b	0	2 min, 20% power	-	48 h (drying on air)	-	-	precursor dispersion was added on top of calcite wafer
Figure S4.12c,d	4	2 min, 20% power	-	6 h	-	-	precursor dispersion was added on top of calcite wafer
Figure S4.12e,f	7	2 min, 20% power	-	4 d	-	-	precursor dispersion was added on top of calcite wafer
Figure S4.12g,h	8	2 min, 20% power	-	18 h	-	-	precursor dispersion was added on top of calcite wafer
Figure S4.13b,d Figure S4.15c-g	21	2 min, 20% power	-	24 h in high humidity, then dried 3d on air	-	-	precursor dispersion was added on top of coin
-	0	2 x, 2 min, 20% power	45	-	-	-	2x centrifugation was performed, water content was significantly reduced
-	8	2 x, 2 min, 20% power	77	-	-	-	In absence of PCE, the water content cannot be significantly reduced, even with multiple centrifugation steps

Chapter 5

Generality of Liquid-like Precursor Phases in Gas Diffusion-based CaCO₃ Synthesis

Contents Chapter 5

Record of Contribution

I performed all preliminary studies to the work, the majority of gas diffusion experiments, SEM analysis as well as corresponding data analysis and evaluation, figure design and writing of the original manuscript draft. Luisa V. Steingrube performed additional mineralization experiments including SEM analysis under my supervision and with my instructions. Prof. Dr. Denis Gebauer developed the project idea and supervised the experimental work.

Publication

This chapter was published in *CrystEngComm* **2021**, 23, 7938-7943 as a front cover. For the sake of readability, figures and materials taken from this publication are not marked additionally.

5.1 Abstract

The ammonia diffusion method (ADM) is one of the most widely used strategies for the bioinspired synthesis of minerals. Herein, we present investigations of the mineralization mechanism using an advanced ADM to solve the limitations of conventional ADM. This allows us confirming the presence of liquid calcium carbonate precursor species in additive-free and polymer-stabilized gas diffusion systems, indicating that liquid-liquid phase separated species exhibit sufficient kinetic stability to be detected. Time-dependent experiments reveal the role of these precursor phases during the early stages of the crystallization process, demonstrating that liquid calcium carbonate mineral precursors play an important role in the precipitation pathway and must be generally considered for the interpretation of gas diffusion experiments, with and without additives. This discovery poses an important step in the understanding of how minerals are formed, highlighting that nonclassical mineralization processes must be considered for material synthesis. Last, but not least, the advanced ADM may be useful for the exploration of the formation mechanism of other minerals than calcium carbonate that are also of broad interest to the materials chemistry community.

5.2 Introduction

The gas diffusion-based synthesis methods are a useful tool to synthesize calcium carbonate and to investigate the effect of additives on the precipitation process, thereby providing new insights into biomineralization and biomimetic synthesis strategies. [6] In recent years, the most widely used diffusion-based method, the ammonia diffusion method (ADM),[250-251] has been utilized to synthesize calcium carbonate minerals for addressing questions in various research fields. The investigation of nucleation and crystal growth processes,[252-253] additive effects on the formation of calcium carbonate,[58, 254-256] the synthesis and characterization of nanocomposites,[257-263] investigations regarding changes in material properties of crystals,[264] as well as syntheses of composite particles for potential use in cancer therapy[265] have been carried out using ADM. In addition, ADM has been used to investigate and characterize polymer-induced liquid-precursor (PILP) phases.[28, 109] Liquid precursor phases are essentially amorphous minerals with such a high degree of hydration that they appear and behave as a liquid and feature a liquid-liquid phase boundary to the mother solution. The liquid precursor species can densify to gel-like or solid amorphous calcium carbonates upon the loss of water. PILP phases are useful for explaining the complex "molded" non-equilibrium mineral morphologies found in organisms such as sea-urchins and present a promising way to new materials, for example for potential uses in biomedical applications[266-267] or as construction materials.[206] Recent results indicate that PILP phases are rather polymer-stabilized than polymer-induced phases, as liquid-liquid binodal demixing and the formation of dense liquid phases have been detected in additive-free aqueous calcium carbonate systems.[18, 22] This can be explained by nonclassical nucleation models. It was shown that the formation of liquid

intermediates in absence of additives is defined by soluble, thermodynamically stable prenucleation clusters (PNCs),[19] where ion association is driven by the entropy gain of releasing hydration waters.[18] If supersaturation is increased and the corresponding liquid-liquid binodal limit is exceeded, PNCs can become phase-separated nanodroplets due to decreased cluster dynamics upon increased calcium carbonate coordination numbers within the clusters. The formed nanodroplets can further aggregate to form larger, dense liquid precursor phases. It is still debated why certain additives can stabilize the liquid precursors. Current results indicate that additives, such as polycarboxylates or Mg^{2+} ions, favor the incorporation of water into the liquid and amorphous structures, preventing their dehydration toward formation of solid amorphous calcium carbonate (ACC).[22, 103] An alternative explanation could be the favorable incorporation of bicarbonate into the liquid phase.[31, 196]

As mentioned above, liquid-liquid phase separation (LLPS) was proven numerous times in case of calcium carbonate, with, but also without additives.[22, 31-32, 268] However, liquid precursor phases received minor attention in the discussion of diffusion-based mineralization experiments so far, even if their liquid character is often useful for rationalizing results that are difficult to explain based on classical nucleation mechanisms.[4] Due to their fast transformation into more stable phases, such as solid ACCs or (metastable) crystals, liquid precursors are difficult to detect. Experimental strategies for the investigation of liquid mineral phases include cryogenic TEM studies,[23, 30, 268] NMR[31] and THz spectroscopy.[22] Another strategy is the investigation of the characteristics of solid amorphous phases that emerge from the dehydration of the initially liquid phases.[269] This strategy is also employed in this work using ADM as method to synthesize calcium carbonate. Although ADM is not a new method and has been used for decades,[270] it was previously not employed for investigating transient precursor phases without additives, as usually volumes of several mL are used, resulting in low concentrations of the transient species which complicates their isolation and investigation. In addition, the transient species rapidly transform before it is possible to isolate them in conventional ADM. Due to these limitations, so far, ADM has been mainly used to investigate more stable amorphous and crystalline minerals. In this work, we present several key advancements to solve these limitations of ADM. The experiments are performed in droplets, thereby reducing the time necessary to remove the liquid and dry the transient species, thereby reducing the likelihood of their transformation before they can be investigated. In addition, performing experiments on wafers allows the transfer and investigation of all species present in the reaction solution at a certain time in the experiment. Another advantage of the mineralization in droplets is their beneficial economy: only small amounts of, potentially expensive, additives are necessary.

Our results confirm and visualize the occurrence, properties and kinetic stability of liquid calcium carbonate precursor species employing ADM, in presence and absence of additives, underlining their general importance for the interpretation of ADM-based experiments. Furthermore, other carbonate minerals can be synthesized using ADM,[271-272] where the

mineralization mechanism and the potential occurrence of liquid intermediates can be studied using the experimental strategy presented herein in the future.

5.3   Experimental section

5.3.1   Gas diffusion mineralization experiments

The experiments were carried out using 24 cell culture microwell plates. Each chamber was covered with a lid with a hole of 0.5 mm in diameter. Inside each chamber, a 5 x 5 mm Si-wafer (TED PELLA, Inc.) was placed, on which 20 µL of calcium chloride solution (prepared by dilution of 1 M stock solution, VWR AVS Titrinorm) was pipetted. Depending on the type of experiment, droplets with different $CaCl_2$ concentrations (10 mM to 40 mM) and PAA concentrations (0 g/L to 1 g/L, Sigma-Aldrich, poly(acrylic acid) DDMAT terminated, $M = 6800$ g/mol) were used. For experiments longer than 2 h, a 5 x 5 mm glass wafer (cut from VWR microscope slides) was used as a substrate. Then, 0.5 g of freshly ground ammonium carbonate (Sigma-Aldrich, $\geq 30\%$ NH_3-basis) was placed inside a petri dish with a cap containing three holes (1 mm diameter) inside a desiccator (2.4 dm^3 internal volume). The well-plate with the $CaCl_2$ solutions was placed on top of the porcelain plate in the desiccator and the desiccator was closed. Experiments ran from 30 min up to 24 h, as stated. Once the experiments were finished, the well plate was removed from the desiccator and the solution was immediately removed using filter paper. Removal of the solvent usually took no longer than 5 min. The wafers were dried on air overnight and characterized. Each experiment was performed at least twice to confirm reproducibility. All aqueous solutions were prepared using Milli-Q water that was degassed by bubbling nitrogen through the solution overnight.

5.3.2   Characterizations

Scanning electron microscopy (SEM) images of the dried wafers were recorded using a JEOL JSM-6610 SEM. The wafers were coated with gold (5-10 nm thick layer) prior to analysis. High resolution SEM images (Figure S5.2 and Figure S5.11b,c) were recorded using a JEOL JSM-6700F SEM without coating the sample prior to analysis. Attenuated total reflectance Fourier-transform infrared (ATR-FTIR) spectra were measured using a BRUKER Tensor 27 FTIR spectrometer. The wafers with the calcium carbonate precipitates were directly put on the ATR unit of the spectrometer. The respective wafer (Si or glass) was used as a background reference. Light microscopy was performed on a Keyence VHX-600 Digital Microscope equipped with a VHZ100UR Zoom Lens.

5.3.3   Carbonate-free reference experiments

Carbonate free experiments were carried out as reference experiments. In regular experiments,[58] $(NH_4)_2CO_3$ decomposes to CO_2 and NH_3 which then diffuse into the calcium chloride solutions raising the pH value. As raising the pH value will lead to deprotonation of PAA and possibly to the precipitation of coacervates,[273-274] gas diffusion experiments with pure NH_3 were carried out to simulate the increase of pH in the solution in absence of CO_2. All solutions were prepared using Milli-Q water that was degassed by bubbling N_2 through the solution overnight. All solutions were stored and handled under nitrogen atmosphere during the execution of the experiments.

Glass wafers (5 x 5 mm) were placed on the bottom of a 200 mL round bottom flask that was flushed with N_2 for 10 minutes. Then, with the N_2 stream running, 20 µL of solutions containing $CaCl_2$ (20 mM) and different concentrations of PAA (0 g/L to 1 g/L) were placed on the wafers using an Eppendorf pipette. Next to the wafers, 0.5 g of ammonium nitrate was placed inside a small dish and 0.5 mL of 1 M NaOH (1 M stock solution, Roth) was added to the NH_4NO_3. Then, the N_2 stream was stopped and the flask closed. After the desired reaction time (1-5 h), the experiments were stopped, and the solutions were removed using a filter paper whilst still being under N_2 atmosphere. The wafers were dried in vacuum overnight and characterized using SEM (Figure S5.1). No film was visible in any experiment, although for high polymer concentrations the solutions turned turbid.

5.3.4   Manipulation of PAA-stabilized calcium carbonate films

Experiments were carried out to try to manipulate and isolate the PAA-stabilized $CaCO_3$ film. Therefore, 1 h experiments with 20 mM $CaCl_2$ and 1.0 g/L PAA were carried out on glass wafers as described before. For these conditions, the film was visible by eye and manipulation of the film could be investigated using light microscopy (Figure S5.13 and Figure S5.14).

5.4   Results and Discussion

5.4.1   Characterization of polymer-stabilized precursor phases

ADM makes use of CO_2 diffusion into droplets of calcium chloride solution (Figure 5.1).[58] After the desired reaction time, the solvent is removed, thereby transferring all species formed near or on the inner surface of the droplet, where calcium carbonate supersaturation is the highest, but also any species from the bulk of the droplet onto the wafer. As no further washing is performed, characterization of the dried wafers by SEM allows the investigation of all species present at this moment in the experiment. First, the effect of the polycarboxylate poly(acrylic acid) (PAA) on the precipitation of calcium carbonate was investigated. The influence of key

parameters such as reaction time (1 h to 24 h), starting calcium chloride concentration (10 mM to 40 mM) and PAA concentration (0.01 to 1 g/L) was examined. Note that the formation of Ca-PAA coacervates and hydrogels is not relevant in the systems of this work (Figure S5.1). For all investigated PAA concentrations, one-hour experiments showed the formation of a macroscopic film on the surface of the droplet that was visible by eye (Figure 5.2a). ATR-FTIR characterization (Figure 5.2b) of the dried film on the wafer shows that the precipitates are predominately ACC, confirmed by the band at 861 cm^{-1}. The dried film was further investigated using SEM (Figure 5.2c and d), showing thin films of several 100 μm in their lateral dimension.
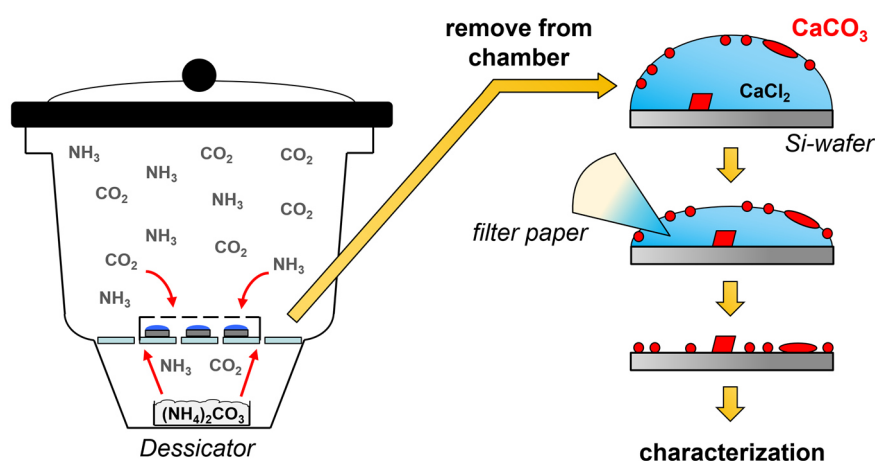
Figure 5.1   Schematic view of the droplet-based ammonia diffusion method. Experiments are performed in 20 μL CaCl$_2$ droplets on silica wafers. After the reaction is finished, the solvent is quickly removed using a filter paper. The precipitates on the wafer are then dried and investigated.

For high calcium and low PAA concentrations, particles were visible in addition to the film (Figure 5.2d), showing the limited stability of the films for lower additive/calcium ratios. The morphology of the dried film showed differences in the top surface and the bottom surface of the film (Figure S5.2). The formation of liquid mineral phases on the surface of the droplet was expected, as PAA is known to stabilize PILPs,[106, 206] however, the extent and macroscopic visibility of the liquid phase was not anticipated. The PILP films broke apart or dissolved when they were manipulated (Figure S5.3 and Figure S5.13) or upon attempts to isolate the films in their liquid state (Figure S5.14). This is due to the liquid phase being only stable when in equilibrium with the mother phase. Liquid-liquid coexistence relies on the presence of two phases, so if the dense liquid is attempted to be isolated, it will fall apart.[58] The film can only be isolated when quickly dried and transferred into the solid state. Nevertheless, the liquid properties are evident if the structures of dried liquid phases are closely examined (Figure S5.4).
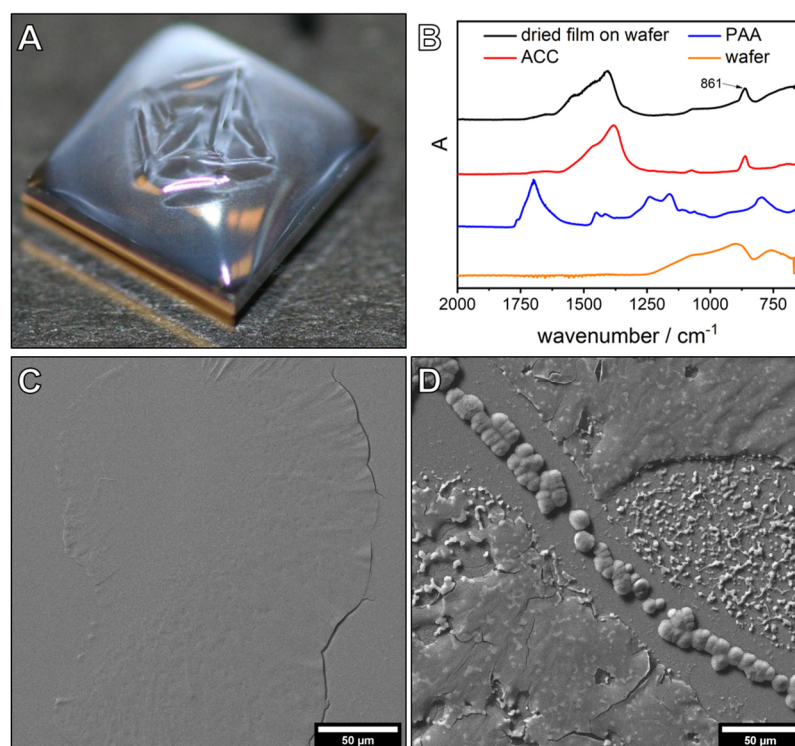
Figure 5.2   Characterization of wafers after 1 h gas diffusion experiments with PAA. a) The film is visible by eye, here shown for a PAA concentration of 0.5 g/L. **b)** ATR-FTIR spectra show that the precipitates on the wafer are ACC, visible by the band at 861 cm^{-1}, even for the highest additive concentration of 1 g/L. For comparison, spectra of pure ACC, pure PAA and the wafer are shown as well. Experimental conditions: 2 h gas diffusion experiment using 20 mM CaCl$_2$ solution with 1 g/L PAA. **c)** SEM image of the dried film on the wafer using 10 mM CaCl$_2$ and 0.01 g/L PAA and **d)** using 40 mM CaCl$_2$ and 0.01 mg/L PAA.

Concentration dependent experiments confirmed the stabilizing effect of PAA on amorphous structures,[103] as for polymer contents higher than 0.5 g/L no crystalline particles were visible in 1 h experiments (Figure S5.5). Time dependent experiments were used to resolve the evolution of the PILP film (Figure S5.6), showing that with increasing PAA concentration, films were detectable for several hours. If reaction times were long enough, however, the structures eventually crystallized and formed calcite particles with different morphologies and superstructures (Figure S5.6). In several experiments, semi-spherical calcite particles were detected (Figure S5.7), indicating that growth of the particles occurred from the precursor film, which can act as a substrate for particle growth, into the solution, accompanied by the densification of the precursor toward the crystalline phase. When the experiments were stopped before the growth into spherical particles was completed, semi-spherical structures were visible. Also, ACC particles already precipitated on the wafer when the film was still present on the surface of the solution (Figure S5.15). This could be due to simultaneous formation of ACC in the volume of the droplet, which then precipitates, or due to the release of ACC particles from the film into the solution.

5.4.2   Liquid precursor phases in absence of additives

The previously described conditions of gas diffusion-based $CaCO_3$ synthesis in droplets apparently favor the formation of continuous liquid precursor films. As liquid phases are also expected to exist in the additive-free calcium carbonate system,[18, 22] we investigated the crystallization without PAA using the same conditions. The PNC pathway allows the quantitative description of liquid-liquid phase separation (LLPS) in the aqueous calcium carbonate system.[18] We applied this quantitative model to estimate the time required for LLPS in gas diffusion systems described here (see supplementary discussion in section 5.6.1). Recent studies showed that the liquid-liquid binodal limit is defined by the solubility threshold of proto-structured ACCs.[22] Therefore, in general, from the solubility product of this ACC[19] and the known starting concentration of $CaCl_2$, the amount of carbonate necessary to exceed the binodal limit was calculated. Then, from previously established effects of different parameters on gas diffusion experiments,[251] the carbonate addition rate due to CO_2 in-diffusion was calculated. For the given experiments the PNC model predicted that liquid-liquid phase-separation takes place on the timescale of 30 minutes, which was experimentally investigated.

The 1 h additive-free experiments yielded many different structures and particles (Figure 5.3a and Figure S5.8). Most importantly and as predicted by the PNC model, also without polymeric additives films of several 100 µm in diameter with smooth surfaces at the edges were visible (Figure 5.3b). These films were not observed close to amorphous and crystalline particles (Figure 5.3a), which indicates that they served as the precursor phase to the denser amorphous and crystalline structures, and that the transformation took place by a dissolution-reprecipitation mechanism.[38] The presence of calcium carbonate in the films was supported by EDX (Figure S5.9). The large size of these films implies that a considerable amount of the calcium carbonate in the system was present in the form of these liquid precursors. It must be emphasized that the structures visible in the SEM are dried, solid residues of the once heavily hydrated species,[36] formed on the surface of the droplet upon blotting and quick drying of the mother solution. The native state and the dynamics of these species could not be assessed due to their rapid transformation to more stable phases. However, the dried films allowed insights into the characteristics and transformation mechanisms of the precursor species. It was observed that the film covered crystalline particles like a cloth (Figure 5.3c), again visualizing the initially liquid- or gel-like properties of the detected phase. Time-dependent experiments showed the formation and evolution of the film (Figure 5.3d-f). After 30 minutes, films of several hundred µm in their lateral dimension were visible (Figure 5.3d). In some spots, the precursor phase already formed denser structures, resulting in holes in the film (Figure S5.10). In 1 h experiments, additional amorphous and crystalline structures were present (Figure 5.3e and Figure S5.8) whilst after two hours, only calcite particles were visible (Figure 5.3f). The transformation of the film into particles was recorded (Figure S5.11), indicating a densification of the film toward the formation of 50 to 150 nm sized particles. The amorphous particles then

dissolved and reprecipitated to form larger amorphous structures with a size of 10 to 50 µm (Figure S5.8). The film breaking apart to particles is a rather compelling proof for the liquid nature of the precursor structures based on thermodynamics of phase transformations.[58] It would be thermodynamically impossible for a macroscopic, solid ACC film of 100 nm thickness to transform into smaller ACC nanoparticles, as this would correspond to anti-Ostwald ripening. It is possible for liquids, however, as liquids can change their composition drastically and macroscopic dense liquid films are metastable with respect to ACC nanoparticles.
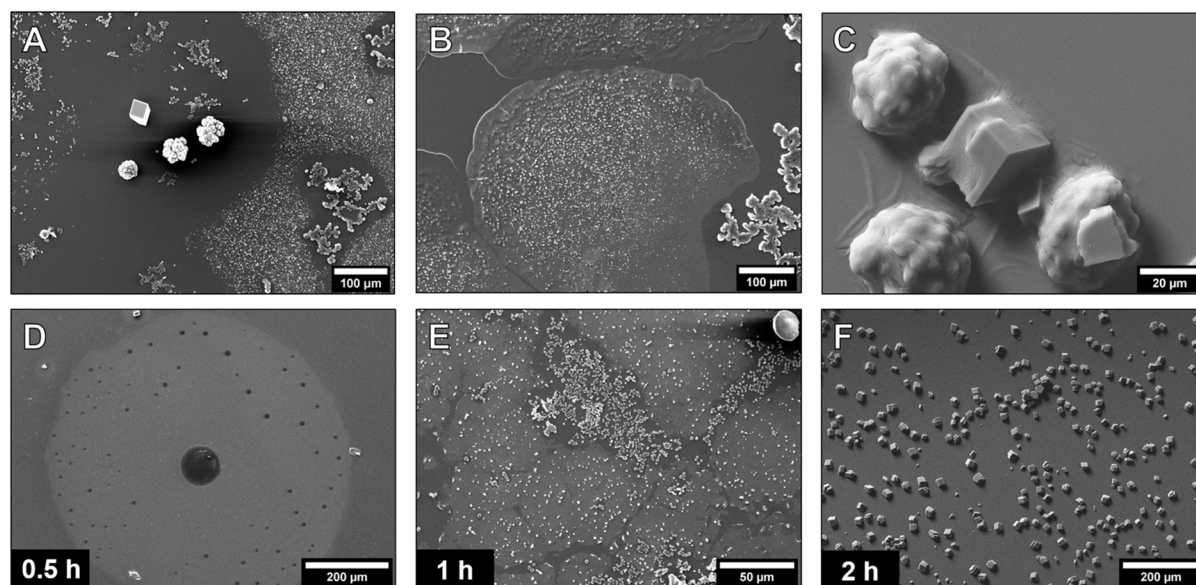
Figure 5.3 SEM micrographs for 1 h additive-free gas diffusion experiments. a) Different structures are visible on the wafer. No films or smaller particles are visible around larger amorphous or crystalline structures, therefore, likely a dissolution-reprecipitation mechanism occurs. **b)** In many areas of the wafer, large films with smooth edges were detected. Closer to the center of the spherical structures, smaller particles are visible. **c)** Calcite and vaterite particles are covered by the film. **d-f)** Time-dependent development of the precursor films in additive-free experiments using 10 mM $CaCl_2$. The used concentrations are a) 10 mM b) 20 mM and c) 40 mM $CaCl_2$.

When the experimental conditions were changed, e.g., droplets with a larger volume were used, no large films were visible by eye in additive-stabilized systems. This indicates that droplet surface area, surface tension, diffusion barriers and used concentrations determine whether large precursor films are detectable or not, which might be the reason why this effect was not reported in the literature before. Even if no large films are detected, LLPS is still expected to take place in gas diffusion experiments, although the liquid species could occur in different forms, such as dispersed liquid (nano-)droplets (Figure 5.4).[24, 151]
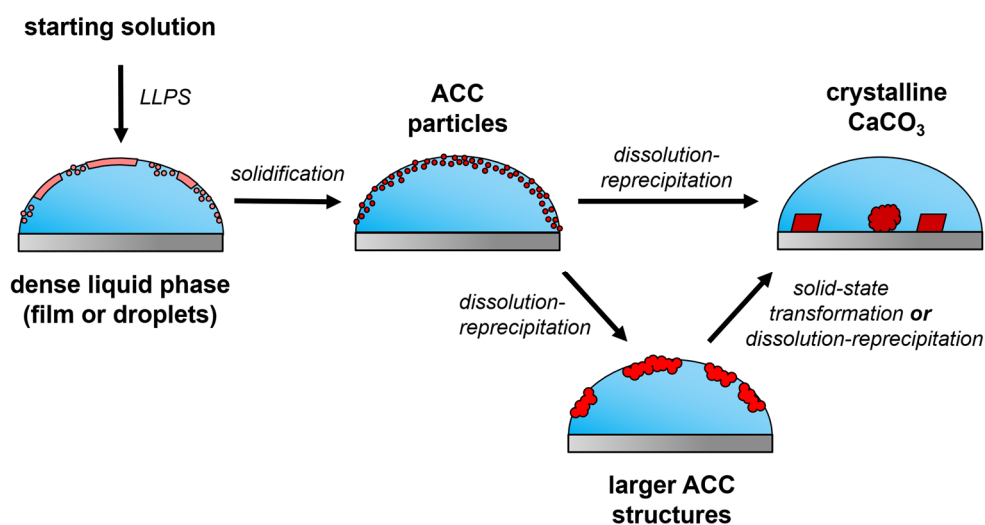
Figure 5.4   The proposed mechanism of CaCO₃ crystallization in diffusion-based experiments. The first phase separation in the system is LLPS forming a dense liquid mineral phase. This phase can appear as a film or droplets, depending on the experimental conditions. The liquid precursor phase then solidifies to ACC particles, which in turn dissolve to form larger amorphous structures or directly the crystalline polymorphs. In parallel to the processes shown, ACC particles could form in solution, or crystalline calcium carbonates on the surface of the wafer can occur (not shown in the scheme). Solid-state transformations were also observed for dried ACC precipitates (Figure S5.12).

5.5   Conclusions

Our results confirm and visualize the dense liquid calcium carbonate precursor phase in the absence (and presence) of additives. This is possible due to the precursors exhibiting sufficient kinetic stability in gas diffusion-based syntheses to be detected. Thus, it is important to consider liquid precursor species for the discussion of diffusion-based experiments, even if no stabilizing additives are present. Liquid species and their interactions with additives open a new perspective on crystallization processes of minerals and beyond. Exploiting the liquid properties of mineral precursors can be used to synthesize new materials. In addition, we present an advancement of the ammonia diffusion method that can be employed to address various questions in carbonate material syntheses. Besides detection and isolation of transient phases, this method can help to optimize synthesis conditions in ADM by allowing efficient screening of large arrays of experimental parameters and allows the economical use of additives due to the low volumes of the experiments.

5.6 Supplementary Information

5.6.1 Calculation of time of LLPS in gas diffusion experiments

It is demonstrated how the time of liquid-liquid phase separation (LLPS) in gas diffusion-based experiments can be estimated in case of the aqueous calcium carbonate system.

Previous results showed that the liquid-liquid binodal limit is defined by the solubility threshold of proto-structured ACCs.[22] In the following, it is assumed that the pH value of the solution quickly reaches a constant value of 9.8 in the first few minutes after the start of the experiments, as previously established.[251]

From the known starting concentration of $CaCl_2$ (10 mM) and the solubility product of ACC (3.8×10^{-8} M^2)[19] the amount of carbonate necessary to cross the binodal limit can be calculated according to (expressed in concentrations):[120]

$$c_{\text{free}}(CO_3^{2-}) = \frac{IAP(\text{ACC})}{c_{\text{free}}(Ca^{2+})} \tag{S5.1}$$

The calculated free carbonate concentration is $c_{\text{free}}(CO_3^{2-}) = 3.8$ µM. From this carbonate concentration and the estimated carbonate addition rate $d[CO_3]/dt$ due to in-diffusion in the vapor diffusion experiment, we can estimate the time at which LLPS occurs.

Meldrum et. al. investigated the effects of different parameters on the gas diffusion.[251] They determined $d[CO_3]/dt$ to be linear dependent on the solution surface area, exponentially dependent on the cross sectional area of diffusion barriers and on the initial calcium concentrations, and independent of the amount of $(NH_4)_2CO_3$ used for the experiments. In addition, they provided carbonate addition rates for conditions similar to our experiments, with 25 mM $CaCl_2$ and a 2.6 dm^3 desiccator used for the gas diffusion experiments.

Based on these investigations, the carbonate addition rate was calculated. The surface area of the droplets was estimated using a hemispherical droplet with a radius of 2.5 mm. As described in experimental section 5.3.1, two diffusion barriers were used in our experiments, the first barrier has 3 holes of 1 mm diameter and the second one has one hole of 0.1 mm diameter for each chamber. The cross-sectional area of the first barrier is therefore more than 2 orders of magnitude larger than the second barrier (2.4 mm^2 vs. 7.8×10^{-3} mm^2). Due to the exponential dependency of cross-sectional area and diffusion speed, the second diffusion barrier can be seen as the rate determining step in this system and the first barrier was not used for the calculations.

Using these assumptions, the provided general conditions, and the relationships of parameters and carbonate addition rate, we determine $d[CO_3]/dt = 0.14$ µM/min. The diffusion of 3.8 µM carbonate in the droplet therefore roughly takes **28 minutes**.

Using this estimation, we predict that the phase separation takes place on the timescale of minutes. It also agrees with our results, as no film was detected if experiments are stopped after 5 min (data not shown) and precursor films were detectable in 30-minute experiments (Figure 5.3c).

5.6.2   Supplementary figures
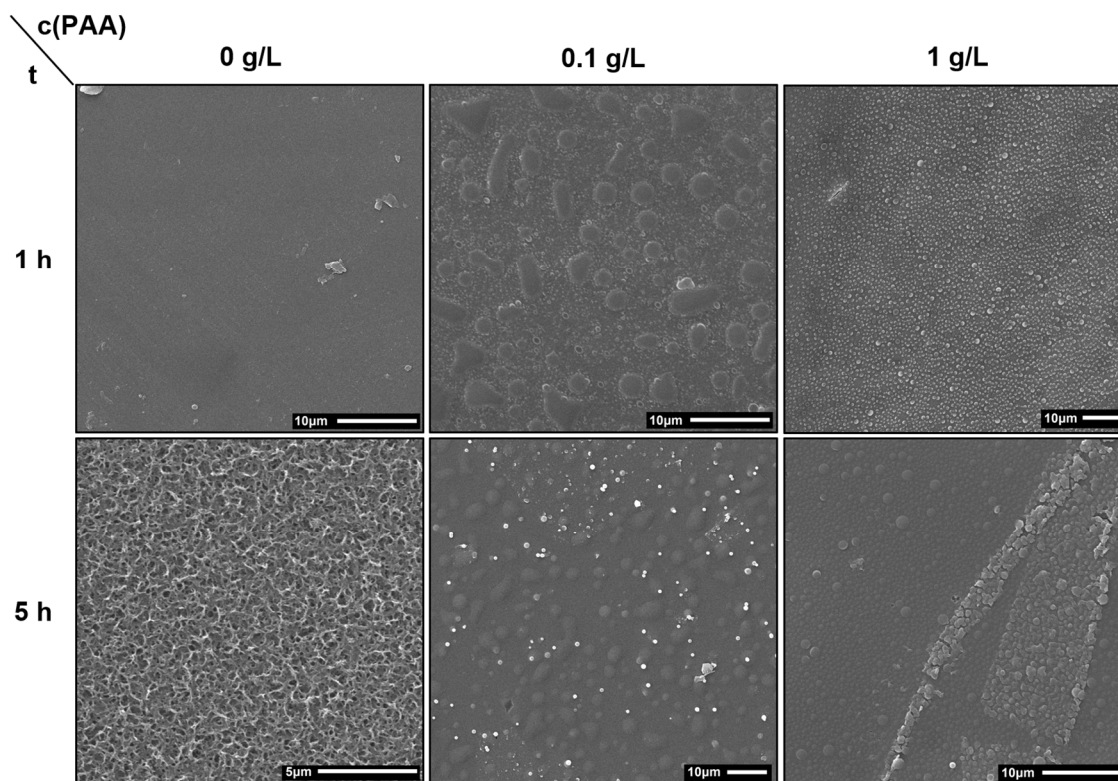
Figure S5.1 SEM characterization of carbonate free reference experiments. Experiments were performed using 20 mM $CaCl_2$ concentrations and experiments were carried out for 1 h to 5 h. In the experiments, no film was detected, although for PAA concentrations higher than 0.01 g/L, the solution turned turbid, indicating the precipitation of a Ca-PAA coacervate. The precipitated coacervates possess a different structure compared to the species found in the regular experiments with carbonate, as they primarily form droplets with irregular shapes, instead of spherical particles or smooth films. Therefore, for the PAA concentrations used in this work, the coprecipitation of coacervate cannot be excluded, but the primary phase in all cases is $CaCO_3$, as confirmed by ATR-IR (Figure 5.2b), showing that the formation of coacervates only plays an insignificant role in this work.
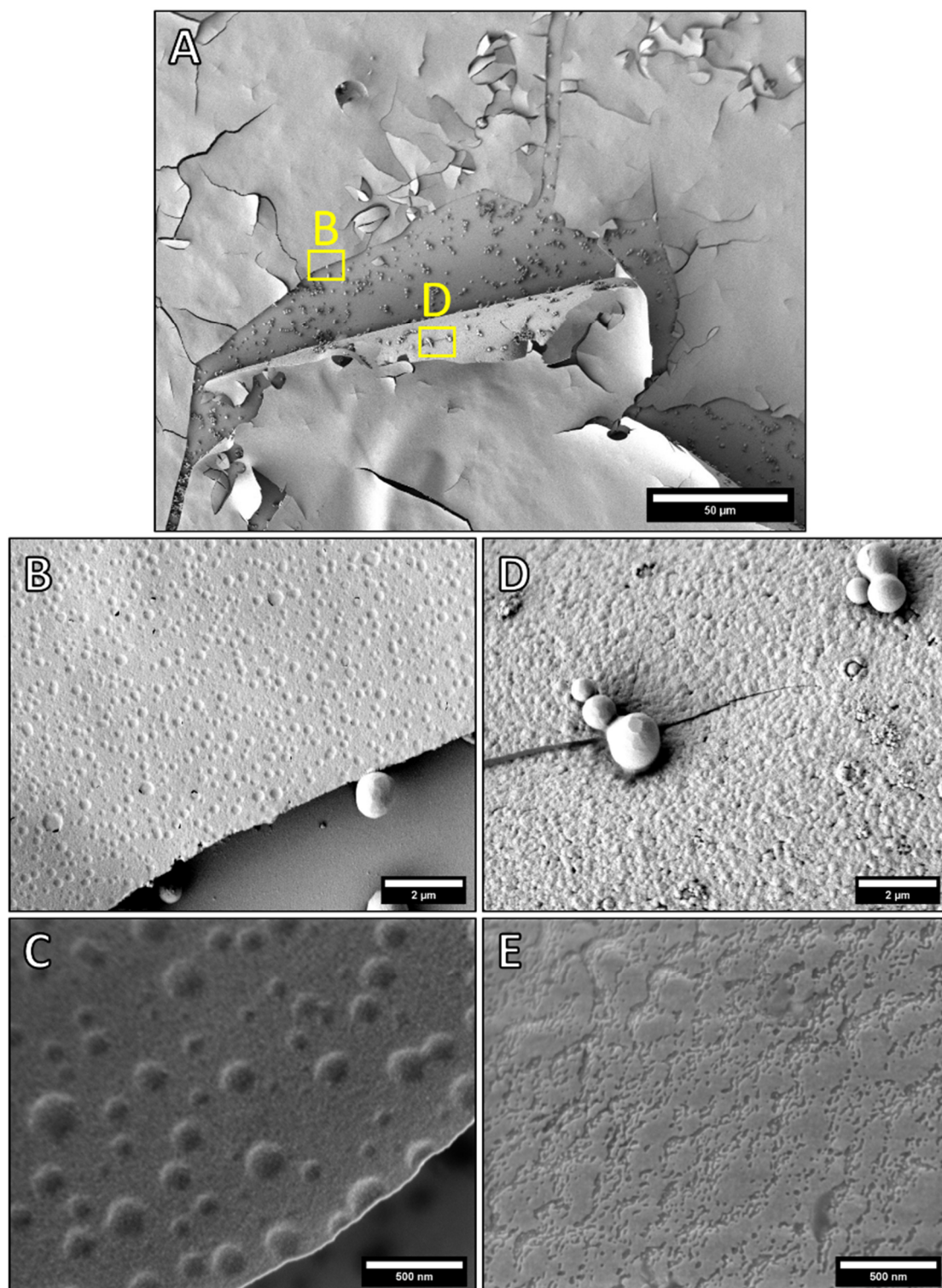
Figure S5.2 High resolution SEM micrographs of the dried liquid-like precursor film. a) Overview SEM image of the dried film. The difference in morphology of the **b, c)** top surface and **d, e)** bottom surface of the film is visible. Experimental conditions: 2 h gas diffusion experiment using 20 mM $CaCl_2$ with 0.1 g/L PAA.
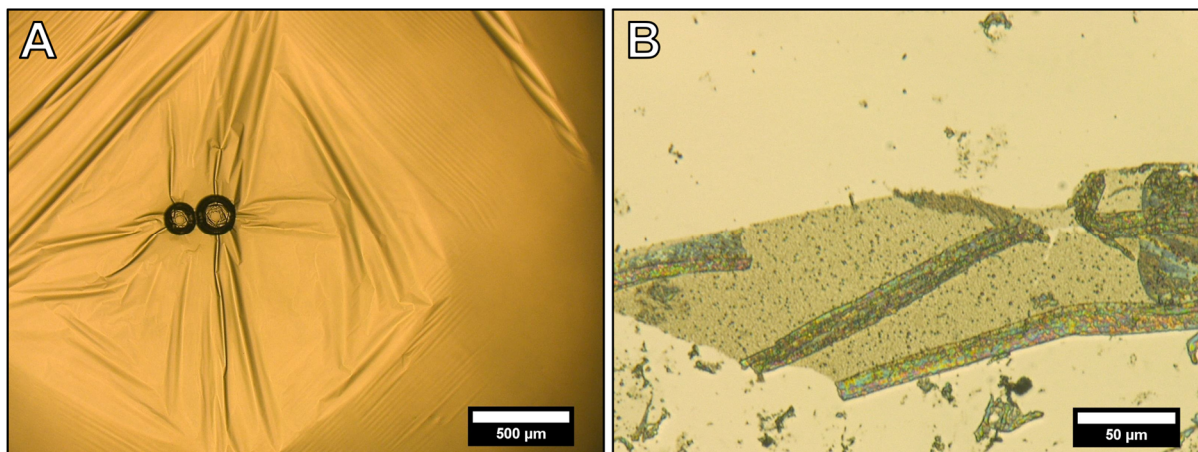
Figure S5.3 Light microscopy images for 1 h gas diffusion experiments. Images were taken before the solution was removed. **a)** Film in presence of 0.5 g/L PAA and 20 mM CaCl$_2$. If the film is manipulated it breaks apart into smaller fragments (Figure S5.13). **b)** Fragment of a broken film. Particles are visible in the structure once the film is broken up. It was not possible to isolate the film (Figure S5.14).
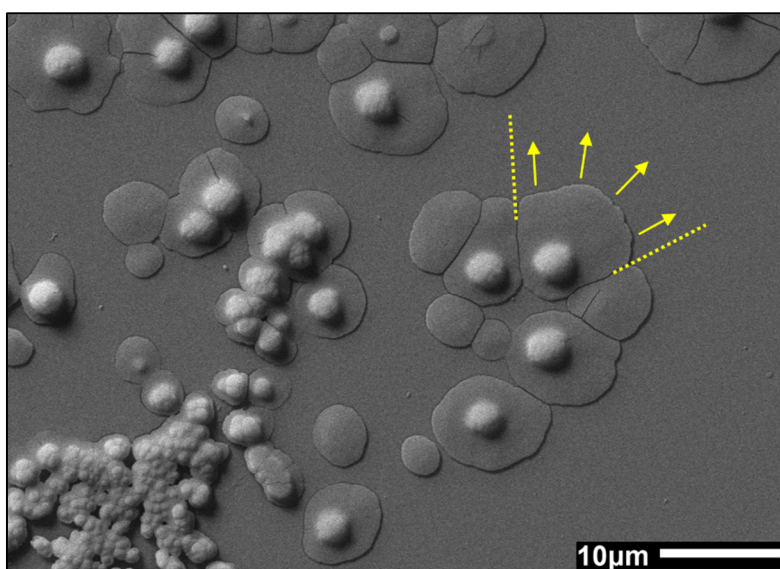
Figure S5.4 Precursor particles formed in 1 h gas diffusion experiments. Concentrations of 20 mM CaCl$_2$ and 0.01 g/L PAA were used. The picture shows dried residues of precursor droplets that precipitated onto the wafer. In several experiments, these droplets could be detected in addition to the films. Using this, we can discuss whether the droplets are indeed liquid. Macroscopically, we can use the following definition for a liquid: "When a substance conforms to the shape of its container without necessarily filling it, it is said to be in the liquid state."[275] Using this macroscopic definition we can evaluate the shown SEM analysis. Due to the liquid character of the precursor droplets in the solution in their hydrated state, the droplets spread upon precipitation on the wafer. It is clear that the droplets spread out and conform to the shape of the container. If no material is present besides the droplet, the droplets spread regularly, and the liquid forms a circle around the droplet. If material had already precipitated besides the droplet, the liquid mineral conforms to the set boundaries and flows in one direction, as indicated by the arrows. Using the macroscopic definition, the precursor phases would qualify as a liquid, at least on a μm scale (although the microscopic structure of the liquid precursor can be different).[109]
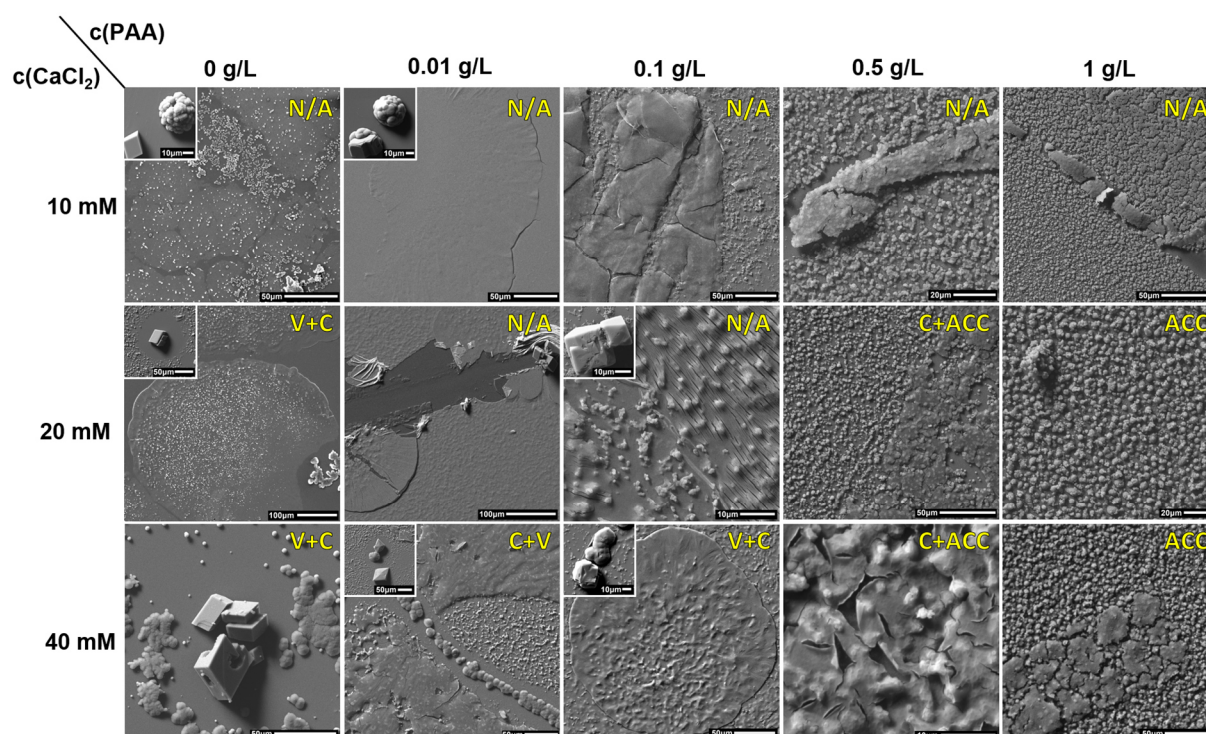
Figure S5.5 SEM micrographs for 1 h gas diffusion experiments with varying CaCl₂ and PAA concentrations. For experiments with PAA, usually the whole wafer was covered with films or particles. If larger particles were observed as well, these are shown in the inset in the top left corner. In the top right corner, the polymorph determined by ATR-FTIR is stated (C: calcite; V: vaterite; ACC: amorphous calcium carbonate; N/A: not available). It was not possible to recorded IR spectra for all samples as the concentration of $CaCO_3$ on the wafers is very low, especially for experiments with 10 mM $CaCl_2$.
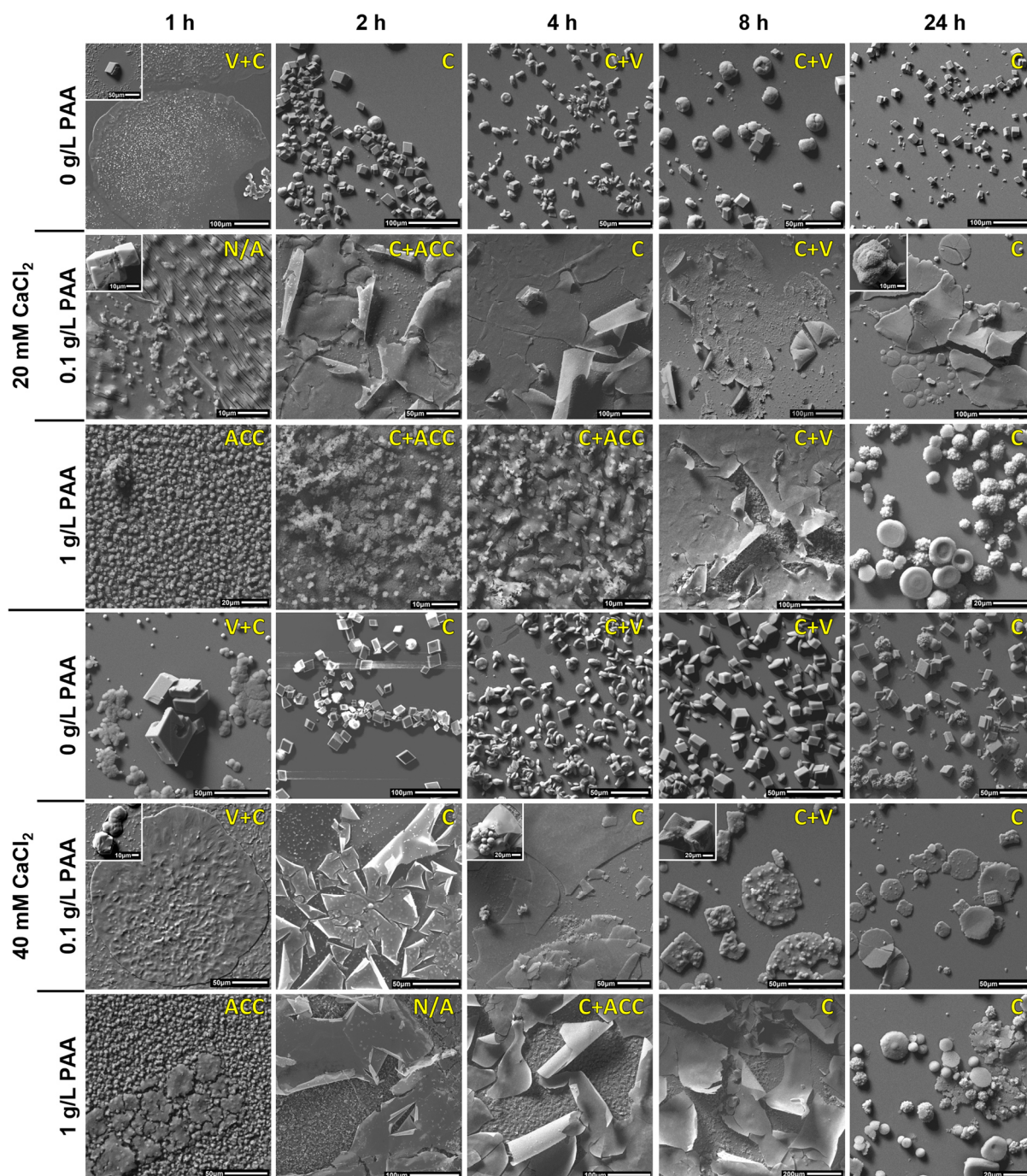
Figure S5.6 Time-dependent gas diffusion experiments. CaCl$_2$ and PAA concentrations are stated on the left side. In the top right corner, the determined polymorph by ATR-FTIR is stated (C: calcite; V: vaterite; ACC: amorphous calcium carbonate; N/A: not available).
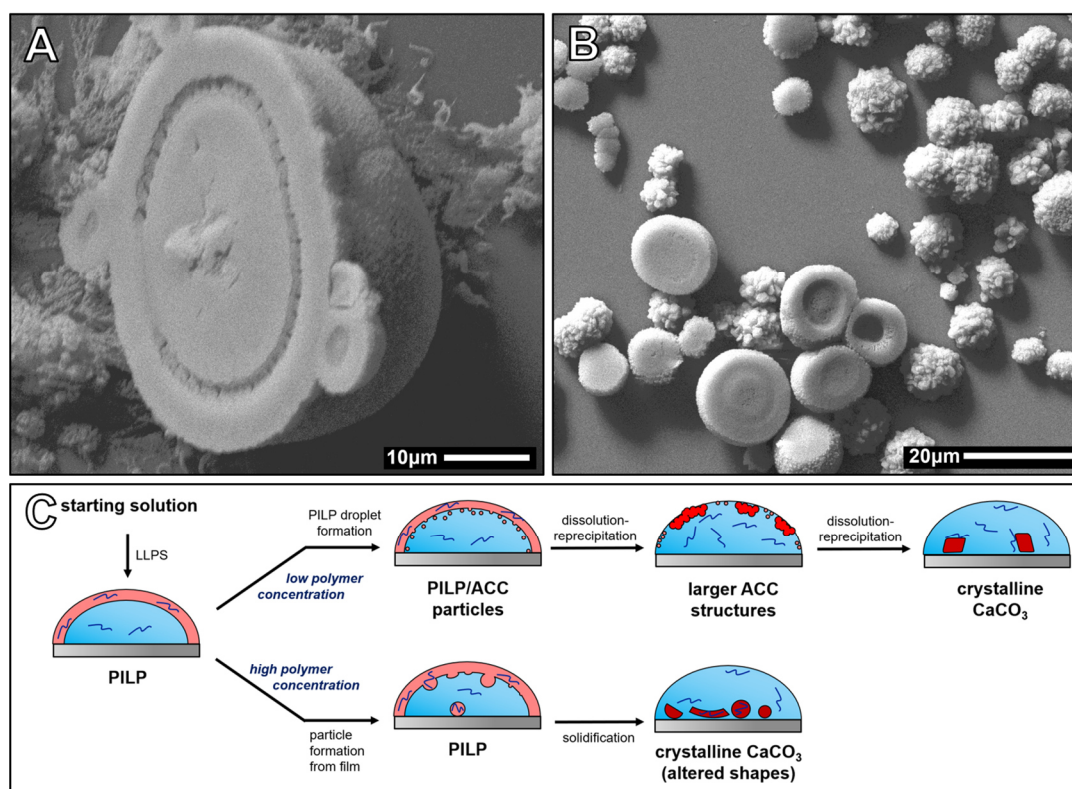
Figure S5.7 SEM micrographs of spherical particles in gas diffusion experiments with PAA. Experimental conditions: **a)** 8 h experiment with 10 mM $CaCl_2$ and 0.5 g/L PAA. **b)** 24 h gas diffusion experiment with 20 mM $CaCl_2$ and 1 g/L PAA. **c)** Proposed mechanism for crystallization in presence of PAA in gas diffusion experiments. Higher concentrations of polymer additives stabilize the liquid and amorphous phases, therefore preventing dissolution, resulting in formation of complex particle shapes from the liquid precursor phase.
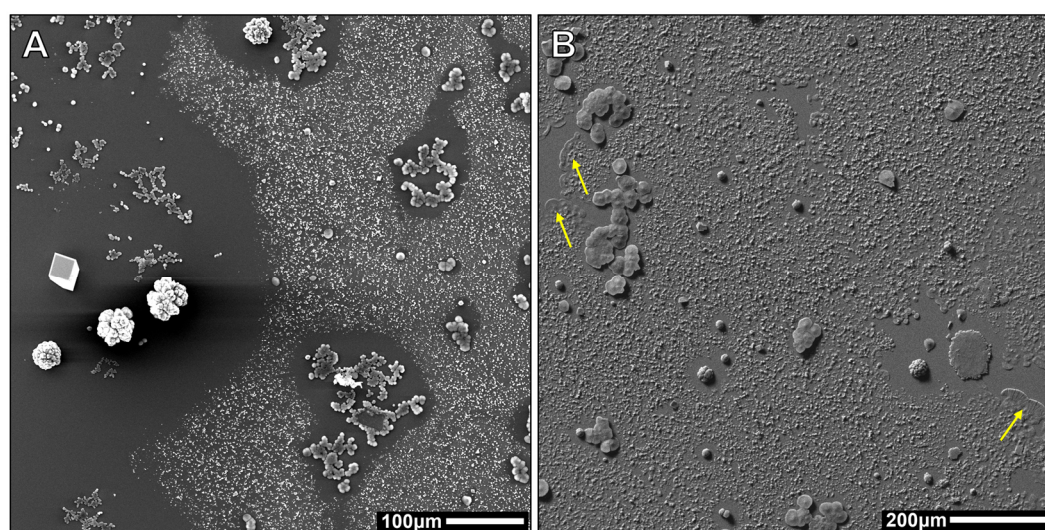
Figure S5.8 Structures observed in 1 h additive-free gas diffusion experiments. $CaCl_2$ concentrations are **a)** 10 mM and **b)** 40 mM. As there are no films or smaller particles visible around the larger amorphous or crystalline structures, a dissolution-reprecipitation mechanism is expected. Continuous parts of the film are visible as well (arrows in b).
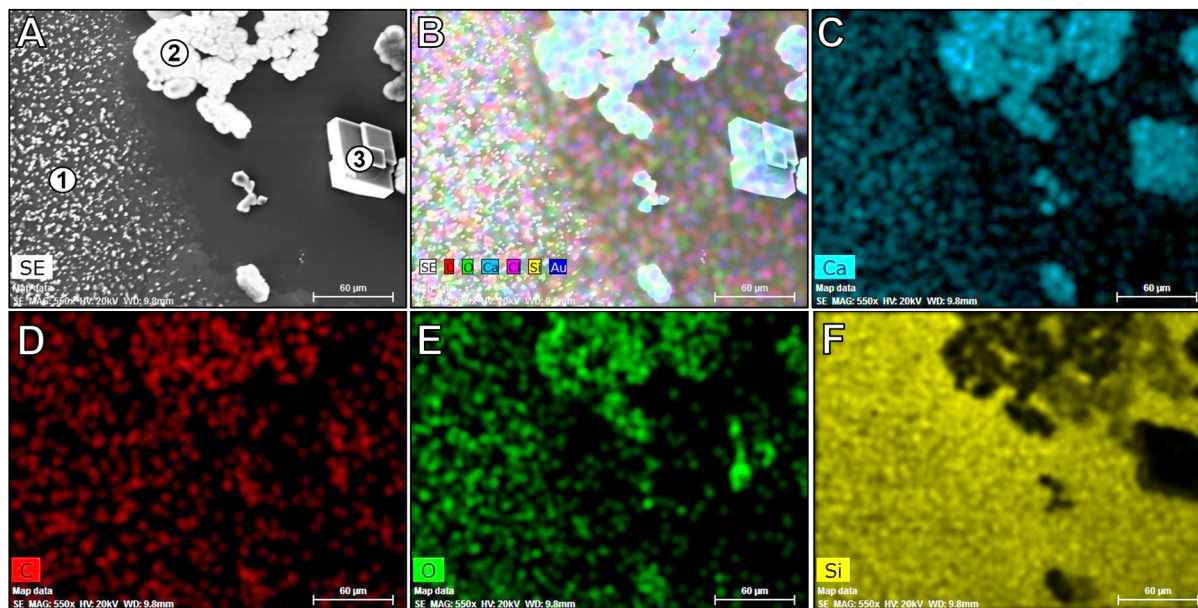
Figure S5.9 EDX characterization of different detected CaCO₃ species. a) Chosen area for mapping from an 1 h additive-free gas diffusion experiment using 20 mM CaCl₂. The film (1, film has already partially transformed to particles, as described in the results section), amorphous structures (2) and crystalline structures (3) are visible. **b)** Combined elemental mappings. **c-f)** individual mappings for Ca, C, O and Si. It is evident that all structures contain Ca, O and C. A quantitative EDX determination was not possible, as the film is very thin and mainly Si from the wafer beneath (f) was detected.
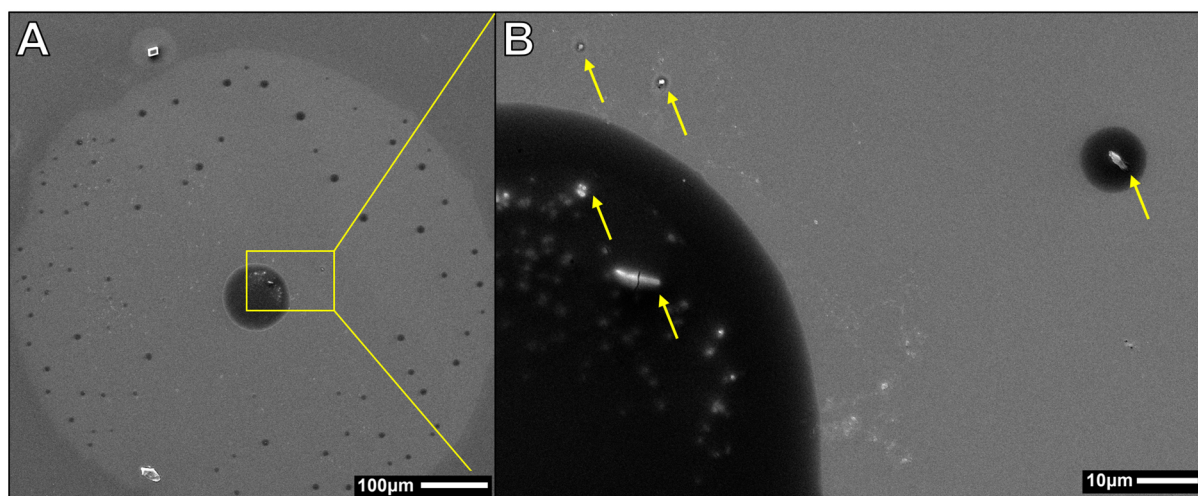
Figure S5.10   SEM micrographs of a 30 min gas diffusion experiment. A concentration of 10 mM CaCl₂ was used. **a)** A large film with a diameter of 0.7 mm is visible, suspected to be the precursor to the films seen in 1 h experiments. **b)** Higher resolution image of the holes in the film. Inside the holes, particles are visible (arrows), indicating that this film is indeed a precursor to other solid species. The drastic difference in brightness of the holes compared to the film most likely arises from the densification of the film after the wafer was coated with gold for SEM analysis. This densification was most likely induced by the electron beam during analysis of the sample.
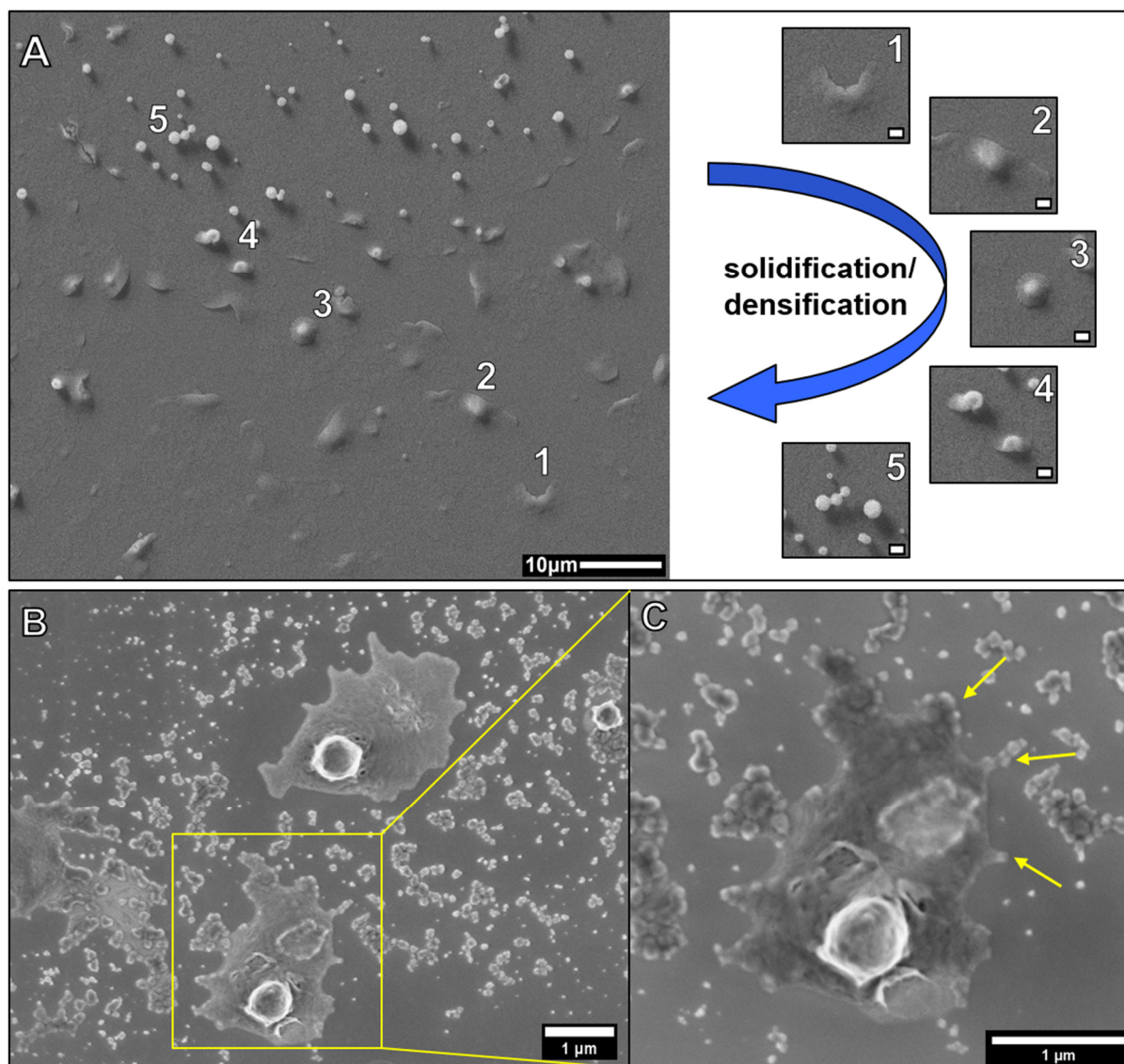
Figure S5.11 **Transformation of the precursor film to particles. a)** The transformation of the film to µm sized particles is captured in the image. Intermediate stages of the transformation are visible hinting towards a solidification/densification process instead of a dissolution-reprecipitation process. This most likely happens through dehydration of the dense liquid phases. Experimental conditions: 1 h gas diffusion experiment using 10 mM CaCl$_2$ without additive. Scale bar in insets 1 to 5 is 1 µm. **b, c)** Higher resolution SEM images of the formation of a µm sized particle. Around the particles, films are visible that transform to 50 to 150 nm particles (yellow arrows). Experimental conditions: 1 h gas diffusion experiment using 20 mM CaCl$_2$ without additive.
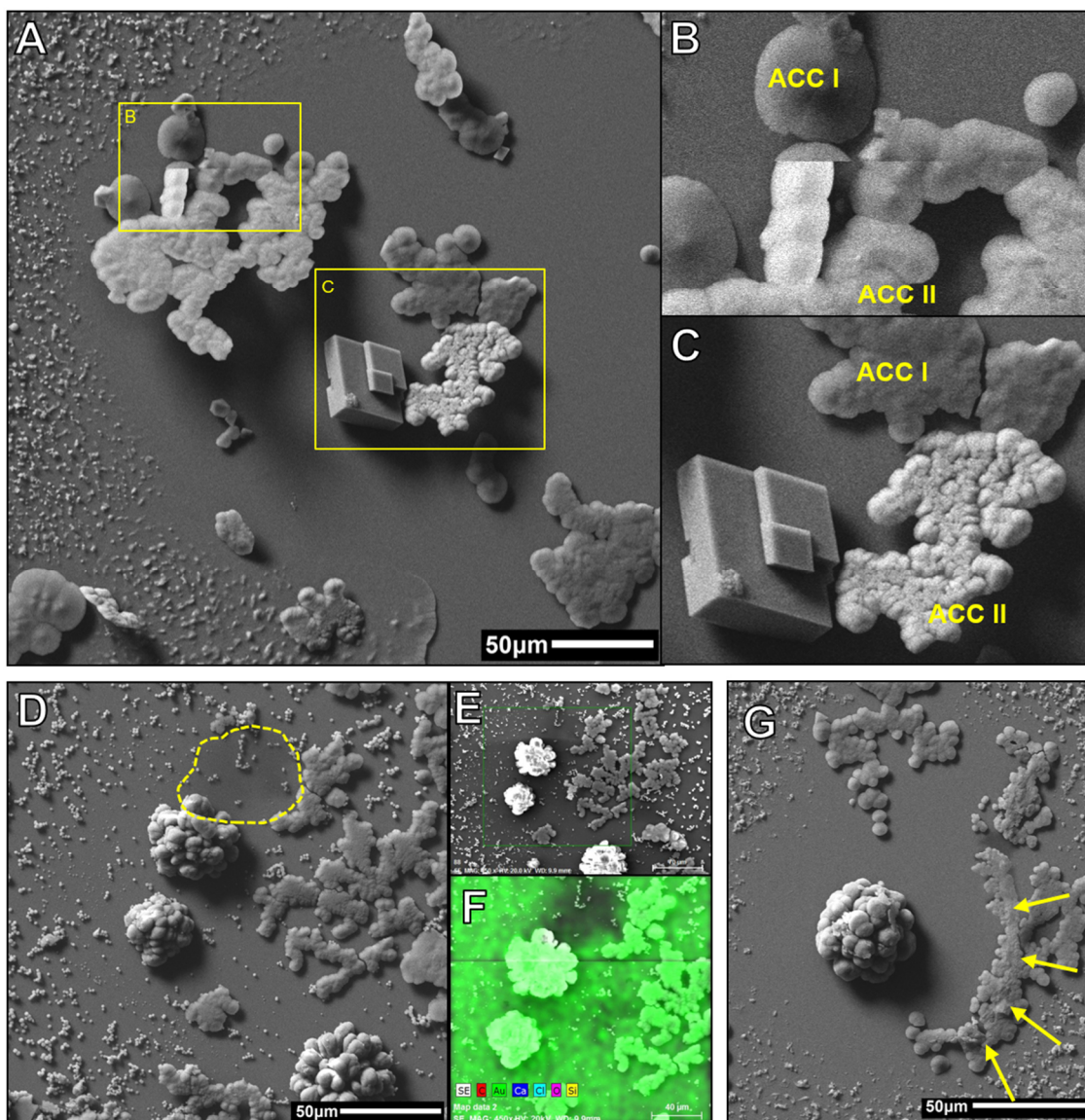
Figure S5.12   Transformation mechanisms for ACCs induced by the electron beam during SEM investigations in additive-free experiments. a) Overview image for a 1 h gas diffusion experiment using 20 mM CaCl₂. Different amorphous and crystalline structures can be seen. **b)** Magnification of the transformation of one ACC phase (ACC I) into a second ACC phase (ACC II). Due to the decrease in size toward a smaller volume of the ACCII particles upon imaging (see the line in the middle of the image), the ACCII phase seems to possess a higher density. The solid-state transformation is very fast and finished within one recorded row of pixels (less than 0.1 s). **c)** ACC I and ACC II besides a calcite crystal. The difference in structure and brightness (detected secondary electrons) between the ACC structures is obvious. The occurrence of different types of ACC was reported in the literature before.[46, 230, 276-278] **d)** Solid-state transformation of an amorphous intermediate to vaterite. The transition could not be captured in an image, but **e, f)** EDX shows the lack of Au-coating at which the amorphous phase used to be (highlighted region in D). The densification of the phase is obvious as the area covered before transformation is much larger than afterwards. **g)** Evidence for a dissolution-reprecipitation mechanism of the transformation of amorphous structures to crystalline CaCO₃. The ACC phase dissolved in a circular fashion around a vaterite particle (arrows). The formation of a preferential polymorph (calcite vs. vaterite) via the crystallization of the different ACC phases (ACCI and ACCII) could not be observed.
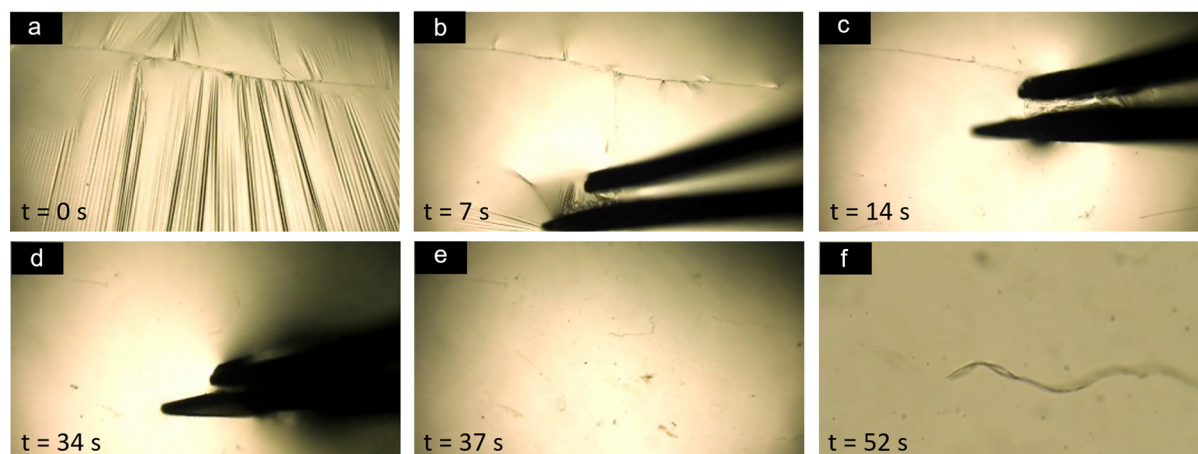
Figure S5.13   Light microscopy images of manipulation of PILP film with tweezers. If **a)** the pristine film is treated with **b-d)** tweezers, it was not possible to isolate the thin, fragile film, as it **e-f)** broke apart into smaller fragments (Figure S5.3b), which seemed to dissolve. The images shown are taken from a movie that is available as online supplementary material to the original publication.[154]
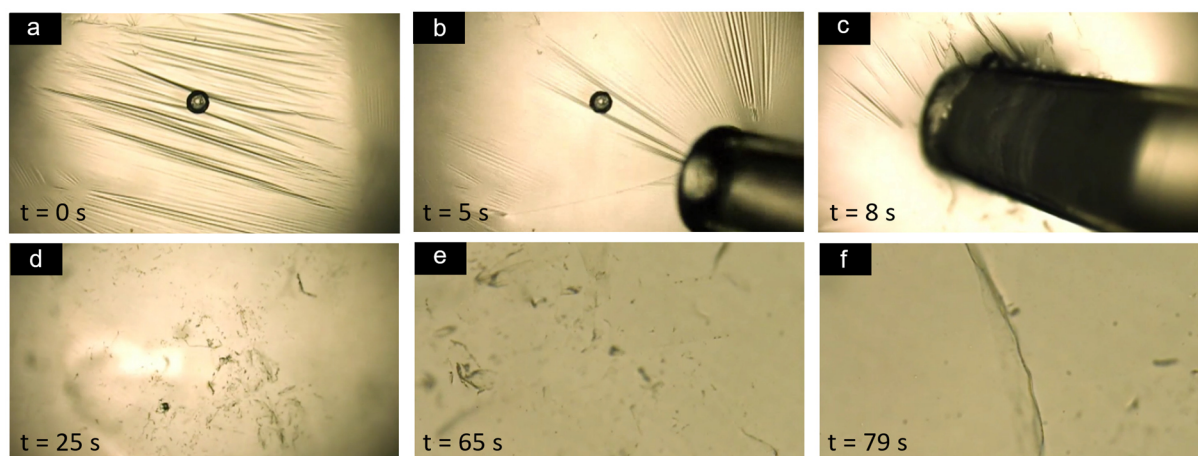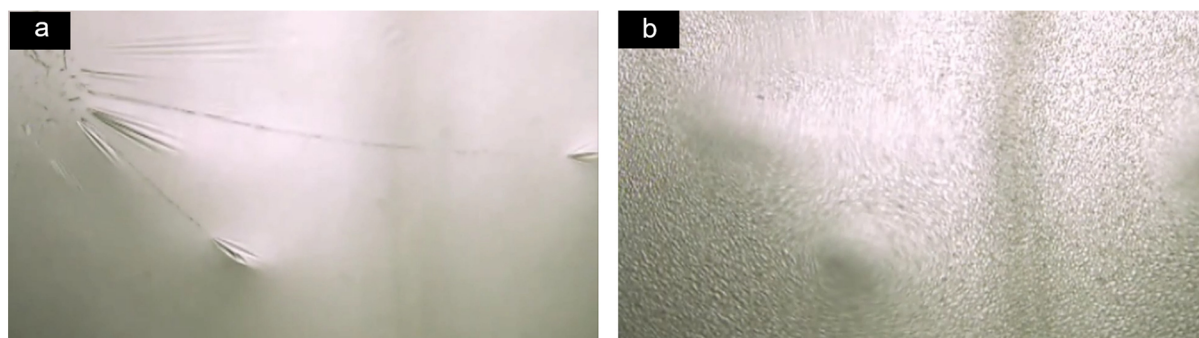

Figure S5.14   Light microscopy images of the attempt to isolate the PILP film using an Eppendorf pipette. If the **a)** PILP film is treated with **b, c)** the Eppendorf pipette, it was not possible to isolate the film due to its thinness and fragility and **d-f)** it fell apart into smaller fragments. The isolated solution was transferred to another wafer, but no $CaCO_3$ mineralization was observed, as the concentration of the precursor phase in the isolated solution was too low for sustaining liquid-liquid coexistence. The images shown are taken from a movie that is available as online supplementary material to the original publication.[154]

Figure S5.15   Light microscopy images of the PILP film. Shown is **a)** film on the surface of droplet with **b)** already precipitated PILP/ACC particles at the bottom of the wafer. The images shown are taken from a movie that is available as online supplementary material to the original publication.[154]

Conclusion and Outlook

This thesis presents a comprehensive study of the manifold effects of polymer additives on the different stages of mineral formation. It is shown that the interaction of polycarboxylates with liquid-like mineral precursors alongside bicarbonate incorporation are essential for nucleation inhibition. In addition, new insights into the mechanism underlying the stabilization and how these polymer-stabilized mineral precursors can be utilized in technological applications are provided. In combination with the reassessment of the interactions of polymer additives with ions and their effects in gas diffusion-based experiments, this provides an advanced overview of additive-controlled mineralization from the viewpoint of recent advancements in the area of fundamental mineral nucleation and crystallization mechanisms.

In the first part, the binding mechanisms of calcium ions by polycarboxylates were investigated using titration techniques. As first step, the strategy for performing potentiometric titration experiments in presence of polycarboxylates was optimized to allow for quantitative determinations, as in earlier studies the presence of polycarboxylates resulted in damage to the electrodes and no quantitative evaluation was possible.[95] As a result, a better understanding of the titration essay and the interactions of polymer additives with ion selective electrodes was gained, which will benefit future investigations using comparable experimental setups. The effects of polymer additives on individual ions, i.e., ion adsorption, can be seen as the first step in the prenucleation cluster pathway and needs to be understood before moving on to the more challenging additive-controlled mineralization scenarios. Systematic investigation of chain length, pH and side chain chemistry by potentiometric titration and isothermal titration calorimetry revealed that higher order effects are at play during the adsorption process, such as changes in apparent pK_a of carboxyl groups, contradicting the basic assumptions by the Langmuir model that assumes noninteracting binding sites. Furthermore, the necessity of initially deprotonated binding sites as starting point for successive binding events was identified. Importantly, the binding process depends on chain length and contributions arising from the whole polymer chain rather than on the chemistry of the monomer units that build up the polymer. In addition, the binding characteristics change between a chain length of 20 and 50 amino acids. No single mechanism can holistically describe all results, illustrating that care needs to be taken when interpretating binding data. The important role of polymer chain length is relevant for all research activities that attempt to describe polymer-ion interactions based on investigations of a small section of the polymer chain, or only the monomeric units, e.g., in computational studies that often employ shorter chain lengths in simulations due to limitations in computational power. As the presented study does not reveal the precise mechanisms of how the binding of calcium ions to the polymers takes place, future computational studies employing polymers with the same chain length could complement the experimental investigations and allow further insights into the underlying processes occurring on a molecular level. Especially

in the case of poly(acrylic acid), the experimental data is difficult to rationalize, and computational studies could provide mechanistic explanations, e.g., regarding the proposed strong chelation effects. Further elucidating the mechanistic details of the binding process could open up new horizons for synthetic chemists to design ion-binding polymers with specific binding sites for greatly improved adsorption capacities, for example to remove heavy metal ions from wastewaters.

In the second part of this thesis, the fundamental interactions of polymer additives with the following stages along the calcium carbonate crystallization pathway, i.e., subsequently, prenucleation clusters (PNCs), liquid-like precursors, amorphous calcium carbonates (ACCs), and crystalline phases, were elucidated. Special attention was paid towards the recently described relevance of liquid-liquid phase separation in the early stages of the calcium carbonate formation. Based on potentiometric titration experiments, the nucleation inhibition of polycarboxylates was quantified. Even if low concentrations of only 10 mg/L were used, up to 10-times nucleation inhibition was detected for poly(aspartic acid) at pH 9.0, while pH-dependent experiments revealed an increase in inhibition if the pH value was lowered. No effects of the polymers on ion binding and PNC equilibria were visible at the chosen concentrations but a strong stabilizing effect on liquid-like and amorphous mineral precursors was detected. Quantitative evaluation of the titration data showed that in presence of polymers, bicarbonate ions make up ~20% of all bound carbonate species in the prenucleation regime at pH 9.8. Due to the large quantity detected in the mineral precursors, bicarbonate binding is likely an essential step in the additive-controlled crystallization pathway and plays a key role in explaining the strong nucleation inhibition of additives. This result extends the known additive-mineral interactions, as in previous research the strong inhibition was mainly attributed to polymer-driven incorporation of water into the amorphous phase or adsorption of polymers on ACC particles. Isolation of the polymer-stabilized precursor phase and characterization with thermogravimetric analysis coupled with mass spectrometry and infrared spectroscopy (TGA-MS-IR) confirmed the presence of bicarbonate in the dried sample. It is still unknown how the polymers can facilitate bicarbonate binding, and further research based on magic angle spinning nuclear magnetic resonance (MAS NMR) spectroscopy is already in progress in order to elucidate how the polymer-mineral interaction mechanistically takes place. In this regard it is also of high interest, whether mechanistic differences between poly(aspartic acid) and poly(glutamic acid) can be detected, which could explain the higher bicarbonate binding efficiency of poly(aspartic acid) compared to poly(glutamic acid). In addition, investigations regarding the interactions of polymers with different proto-structured ACCs can help to gain more insights into the mechanistic molecular details underlying polymorph control that can be facilitated by these additives. Surprisingly, the bicarbonate content was hardly detectable by cross polarization (CP) MAS NMR experiments, suggesting that the protons introduced by bicarbonate ion incorporation exhibit significant mobility within the ACC, effectively rendering the ACC a solid proton conductor. To investigate the conductivity of ACC particles, a novel

experimental method was developed based on conductive atomic force microscopy (C-AFM). The method allows quick and qualitative analysis of the conductivity of a large number of individual nanoparticles with particle sizes below 100 nm. As the method and sample preparation is quite simple compared to established methods for determining conductivity of individual nanoparticles,[199-201] it will be appealing to a broad community. The C-AFM studies indeed revealed electrical conductivity for the ACCs, which opens up potential new applications of amorphous minerals as green ion conductors in numerous electrochemical devices. Detailed investigations regarding the performance of amorphous ion conductors in application-relevant conditions remains a hot topic for the future, especially regarding quantitative determination of the ionic conductivity and benchmarking the performance against industry standards. The demonstration of the prominent role of bicarbonate in the calcium carbonate formation pathway and its consequences for the structure of ACC in this thesis is a crucial step towards gaining a better understanding of additive-controlled crystallization. The results also underscore the great use of elucidating ion association in the prenucleation regime and early stages of crystallization for improving the understanding of mineral formation pathways. Future work will show if similar phenomena can be detected for other minerals, e.g., regarding binding of hydrogen phosphate species in calcium phosphate formation, or for other additives, ranging from ions to simple molecules, to polymers and proteins. All of this may then allow to even design more efficient antiscalants, in the future.

The third part of this study targeted the long-standing question how the beneficial properties of liquid-like mineral phases can be practically utilized in material synthesis. It is of high interest to make liquid-like mineral precursor phases accessible for technological applications, as their ability to infiltrate small pores, their use in the production of non-equilibrium crystal morphologies or their potential toward mimicking biomaterial textures can be used for the production of advanced minerals and biomimetic materials. In the last decades, the production, and investigation of liquid-like mineral precursors was highly limited due to the lack of a scalable synthesis method. Usually only several mg of precursor could be produced using gas diffusion techniques — and were actually never isolated until now. Based on our mechanistic insights into the strong inhibiting effect of poly(acrylic acid) in potentiometric titration experiments, we developed a new synthesis method to solve previously existing limitations. The novel "scalable controlled synthesis and utilization of liquid-like precursors for technological applications" (SCULPT) method allowed to synthesize, and isolate, the liquid-like mineral on a gram scale for the first time. It was shown, how organic and inorganic additives, such as magnesium ions or concrete superplasticizers, can be used to optimize the stability and workability of the liquid-like mineral precursor. Finally, it was shown how the precursor can be used for the synthesis of crystalline minerals, e.g., for the production of mineral coatings or the casting of high-resolution mineral molds. In addition, if the

concentrations of starting solutions in the synthesis were tuned, further products are accessible, such as organic-inorganic composite materials or amorphous mineral coatings, demonstrating the versatility of SCULPT. As the method is based on the controlled addition of starting solutions, it is in principle easily applicable and scalable, thereby opening up the use of liquid-like minerals for a broad scientific community to experiment with their properties and potential, as well as presenting a pathway towards large-scale industrial applications. In case of calcium carbonate-based liquid-like minerals, promising applications include the field of restoration and conservation, as well as the production of calcium carbonate-based, CO_2-fixating cements. Also, the potential generation of mineral-based proton conductors for various applications via SCULPT seems to be a promising prospect. Beyond calcium carbonate, SCULPT can in theory be used for any mineral system that forms liquid-like precursors, and further research needs to be performed to explore whether or not a sufficient stabilization of the liquid-like minerals can be achieved in other systems. The most intriguing mineral system in this regard is certainly calcium phosphate, possessing numerous biomedical applications, e.g., as bone cement or teeth fillings, in which the advantages of liquid-like minerals are highly desired.

Finally, one of the most widely used synthesis methods for precipitating carbonate-based materials, the ammonia diffusion method (ADM), was investigated with special emphasis on the importance of liquid-like precursors and amorphous intermediates for the mineral formation. In literature employing ADM, the importance of these precursors was previously seldomly discussed, although they possess tremendous explanatory power, and explanations based on the notions of classical nucleation theory were often preferred when interpreting the outcomes of ADM experiments. Based on an advanced ADM method using much shorter reaction times to resolve earlier stages of mineral formation, the relevance of liquid-like mineral species in presence, as well as absence of polymer additive was confirmed and directly visualized for the first time. The fact that the liquid-liquid phase separated mineral precursors showed sufficient kinetic stability to be detected in the experiments emphasizes their importance to be considered in the evaluation of gas diffusion-based experiments. Further investigations employing different reaction times and additive concentrations showed how the precursors are formed and how they transform into solid amorphous and crystalline minerals, establishing a full picture of mineral formation pathways in ADM-based synthesis. The results are an important step by underlining the importance of liquid-like minerals and that nonclassical mineralization mechanisms must be generally considered also in ADM experiments. The presented ADM method can be used to investigate the formation of other minerals than calcium carbonate, e.g., barium or strontium carbonates, and further work will reveal whether liquid-like minerals can be detected in these systems as well.

Altogether, this thesis presents numerous advancements in the field of additive-controlled crystallization, ranging from the questioning of previous assumptions on fundamental ion adsorption mechanisms by polycarboxylates, discovering a previously overlooked key

interaction of how polymers can stabilize liquid-like mineral precursors, to the development of a powerful method to synthesize liquid-like intermediates on a large scale. While the research in this thesis focused on calcium carbonate and polycarboxylate additives as a model system within a predominately academic framework, the presented tools will allow the academic and industrial communities to explore additional systems as well as to implement the discoveries presented herein and those made in follow-up studies in tangible technological applications.

References

[1] Cölfen, H.; Antonietti, M., *Mesocrystals and Nonclassical Crystallization*. John Wiley & Sons: 2008.

[2] Myerson, A., *Handbook of industrial crystallization*. Butterworth-Heinemann: 2002.

[3] Sunagawa, I., *Crystals: Growth, Morphology, & Perfection*. Cambridge University Press: 2005.

[4] Gower, L. B., Biomimetic Model Systems for Investigating the Amorphous Precursor Pathway and Its Role in Biomineralization. *Chem. Rev.* **2008,** *108*, 4551-4627.

[5] Meldrum, F., Calcium carbonate in biomineralisation and biomimetic chemistry. *Int. Mater. Rev.* **2003,** *48*, 187-224.

[6] Meldrum, F. C.; Cölfen, H., Controlling mineral morphologies and structures in biological and synthetic systems. *Chem. Rev.* **2008,** *108*, 4332-4432.

[7] De Yoreo, J. J.; Vekilov, P. G., Principles of crystal nucleation and growth. *Reviews in mineralogy and geochemistry* **2003,** *54*, 57-93.

[8] Gebauer, D.; Kellermeier, M.; Gale, J. D.; Bergström, L.; Cölfen, H., Pre-nucleation clusters as solute precursors in crystallisation. *Chem. Soc. Rev.* **2014,** *43*, 2348-2371.

[9] Jin, B.; Liu, Z. M.; Tang, R. K., Recent experimental explorations of non-classical nucleation. *CrystEngComm* **2020,** *22*, 4057-4073.

[10] Van Driessche, A. E.; Kellermeier, M.; Benning, L. G.; Gebauer, D., *New perspectives on mineral nucleation and growth: From solution precursors to solid materials*. Springer: 2016.

[11] Gebauer, D., How Can Additives Control the Early Stages of Mineralisation? *Minerals* **2018,** *8*, 179.

[12] Gránásy, L. In *Comparison of modern theories of vapor condensation*, AIP Conference Proceedings, American Institute of Physics: 2000; 209-212.

[13] Petsev, D. N.; Chen, K.; Gliko, O.; Vekilov, P. G., Diffusion-limited kinetics of the solution–solid phase transition of molecular substances. *Proc. Natl. Acad. Sci. U.S.A.* **2003,** *100*, 792-796.

[14] Giuffre, A. J.; Hamm, L. M.; Han, N.; De Yoreo, J. J.; Dove, P. M., Polysaccharide chemistry regulates kinetics of calcite nucleation through competition of interfacial energies. *Proc. Natl. Acad. Sci. U.S.A.* **2013,** *110*, 9261-9266.

[15] De Yoreo, J. J.; Gilbert, P. U.; Sommerdijk, N. A.; Penn, R. L.; Whitelam, S.; Joester, D.; Zhang, H.; Rimer, J. D.; Navrotsky, A.; Banfield, J. F., Crystallization by particle attachment in synthetic, biogenic, and geologic environments. *Science* **2015,** *349*, aaa6760.

[16] Gebauer, D.; Gale, J. D.; Cölfen, H., Crystal Nucleation and Growth of Inorganic Ionic Materials from Aqueous Solution: Selected Recent Developments, and Implications. *Small* **2022**, 2107735.

[17] Lukić, M. J.; Gebauer, D.; Rose, A., Nonclassical Nucleation towards Separation and Recycling Science: Iron and Aluminium (Oxy)(hydr)oxides. *Curr. Opin. Colloid Interface Sci.* **2020,** *46*, 114-127.

[18] Avaro, J. T.; Wolf, S. L. P.; Hauser, K.; Gebauer, D., Stable Prenucleation Calcium Carbonate Clusters Define Liquid-Liquid Phase Separation. *Angew. Chem. Int. Ed.* **2020,** *59*, 6155-6159.

[19] Gebauer, D.; Völkel, A.; Cölfen, H., Stable prenucleation calcium carbonate clusters. *Science* **2008,** *322*, 1819-22.

[20] Demichelis, R.; Raiteri, P.; Gale, J. D.; Quigley, D.; Gebauer, D., Stable prenucleation mineral clusters are liquid-like ionic polymers. *Nat. Commun.* **2011,** *2*, 590.

[21] Matthias, K.; Denis, G.; Emilio, M. G.; Markus, D.; Yeshayahu, T.; Lorenz, K.; Helmut, C.; Manuel, G. R. J.; Werner, K., Colloidal Stabilization of Calcium Carbonate Prenucleation Clusters with Silica. *Adv. Funct. Mater.* **2012,** *22*, 4301-4311.

[22] Sebastiani, F.; Wolf, S. L.; Born, B.; Luong, T. Q.; Cölfen, H.; Gebauer, D.; Havenith, M., Water dynamics from THz spectroscopy reveal the locus of a liquid–liquid binodal limit in aqueous $CaCO_3$ solutions. *Angew. Chem. Int. Ed.* **2017,** *56*, 490-495.

[23] Nielsen, M. H.; Aloni, S.; De Yoreo, J. J., In situ TEM imaging of $CaCO_3$ nucleation reveals coexistence of direct and indirect pathways. *Science* **2014,** *345*, 1158-1162.

[24] Smeets, P. J. M.; Finney, A. R.; Habraken, W. J. E. M.; Nudelman, F.; Friedrich, H.; Laven, J.; De Yoreo, J. J.; Rodger, P. M.; Sommerdijk, N. A. J. M., A classical view on nonclassical nucleation. *Proc. Natl. Acad. Sci. U.S.A.* **2017,** *114*, E7882-E7890.

[25] Henzler, K.; Fetisov, E. O.; Galib, M.; Baer, M. D.; Legg, B. A.; Borca, C.; Xto, J. M.; Pin, S.; Fulton, J. L.; Schenter, G. K., Supersaturated calcium carbonate solutions are classical. *Science Advances* **2018,** *4*, eaao6283.

[26] Gebauer, D.; Raiteri, P.; Gale, J. D.; Cölfen, H., On classical and non-classical views on nucleation. *American Journal of Science* **2018,** *318*, 969-988.

[27] Gower, L. A. The influence of polyaspartate additive on the growth and morphology of calcium carbonate crystals. Dissertation, University of Massachusetts Amherst, 1997.

[28] Gower, L. B.; Odom, D. J., Deposition of calcium carbonate films by a polymer-induced liquid-precursor (PILP) process. *J. Cryst. Growth* **2000,** *210*, 719-734.

[29] Faatz, M.; Gröhn, F.; Wegner, G., Amorphous calcium carbonate: synthesis and potential intermediate in biomineralization. *Adv. Mater.* **2004,** *16*, 996-1000.

[30] Wolf, S. E.; Leiterer, J.; Kappl, M.; Emmerling, F.; Tremel, W., Early homogenous amorphous precursor stages of calcium carbonate and subsequent crystal growth in levitated droplets. *J. Am. Chem. Soc.* **2008,** *130*, 12342-12347.

[31] Bewernitz, M. A.; Gebauer, D.; Long, J.; Cölfen, H.; Gower, L. B., A metastable liquid precursor phase of calcium carbonate and its interactions with polyaspartate. *Faraday Discuss.* **2012,** *159*, 291-312.

[32] Wallace, A. F.; Hedges, L. O.; Fernandez-Martinez, A.; Raiteri, P.; Gale, J. D.; Waychunas, G. A.; Whitelam, S.; Banfield, J. F.; De Yoreo, J. J., Microscopic evidence for liquid-liquid separation in supersaturated $CaCO_3$ solutions. *Science* **2013,** *341*, 885-889.

[33] De Yoreo, J.; Jin, B.; Chen, Y.; Pyles, H.; Baer, M.; Legg, B.; Wang, Z.; Washton, N.; Mueller, K.; Baker, D., Formation, Chemical Evolution, and Solidification of the Calcium Carbonate Dense Liquid Phase. **2022,** https://doi.org/10.21203/rs.3.rs-1743346/v1.

[34] Huang, Y.-C.; Rao, A.; Huang, S.-J.; Chang, C.-Y.; Drechsler, M.; Knaus, J.; Chan, J. C.; Raiteri, P.; Gale, J. D.; Gebauer, D., Uncovering the Role of Bicarbonate in Calcium Carbonate Formation at Near‐Neutral pH. *Angew. Chem. Int. Ed.* **2021,** *60*, 16707-16713.

[35] Gower, L.; Elias, J., Colloid assembly and transformation (CAT): The relationship of PILP to biomineralization. *Journal of Structural Biology: X* **2022,** *6*, 100059.

[36] Du, H.; Amstad, E., Water: How Does It Influence the $CaCO_3$ Formation? *Angew. Chem. Int. Ed.* **2020,** *59*, 1798-1816.

[37] Aizenberg, J.; Muller, D. A.; Grazul, J. L.; Hamann, D., Direct fabrication of large micropatterned single crystals. *Science* **2003,** *299*, 1205-1208.

[38] Du, H.; Steinacher, M.; Borca, C.; Huthwelker, T.; Murello, A.; Stellacci, F.; Amstad, E., Amorphous $CaCO_3$: Influence of the formation time on its degree of hydration and stability. *J. Am. Chem. Soc.* **2018,** *140*, 14289-14299.

[39] Rodriguez-Navarro, C.; Kudłacz, K.; Cizer, Ö.; Ruiz-Agudo, E., Formation of amorphous calcium carbonate and its transformation into mesostructured calcite. *CrystEngComm* **2015,** *17*, 58-72.

[40] Xu, X.; Han, J. T.; Kim, D. H.; Cho, K., Two modes of transformation of amorphous calcium carbonate films in air. *J. Phys. Chem. B* **2006,** *110*, 2764-2770.

[41] Tobler, D. J.; Rodriguez Blanco, J. D.; Sørensen, H. O.; Stipp, S. L.; Dideriksen, K., Effect of pH on amorphous calcium carbonate structure and transformation. *Crystal Growth & Design* **2016,** *16*, 4500-4508.

[42] Zou, Z.; Bertinetti, L.; Politi, Y.; Jensen, A. C.; Weiner, S.; Addadi, L.; Fratzl, P.; Habraken, W. J., Opposite particle size effect on amorphous calcium carbonate crystallization in water and during heating in air. *Chem. Mater.* **2015,** *27*, 4237-4246.

[43] Zhang, S.; Nahi, O.; He, X.; Chen, L.; Aslam, Z.; Kapur, N.; Kim, Y. Y.; Meldrum, F. C., Local Heating Transforms Amorphous Calcium Carbonate to Single Crystals with Defined Morphologies. *Adv. Funct. Mater.* **2022,** 2207019.

[44] Schmidt, M. P.; Ilott, A. J.; Phillips, B. L.; Reeder, R. J., Structural changes upon dehydration of amorphous calcium carbonate. *Crystal Growth & Design* **2014,** *14*, 938-951.

[45] Cartwright, J. H.; Checa, A. G.; Gale, J. D.; Gebauer, D.; Sainz-Díaz, C. I., Calcium carbonate polyamorphism and its role in biomineralization: how many amorphous calcium carbonates are there? *Angew. Chem. Int. Ed.* **2012,** *51*, 11960-11970.

[46] Gebauer, D.; Gunawidjaja, P. N.; Ko, J. Y. P.; Bacsik, Z.; Aziz, B.; Liu, L.; Hu, Y.; Bergström, L.; Tai, C.-W.; Sham, T.-K.; Edén, M.; Hedin, N., Proto-Calcite and Proto-Vaterite in Amorphous Calcium Carbonates. *Angew. Chem. Int. Ed.* **2010,** *49*, 8889-8891.

[47] Sun, S.; Chevrier, D. M.; Zhang, P.; Gebauer, D.; Cölfen, H., Distinct Short-Range Order Is Inherent to Small Amorphous Calcium Carbonate Clusters (< 2 nm). *Angew. Chem. Int. Ed.* **2016,** *55*, 12206-12209.

[48] Berner, R., The role of magnesium in the crystal growth of calcite and aragonite from sea water. *Geochim. Cosmochim. Acta* **1975,** *39*, 489-504.

[49] Huang, Y.-C.; Gindele, M. B.; Knaus, J.; Rao, A.; Gebauer, D., On Mechanisms for Mesocrystal Formation: Magnesium Ions and Water Environments Regulate Crystallization of Amorphous Minerals. *CrystEngComm* **2018,** *20*, 4395-4405.

[50] Falini, G.; Gazzano, M.; Ripamonti, A., Crystallization of calcium carbonate in presence of magnesium and polyelectrolytes. *J. Cryst. Growth* **1994,** *137*, 577-584.

[51] Raz, S.; Weiner, S.; Addadi, L., Formation of high-magnesian calcites via an amorphous precursor phase: possible biological implications. *Adv. Mater.* **2000,** *12*, 38-42.

[52] Wang, D.; Wallace, A. F.; De Yoreo, J. J.; Dove, P. M., Carboxylated molecules regulate magnesium content of amorphous calcium carbonates during calcification. *Proc. Natl. Acad. Sci. U.S.A.* **2009,** *106*, 21511-21516.

[53] Weiner, S.; Addadi, L., Design strategies in mineralized biological materials. *J. Mater. Chem.* **1997,** *7*, 689-702.

[54] Addadi, L.; Joester, D.; Nudelman, F.; Weiner, S., Mollusk shell formation: a source of new concepts for understanding biomineralization processes. *Chem. Eur. J.* **2006,** *12*, 980-987.

[55] Falini, G.; Albeck, S.; Weiner, S.; Addadi, L., Control of aragonite or calcite polymorphism by mollusk shell macromolecules. *Science* **1996,** *271*, 67-69.

[56] Bissi, V.; Sun, C.-Y.; Falini, G.; Gilbert, P. U.; Mass, T., Coral acid rich protein selects vaterite polymorph *in vitro*. *J. Struct. Biol.* **2020,** *209*, 107431.

[57] Sedlák, M.; Antonietti, M.; Cölfen, H., Synthesis of a new class of double-hydrophilic block copolymers with calcium binding capacity as builders and for biomimetic structure control of minerals. *Macromol. Chem. Phys.* **1998,** *199*, 247-254.

[58] Ruiz-Agudo, C.; Lutz, J.; Keckeis, P.; King, M.; Marx, A.; Gebauer, D., Ubiquitin Designer Proteins as a New Additive Generation toward Controlling Crystallization. *J. Am. Chem. Soc.* **2019,** *141*, 12240-12245.

[59] Weijnen, M.; Van Rosmalen, G., The influence of various polyelectrolytes on the precipitation of gypsum. *Desalination* **1985,** *54*, 239-261.

[60] Loy, J. E.; Guo, J. H.; Severtson, S. J., Role of adsorption fractionation in determining the $CaCO_3$ scale inhibition performance of polydisperse sodium polyacrylate. *Industrial & Engineering Chemistry Research* **2004,** *43*, 1882-1887.

[61] MacAdam, J.; Parsons, S. A., Calcium carbonate scale formation and control. *Reviews in Environmental Science & Biotechnology* **2004,** *3*, 159-169.

[62] Gotliv, B. A.; Kessler, N.; Sumerel, J. L.; Morse, D. E.; Tuross, N.; Addadi, L.; Weiner, S., Asprich: A novel aspartic acid-rich protein family from the prismatic shell matrix of the bivalve Atrina rigida. *ChemBioChem* **2005,** *6*, 304-314.

[63] Belcher, A. M.; Wu, X.; Christensen, R.; Hansma, P.; Stucky, G.; Morse, D., Control of crystal phase switching and orientation by soluble mollusc-shell proteins. *Nature* **1996,** *381*, 56-58.

[64] Herman, A.; Addadi, L.; Weiner, S., Interactions of sea-urchin skeleton macromolecules with growing calcite crystals—a study of intracrystalline proteins. *Nature* **1988,** *331*, 546-548.

[65] Addadi, L.; Weiner, S., Interactions between acidic proteins and crystals: stereochemical requirements in biomineralization. *Proc. Natl. Acad. Sci. U.S.A.* **1985,** *82*, 4110-4114.

[66] Levi, Y.; Albeck, S.; Brack, A.; Weiner, S.; Addadi, L., Control over aragonite crystal nucleation and growth: an in vitro study of biomineralization. *Chem. Eur. J.* **1998,** *4*, 389-396.

[67] Aizenberg, J.; Lambert, G.; Weiner, S.; Addadi, L., Factors involved in the formation of amorphous and crystalline calcium carbonate: a study of an ascidian skeleton. *J. Am. Chem. Soc.* **2002,** *124*, 32-39.

[68] Endo, H.; Takagi, Y.; Ozaki, N.; Kogure, T.; Watanabe, T., A crustacean Ca^{2+}-binding protein with a glutamate-rich sequence promotes $CaCO_3$ crystallization. *Biochem. J* **2004,** *384*, 159-167.

[69] Mann, S., Molecular recognition in biomineralization. *Nature* **1988,** *332*, 119-124.

[70] Weiner, S., Aspartic acid-rich proteins: major components of the soluble organic matrix of mollusk shells. *Calcified Tissue International* **1979,** *29*, 163-167.

[71] Albeck, S.; Weiner, S.; Addadi, L., Polysaccharides of intracrystalline glycoproteins modulate calcite crystal growth in vitro. *Chem. Eur. J.* **1996,** *2*, 278-284.

[72] Aizenberg, J.; Addadi, L.; Weiner, S.; Lambert, G., Stabilization of amorphous calcium carbonate by specialized macromolecules in biological and synthetic precipitates. *Adv. Mater.* **1996,** *8*, 222-226.

[73] Sarashina, I.; Endo, K., The complete primary structure of molluscan shell protein 1 (MSP-1), an acidic glycoprotein in the shell matrix of the scallop Patinopecten yessoensis. *Mar. Biotechnol.* **2001,** *3*, 362-369.

[74] Sarashina, I.; Endo, K., Primary structure of a soluble matrix protein of scallop shell; implications for calcium carbonate biomineralization. *Am. Mineral.* **1998,** *83*, 1510-1515.

[75] Takeuchi, T.; Sarashina, I.; Iijima, M.; Endo, K., In vitro regulation of $CaCO_3$ crystal polymorphism by the highly acidic molluscan shell protein Aspein. *FEBS Lett.* **2008,** *582*, 591-596.

[76] Tsukamoto, D.; Sarashina, I.; Endo, K., Structure and expression of an unusually acidic matrix protein of pearl oyster shells. *Biochem. Biophys. Res. Commun.* **2004,** *320*, 1175-1180.

[77] De Yoreo, J. J.; Wierzbicki, A.; Dove, P. M., New insights into mechanisms of biomolecular control on growth of inorganic crystals. *CrystEngComm* **2007,** *9*, 1144-1152.

[78] Addadi, L.; Raz, S.; Weiner, S., Taking advantage of disorder: amorphous calcium carbonate and its roles in biomineralization. *Adv. Mater.* **2003,** *15*, 959-970.

[79] Weiss, I. M.; Tuross, N.; Addadi, L.; Weiner, S., Mollusc larval shell formation: amorphous calcium carbonate is a precursor phase for aragonite. *Journal of Experimental Zoology* **2002,** *293*, 478-491.

[80] Raz, S.; Testeniere, O.; Hecker, A.; Weiner, S.; Luquet, G., Stable amorphous calcium carbonate is the main component of the calcium storage structures of the crustacean Orchestia cavimana. *The Biological Bulletin* **2002,** *203*, 269-274.

[81] Politi, Y.; Arad, T.; Klein, E.; Weiner, S.; Addadi, L., Sea urchin spine calcite forms via a transient amorphous calcium carbonate phase. *Science* **2004,** *306*, 1161-1164.

[82] Raz, S.; Hamilton, P. C.; Wilt, F. H.; Weiner, S.; Addadi, L., The transient phase of amorphous calcium carbonate in sea urchin larval spicules: the involvement of proteins and magnesium ions in its formation and stabilization. *Adv. Funct. Mater.* **2003,** *13*, 480-486.

[83] Akiva, A.; Neder, M.; Kahil, K.; Gavriel, R.; Pinkas, I.; Goobes, G.; Mass, T., Minerals in the pre-settled coral Stylophora pistillata crystallize via protein and ion changes. *Nat. Commun.* **2018,** *9*, 1-9.

[84] Kong, J.; Liu, C.; Yang, D.; Yan, Y.; Chen, Y.; Liu, Y.; Zheng, G.; Xie, L.; Zhang, R., A novel basic matrix protein of Pinctada fucata, PNU9, functions as inhibitor during crystallization of aragonite. *CrystEngComm* **2019,** *21*, 1250-1261.

[85] Stifler, C. A.; Killian, C. E.; Gilbert, P. U., Evidence for a liquid precursor to biomineral formation. *Crystal Growth & Design* **2021,** *21*, 6635-6641.

[86] Gilbert, P. U.; Bergmann, K. D.; Boekelheide, N.; Tambutté, S.; Mass, T.; Marin, F.; Adkins, J. F.; Erez, J.; Gilbert, B.; Knutson, V., Biomineralization: Integrating mechanism and evolutionary history. *Science Advances* **2022,** *8*, eabl9653.

[87] Njegić-Džakula, B.; Falini, G.; Brečević, L.; Skoko, Ž.; Kralj, D., Effects of initial supersaturation on spontaneous precipitation of calcium carbonate in the presence of charged poly-L-amino acids. *J. Colloid Interface Sci.* **2010,** *343*, 553-563.

[88] Njegić Džakula, B.; Falini, G.; Kralj, D., Crystal Growth Mechanism of Vaterite in the Systems Containing Charged Synthetic Poly(Amino Acids). *Croat. Chem. Acta* **2017,** *90*, 1-10.

[89] Kato, T.; Suzuki, T.; Amamiya, T.; Irie, T.; Komiyama, M.; Yui, H., Effects of macromolecules on the crystallization of $CaCO_3$ the formation of organic/inorganic composites. *Supramol. Sci.* **1998,** *5*, 411-415.

[90] Zou, Z.; Bertinetti, L.; Politi, Y.; Fratzl, P.; Habraken, W. J., Control of Polymorph Selection in Amorphous Calcium Carbonate Crystallization by Poly(Aspartic Acid): Two Different Mechanisms. *Small* **2017,** *13*, 1603100.

[91] Wolf, S. L.; Jähme, K.; Gebauer, D., Synergy of Mg^{2+} and poly(aspartic acid) in additive-controlled calcium carbonate precipitation. *CrystEngComm* **2015,** *17*, 6857-6862.

[92] Zou, Z.; Polishchuk, I.; Bertinetti, L.; Pokroy, B.; Politi, Y.; Fratzl, P.; Habraken, W., Additives influence the phase behavior of calcium carbonate solution by a cooperative ion-association process. *J. Mater. Chem. B* **2018,** *6*, 449-457.

[93] Zou, Z.; Yang, X.; Albéric, M.; Heil, T.; Wang, Q.; Pokroy, B.; Politi, Y.; Bertinetti, L., Additives Control the Stability of Amorphous Calcium Carbonate via Two Different Mechanisms: Surface Adsorption versus Bulk Incorporation. *Adv. Funct. Mater.* **2020,** 2000003.

[94] Huang, W.; Wang, Q.; Chi, W.; Cai, M.; Wang, R.; Fu, Z.; Xie, J.; Zou, Z., Multiple crystallization pathways of amorphous calcium carbonate in the presence of poly(aspartic acid) with a chain length of 30. *CrystEngComm* **2022,** *24*, 4809-4818.

[95] Sinn, C. G.; Dimova, R.; Antonietti, M., Isothermal titration calorimetry of the polyelectrolyte/water interaction and binding of Ca^{2+}: effects determining the quality of polymeric scale inhibitors. *Macromolecules* **2004,** *37*, 3444-3450.

[96] Borkovec, M.; Koper, G. J.; Piguet, C., Ion binding to polyelectrolytes. *Curr. Opin. Colloid Interface Sci.* **2006,** *11*, 280-289.

[97] Lemke, T.; Edte, M.; Gebauer, D.; Peter, C., Three Reasons Why Aspartic Acid and Glutamic Acid Sequences Have a Surprisingly Different Influence on Mineralization. *J. Phys. Chem. B* **2021,** *125*, 10335-10343.

[98] Verch, A.; Gebauer, D.; Antonietti, M.; Cölfen, H., How to control the scaling of CaCO₃: A "fingerprinting technique" to classify additives. *Phys. Chem. Chem. Phys.* **2011,** *13*, 16811-16820.

[99] Morse, J. W.; Arvidson, R. S.; Lüttge, A., Calcium carbonate formation and dissolution. *Chem. Rev.* **2007,** *107*, 342-381.

[100] Hamm, L. M.; Giuffre, A. J.; Han, N.; Tao, J.; Wang, D.; De Yoreo, J. J.; Dove, P. M., Reconciling disparate views of template-directed nucleation through measurement of calcite nucleation kinetics and binding energies. *Proc. Natl. Acad. Sci. U.S.A.* **2014,** *111*, 1304-1309.

[101] Schodder, P. I.; Gindele, M. B.; Ott, A.; Ruckel, M.; Ettl, R.; Boyko, V.; Kellermeier, M., Probing the effects of polymers on the early stages of calcium carbonate formation by stoichiometric co-titration. *Phys. Chem. Chem. Phys.* **2022,** *24*, 9978-9989.

[102] Xu, X.-R.; Cai, A.-H.; Liu, R.; Pan, H.-H.; Tang, R.-K.; Cho, K., The roles of water and polyelectrolytes in the phase transformation of amorphous calcium carbonate. *J. Cryst. Growth* **2008,** *310*, 3779-3787.

[103] Du, H.; Courregelongue, C.; Xto, J.; Bohlen, A.; Steinacher, M.; Borca, C. N.; Huthwelker, T.; Amstad, E., Additives: Their Influence on the Humidity- and Pressure-Induced Crystallization of Amorphous CaCO₃. *Chem. Mater.* **2020,** *32*, 4282-4291.

[104] Jehannin, M.; Rao, A.; Cölfen, H., New horizons of nonclassical crystallization. *J. Am. Chem. Soc.* **2019,** *141*, 10120-10136.

[105] Cheng, X.; Gower, L. B., Molding Mineral within Microporous Hydrogels by a Polymer-Induced Liquid-Precursor (PILP) Process. *Biotechnol. Progr.* **2006,** *22*, 141-149.

[106] Kim, Y.-Y.; Douglas, E. P.; Gower, L. B., Patterning inorganic (CaCO₃) thin films via a polymer-induced liquid-precursor process. *Langmuir* **2007,** *23*, 4862-4870.

[107] Homeijer, S. J.; Barrett, R. A.; Gower, L. B., Polymer-Induced Liquid-Precursor (PILP) Process in the Non-Calcium Based Systems of Barium and Strontium Carbonate. *Crystal Growth & Design* **2010,** *10*, 1040-1052.

[108] Dai, L.; Douglas, E. P.; Gower, L. B., Compositional analysis of a polymer-induced liquid-precursor (PILP) amorphous CaCO₃ phase. *J. Non-Cryst. Solids* **2008,** *354*, 1845-1854.

[109] Xu, Y.; Tijssen, K. C. H.; Bomans, P. H. H.; Akiva, A.; Friedrich, H.; Kentgens, A. P. M.; Sommerdijk, N., Microscopic structure of the polymer-induced liquid precursor for calcium carbonate. *Nat. Commun.* **2018,** *9*, 2582.

[110] Kellermeier, M.; Cölfen, H.; Gebauer, D., Chapter Three - Investigating the Early Stages of Mineral Precipitation by Potentiometric Titration and Analytical

Ultracentrifugation. In *Methods Enzymol.*, De Yoreo, J. J., Ed. Academic Press: 2013; Vol. 532, 45-69.

[111] Eiblmeier, J.; Schürmann, U.; Kienle, L.; Gebauer, D.; Kunz, W.; Kellermeier, M., New insights into the early stages of silica-controlled barium carbonate crystallisation. *Nanoscale* **2014,** *6*, 14939-14949.

[112] Ibsen, C. J. S.; Gebauer, D.; Birkedal, H., Osteopontin Stabilizes Metastable States Prior to Nucleation during Apatite Formation. *Chem. Mater.* **2016,** *28*, 8550-8555.

[113] Ruiz-Agudo, C.; McDonogh, D.; Avaro, J. T.; Schupp, D. J.; Gebauer, D., Capturing an amorphous $BaSO_4$ intermediate precursor to barite. *CrystEngComm* **2020,** *22*, 1310-1313.

[114] Rodriguez-Navarro, C.; Burgos-Cara, A.; Di Lorenzo, F.; Ruiz-Agudo, E.; Elert, K., Nonclassical Crystallization of Calcium Hydroxide via Amorphous Precursors and the Role of Additives. *Crystal Growth & Design* **2020,** *20*, 4418-4432.

[115] Ruiz-Agudo, C.; Putnis, C. V.; Ibañez-Velasco, A.; Ruiz-Agudo, E.; Putnis, A., A potentiometric study of the performance of a commercial copolymer in the precipitation of scale forming minerals. *CrystEngComm* **2016,** *18*, 5744-5753.

[116] Wiedenbeck, E.; Kovermann, M.; Gebauer, D.; Colfen, H., Liquid Metastable Precursors of Ibuprofen as Aqueous Nucleation Intermediates. *Angew. Chem. Int. Ed.* **2019,** *58*, 19103-19109.

[117] Schneider, C. M.; Cölfen, H., High-resolution analysis of small silver clusters by analytical ultracentrifugation. *J. Phys. Chem. Lett.* **2019,** *10*, 6558-6564.

[118] Lukić, M. J.; Wiedenbeck, E.; Reiner, H.; Gebauer, D., Chemical trigger toward phase separation in the aqueous Al(III) system revealed. *Science Advances* **2020,** *6*, eaba6878.

[119] Scheck, J.; Wu, B.; Drechsler, M.; Rosenberg, R.; Van Driessche, A. E.; Stawski, T. M.; Gebauer, D., The molecular mechanism of iron(III) oxide nucleation. *J. Phys. Chem. Lett.* **2016,** *7*, 3123-3130.

[120] Kellermeier, M.; Picker, A.; Kempter, A.; Cölfen, H.; Gebauer, D., A straightforward treatment of activity in aqueous $CaCO_3$ solutions and the consequences for nucleation theory. *Adv. Mater.* **2014,** *26*, 752-757.

[121] Gindele, M. B.; Malaszuk, K. K.; Peter, C.; Gebauer, D., On the Binding Mechanisms of Calcium Ions to Polycarboxylates: Effects of Molecular Weight, Side Chain, and Backbone Chemistry. *Langmuir* **2022,** https://doi.org/10.1021/acs.langmuir.2c01662.

[122] Picker, A.; Kellermeier, M.; Seto, J.; Gebauer, D.; Cölfen, H., The multiple effects of amino acids on the early stages of calcium carbonate crystallization. *Zeitschrift für Kristallographie - Crystalline Materials* **2012,** *227*, 744-757.

[123] Rao, A.; Berg, J. K.; Kellermeier, M.; Gebauer, D., Sweet on biomineralization: effects of carbohydrates on the early stages of calcium carbonate crystallization. *Eur. J. Mineral.* **2014,** *26*, 537-552.

[124] Pendola, M.; Jain, G.; Huang, Y.-C.; Gebauer, D.; Evans, J. S., Secrets of the Sea Urchin Spicule Revealed: Protein Cooperativity Is Responsible for ACC Transformation, Intracrystalline Incorporation, and Guided Mineral Particle Assembly in Biocomposite Material Formation. *ACS Omega* **2018**, *3*, 11823-11830.

[125] Huang, Y.-C. Multistep Crystallization via Biomolecular and Ionic Additives: Bidirectional Synergetic Interactions in Protein-Directed Mineralization. Dissertation, University of Konstanz, 2019.

[126] Gebauer, D.; Cölfen, H.; Verch, A.; Antonietti, M., The multiple roles of additives in $CaCO_3$ crystallization: A quantitative case study. *Adv. Mater.* **2009,** *21*, 435-439.

[127] Dąbrowski, A., Adsorption—from theory to practice. *Adv. Colloid Interface Sci.* **2001,** *93*, 135-224.

[128] Pandey, L. M., Surface engineering of nano-sorbents for the removal of heavy metals: Interfacial aspects. *Journal of Environmental Chemical Engineering* **2021,** *9*, 104586.

[129] Dudev, T.; Lim, C., Principles governing Mg, Ca, and Zn binding and selectivity in proteins. *Chem. Rev.* **2003,** *103*, 773-788.

[130] Dokmanić, I.; Šikić, M.; Tomić, S., Metals in proteins: correlation between the metal-ion type, coordination number and the amino-acid residues involved in the coordination. *Acta Crystallogr. Sect. D. Biol. Crystallogr.* **2008,** *64*, 257-263.

[131] Tsortos, A.; Nancollas, G. H., The role of polycarboxylic acids in calcium phosphate mineralization. *J. Colloid Interface Sci.* **2002,** *250*, 159-167.

[132] Campbell, A.; Ebrahimpour, A.; Perez, L.; Smesko, S.; Nancollas, G., The dual role of polyelectrolytes and proteins as mineralization promoters and inhibitors of calcium oxalate monohydrate. *Calcified tissue international* **1989,** *45*, 122-128.

[133] Liu, G., Tuning the properties of charged polymers at the solid/liquid interface with ions. *Langmuir* **2018,** *35*, 3232-3247.

[134] Misak, N. Z., Langmuir isotherm and its application in ion-exchange reactions. *Reactive polymers* **1993,** *21*, 53-64.

[135] Molnar, F.; Rieger, J., "Like-charge attraction" between anionic polyelectrolytes: molecular dynamics simulations. *Langmuir* **2005,** *21*, 786-789.

[136] Fantinel, F.; Rieger, J.; Molnar, F.; Hübler, P., Complexation of polyacrylates by Ca^{2+} ions. Time-resolved studies using attenuated total reflectance Fourier transform infrared dialysis spectroscopy. *Langmuir* **2004,** *20*, 2539-2542.

[137] Ayawei, N.; Ebelegi, A. N.; Wankasi, D., Modelling and Interpretation of Adsorption Isotherms. *Journal of Chemistry* **2017,** *2017*, 3039817.

[138] SenthilKumar, P.; Ramalingam, S.; Abhinaya, R.; Kirupha, S. D.; Vidhyadevi, T.; Sivanesan, S., Adsorption equilibrium, thermodynamics, kinetics, mechanism and process design of zinc(II) ions onto cashew nut shell. *The Canadian Journal of Chemical Engineering* **2012,** *90*, 973-982.

[139] Fard, R. F.; Azimi, A.; Bidhendi, G. N., Batch kinetics and isotherms for biosorption of cadmium onto biosolids. *Desalination and Water Treatment* **2011,** *28*, 69-74.

[140] Ringot, D.; Lerzy, B.; Chaplain, K.; Bonhoure, J.-P.; Auclair, E.; Larondelle, Y., In vitro biosorption of ochratoxin A on the yeast industry by-products: Comparison of isotherm models. *Bioresour. Technol.* **2007,** *98*, 1812-1821.

[141] Pandey, A.; Bera, D.; Anupam, S.; Ray, L., Potential of Agarose for Biosorption of Cu(II) In Aqueous System. *American Journal of Biochemistry and Biotechnology* **2007,** *3*, 55-59.

[142] Wang, Z.; Liao, F., Synthesis of poly(ortho-phenylenediamine) fluffy microspheres and application for the removal of Cr(VI). *Journal of Nanomaterials* **2012,** *2012*, 682802.

[143] Batzias, F.; Sidiras, D., Dye adsorption by calcium chloride treated beech sawdust in batch and fixed-bed systems. *J. Hazard. Mater.* **2004,** *114*, 167-174.

[144] Benmaamar, Z.; Bengueddach, A., Correlation with different models for adsorption isotherms of m-xylene and toluene on zeolites. *J. Appl. Sci. Environ. Sanit* **2007,** *2*, 43-56.

[145] Nodehi, A.; Moosavian, M. A.; Haghighi, M. N.; Sadr, A., A new method for determination of the adsorption isotherm of SDS on polystyrene latex particles using conductometric titrations. *Chemical Engineering & Technology* **2007,** *30*, 1732-1738.

[146] Mai, S.; Wei, C. C.; Gu, L. S.; Tian, F. C.; Arola, D. D.; Chen, J. H.; Jiao, Y.; Pashley, D. H.; Niu, L. N.; Tay, F. R., Extrafibrillar collagen demineralization-based chelate-and-rinse technique bridges the gap between wet and dry dentin bonding. *Acta Biomaterialia* **2017,** *57*, 435-448.

[147] Sha, F. R.; Tai, T. Y.; Gaidimas, M. A.; Son, F. A.; Farha, O. K., Leveraging Isothermal Titration Calorimetry to Obtain Thermodynamic Insights into the Binding Behavior and Formation of Metal-Organic Frameworks. *Langmuir* **2022,** *38*, 6771-6779.

[148] Peydayesh, M.; Bolisetty, S.; Mohammadi, T.; Mezzenga, R., Assessing the binding performance of amyloid–carbon membranes toward heavy metal ions. *Langmuir* **2019,** *35*, 4161-4170.

[149] Scheck, J.; Drechsler, M.; Ma, X.; Stockl, M. T.; Konsek, J.; Schwaderer, J. B.; Stadler, S. M.; De Yoreo, J. J.; Gebauer, D., Polyaspartic acid facilitates oxolation within iron(III) oxide pre-nucleation clusters and drives the formation of organic-inorganic composites. *J. Chem. Phys.* **2016,** *145*, 211917.

[150] Politi, Y.; Mahamid, J.; Goldberg, H.; Weiner, S.; Addadi, L., Asprich mollusk shell protein: in vitro experiments aimed at elucidating function in $CaCO_3$ crystallization. *CrystEngComm* **2007,** *9*, 1171-1177.

[151] Rieger, J.; Frechen, T.; Cox, G.; Heckmann, W.; Schmidt, C.; Thieme, J., Precursor structures in the crystallization/precipitation processes of $CaCO_3$ and control of particle formation by polyelectrolytes. *Faraday Discuss.* **2007,** *136*, 265-277.

[152] Al-Hamzah, A. A.; East, C. P.; Doherty, W. O. S.; Fellows, C. M., Inhibition of homogenous formation of calcium carbonate by poly(acrylic acid). The effect of molar mass and end-group functionality. *Desalination* **2014,** *338*, 93-105.

[153] Chhim, N.; Kharbachi, C.; Neveux, T.; Bouteleux, C.; Teychené, S.; Biscans, B., Inhibition of calcium carbonate crystal growth by organic additives using the constant composition method in conditions of recirculating cooling circuits. *J. Cryst. Growth* **2017,** *472*, 35-45.

[154] Gindele, M. B.; Steingrube, L. V.; Gebauer, D., Generality of liquid precursor phases in gas diffusion-based calcium carbonate synthesis. *CrystEngComm* **2021,** *23*, 7938-7943.

[155] Wang, Y. W.; Kim, Y. Y.; Stephens, C. J.; Meldrum, F. C.; Christenson, H. K., In Situ Study of the Precipitation and Crystallization of Amorphous Calcium Carbonate (ACC). *Crystal Growth & Design* **2012,** *12*, 1212-1217.

[156] Wada, N.; Horiuchi, N.; Nakamura, M.; Hiyama, T.; Nagai, A.; Yamashita, K., Effect of Poly(acrylic acid) and Polarization on the Controlled Crystallization of Calcium Carbonate on Single-Phase Calcite Substrates. *Crystal Growth & Design* **2013,** *13*, 2928-2937.

[157] Sun, S.; Mao, L. B.; Lei, Z.; Yu, S. H.; Cölfen, H., Hydrogels from amorphous calcium carbonate and polyacrylic acid: bio‐inspired materials for "mineral plastics". *Angew. Chem. Int. Ed.* **2016,** *55*, 11765-11769.

[158] Wu, Y.-T.; Grant, C., Effect of chelation chemistry of sodium polyaspartate on the dissolution of calcite. *Langmuir* **2002,** *18*, 6813-6820.

[159] Lumb, R.; Martell, A. E., Metal chelating tendencies of glutamic and aspartic acids. *The Journal of Physical Chemistry* **1953,** *57*, 690-693.

[160] Vavrusova, M.; Skibsted, L. H., Calcium binding to dipeptides of aspartate and glutamate in comparison with orthophosphoserine. *J. Agric. Food. Chem.* **2013,** *61*, 5380-5384.

[161] Kołodyńska, D., Chitosan as an effective low-cost sorbent of heavy metal complexes with the polyaspartic acid. *Chem. Eng. J.* **2011,** *173*, 520-529.

[162] Bolster, C. H.; Hornberger, G. M., On the use of linearized Langmuir equations. *Soil Science Society of America Journal* **2007,** *71*, 1796-1806.

[163] van Duin, M.; Peters, J. A.; Kieboom, A. P.; van Bekkum, H., Synergic coordination of calcium in borate-polyhydroxycarboxylate systems. *Carbohydr. Res.* **1987,** *162*, 65-78.

[164] Wiseman, T.; Williston, S.; Brandts, J. F.; Lin, L.-N., Rapid measurement of binding constants and heats of binding using a new titration calorimeter. *Anal. Biochem.* **1989,** *179*, 131-137.

[165] Freire, E.; Mayorga, O. L.; Straume, M., Isothermal titration calorimetry. *Anal. Chem.* **1990,** *62*, 950A-959A.

[166] Lan, Q.; Bassi, A. S.; Zhu, J.-X. J.; Margaritis, A., A modified Langmuir model for the prediction of the effects of ionic strength on the equilibrium characteristics of protein adsorption onto ion exchange/affinity adsorbents. *Chem. Eng. J.* **2001,** *81*, 179-186.

[167] O'Brien, L. C.; Root, H. B.; Wei, C.-C.; Jensen, D.; Shabestary, N.; De Meo, C.; Eder, D. J., $M^{2+}\bullet$ EDTA binding affinities: A modern experiment in thermodynamics for the physical chemistry laboratory. *J. Chem. Educ.* **2015,** *92*, 1547-1551.

[168] Paris, S.; Gruber, D.; Cölfen, H.; Bulgun, N.; Prause, E. Calcium coacervates for remineralization and for demineralization inhibition. US 2022/0202657 A1, 2022.

[169] Lappan, U.; Geißler, U.; Oelmann, M.; Schwarz, S., Apparent dissociation constants of polycarboxylic acids in presence of polycations. *Colloid. Polym. Sci.* **2012,** *290*, 1665-1670.

[170] Tang, N.; Skibsted, L. H., Calcium binding to amino acids and small glycine peptides in aqueous solution: Toward peptide design for better calcium bioavailability. *J. Agric. Food. Chem.* **2016,** *64*, 4376-4389.

[171] Leavitt, S.; Freire, E., Direct measurement of protein binding energetics by isothermal titration calorimetry. *Current opinion in structural biology* **2001,** *11*, 560-566.

[172] Tiffany, M. L.; Krimm, S., New chain conformations of poly(glutamic acid) and polylysine. *Biopolymers* **1968,** *6*, 1379-82.

[173] Song, S. H.; Asher, S. A., UV Resonance Raman Studies of Peptide Conformation in Poly(L-Lysine), Poly(L-Glutamic Acid), and Model Complexes: the Basis for Protein Secondary Structure Determinations. *J. Am. Chem. Soc.* **1989,** *111*, 4295-4305.

[174] Horkay, F.; Hecht, A. M.; Geissler, E., Similarities between polyelectrolyte gels and biopolymer solutions. *J. Polym. Sci., Part B: Polym. Phys.* **2006,** *44*, 3679-3686.

[175] Blasie, C. A.; Berg, J. M., Structure-Based Thermodynamic Analysis of a Coupled Metal Binding−Protein Folding Reaction Involving a Zinc Finger Peptide. *Biochemistry* **2002,** *41*, 15068-15073.

[176] Murphy, K. P.; Xie, D.; Garcia, K. C.; Amzel, L. M.; Freire, E., Structural energetics of peptide recognition: angiotensin II/antibody binding. *Proteins: Structure, Function, and Bioinformatics* **1993,** *15*, 113-120.

[177] D'aquino, J. A.; Gómez, J.; Hilser, V. J.; Lee, K. H.; Amzel, L. M.; Freire, E., The magnitude of the backbone conformational entropy change in protein folding. *Proteins: Structure, Function, and Bioinformatics* **1996,** *25*, 143-156.

[178] Wei, J.; Hoagland, D. A.; Zhang, G.; Su, Z., Effect of divalent counterions on polyelectrolyte multilayer properties. *Macromolecules* **2016,** *49*, 1790-1797.

[179] Urry, D. W.; Peng, S. Q.; Parker, T. M.; Gowda, D. C.; Harris, R. D., Relative significance of electrostatic- and hydrophobic-induced pK_a shifts in a model protein: The aspartic acid residue. *Angew. Chem. Int. Ed.* **1993,** *32*, 1440-1442.

[180] Urry, D. W.; Peng, S.; Parker, T., Delineation of electrostatic- and hydrophobic-induced pK_a shifts in polypentapeptides: the glutamic acid residue. *J. Am. Chem. Soc.* **1993,** *115*, 7509-7510.

[181] Silverman, D.; Kalota, D.; Stover, F., Effect of pH on corrosion inhibition of steel by polyaspartic acid. *Corrosion* **1995,** *51*, 818-825.

[182] Ho, G. H.; Ho, T. I.; Hsieh, K. H.; Su, Y. C.; Lin, P. Y.; Yang, J.; Yang, K. H.; Yang, S. C., γ-polyglutamic acid produced by Bacillus Subtilis (Natto): Structural characteristics, chemical properties and biological functionalities. *J. Chin. Chem. Soc.* **2006,** *53*, 1363-1384.

[183] Sadeghpour, A.; Vaccaro, A.; Rentsch, S.; Borkovec, M., Influence of alkali metal counterions on the charging behavior of poly(acrylic acid). *Polymer* **2009,** *50*, 3950-3954.

[184] Po, H. N.; Senozan, N., The Henderson-Hasselbalch equation: its history and limitations. *J. Chem. Educ.* **2001,** *78*, 1499.

[185] Spencer, H., A note on dissociation constants of polycarboxylic acids. *Journal of Polymer Science* **1962,** *56*, S25-S28.

[186] Lebrón-Paler, A.; Pemberton, J. E.; Becker, B. A.; Otto, W. H.; Larive, C. K.; Maier, R. M., Determination of the acid dissociation constant of the biosurfactant monorhamnolipid in aqueous solution by potentiometric and spectroscopic methods. *Anal. Chem.* **2006,** *78*, 7649-7658.

[187] Agostinho Neto, A.; Drigo Filho, E.; Fossey, M. A.; Ruggiero Neto, J., Polyacids self-dissociation model. *J. Phys. Chem. B* **1997,** *101*, 9833-9837.

[188] Ostolska, I.; Wiśniewska, M., Comparison of the influence of polyaspartic acid and polylysine functional groups on the adsorption at the Cr_2O_3—aqueous polymer solution interface. *Appl. Surf. Sci.* **2014,** *311*, 734-739.

[189] Kokufuta, E.; Suzuki, S.; Harada, K., Potentiometric titration behavior of polyaspartic acid prepared by thermal polycondensation. *Biosystems* **1977,** *9,* 211-214.

[190] Murai, N.; Sugai, S., Counterion activity of ionizable polypeptides. *Biopolymers: Original Research on Biomolecules* **1974,** *13*, 857-860.

[191] Brown, A., Analysis of cooperativity by isothermal titration calorimetry. *International journal of molecular sciences* **2009,** *10*, 3457-3477.

[192] Kelly, D. J.; Clark, N.; Zhou, M.; Gebauer, D.; Gorbachev, R. V.; Haigh, S. J., In Situ TEM Imaging of Solution‐Phase Chemical Reactions Using 2D‐Heterostructure Mixing Cells. *Adv. Mater.* **2021**, 2100668.

[193] Gebauer, D.; Oliynyk, V.; Salajkova, M.; Sort, J.; Zhou, Q.; Bergström, L.; Salazar-Alvarez, G., A transparent hybrid of nanocrystalline cellulose and amorphous calcium carbonate nanoparticles. *Nanoscale* **2011,** *3*, 3563-3566.

[194] Chang, C.-C.; Wu, H.-L.; Kuo, C.-H.; Huang, M. H., Hydrothermal synthesis of monodispersed octahedral gold nanocrystals with five different size ranges and their self-assembled structures. *Chem. Mater.* **2008,** *20*, 7570-7574.

[195] Schüler, T.; Tremel, W., Versatile wet-chemical synthesis of non-agglomerated CaCO₃ vaterite nanoparticles. *Chem. Commun.* **2011,** *47*, 5208-5210.

[196] Finney, A. R.; Innocenti Malini, R.; Freeman, C. L.; Harding, J. H., Amino Acid and Oligopeptide Effects on Calcium Carbonate Solutions. *Crystal Growth & Design* **2020,** *20*, 3077-3092.

[197] Nebel, H.; Neumann, M.; Mayer, C.; Epple, M., On the structure of amorphous calcium carbonate−A detailed study by solid-state NMR spectroscopy. *Inorg. Chem.* **2008,** *47*, 7874-7879.

[198] McNeill, I.; Sadeghi, S., Thermal stability and degradation mechanisms of poly(acrylic acid) and its salts: Part 3 - Magnesium and calcium salts. *Polym. Degrad. Stab.* **1990,** *30*, 267-282.

[199] Dayen, J.; Faramarzi, V.; Pauly, M.; Kemp, N.; Barbero, M.; Pichon, B.; Majjad, H.; Begin-Colin, S.; Doudin, B., Nanotrench for nano and microparticle electrical interconnects. *Nanotechnology* **2010,** *21*, 335303.

[200] Sun, T.; Bernabini, C.; Morgan, H., Single-colloidal particle impedance spectroscopy: Complete equivalent circuit analysis of polyelectrolyte microcapsules. *Langmuir* **2010,** *26*, 3821-3828.

[201] Sun, L.; Wang, J.; Bonaccurso, E., Conductivity of individual particles measured by a microscopic four-point-probe method. *Scientific reports* **2013,** *3*, 1-5.

[202] Kreuer, K.-D.; Paddison, S. J.; Spohr, E.; Schuster, M., Transport in proton conductors for fuel-cell applications: simulations, elementary reactions, and phenomenology. *Chem. Rev.* **2004,** *104*, 4637-4678.

[203] Sahoo, R.; Mondal, S.; Pal, S. C.; Mukherjee, D.; Das, M. C., Covalent‐Organic Frameworks (COFs) as Proton Conductors. *Advanced Energy Materials* **2021,** *11*, 2102300.

[204] Cao, L.; Wu, H.; He, X.; Geng, H.; Zhang, R.; Qiu, M.; Yang, P.; Shi, B.; Khan, N. A.; Jiang, Z., Flexible, transparent ion-conducting membranes from two-dimensional nanoclays of intrinsic conductivity. *J. Mater. Chem. A* **2019,** *7*, 25657-25664.

[205] Kim, Y. Y.; Hetherington, N. B.; Noel, E. H.; Kröger, R.; Charnock, J. M.; Christenson, H. K.; Meldrum, F. C., Capillarity creates single‐crystal calcite

nanowires from amorphous calcium carbonate. *Angew. Chem. Int. Ed.* **2011,** *50,* 12572-12577.

[206] Jenewein, C.; Ruiz-Agudo, C.; Wasman, S.; Gower, L.; Cölfen, H., Development of a novel $CaCO_3$ PILP based cementation method for quartz sand. *CrystEngComm* **2019,** *21,* 2273-2280.

[207] Swanson, H. E.; Tatge, E., Standard X-ray Diffraction Powder Patterns. *Natl. Bur. Stand. (U.S.)* **1953,** *Circ. 539,* 58.

[208] McMurdie, H. F.; Morris, M. C.; Evans, E. H.; Paretzkin, B.; Wong-Ng, W.; Hubbard, C. R., Standard X-Ray Diffraction Powder Patterns - Calcium Oxide. *Powder Diffr.* **1986,** *1,* 266.

[209] Heda, P. K.; Dollimore, D.; Alexander, K. S.; Chen, D.; Law, E.; Bicknell, P., A method of assessing solid state reactivity illustrated by thermal decomposition experiments on sodium bicarbonate. *Thermochim. Acta* **1995,** *255,* 255-272.

[210] Tudorachi, N.; Chiriac, A. P., TGA/FTIR/MS study on thermal decomposition of poly(succinimide) and sodium poly(aspartate). *Polym. Test.* **2011,** *30,* 397-407.

[211] Farhadi‐Khouzani, M.; Chevrier, D. M.; Zhang, P.; Hedin, N.; Gebauer, D., Water as the key to proto‐aragonite amorphous $CaCO_3$. *Angew. Chem. Int. Ed.* **2016,** *55,* 8117-8120.

[212] Khouzani, M. F.; Chevrier, D. M.; Güttlein, P.; Hauser, K.; Zhang, P.; Hedin, N.; Gebauer, D., Disordered amorphous calcium carbonate from direct precipitation. *CrystEngComm* **2015,** *17,* 4842-4849.

[213] Benhelal, E.; Zahedi, G.; Shamsaei, E.; Bahadori, A., Global strategies and potentials to curb CO_2 emissions in cement industry. *Journal of cleaner production* **2013,** *51,* 142-161.

[214] Figueroa, J. D.; Fout, T.; Plasynski, S.; McIlvried, H.; Srivastava, R. D., Advances in CO_2 capture technology—The U.S. Department of Energy's Carbon Sequestration Program. *International journal of greenhouse gas control* **2008,** *2,* 9-20.

[215] Huang, L.; Krigsvoll, G.; Johansen, F.; Liu, Y.; Zhang, X., Carbon emission of global construction sector. *Renewable and Sustainable Energy Reviews* **2018,** *81,* 1906-1916.

[216] Schneider, M.; Romer, M.; Tschudin, M.; Bolio, H., Sustainable cement production—present and future. *Cem. Concr. Res.* **2011,** *41,* 642-650.

[217] Hendriks, C. A.; Worrell, E.; De Jager, D.; Blok, K.; Riemer, P. In *Emission reduction of greenhouse gases from the cement industry*, Proceedings of the fourth international conference on greenhouse gas control technologies, IEA GHG R&D Programme Interlaken, Austria: 1998; 939-944.

[218] Gartner, E., Industrially interesting approaches to "low-CO_2" cements. *Cem. Concr. Res.* **2004,** *34,* 1489-1498.

[219] Combes, C.; Miao, B.; Bareille, R.; Rey, C., Preparation, physical-chemical characterisation and cytocompatibility of calcium carbonate cements. *Biomaterials* **2006,** *27*, 1945-1954.

[220] Fontaine, M.-L.; Combes, C.; Sillam, T.; Dechambre, G.; Rey, C. In *New calcium carbonate-based cements for bone reconstruction*, Key Eng. Mater., Trans Tech Publ: 2005; 105-108.

[221] Hargis, C. W.; Chen, I. A.; Devenney, M.; Fernandez, M. J.; Gilliam, R. J.; Thatcher, R. P., Calcium Carbonate Cement: A Carbon Capture, Utilization, and Storage (CCUS) Technique. *Materials* **2021,** *14*, 2709.

[222] Gartner, E. In *Potential improvements in cement sustainability*, Proceedings of the 31st Cement and Concrete Science Conference Novel Developments and Innovation in Cementitious Materials, London, UK, 2011; 12-13.

[223] Winters, D.; Boakye, K.; Simske, S., Toward Carbon-Neutral Concrete through Biochar–Cement–Calcium Carbonate Composites: A Critical Review. *Sustainability* **2022,** *14*, 4633.

[224] Cheng, X.; Varona, P. L.; Olszta, M. J.; Gower, L. B., Biomimetic synthesis of calcite films by a polymer-induced liquid-precursor (PILP) process: 1. Influence and incorporation of magnesium. *J. Cryst. Growth* **2007,** *307*, 395-404.

[225] Ropret, P.; Legan, L.; Retko, K.; Špec, T.; Pondelak, A.; Škrlep, L.; Škapin, A. S., Evaluation of vibrational spectroscopic techniques for consolidants' penetration depth determination. *Journal of Cultural Heritage* **2017,** *23*, 148-156.

[226] Gower, L.; Tirrell, D., Calcium carbonate films and helices grown in solutions of poly(aspartate). *J. Cryst. Growth* **1998,** *191*, 153-160.

[227] Oaki, Y.; Kajiyama, S.; Nishimura, T.; Imai, H.; Kato, T., Nanosegregated amorphous composites of calcium carbonate and an organic polymer. *Adv. Mater.* **2008,** *20*, 3633-3637.

[228] Olszta, M. J.; Odom, D. J.; Douglas, E. P.; Gower, L. B., A New Paradigm for Biomineral Formation: Mineralization via an Amorphous Liquid-Phase Precursor. *Connective Tissue Research* **2009,** *44*, 326-334.

[229] Brečević, L.; Nielsen, A. E., Solubility of amorphous calcium carbonate. *J. Cryst. Growth* **1989,** *98*, 504-510.

[230] Politi, Y.; Metzler, R. A.; Abrecht, M.; Gilbert, B.; Wilt, F. H.; Sagi, I.; Addadi, L.; Weiner, S.; Gilbert, P., Transformation mechanism of amorphous calcium carbonate into calcite in the sea urchin larval spicule. *Proc. Natl. Acad. Sci. U.S.A.* **2008,** *105*, 17362-17366.

[231] Dai, L.; Cheng, X.; Gower, L. B., Transition bars during transformation of an amorphous calcium carbonate precursor. *Chem. Mater.* **2008,** *20*, 6917-6928.

[232] Puertas, F.; Santos, H.; Palacios, M.; Martínez-Ramírez, S., Polycarboxylate superplasticiser admixtures: effect on hydration, microstructure and rheological behaviour in cement pastes. *Advances in Cement Research* **2005,** *17*, 77-89.

[233] Bolze, J.; Peng, B.; Dingenouts, N.; Panine, P.; Narayanan, T.; Ballauff, M., Formation and growth of amorphous colloidal CaCO$_3$ precursor particles as detected by time-resolved SAXS. *Langmuir* **2002,** *18*, 8364-8369.

[234] Sun, C. Y.; Stifler, C. A.; Chopdekar, R. V.; Schmidt, C. A.; Parida, G.; Schoeppler, V.; Fordyce, B. I.; Brau, J. H.; Mass, T.; Tambutte, S.; Gilbert, P., From particle attachment to space-filling coral skeletons. *Proc. Natl. Acad. Sci. U.S.A.* **2020,** *117*, 30159-30170.

[235] Rodriguez-Navarro, C.; Suzuki, A.; Ruiz-Agudo, E., Alcohol dispersions of calcium hydroxide nanoparticles for stone conservation. *Langmuir* **2013,** *29*, 11457-11470.

[236] Tedesco, E.; Mičetić, I.; Ciappellano, S. G.; Micheletti, C.; Venturini, M.; Benetti, F., Cytotoxicity and antibacterial activity of a new generation of nanoparticle-based consolidants for restoration and contribution to the safe-by-design implementation. *Toxicology in Vitro* **2015,** *29*, 1736-1744.

[237] Gates, B. D.; Xu, Q.; Stewart, M.; Ryan, D.; Willson, C. G.; Whitesides, G. M., New approaches to nanofabrication: molding, printing, and other techniques. *Chem. Rev.* **2005,** *105*, 1171-1196.

[238] Rodriguez-Navarro, C.; Elert, K.; Ševčík, R., Amorphous and crystalline calcium carbonate phases during carbonation of nanolimes: implications in heritage conservation. *CrystEngComm* **2016,** *18*, 6594-6607.

[239] Mao, L. B.; Meng, Y. F.; Meng, X. S.; Yang, B.; Yang, Y. L.; Lu, Y. J.; Yang, Z. Y.; Shang, L. M.; Yu, S. H., Matrix-Directed Mineralization for Bulk Structural Materials. *J. Am. Chem. Soc.* **2022,** *144*, 18175-18194.

[240] Xiao, C.; Li, M.; Wang, B.; Liu, M.-F.; Shao, C.; Pan, H.; Lu, Y.; Xu, B.-B.; Li, S.; Zhan, D., Total morphosynthesis of biomimetic prismatic-type CaCO$_3$ thin films. *Nat. Commun.* **2017,** *8*, 1-9.

[241] Li, M.; Chen, Y.; Mao, L. B.; Jiang, Y.; Liu, M. F.; Huang, Q.; Yu, Z.; Wang, S.; Yu, S. H.; Lin, C.; Liu, X. Y.; Colfen, H., Seeded Mineralization Leads to Hierarchical CaCO$_3$ Thin Coatings on Fibers for Oil/Water Separation Applications. *Langmuir* **2018,** *34*, 2942-2951.

[242] Saito, T.; Oaki, Y.; Nishimura, T.; Isogai, A.; Kato, T., Bioinspired stiff and flexible composites of nanocellulose-reinforced amorphous CaCO$_3$. *Materials Horizons* **2014,** *1*, 321-325.

[243] Mu, Z.; Kong, K.; Jiang, K.; Dong, H.; Xu, X.; Liu, Z.; Tang, R., Pressure-driven fusion of amorphous particles into integrated monoliths. *Science* **2021,** *372*, 1466-1470.

[244] Xu, X.; Han, J. T.; Cho, K., Formation of amorphous calcium carbonate thin films and their role in biomineralization. *Chem. Mater.* **2004,** *16*, 1740-1746.

[245] Yu, J.; Lei, M.; Cheng, B., Facile preparation of monodispersed calcium carbonate spherical particles via a simple precipitation reaction. *Mater. Chem. Phys.* **2004,** *88*, 1-4.

[246] Boyjoo, Y.; Pareek, V. K.; Liu, J., Synthesis of micro and nano-sized calcium carbonate particles and their applications. *J. Mater. Chem. A* **2014,** *2*, 14270-14288.

[247] Yao, H. B.; Ge, J.; Mao, L. B.; Yan, Y. X.; Yu, S. H., 25th anniversary article: artificial carbonate nanocrystals and layered structural nanocomposites inspired by nacre: synthesis, fabrication and applications. *Adv. Mater.* **2014,** *26*, 163-188.

[248] Cantaert, B.; Kuo, D.; Matsumura, S.; Nishimura, T.; Sakamoto, T.; Kato, T., Use of amorphous calcium carbonate for the design of new materials. *ChemPlusChem* **2017,** *82*, 107-120.

[249] Ihli, J.; Wong, W. C.; Noel, E. H.; Kim, Y.-Y.; Kulak, A. N.; Christenson, H. K.; Duer, M. J.; Meldrum, F. C., Dehydration and crystallization of amorphous calcium carbonate in solution and in air. *Nat. Commun.* **2014,** *5*, 3169.

[250] Addadi, L.; Moradian, J.; Shay, E.; Maroudas, N.; Weiner, S., A chemical model for the cooperation of sulfates and carboxylates in calcite crystal nucleation: relevance to biomineralization. *Proc. Natl. Acad. Sci. U.S.A.* **1987,** *84*, 2732-2736.

[251] Ihli, J.; Bots, P.; Kulak, A.; Benning, L. G.; Meldrum, F. C., Elucidating Mechanisms of Diffusion-Based Calcium Carbonate Synthesis Leads to Controlled Mesocrystal Formation. *Adv. Funct. Mater.* **2013,** *23*, 1965-1973.

[252] Smeets, P. J.; Cho, K. R.; Kempen, R. G.; Sommerdijk, N. A.; De Yoreo, J. J., Calcium carbonate nucleation driven by ion binding in a biomimetic matrix revealed by in situ electron microscopy. *Nat. Mater.* **2015,** *14*, 394-9.

[253] Smeets, P. J.; Cho, K. R.; Sommerdijk, N. A.; De Yoreo, J. J., A Mesocrystal-Like Morphology Formed by Classical Polymer-Mediated Crystal Growth. *Adv. Funct. Mater.* **2017,** *27*, 1701658.

[254] Kim, Y. Y.; Freeman, C. L.; Gong, X.; Levenstein, M. A.; Wang, Y.; Kulak, A.; Anduix-Canto, C.; Lee, P. A.; Li, S.; Chen, L.; Christenson, H. K.; Meldrum, F. C., The Effect of Additives on the Early Stages of Growth of Calcite Single Crystals. *Angew. Chem. Int. Ed.* **2017,** *56*, 11885-11890.

[255] Kim, Y. Y.; Fielding, L. A.; Kulak, A. N.; Nahi, O.; Mercer, W.; Jones, E. R.; Armes, S. P.; Meldrum, F. C., Influence of the Structure of Block Copolymer Nanoparticles on the Growth of Calcium Carbonate. *Chem. Mater.* **2018,** *30*, 7091-7099.

[256] Ihli, J.; Clark, J. N.; Kanwal, N.; Kim, Y. Y.; Holden, M. A.; Harder, R. J.; Tang, C. C.; Ashbrook, S. E.; Robinson, I. K.; Meldrum, F. C., Visualization of the effect of additives on the nanostructures of individual bio-inspired calcite crystals. *Chem. Sci.* **2019,** *10*, 1176-1185.

[257] Ihli, J.; Levenstein, M. A.; Kim, Y. Y.; Wakonig, K.; Ning, Y.; Tatani, A.; Kulak, A. N.; Green, D. C.; Holler, M.; Armes, S. P.; Meldrum, F. C., Ptychographic X-ray tomography reveals additive zoning in nanocomposite single crystals. *Chem. Sci.* **2020,** *11*, 355-363.

[258] Ning, Y.; Meldrum, F. C.; Armes, S. P., Efficient occlusion of oil droplets within calcite crystals. *Chem. Sci.* **2019,** *10*, 8964-8972.

[259] Douverne, M.; Ning, Y.; Tatani, A.; Meldrum, F. C.; Armes, S. P., How Many Phosphoric Acid Units Are Required to Ensure Uniform Occlusion of Sterically Stabilized Nanoparticles within Calcite? *Angew. Chem. Int. Ed.* **2019,** *58*, 8692-8697.

[260] Ning, Y.; Han, L.; Derry, M. J.; Meldrum, F. C.; Armes, S. P., Model Anionic Block Copolymer Vesicles Provide Important Design Rules for Efficient Nanoparticle Occlusion within Calcite. *J. Am. Chem. Soc.* **2019,** *141*, 2557-2567.

[261] Ning, Y.; Han, L.; Douverne, M.; Penfold, N. J.; Derry, M. J.; Meldrum, F. C.; Armes, S. P., What Dictates the Spatial Distribution of Nanoparticles within Calcite? *J. Am. Chem. Soc.* **2019,** *141*, 2481-2489.

[262] Kim, Y. Y.; Darkins, R.; Broad, A.; Kulak, A. N.; Holden, M. A.; Nahi, O.; Armes, S. P.; Tang, C. C.; Thompson, R. F.; Marin, F.; Duffy, D. M.; Meldrum, F. C., Hydroxyl-rich macromolecules enable the bio-inspired synthesis of single crystal nanocomposites. *Nat. Commun.* **2019,** *10*, 5682.

[263] Ihli, J.; Green, D. C.; Lynch, C.; Holden, M. A.; Lee, P. A.; Zhang, S.; Robinson, I. K.; Webb, S. E. D.; Meldrum, F. C., Super-Resolution Microscopy Reveals Shape and Distribution of Dislocations in Single-Crystal Nanocomposites. *Angew. Chem. Int. Ed.* **2019,** *58*, 17328-17334.

[264] Kim, Y. Y.; Carloni, J. D.; Demarchi, B.; Sparks, D.; Reid, D. G.; Kunitake, M. E.; Tang, C. C.; Duer, M. J.; Freeman, C. L.; Pokroy, B.; Penkman, K.; Harding, J. H.; Estroff, L. A.; Baker, S. P.; Meldrum, F. C., Tuning hardness in calcite by incorporation of amino acids. *Nat. Mater.* **2016,** *15*, 903-10.

[265] Dong, Z.; Feng, L.; Hao, Y.; Chen, M.; Gao, M.; Chao, Y.; Zhao, H.; Zhu, W.; Liu, J.; Liang, C., Synthesis of hollow biomineralized $CaCO_3$–polydopamine nanoparticles for multimodal imaging-guided cancer photodynamic therapy with reduced skin photosensitivity. *J. Am. Chem. Soc.* **2018,** *140*, 2165-2178.

[266] Yao, S.; Lin, X.; Xu, Y.; Chen, Y.; Qiu, P.; Shao, C.; Jin, B.; Mu, Z.; Sommerdijk, N. A.; Tang, R., Osteoporotic Bone Recovery by a Highly Bone‐Inductive Calcium Phosphate Polymer‐Induced Liquid‐Precursor. *Advanced Science* **2019,** *6*, 1900683.

[267] Bacino, M.; Girn, V.; Nurrohman, H.; Saeki, K.; Marshall, S. J.; Gower, L.; Saeed, E.; Stewart, R.; Le, T.; Marshall, G. W., Integrating the PILP-mineralization process into a restorative dental treatment. *Dent. Mater.* **2019,** *35*, 53-63.

[268] Wolf, S. E.; Müller, L.; Barrea, R.; Kampf, C. J.; Leiterer, J.; Panne, U.; Hoffmann, T.; Emmerling, F.; Tremel, W., Carbonate-coordinated metal complexes precede the formation of liquid amorphous mineral emulsions of divalent metal carbonates. *Nanoscale* **2011,** *3*, 1158-1165.

[269] Zou, Z.; Habraken, W. J.; Bertinetti, L.; Politi, Y.; Gal, A.; Weiner, S.; Addadi, L.; Fratzl, P., On the phase diagram of calcium carbonate solutions. *Adv. Mater. Interfaces* **2017,** *4*, 1600076.

[270] Aizenberg, J.; Albeck, S.; Weiner, S.; Addadi, L., Crystal-protein interactions studied by overgrowth of calcite on biogenic skeletal elements. *J. Cryst. Growth* **1994,** *142*, 156-164.

[271] Homeijer, S. J.; Olszta, M. J.; Barrett, R. A.; Gower, L. B., Growth of nanofibrous barium carbonate on calcium carbonate seeds. *J. Cryst. Growth* **2008,** *310*, 2938-2945.

[272] Han, Y.; Nishimura, T.; Kato, T., Biomineralization-inspired approach to the development of hybrid materials: preparation of patterned polymer/strontium carbonate thin films using thermoresponsive polymer brush matrices. *Polym. J.* **2014,** *46*, 499-504.

[273] Ikegami, A.; Imai, N., Precipitation of polyelectrolytes by salts. *J. Polym. Sci.* **1962,** *56*, 133-152.

[274] Mureşan, L.; Sinha, P.; Maroni, P.; Borkovec, M., Adsorption and surface-induced precipitation of poly(acrylic acid) on calcite revealed with atomic force microscopy. *Colloids Surf. A Physicochem. Eng. Asp.* **2011,** *390*, 225-230.

[275] Rowlinson, J. S.; Swinton, F. L., *Liquids and Liquid Mixtures, 3rd Edition*. Butterworths: London, 1982.

[276] Bots, P.; Benning, L. G.; Rodriguez-Blanco, J.-D.; Roncal-Herrero, T.; Shaw, S., Mechanistic insights into the crystallization of amorphous calcium carbonate (ACC). *Cryst. Growth Des.* **2012,** *12*, 3806-3814.

[277] Pichon, B. P.; Bomans, P. H.; Frederik, P. M.; Sommerdijk, N. A., A quasi-time-resolved cryoTEM study of the nucleation of $CaCO_3$ under Langmuir monolayers. *J. Am. Chem. Soc.* **2008,** *130*, 4034-4040.

[278] Levi-Kalisman, Y.; Raz, S.; Weiner, S.; Addadi, L.; Sagi, I., Structural differences between biogenic amorphous calcium carbonate phases using X-ray absorption spectroscopy. *Adv. Funct. Mater.* **2002,** *12*, 43-48.

List of Figures

List of Tables

List of Abbreviations

Abbreviations

AAS	atomic absorption spectroscopy
Ac	acetate
ACC	amorphous calcium carbonate
ADM	ammonia diffusion method
AFM	atomic force microscopy
Asp	aspartic acid
Asp1	aspartic acid monomer (protected); Ac-Asp-NH$_2$
Asp3	triaspartic acid (unprotected); H-Asp-Asp-Asp-OH
ATR	attenuated total reflectance
C-AFM	conductive atomic force microscopy
CAT	colloid assembly and transformation
CNT	classical nucleation theory
CCS	carbon capture and storage
DDMAT	2-(dodecylthiocarbonothioylthio)-2-methylpropanoic acid
DLP	dense liquid phase
DOLLOP	dynamically ordered liquid-like oxyanion polymer
e.g.	exempli gratia (engl. "for example")
EDTA	ethylenediaminetetraacetic acid
EDX	energy-dispersive X-ray spectroscopy
et al.	et alii (engl. "and others")
FTIR	Fourier-transform infrared spectroscopy
Glu	glutamic acid
Glu1	glutamic acid monomer (protected); Ac-Glu-NH$_2$
Glu3	triglutamic acid (unprotected); H-Glu-Glu-Glu-OH
GPC	gel permeation chromatography
HEPES	4-(2-hydroxyethyl)-1-piperazineethanesulfonic acid
HPLC	high-performance liquid chromatography
i.e.	id est (engl. "that is")
IAP	ion activity product
IR	infrared / infrared spectroscopy
ISE	ion selective electrode
ITC	isothermal titration calorimetry
LLPS	liquid–liquid phase separation
MAS NMR	magic angle spinning nuclear magnetic resonance spectroscopy
MD	molecular dynamics

MS	mass spectrometry
N/A	not available
NCM	non-contact mode
NMR	nuclear magnetic resonance
No.	numero (engl. „number")
PAA	poly(acrylic acid)
PAsp	poly(aspartic acid)
PAsp20	poly(aspartic acid) with $DP_n \sim 20$
PAsp50	poly(aspartic acid) with $DP_n \sim 50$
pcACC	proto-calcite amorphous calcium carbonate
PCE	polycarboxylate ether
PD	polydispersity
PDMS	polydimethylsiloxane
PGlu	poly(glutamic acid)
PGlu20	poly(glutamic acid) with $DP_n \sim 20$
PGlu50	poly(glutamic acid) with $DP_n \sim 50$
PILP	polymer-induced liquid-precursor
PNC	prenucleation cluster
PTFE	polytetrafluoroethylene
pvACC	proto-vaterite amorphous calcium carbonate
PVC	poly(vinyl chloride)
rpm	revolutions per minute
SCULPT	scalable controlled synthesis and utilization of liquid-like precursors for technological applications
SEM	scanning electron microscopy
SI	supplementary information
ssNMR	solid-state nuclear magnetic resonance spectroscopy
TEM	transmission electron microscopy
TGA	thermogravimetric analysis
wt-%	weight-%

Symbols

(M)	adsorbent concentration
(MX)	adsorbent-adsorbate complex concentration
(X)	adsorbate concentration
a	activity
A_1	exponential growth function amplitude parameter 1
A_2	exponential growth function amplitude parameter 2
c	concentration

c^0	standard concentration
DP_n	degree of polymerization
F	Faraday constant
I	ionic strength
I/V	current/voltage (diagram)
K	microscopic binding equilibrium constant of cluster association
K_{corr}	linear correction factor
K_{ITC}	binding constant (determined by ITC)
K_L	binding constant (determined by Langmuir isotherm fit)
K_R	binding constant (simple hetero association model)
M	molar mass
M_{tot}	total adsorbent concentration
n	molar amount
n_{max}	maximum binding capacity
Q	heat
R	universal gas constant
T	temperature
t	time
t_1	exponential growth function time constant 1
t_2	exponential growth function time constant 2
U	potential
U_0	starting potential
v	addition speed
V	volume
V_0	starting volume
x	microscopic number of calcium ions that bind a carbonate ion
X_R	ratio of total adsorbate to total adsorbent concentration
X_{tot}	total adsorbate concentration
y_0	exponential growth function offset parameter
Z	absolute distance of AFM tip to internal reference point
α_D	dissociation degree
Δ_{bound}	molar amount of carbonate binding not detected by pH change
ΔG^0	standard Gibbs free energy
ΔH^0	standard enthalpy
ΔS^0	standard entropy
ν	wavenumber
ρ	density
σ	standard deviation

Curriculum Vitae

Maxim Benjamin Gindele, M.Sc.
Born: 18.11.1994 in Weingarten, Germany
Nationality: German
Email: gindele@acc.uni-hannover.de

Education

06/2018 – present	**Leibniz University Hannover, Doctoral Degree in Chemistry** Hannover, Germany; started at University of Konstanz (06/2018 – 03/2019) • *Research Area:* Inorganic chemistry • *Doctoral thesis:* Control of crystallization by polymer additives
10/2016 – 11/2018	**University of Konstanz, Master Studies in Chemistry** Konstanz, Germany • *Core courses:* Physical chemistry • Qualification for fast track Ph.D. (master thesis was part of Ph.D. project)
10/2013 – 09/2016	**University of Konstanz, Bachelor Studies in Chemistry** Konstanz, Germany • *Bachelor thesis:* Polymerization of macromonomers in the ultracentrifuge
06/2013	**Studienkolleg St. Johann Blönried, High School Diploma / Abitur** Aulendorf, Germany • *Core subjects:* Chemistry, Physics, Mathematics, German, English

Work Experience

06/2018 – present	**Institute of Inorganic Chemistry, Research Associate / Ph.D. Student** **Leibniz University Hannover,** Hannover, Germany • Autonomous work on research projects including publication of results and patent application • Active participation in international conferences including a GRC Conference in the United States • Coordination and supervising of scientific projects of 6 bachelor students and 2 international students; supervising of laboratories of student practical training classes with up to 30 students

03/2018 – 05/2018	**Material Physics & Analytics Research Department, Intern**
	BASF SE, Ludwigshafen, Germany
	• Investigation of additive effects on calcium carbonate precipitation using automated titration

02/2017 – 10/2017	**Department of Chemistry, Student Research Assistant**
	University of Konstanz, Konstanz, Germany
	• Work on two research projects including polymer synthesis and polymer characterization using AUC

Skills

Languages	**German** (mother tongue)
	English (fluent)
	Mandarin Chinese (limited working proficiency)
IT	Microsoft Office, Origin, LaTeX, Blender, MestReNova
Methods	Titration, AUC, GPC, NMR, AFM, TGA, SEM, EDX, TEM and ITC
Certificates	• European Business Competence License (EBC*L) Certified Manager
	• GDCh Examined Project Manager in Business Chemistry
	• Good Manufacturing Practice (GMP) and Good Laboratory Practice (GLP) Certificates
Volunteering	• **GDCh JungChemikerForum (JCF):** Treasurer and Vice-Chair of Hannover regional section (09/2020-11/2022)
	• **Head of Conference** of JCF Frühjahrssymposium 2022 in Hannover

List of Publications

1. <u>M. B. Gindele</u>, K. K. Malaszuk, C. Peter, Christine, D. Gebauer, On the binding mechanisms of calcium ions to polycarboxylates: Effects of molecular weight, side chain and backbone chemistry, *Langmuir* **2022**, https://doi.org/10.1021/acs.langmuir.2c01662.

2. P. I. Schodder, <u>M. B. Gindele</u>, A. Ott, M. Rückel, R. Ettl, V. Boyko, M. Kellermeier, Probing the effects of polymers on the early stages of calcium carbonate formation by stoichiometric co-titration, *Phys. Chem. Chem. Phys.* **2022**, *24*, 9978 – 9989.

3. <u>M. Gindele</u>, K. Hindricks, J. C. Höner, „Communicating the Future": 24. Frühjahrssymposium. *Nachrichten aus der Chemie* **2022**, 70 (7-8), 110.

4. <u>M. B. Gindele</u>, L. V. Steingrube, D. Gebauer, Generality of liquid precursor phases in gas diffusion-based calcium carbonate synthesis, *CrystEngComm* **2021**, *23*, 7938-7943.

5. B. Häusele, <u>M. B. Gindele</u>, H. Cölfen, Revision of the calibration experiment in asymmetrical flow field-flow fractionation, *J. Chromatogr. A* **2021**, *1635*, 461631.

6. Y.-C. Huang, <u>M. B. Gindele</u>, J. Knaus, A. Rao, D. Gebauer, On mechanisms of mesocrystal formation: magnesium ions and water environments regulate the crystallization of amorphous minerals, *CrystEngComm* **2018**, 20, 4395 – 4405.

Conference Contributions

09/2022 LNQE NanoDay 2022, Hannover, DE
Poster presentation

03/2022 Faraday Discussion 2022: Understanding Crystallisation, Online
Poster presentation

03/2022 24th JCF Frühjahrssymposium, Hannover, DE
Poster presentation

11/2021 8th Granada Münster Discussion Meeting, Münster, DE
Oral presentation

09/2021 LNQE NanoDay 2021, Online
Oral presentation

08/2021 GDCh Science Forum Chemistry, Online
Oral presentation

03/2021 23rd JCF Frühjahrssymposium, Online
Poster presentation

11/2019 7th Granada Münster Discussion Meeting, Granada, ES
Oral presentation

10/2019 LNQE NanoDay 2019, Hannover, DE
Poster presentation

06/2019 Crystal Growth and Assembly GRC, Manchester, NH, US
Poster presentation

03/2019 21st JCF Frühjahrssymposium, Bremen, DE
Poster presentation